A multi-axial optical fibre and linear polarizer based force and torque sensor for dexterous robotic fingertips

Sargeant, Ramon Bradley

Awarding institution:
King's College London

A MULTI-AXIAL OPTICAL FIBRE AND LINEAR POLARIZER BASED FORCE AND TORQUE SENSOR FOR DEXTEROUS ROBOTIC FINGERTIPS

A thesis submitted in partial fulfilment of the requirements for the degree

of

Doctor of Philosophy in Mechanical Engineering

Division of Engineering

King's College London

London

2013

ABSTRACT

As robots play a more pervasive role in our everyday activities more and more research emphasis is being placed on having robots interact directly with humans, whether in terms of taking care of the elderly, medical interventions or performing dangerous or hazardous tasks. Another trend is for robots to use existing human tools to perform desired actions since it is also not always possible or cost effective to design special tools for every robot. This trend has led to the development of anthropomorphic dexterous manipulators that can perform equally or better than the human hand. Thus the accelerating trend is not only to design a dexterous manipulator but to focus on its ability to grasp and manipulate different and sometimes unknown objects.

One of the most researched types of grasp is the precision grasp which accounts for over 80 % of the grasps performed by humans on a daily basis. Precision grasps are grasps involving the fingertips and are generally used for tasks that require fine manipulation skills. Fingertip sensors are therefore important for dexterous manipulators since humans can identify salient properties of an object and formulate effective manipulation strategies solely by grasping the object. This PhD project focuses on developing fingertip sensors, specifically force and torque fingertip sensors that can be integrated into the fingertip of an existing dexterous manipulator and gather contact force and torque information during a grasping event. Another goal is to make the sensor magnetic resonant (MR) compatible so that it can be used in high magnetic environments, as in the case of medical, magnetic resonance imagining applications.

To accomplish these goals two sensors were developed based on light intensity modulation and novel sensing structures. Optical sensing schemes were chosen because they are not susceptible to magnetic interference, the sensor and its light source can be separated by long distances without significant signal attenuation and the size and weight of the actual sensing element can be reduced since the processing electronics can be positioned far from the sensing structure. The first

sensor developed, as part of this PhD work, was a 2-DOF sensor which used a combination of axially-aligned fibres and linear polarizers to modulate the light to measure the applied force and torque respectively. The use of linear polarizers as the main sensing technique for force and torque sensing is a new area of research since linear polarizers have a defined response curve and can be easily cut into any desired shape and size. The experiments conducted with the 2-DOF sensor showed that the linear polarizer response was superior to traditional axially-aligned and reflective techniques and it was tolerant of small deviations and twists in the sensing structure.

The second sensor improved on the first sensor by increasing the number of degrees of freedom from two to six by using a parallel-type 3-UPS (Universal Prismatic Spherical) sensing structure to allow measuring six degrees of movement. All of the joints of the sensing structure were made of nitinol flexures to reduce friction and all of the links were made of plastic and bonded together to produce a flexible but light and strong structure. Another improvement was that all of the optical modulation sensors on the sensing structure were based on linear polarizers thereby reducing the possibility of misalignment errors caused by the transmitting and receiving fibres moving out of axial alignment. The new sensor therefore satisfies the design requirements and the experiments conducted showed that Light Intensity Modulation (LIM) using linear polarizers and an appropriate sensing structure can produce an accurate and versatile force and torque sensor.

ACKNOWLEDGEMENTS

I would like thank my supervisors, staff, colleagues, friends and family for their help and support during the long days and nights of my research.

First, I would like to thank my supervisors Prof. Kaspar Althoefer and Prof. Lakmal Seneviratne whose support, advice and guidance have allowed me to progress through my research and achieving this stage of my academic development.

I would also like to thank the staff of the Division of Engineering and Department of Informatics who provided valuable assistance and technical support during the construction and development of my devices.

In addition I would like to acknowledge the help of my colleagues in the Centre for Robotics Research at King's College London. I would especially like to thank Panagiotis Polygerinos, Dinusha Zbyszewski, Asghar Ataollahi, Allan Jiang, Helge Wurdemann, Christian Deters, Georgia Kyriakidou, Savan Chhaniyara, Emanuele Secco, Hongbin Liu and Xiaojing Song.

I would also like to thank my friends and family for their support through this time.

TABLE OF CONTENTS

LIST OF FIGURES

LIST OF TABLES

LIST OF EQUATIONS

$$I(r,z) = I_0\left(\frac{w_0}{w(z)}\right)^2 e^{\left(\frac{-2r^2}{w^2(z)}\right)}$$ (cd) (3-5) 80

$$w(z) = w_0\left[1+\left(\frac{z\lambda M^2}{\pi w_0^{\,2}}\right)^2\right]^{1/2}$$ (m) (3-6)..... 80

$$z = z_0 + \delta z$$ (m) (3-7)..... 80

$$P(r,z) = \int_0^r I(r,z)\cdot 2\pi r dr$$ (3-8)..... 81

$$\therefore \qquad P(r,z) = \frac{\pi I_0 w_0^{\,2}}{2}\left(1-e^{\frac{-2r^2}{w(z)^2}}\right)$$ (W). **(3-9)**..... 81

$$I_R(z) = K_p \cdot S_k \cdot \frac{\pi I_0 w_0^{\,2}}{2}\left(1-e^{\frac{-2r^2}{w(z)^2}}\right)$$ (A) (3-10)..... 82

$$V_R(z) = R\cdot K_p \cdot S_k \cdot \frac{\pi I_0 w_0^{\,2}}{2}\left(1-e^{\frac{-2r^2}{w(z)^2}}\right)$$ (V) (3-11) 83

$$V_R(z) = q(z-z_0)+V_o$$ (3-12)..... 83

$$\Rightarrow \qquad \delta z = \frac{V_R(z)-V_o}{q}$$ (m) **(3-13)** 83

$$F = \frac{k}{q}\left(V_R(z) - V_o\right)$$ (N) (3-14) 84

$$\Delta r = r_0 \alpha \Delta T$$ (3-15) 85

$$P(\Delta r, z) = \frac{\pi I_0 {w_0}^2}{2}\left(1 - e^{\frac{-2(r_0 \alpha \Delta T)^2}{w(z)^2}}\right).$$ (3-16) 85

$$\frac{\partial V}{\partial T} = R \cdot K_p \cdot S_k \cdot \frac{2\pi I_0 {w_0}^2 {r_0}^2 \alpha^2}{w(z)^2}\left(e^{\frac{-2(r_0 \alpha \Delta T)^2}{w(z)^2}}\right)\Delta T .$$ (3-17) 85

$$T = \frac{JG\theta_r}{L}$$ (3-18) 86

$$J = ab^3\left[\frac{1}{3} - 0.21\frac{b}{a}\left(1 - \frac{b^4}{12a^4}\right)\right]$$ (m^4). (3-19) 88

$$I(\theta) = \eta_p I_0 \cos^2(\theta)$$ (cd) (3-20) 88

$$P(\theta) = \frac{\pi I(\theta) {w_0}^2}{2}\left(1 - e^{\frac{-2r^2}{w^2}}\right)$$ (W) (3-21) 89

$$P(\theta) = \frac{\pi {w_0}^2 \eta_p I_0 \cos^2(\theta)}{2}\left(1 - e^{\frac{-2r^2}{w^2}}\right)$$ (W). (3-22) 89

$$I_R = K_p \cdot S_k \cdot \frac{\pi {w_0}^2 \eta I_0 \cos^2(\theta)}{2}\left(1 - e^{\frac{-2r^2}{w^2}}\right)$$ (A) (3-23) 89

$$V_R = R \cdot K_p \cdot S_k \cdot \frac{\pi {w_0}^2 \eta I_0 \cos^2(\theta)}{2}\left(1 - e^{\frac{-2r^2}{w^2}}\right) \quad \text{(V)} \quad \text{(3-24)} \ldots\ldots 89$$

$$\frac{\partial V}{\partial T} = 2 \cdot R \cdot K_p \cdot S_k \cdot \frac{\pi {w_0}^2 \eta I_0 \cos^2(\theta) {r_0}^2 \alpha^2}{w^2}\left(e^{\frac{-2(r_0 \alpha \Delta T)^2}{w^2}}\right)\Delta T \quad \text{(V/K).} \quad \text{(3-25)} \ldots\ldots 89$$

$$V_R(\theta_r) = c\left(\theta_r - \frac{\pi}{4}\right) + V_1 \quad \text{(V)} \quad \text{(3-26)} \ldots\ldots 91$$

$$T = \frac{JG}{Lc}\left[V_R(\theta_r) - V_1\right] \quad \text{(Nm)} \quad \text{(3-27)} \ldots\ldots 91$$

$$\delta z = \frac{2a^3 F(L-a)^2}{3EI_{xx}(2a+L)^2} \quad \text{(m)} \quad \text{(4-1)} \ldots\ldots 100$$

$$hysteresis(\%) = \left|\frac{F_{load(i)} - F_{unload(i)}}{F_{scale}}\right| \times 100\% \quad \text{(4-2)} \ldots\ldots 104$$

$$F_v = F\cos^2\theta \quad \text{(4-3)} \ldots\ldots 108$$

$$F_A = F\sin\theta \quad \text{(4-4)} \ldots\ldots 108$$

$$\theta_s = \tan^{-1}(\mu) \quad \text{(4-5)} \ldots\ldots 108$$

$$\frac{dT}{d\theta_r} = \frac{\partial T}{\partial \theta_r} + \frac{\partial T}{\partial L}\frac{dL}{d\theta_r} \quad \text{(4-6)} \ldots\ldots 111$$

$$\frac{dT}{dL} = \frac{\partial T}{\partial L} + \frac{\partial T}{\partial \theta_r}\frac{d\theta_r}{dL} \quad \text{(4-7)} \ldots\ldots 111$$

$$\frac{dT}{d\theta_r} = \frac{JG}{L}$$ (4-8) 111

$$\frac{dT}{dL} = -\frac{JG\theta_r}{L^2}.$$ (4-9) 111

$$V(\theta) = V_0 \cos^2(\theta)$$ (V) (4-10) 113

$$\theta = \cos^{-1}\sqrt{\frac{V(\theta)}{V_0}}.$$ (4-11) 114

$$\vec{q} = \vec{p} + [T]\vec{a}$$ (5-1) 143

$$\vec{q} = \vec{b} + \vec{s}$$ (5-2) 143

$$p = \vec{b} + \vec{s} - [T]\vec{a}.$$ **(5-3)** 143

$$s = 2L_p\sqrt{1-\cos^2\gamma}$$ (5-4) 144

$$\vec{B}_1 = R_B\hat{i}$$ (m) (5-5) 145

$$\vec{B}_2 = \frac{R_B}{2}\left(-\hat{i} + \sqrt{3}\hat{j}\right)$$ (m) (5-6) 145

$$\vec{B}_3 = -\frac{R_B}{2}\left(\hat{i} + \sqrt{3}\hat{j}\right)$$ (m) (5-7) 145

$$\vec{Q} = \begin{pmatrix} 0 \\ s\cos\beta \\ s\sin\beta \end{pmatrix}$$ (m) (5-8) 146

$$\vec{E} = R(y,\alpha)\cdot\vec{Q}$$ (5-9) 146

$$\Rightarrow \qquad \vec{E} = \begin{pmatrix} s\sin\alpha\sin\beta \\ s\cos\beta \\ s\cos\alpha\sin\beta \end{pmatrix} \quad \text{(m)} \quad \text{(5-10)} \ldots\ldots 147$$

$$E = \begin{pmatrix} 2L_p \sin\gamma\sin\alpha\sin\beta \\ 2L_p \sin\gamma\cos\beta \\ 2L_p \sin\gamma\cos\alpha\sin\beta \end{pmatrix} \quad \text{(m)} \quad \text{(5-11)} \ldots\ldots 147$$

$$R(z,\psi) = \begin{pmatrix} \cos\psi & -\sin\psi & 0 \\ \sin\psi & \cos\psi & 0 \\ 0 & 0 & 1 \end{pmatrix} \quad \text{(5-12)} \ldots\ldots 149$$

$$T(x, y) = \begin{pmatrix} R_B\cos\psi \\ R_B\sin\psi \\ 0 \end{pmatrix} \quad \text{(5-13)} \ldots\ldots 149$$

$$A = T(x, y)R(z,\psi) \quad \text{(5-14)} \ldots\ldots 149$$

$$\Rightarrow \qquad A = \begin{pmatrix} \cos\psi & -\sin\psi & 0 & R_B\cos\psi \\ \sin\psi & \cos\psi & 0 & R_B\sin\psi \\ 0 & 0 & 1 & 0 \\ 0 & 0 & 0 & 1 \end{pmatrix} \quad \text{(5-15)} \ldots\ldots 150$$

$$\Rightarrow \qquad \vec{P} = \begin{pmatrix} 2L_p \sin\gamma(\sin\alpha\sin\beta\cos\psi - \cos\beta\sin\psi) + R_B\cos\psi \\ 2L_p \sin\gamma(\sin\alpha\sin\beta\sin\psi + \cos\beta\cos\psi) + R_B\sin\psi \\ 2L_p \sin\gamma\cos\alpha\sin\beta \\ 1 \end{pmatrix} \quad \text{(5-16)} \ldots\ldots 150$$

$$\vec{P}_m = \begin{pmatrix} 2L_p \sin\gamma_m(\sin\alpha_m\sin\beta_m\cos\psi_m - \cos\beta_m\sin\psi_m) + R_B\cos\psi_m \\ 2L_p \sin\gamma_m(\sin\alpha_m\sin\beta_m\sin\psi_m + \cos\beta_m\cos\psi_m) + R_B\sin\psi_m \\ 2L_p \sin\gamma_m\cos\alpha_m\sin\beta_m \\ 1 \end{pmatrix} \quad \text{(5-17)} \ldots\ldots 150$$

$$\Rightarrow \qquad c = \sqrt{3}R_B \quad \text{(5-18)} \ldots\ldots 151$$

$$\vec{n} = \left(\vec{P}_2 - \vec{P}_1\right) \times \left(\vec{P}_3 - \vec{P}_1\right) \quad \text{(5-19)} \ldots\ldots 151$$

$$P_1 = \begin{pmatrix} 2L_p \sin\gamma_1 \sin\beta_1 + R_B \\ 2L_p \sin\gamma_1 \cos\beta_1 \\ 2L_p \sin\gamma_1 \cos\alpha_1 \sin\beta_1 \end{pmatrix} \quad \text{(5-20)} \ldots\ldots 152$$

$$P_2 = \begin{pmatrix} -L_p \sin\gamma_2 \left(\sin\alpha_2 \sin\beta_2 + \sqrt{3}\cos\beta_2\right) - \dfrac{R_B}{2} \\ L_p \sin\gamma_2 \left(\sqrt{3}\sin\alpha_2 \sin\beta_2 - \cos\beta_2\right) + \dfrac{\sqrt{3}R_B}{2} \\ 2L_p \sin\gamma_2 \cos\alpha_2 \sin\beta_2 \end{pmatrix} \quad \text{(5-21)} \ldots\ldots 153$$

$$P_3 = \begin{pmatrix} L_p \sin\gamma_3 \left(-\sin\alpha_3 \sin\beta_3 + \sqrt{3}\cos\beta_3\right) - \dfrac{R_B}{2} \\ -L_p \sin\gamma_3 \left(\sqrt{3}\sin\alpha_3 \sin\beta + \cos\beta_3\right) - \dfrac{\sqrt{3}R_B}{2} \\ 2L_p \sin\gamma_3 \cos\alpha_3 \sin\beta_3 \end{pmatrix} \quad \text{(5-22)} \ldots\ldots 153$$

$$\vec{n} = \left[\left(P_{2x} - P_{1x}\right)\hat{i} + \left(P_{2y} - P_{1y}\right)\hat{j} + \left(P_{2z} - P_{1z}\right)\hat{k}\right] \times \left[\left(P_{3x} - P_{1x}\right)\hat{i} + \left(P_{3y} - P_{1y}\right)\hat{j} + \left(P_{3z} - P_{1z}\right)\hat{k}\right] \quad \text{(5-23)} \ldots\ldots 153$$

$$\Rightarrow \begin{aligned} \vec{n} = {} & \left[\left(P_{2y} - P_{1y}\right)\left(P_{3z} - P_{1z}\right) - \left(P_{2z} - P_{1z}\right)\left(P_{3y} - P_{1y}\right)\right] \\ & - \left[\left(P_{2x} - P_{1x}\right)\left(P_{3z} - P_{1z}\right) - \left(P_{2z} - P_{1z}\right)\left(P_{3x} - P_{1x}\right)\right]\hat{j} \\ & + \left[\left(P_{2x} - P_{1x}\right)\left(P_{3y} - P_{1y}\right) - \left(P_{2y} - P_{1y}\right)\left(P_{3x} - P_{1x}\right)\right]\hat{k} \end{aligned} \quad \text{. (5-24)} \ldots\ldots 153$$

$$\Rightarrow \qquad \vec{L}_1 = \left(a_y n_z - a_z n_y\right)\hat{i} - \left(a_x n_z - a_z n_x\right)\hat{j} + \left(a_x n_y - a_y n_x\right)\hat{k} \quad \textbf{(5-25)} \ldots\ldots 154$$

$$\Rightarrow \qquad \vec{L}_2 = \left(b_y n_z - b_z n_y\right)\hat{i} - \left(b_x n_z - b_z n_x\right)\hat{j} + \left(b_x n_y - b_y n_x\right)\hat{k} \quad \textbf{(5-26)} \ldots\ldots 155$$

$$\Rightarrow \qquad \vec{L}_{M1} = \frac{(P_{2x} + P_{1x})}{2}\hat{i} + \frac{(P_{2y} - P_{1y})}{2}\hat{j} + \frac{(P_{2z} - P_{1z}))}{2}\hat{k} \quad \text{(5-27)} \ldots\ldots 155$$

$$\Rightarrow \qquad \vec{L}_{M2} = \frac{(P_{3x} + P_{1x})}{2}\hat{i} + \frac{(P_{3y} - P_{1y})}{2}\hat{j} + \frac{(P_{3z} - P_{1z}))}{2}\hat{k} \quad \text{(5-28)} \ldots\ldots 155$$

$$\vec{r}_c = \vec{L}_{M1} + \vec{L}_1 t \quad \text{(5-29)} \ldots\ldots 155$$

$$\vec{r}_c = \vec{L}_{M2} + \vec{L}_2 k \quad . \quad \text{(5-30)} \ldots\ldots 155$$

$$\vec{L}_2 k - \vec{L}_1 t = \vec{L}_{M1} - \vec{L}_{M2} \quad \text{(5-31)} \ldots\ldots 155$$

$$\vec{L}_{2x} k - \vec{L}_{1x} t = \vec{L}_{M1x} - \vec{L}_{M2x} \quad \text{(5-32)} \ldots\ldots 156$$

$$\vec{L}_{2y} k - \vec{L}_{1y} t = \vec{L}_{M1y} - \vec{L}_{M2y} \quad \text{(5-33)} \ldots\ldots 156$$

$$\vec{L}_{2z} k - \vec{L}_{1z} t = \vec{L}_{M1z} - \vec{L}_{M2z} \; . \quad \text{(5-34)} \ldots\ldots 156$$

$$\begin{pmatrix} L_{2x} & -L_{1x} \\ L_{2y} & -L_{1y} \end{pmatrix} \begin{pmatrix} k \\ t \end{pmatrix} = \begin{pmatrix} L_{M1x} - L_{M2x} \\ L_{M1y} - L_{M2y} \end{pmatrix} \quad \text{(5-35)} \ldots\ldots 156$$

$$k = \frac{L_{1x}\left(L_{M1y} - L_{M2y}\right) - L_{1y}\left(L_{M1x} - L_{M2x}\right)}{L_{2y}L_{1x} - L_{1y}L_{2x}} \quad \text{(5-36)} \ldots\ldots 157$$

$$t = \frac{L_{2x}\left(L_{M1y} - L_{M2y}\right) - L_{2y}\left(L_{M1x} - L_{M2x}\right)}{L_{2y}L_{1x} - L_{1y}L_{2x}} \; . \quad \text{(5-37)} \ldots\ldots 157$$

$$r_{cx} = L_{M1x} + L_{1x}\left(\frac{L_{2x}\left(L_{M1y} - L_{M2y}\right) - L_{2y}\left(L_{M1x} - L_{M2x}\right)}{L_{2y}L_{1x} - L_{1y}L_{2x}}\right) \quad \text{(5-38)} \ldots\ldots 157$$

$$r_{cy} = L_{M1y} + L_{1y}\left(\frac{L_{2x}\left(L_{M1y} - L_{M2y}\right) - L_{2y}\left(L_{M1x} - L_{M2x}\right)}{L_{2y}L_{1x} - L_{1y}L_{2x}}\right) \quad \text{(5-39)} \ldots\ldots 157$$

$$r_{cz} = L_{M1z} + L_{1z}\left(\frac{L_{2x}\left(L_{M1y} - L_{M2y}\right) - L_{2y}\left(L_{M1x} - L_{M2x}\right)}{L_{2y}L_{1x} - L_{1y}L_{2x}}\right) \quad \text{(5-40)} \ldots\ldots 157$$

$$\vec{n}_c \bullet \vec{n}_b = \left|n_c\right|\left|n_b\right|\cos\chi \quad \text{(5-41)} \ldots\ldots 157$$

$$\chi_x = \cos^{-1}\frac{n_{cx}}{\sqrt{{n_{cx}}^2 + {n_{cy}}^2 + {n_{cz}}^2}} \quad \text{(5-42)} \ldots\ldots 158$$

$$\chi_y = \cos^{-1}\frac{n_{cy}}{\sqrt{{n_{cx}}^2 + {n_{cy}}^2 + {n_{cz}}^2}} \quad \text{(5-43)} \ldots\ldots 158$$

$$\chi_z = \cos^{-1}\frac{n_{cz}}{\sqrt{{n_{cx}}^2 + {n_{cy}}^2 + {n_{cz}}^2}} \quad \text{(5-44)} \ldots\ldots 158$$

$$\phi = \chi_x - 90° = \left(\cos^{-1}\frac{n_{cx}}{\sqrt{{n_{cx}}^2 + {n_{cy}}^2 + {n_{cz}}^2}}\right) - 90° \quad \text{(5-45)} \ldots\ldots 159$$

$$\delta = \chi_y - 90° = \left(\cos^{-1}\frac{n_{cy}}{\sqrt{{n_{cx}}^2 + {n_{cy}}^2 + {n_{cz}}^2}}\right) - 90° \quad \text{(5-46)} \ldots\ldots 159$$

$$\psi = \chi_z = \left(\cos^{-1}\frac{n_{cz}}{\sqrt{{n_{cx}}^2 + {n_{cy}}^2 + {n_{cz}}^2}}\right) \quad \text{(5-47)} \ldots\ldots 159$$

$$\sum_{m=1}^{3} F_m - F_{ext} = 0 \quad \text{(5-48)} \quad \text{162}$$

$$\sum_{m=1}^{3} M_m - M_{ext} = 0 \quad \text{(5-49)} \quad \text{162}$$

$$\vec{F}_1 + \vec{F}_2 + \vec{F}_3 = \vec{F}_{ext} \quad \text{(5-50)} \quad \text{162}$$

$$T = k_T \theta_r \quad \text{(5-51)} \quad \text{162}$$

$$\vec{T} = \vec{d} \times \vec{F} \quad \text{(5-52)} \quad \text{163}$$

$$T = \left|d\right|\left|F\right| \sin\phi \quad \text{(5-53)} \quad \text{163}$$

$$T_x = k_T \beta_r \quad \text{(5-54)} \quad \text{163}$$

$$T_y = k_T \alpha_r \quad \text{(5-55)} \quad \text{163}$$

$$T = \left(E_y F_z - E_z F_y\right)\hat{i} - \left(E_x F_z - E_z F_x\right)\hat{j} + \left(E_x F_y - E_y F_x\right)\hat{k} \quad \text{(5-56)} \quad \text{163}$$

$$k_T \beta_r = E_y F_z - E_z F_y \quad \text{(5-57)} \quad \text{163}$$

$$k_T \alpha_r = E_z F_x - E_x F_z \; . \quad \text{(5-58)} \quad \text{164}$$

$$\hat{e} = \frac{\vec{E}}{\left|\vec{E}\right|} \quad \text{(5-59)} \quad \text{164}$$

$$\hat{e} = \frac{\vec{E}}{2L_p\sqrt{1-\cos^2\gamma}} \quad \text{(5-60)} \quad \text{164}$$

$$\Rightarrow \qquad F_p = \frac{k_T \gamma_r}{L_p \cos\gamma} \qquad \text{(5-61)} \ldots\ldots 165$$

$$F_{pT} = \frac{8 k_T \gamma_r}{L_p \cos\gamma} \qquad \text{(5-62)} \ldots\ldots 165$$

$$\vec{F} = \frac{8 k_T \gamma_r}{L_p \cos\gamma} \bullet \hat{e} \qquad \text{(5-63)} \ldots\ldots 166$$

$$F_z = \vec{F} \bullet \hat{k} = \frac{8 k_T \gamma_r}{L_p \cos\gamma} \left(\frac{E_z}{2 L_p \sqrt{1 - \cos^2 \gamma}} \right) \qquad \text{(5-64)} \ldots\ldots 166$$

$$V = V_m \cos^2 \gamma \qquad \text{(5-65)} \ldots\ldots 166$$

$$F_z = \frac{8 k_T \gamma_r}{L_p \cos\gamma} \left(\frac{E_z}{2 L_p \sqrt{1 - \frac{V}{V_m}}} \right) \qquad \text{(5-66)} \ldots\ldots 166$$

$$F_y = \frac{E_y F_z - k_T \beta_r}{E_z} \qquad \text{(5-67)} \ldots\ldots 166$$

$$F_x = \frac{k_T \alpha_r + E_x F_z}{E_z} \qquad \text{(5-68)} \ldots\ldots 166$$

$$+ \left(F_{mx} \sin\psi_m + F_{my} \cos\psi_m \right) \hat{j} + F_{mz} \hat{k} \qquad \text{(5-69)} \ldots\ldots 167$$

$$\vec{F}_{1T} + \vec{F}_{2T} + \vec{F}_{3T} = \vec{F}_{ext} \qquad \text{(5-70)} \ldots\ldots 167$$

$$F_{extx} = F_{1Tx} + F_{2Tx} + F_{3Tx} \qquad \text{(5-71)} \ldots\ldots 167$$

$$F_{exty} = F_{1Ty} + F_{2Ty} + F_{3Ty}$$ (5-72)..... 167

$$F_{extz} = F_{1Tz} + F_{2Tz} + F_{3Tz}$$ (5-73)..... 167

$$\vec{M} = \vec{p} \times \vec{F}$$ (5-74) 167

$$\vec{M}_m = \left(p_{my}F_{mz} - p_{mz}F_{my}\right)\hat{i} - \left(p_{mx}F_{mz} - p_{mz}F_{mx}\right)\hat{j} + \left(p_{mx}F_{my} - p_{my}F_{mx}\right)\hat{k}$$ (5-75)..... 168

$$M_{extx} = \left(p_{1y}F_{1z} - p_{1z}F_{1y}\right) + \left(p_{2y}F_{2z} - p_{2z}F_{2y}\right) + \left(p_{3y}F_{3z} - p_{3z}F_{3y}\right)$$ (5-76)..... 168

$$M_{exty} = -\left[\left(p_{1x}F_{1z} - p_{1z}F_{1x}\right) + \left(p_{2x}F_{2z} - p_{2z}F_{2x}\right) + \left(p_{3x}F_{3z} - p_{3z}F_{3x}\right)\right]$$ (5-77)..... 168

$$M_{extz} = \left(p_{1x}F_{1y} - p_{1y}F_{1x}\right) + \left(p_{2x}F_{2y} - p_{2y}F_{2x}\right) + \left(p_{3x}F_{3y} - p_{3y}F_{3x}\right)$$ (5-78)..... 168

NOMENCLATURE

α	Angle between the local y-axis and the universal joint (degrees)
α_r	Angle between the local y-axis and the universal joint (radians)
β	Angle between the local x-axis and the universal joint (degrees)
β_r	Angle between the local x-axis and the universal joint (radians)
γ	Angle between the links of the prismatic link (degrees)
γ_r	Angle between the links of the prismatic link (radians)
$\vec{n}$	Normal vector to the contact plane of the 6-DOF sensor
ϕ	Orientation of the 6-DOF contact sensor plate about the global x-axis (degrees)
δ	Orientation of the 6-DOF contact sensor plate about the global y-axis (degrees)
ψ	Orientation of the 6-DOF contact sensor plate about the global z-axis (degrees)
λ_B	Bragg wavelength (nm)
$\vec{s}$	Displacement vector for the prismatic link
ε_d	Dielectric Permittivity (F/m)
ε_m	Mechanical Strain
τ	Time constant (s)
R_B	Radius of the circle on which the universal joints lie in the base plate
R_C	Radius of the circle on which the spherical joints lie in the contact plate
A/D	Analogue-to-Digital
CCC	Computing Community Consortium
DOF	Degree of Freedom
ER	Electrorheological
EURON	European Robotics Research Network
F_x	Force along the x-axis

F_y	Force along the y-axis
F_z	Force along the z-axis
M_x	Torque about the x-axis
M_y	Torque about the y-axis
M_z	Torque about the x-axisz
F/T	Force/Torque
FEA	Finite Element Analysis
FEM	Finite Element Model
FET	Field Effect Transistor
fMRI	Functional Magnetic Resonance Imaging
FODS	Fibre Optic Displacement Sensor
IR	Infra Red
LIDAR	Light Detection and Ranging
LIM	Light Intensity Modulation
LED	Light Emitting Diode
MEMS	MicroElectroMechanical Systems
MOSFET	Metal Oxide Semiconductor Field Effect Transistor
MRI	Magnet Resonance Imaging
MR-	Magnetic Resonance
NA	Numerical Aperture
NASA	National Aeronautics and Space Administration
OTDR	Optical Time-Domain Reflectometer
PDMS	Polydimethylsiloxsane
PVDF	Polyvinylidene Fluoride
RADAR	Radio Detection and Ranging
UPS	Universal Prismatic Spherical

CHAPTER 1 – Introduction, Aims and Objectives

This research focuses on the development of a multi-DOF force and torque sensor that can be integrated into the fingertip of a dexterous robot hand to measure the contact forces during a grasping event. This contact data is very important because it provides information about the object's surface features such as texture, flexibility and malleability that other sensing solutions, such as camera vision, cannot entirely provide. Also, camera and radar/lidar systems are ineffective in smoke or fog-filled environments whereas tactile and force information can still be used to navigate the environment, even in complete darkness.

In addition to the above benefits information about the grasped object's surface features can greatly enhance the manipulation of the object. For example, grasping a donut without adequate contact information can result in the donut breaking apart, slipping out of the grasp or leaking filling from the contact points, resulting in a failed and messy experiment. This research focuses on the development of a sensor that can be integrated into the fingertips of dexterous robotic manipulators to allow the robot to enhance its grasping and manipulation capabilities without hindering the normal operation of the robot. The remainder of this chapter presents an introduction to grasping, the aims and objectives of this research, a list of contributions that this research provides to the area of robotic grasping and a short summary of the remaining chapters of this thesis.

1.1 Introduction

The initial trend in robotics development concentrated on the areas of robot kinematics/inverse kinematics and the actuation of the linkages and manipulators. Less consideration was placed on sensing the robot's environment with the few sensors present in the system geared toward providing information for the joint or tool control e.g. current sensors, joint encoders or simple on/off sensors at the manipulator tip to indicate contact/no-contact events. Presently, with the kinematics/inverse kinematics of many robots extensively defined and documented and with advances in hardware and software technologies, more emphasis is being placed on tactile and force/torque sensing so that robots can operate autonomously within their environment.

In 2004, the European Robotics Research Network (EURON) developed a roadmap for the further development of robotics that listed eleven key areas in which robots would play an ever increasing role in the development of human life and economy [1]. The general areas of development highlighted were: automation and manufacturing, working and production assistance, service robots, care assistant/intelligent homes, medical robotics, intelligent vehicles, logistics, field robotics, space robotics, underwater systems and edutainment. Although it is not an exhaustive list of research areas it does encompass many of the areas where robots now dominate such as automation and manufacturing to nascent areas such as edutainment were robots or artificial intelligence devices are becoming more popular.

In 2009, the Computing Community Consortium (CCC), comprised of universities including Georgia Institute of Technology, John Hopkins University and the University of California Berkley, produced a guide detailing the vision of robotics for the United States of America for the next fifteen years [2]. The US roadmap for robotics encompassed many of the areas of the EURON roadmap but grouped the

areas into three main categories: robotics and automation research (for US manufacturing), medical and healthcare robotics and service robotics. There is also a section on emerging trends in robotic technology highlighting some of the possible advances in the next fifteen years. A draft of a document produced by NASA that describes the importance of robots and fully autonomous systems in space exploration is also available [3]. One common trend in these three documents is the need for sensors that can be integrated into dexterous manipulators to monitor grasping forces and enhance grasping efficiency.

A good example of the envisioned direction of the robotics is given by the TWENDY-ONE robot. The TWENDY-ONE robot is a human mimetic robot that was developed to investigate the use of anthropomorphic robots that operate in the human environment and how they can assist humans with routine activities such as carrying objects safely and efficiently, assisting patients with disabilities and functioning as a platform to test safety protocols for human-robot interaction [4]-[8]. Figure 1-1 provides a general description of the major components of the TWENDY-ONE system including a vision system, a 7-DOF dexterous arm and an anthropomorphic hand. TWENDY-ONE is a good example of a highly dexterous robot where dexterity can be defined as the ability to effectively and efficiently position and orient an end-effector within the workspace of the robot [42]. Dexterous manipulators are gaining in popularity because they have high degrees of freedom which are useful for in-hand manipulation or very fine motor control, they are dynamically reconfigurable so the end-effector does not have to be changed for every object and they are multifunctional devices.

One of the more important areas of study for the TWENDY-ONE system is that of grasping and object manipulation. The importance of grasping is emphasized by using a 13-DOF human mimetic hand that has both a 6-DOF force/torque sensor and a tactile sensor in each fingertip. The 6-DOF force/torque sensor is bulky but it can measure all of the components of the applied force and torque (F_x, F_y, F_z, T_x, T_y, T_z), however, it is limited to information from a single contact point. Tactile sensors are thin, flexible and measure the contact pressure distribution of the applied force on an area but they are limited to the normal component (F_z) of the applied force on the contact area. Figure 1-2 provides a graphical illustration of some of the general areas required for anthropomorphic manipulation.

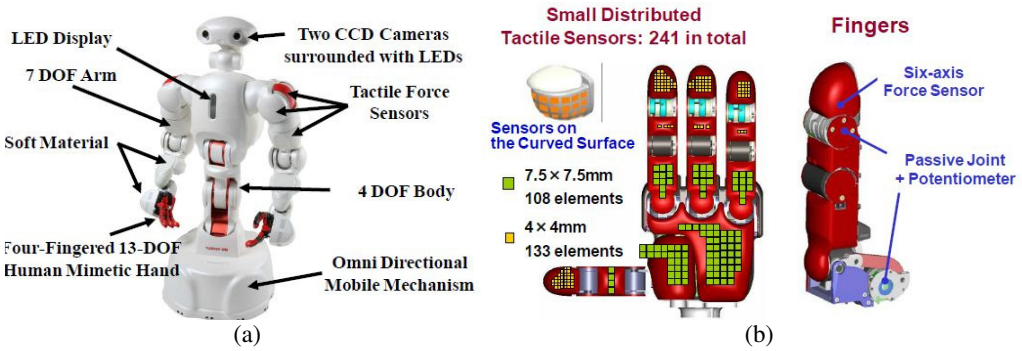

Figure 1-1. The TWENDY-ONE robot. (a) The robot consists of a number of sensors and actuators that try to mimic the capabilities of a human. (b) The human mimetic hand consists of both tactile and force torque sensors to give the force components as well as the pressure distribution of any contact events. Figures adapted from [4].

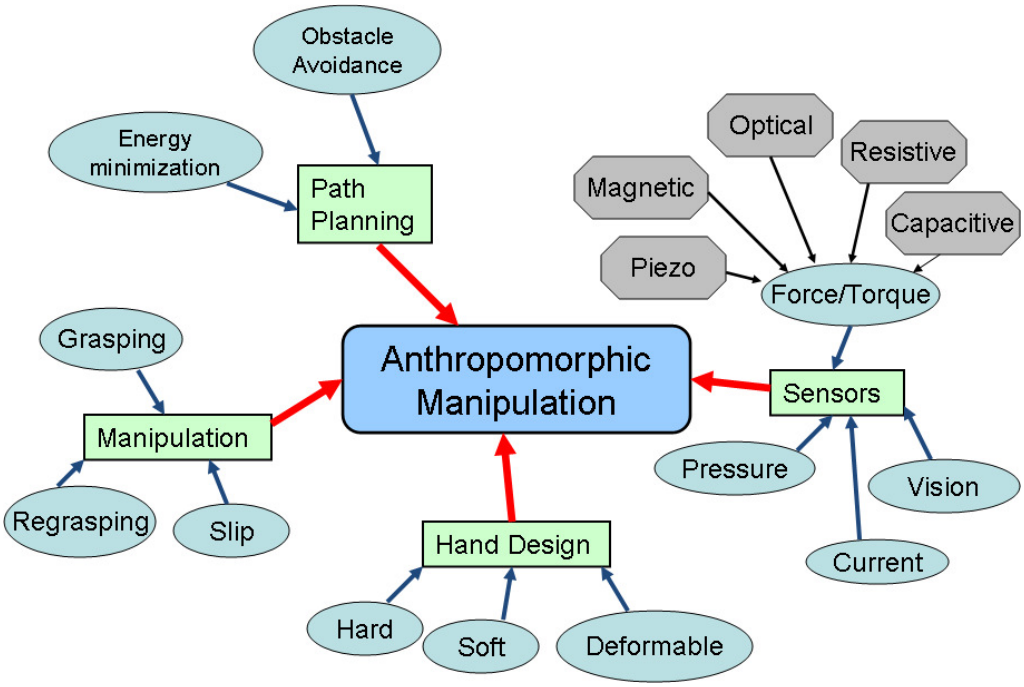

Figure 1-2. An overview of the general areas that are part of research into anthropomorphic manipulation.

Overviews of dexterous grasping and general grasping theory are given in [9]-[33] and highlight the importance of force sensors to stable and effective grasps as well as

object manipulation and detection in general. One of the unique features of force sensors identified in the literature is that the force/tactile data can be used to reconstruct the shape and surface properties such as texture, deformability and flexibility of the contacted object [17]-[22]. This is in contrast to sensors such as vision systems that can provide shape information or limited textural data but not tactile information.

One other feature that is common throughout the grasping literature is the use of hard fingertips for the fingers of the dexterous hand. The hard fingertip represents the simplest option since it can be easily manufactured and it simplifies the simulation of the reaction between the fingertip and the object but it limits the contact area to a single point which can increase the possibility of slippage when grasping an object. Research has since focused on using soft fingertips to improve grasping of objects [34]-[45]. The problem encountered is that trying to simulate the deformation of the finger material can be complex and computationally intensive. The way around this is to use tactile or force sensors to measure the contact force or pressure distribution to give an indication of the change in the deformable material. This represents an evolution in design philosophy from idealistic static fingertips to that of more realistic fingertips similar to that of human skin deformation.

1.2 Research Aims and Objectives

The previous section dealt with the general need for increased dexterity in manipulators, the trade-off between multi-degree-of-freedom sensors and tactile sensors and the shift from hard fingertips to soft-fingertips. This thesis focuses on the sensors required for anthropomorphic/dexterous grasping, specifically 6-DOF force/torque sensors.

The main aim of this research is to develop a 6-DOF force and torque sensor that can be embedded into or onto the fingertip of a dexterous robotic manipulator such that the applied contact force and torque vector can be measured. Adding this

type of sensor greatly increases the information available to the robotic manipulator and it can greatly enhance the grasping ability of the manipulator. An additional aim of this research is to make the sensor MR-compatible so that it can be used for medical applications. Currently there are only a few MR-compatible sensors but none are small enough to fit within the fingertip of a dexterous robotic hand [46]-[49]. The robot can then be used in fMRI experiments.

The objectives of this research are listed below:

- To limit the dimensions of the sensor to fit within a fingertip of dimensions 35 mm × 20 mm × 15 mm (roughly human thumb size).

- Design the sensor to satisfy the following specifications (comparable to the industry standard ATI Nano17 sensor):
  - Maximum dimensions: 17 mm × 17 mm × 20 mm
  - Maximum mass: 9 g
  - $F_z = 0 – 7.5$ N; $F_x = F_y = 5$ N.
  - $T_z = 0 – 0.4$ Nm; $T_x = T_y = 0.2$ Nm

- Develop a mathematical model of the sensor in order to simulate its response to different input experiments in order to study applicability to different environments and possibly to improve the sensor's design.

- Integrate the developed sensor into a dexterous fingertip in order to conduct grasping.

1.3 Research Contributions

This thesis adds a number of novel ideas to the field of force and torque sensing for dexterous manipulation that can be used for future sensor research and development. These contributions are listed below:

- Proposal of the use of linear polarizers to measure the applied force and torque exerted on a grasped object. Currently, measuring torque can be a challenge in LIM sensors. The linear polarizers provide an inexpensive yet robust sensing solution to measure the applied force and torque on an object. More about the principle of linear polarizers and polarized light is given in Chapter 3.

- The proposal and design of a simple 2-DOF sensor (1 force and 1 torque) to measure the force and torque using linear polarizers. The linear polarizers allowed the applied force and torque to be easily decoupled hence improving the effectiveness of the sensor. Details of this sensor's structure and its working principle are given in Chapters 3 and 4.

- The proposal and design of a flexible 6-DOF sensor containing wire flexures and incorporating only linear polarizers as the sensing elements. The structure is based on a lightweight 3-UPS mechanism thereby reducing the dynamic loading on the manipulator when the sensor is placed at the fingertip. Details of the structure are given in Chapter 5.

- Mathematical models describing the light intensity modulation of light passing through two consecutive polarizers. Data from these models can be combined with formulae for the mechanical deformation of the sensing structure to give a full mathematical model of the motion of the developed sensors. Details of the mathematical models are given in Chapters 3 and 5.

1.4 List of Author's Publications

The research presented in this dissertation has resulted in the following peer-reviewed journal and conference publications:

Journal Publications

[1] R. Sargeant, L. D. Seneviratne, and K. Althoefer, "A 2-Axis Optical Force-Torque Fingertip Sensor for Dexterous Grasping Using Linear Polarizers", *IEEE Trans. Instrum. Meas.*, vol. 61, no. 12, pp. 3363-3377, Dec. 2012.

Conference Publications

[2] R. Sargeant, L. D. Seneviratne, and K. Althoefer, "An Investigation of the Use of Linear Polarizers to Measure Force and Torque in Optical 6-DOF Force/Torque Sensors for Dexterous Manipulators", *IEEE Int. Conf. Robotics and Automation*, St. Paul, Minnesota, 2012.

[3] R. Sargeant, H. Liu and K. Althoefer, "An MRI Compatible Optical Multi-Axis Force/Torque Sensors Robotic Surgery", *The 5th Hamlyn Symposium on Medical Robotics*, London, England, 2012.

[4] R. Sargeant, H. Liu, L. D. Seneviratne and K. Althoefer, "An Optical Multi-axial Force/Torque Sensor for Dexterous Grasping and Manipulation", *2012 IEEE Int. Conf. on Multisensor Fusion and Information Integration (MFI 2012)*, Hamburg, Germany, 2012.

1.5 Thesis Structure Summary

This thesis is organised into seven chapters which cover the introduction into dexterous manipulator grasping, a literature review of existing fingertip sensors and what are the limitations of existing sensor designs. The chapters continue with the design, development and demonstration of two force and torques sensors (2-DOF and

6-DOF respectively) incorporating linear polarizers into their design and the results of experiments carried out on the prototypes. The thesis concludes with discussions and conclusions regarding the experimental data and a short look at the future work for the sensors. A short summary of the details of each chapter is given below:

Chapter 1 – Introduction, Aims & Objectives: This chapter presents an overview of force/torque sensors and why they are important for dexterous manipulation. The chapter is comprised of an introduction to robotic grasping, the use of fingertip sensors for dexterous manipulation and the aims and objectives of this research. The chapter ends with a list of contributions that this research brings to the community and a thesis outline and summary.

Chapter 2 – Literature Review: This chapter presents the current state-of-the-art in force/torque sensors for dexterous robot manipulators. This review looks at the design and sensing principles of different types of force sensors that have been proposed or used for dexterous manipulation. Some aspects of integrating the highlighted sensors into dexterous manipulators are also discussed. The chapter ends with a summary of the sensors' features and identification of areas where further sensing capabilities are needed in order to improve autonomous grasping.

Chapter 3 – Design and Development of a 2-DOF force and torque sensor: This chapter focuses on the development of a miniature 2-axis force and torque sensor based on light intensity modulation and linear polarizers. The chapter presents a general description of the sensor's components and its working principle. The mechanical and light intensity analysis of the sensing structure is also presented as well as some simulation results.

Chapter 4 – Testing and Evaluation of the 2-DOF sensor: This chapter presents the assembly and calibration procedure for the 2-axis sensor prototype presented in Chapter 3. The results of experiments conducted

using this sensor are also presented in this chapter and discussions and conclusions about the sensor's features and performance are examined for possible improvements in future designs.

Chapter 5 – Design and Development of a 6-DOF force and torque sensor: This chapter focuses on the design of a parallel mechanism 6-axis force and torque sensor that uses fibre optics and linear polarizers as the sensing elements to measure the applied force and torque. The chapter presents a general description of the proposed sensor before developing the mathematical model of the sensor and the light intensity modulation scheme that allows the applied force and torque to be computed from the intensity modulated light. Simulation results of the proposed sensor are also presented.

Chapter 6 – Testing and Evaluation of the 6-DOF Force and Torque sensor: This chapter presents the assembly, calibration and testing of the proposed 6-axis force and torque sensor. Experiments using the sensor to grasp hard, curved and deformable objects are outlined and the experimental results presented.

Chapter 7 – Conclusions and Future Work: This chapter examines the results of the experiments conducted and compares the theoretical solutions to the observed experimental data. Analysis of individual grasping experiments is conducted as well as comparisons between the results from the experiments with the 2-axis sensor in Chapter 4. The chapter ends with a discussion and conclusion of the results of the experiments conducted and possible future improvements to the sensor.

CHAPTER 2 – Literature Review

2.1 Introduction

Over the past two decades the interest in fingertip sensors for dexterous robotic manipulators has developed from a mere curiosity and theoretical challenge to a full investigation and product development research area. Developed devices have moved form large, momentary contact (ON/OFF) sensors to commercially available sensors that can be integrated directly into a robotic fingertip as shown in Figure 2-1 and [50]-[52]. There are generally two areas that have to be considered when developing sensors: the sensing structure and the sensing element. The sensing structure is the part of the robot that is in direct contact with the applied force. Depending on the application of the sensor the sensing structure may amplify or attenuate the applied force to give better sensing results. The sensing element converts the change in the sensing structure into a measureable change in one of the properties of the sensing material such as length, density or even opacity in some cases. Figure 2-2 shows a representation of a simple and idealistic force sensor where the applied force causes the sensing structure to flex inward (or outward) resulting in a change in the sensing element. The sensing element can convert this change into a change in current, voltage, light intensity or capacitance depending on the transducer technology used. The following sections examine the common materials and methods for the sensing element as well as different types of sensing structures that are used to create fingertip sensors.

Figure 2-1. Fingertip sensors integrated into a SCHUNK Dextrous Hand SDH. Inset is a graphical output from the sensor (larger lines indicate greater force) when the hand is applying varying forces when grasping the circular object [50]-[52].

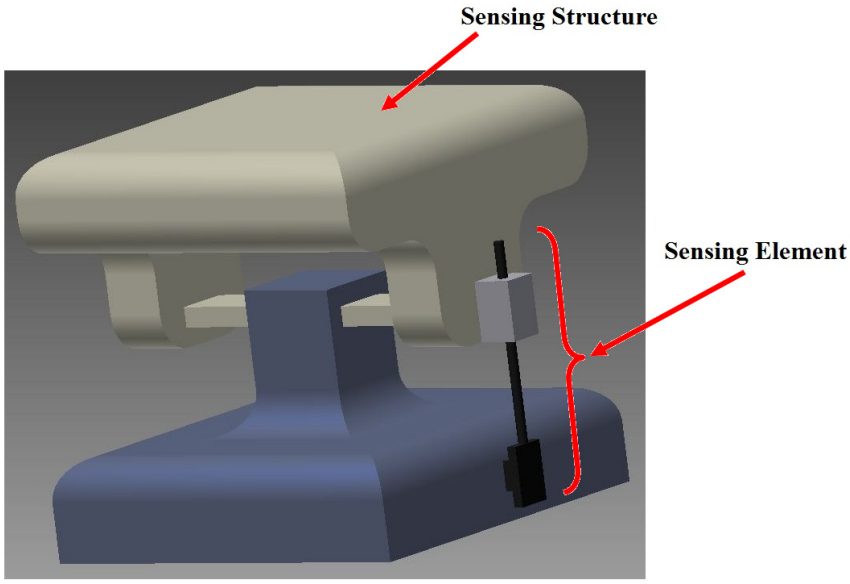

Figure 2-2. An example of a force sensor showing the sensing structure and the sensing element which moves linearly with the applied force.

2.2 Force Sensing Techniques

This section examines four general sensing technologies that are used to create force/torque sensors. The technologies are generally categorised as: strain gauge sensors, piezo-based sensors, capacitance sensors and optical sensors. Each category has certain attributes which make it attractive to certain applications. More about these sensors and their attributes are presented in the following subsections.

2.2.1 Strain Gauge Force Sensing

Strain gauges have been used for force sensing for a number of years due to their simplicity, reliability and linearity. Strain gauges are based on the principle where an applied force produces a minute change in the resistance of a

length of conductor. This change in resistance can then be measured by connecting the strain gauge as one of the four legs of a Wheatstone bridge with the other three legs being known resistances. The Wheatstone bridge converts the change in resistance to a change in voltage which can then be amplified for further processing. The fundamental equation governing resistance change for materials is given by

$$R = \rho \frac{l}{A} \qquad \textbf{(2-1)}$$

where $\boldsymbol{R}$ is the resistance (Ω), $\boldsymbol{\rho}$ is the Resistivity of the material (Ωm), $\boldsymbol{l}$ is the Length of the material (m) and $\boldsymbol{A}$ is the cross-sectional area of the material (m^2) [57]. Figure 2-3 shows a typical foil strain gauge which is simply a thin length of rectangular metal (foil) arranged in a "wave" pattern to increase the length of the conductor and maximize the change in resistance. The entire sensor must then be bonded to or embedded within the sensing structure for best results. Figure 2-4 shows a number of strain gauges bonded to the surface of the sensing structure to measure torsional forces applied to the sensor [54].

Although strain gauge sensors are simple and easy to use they have some drawbacks that have to be compensated for to achieve accurate results. Firstly, strain gauges are sensitive to temperature fluctuations since this also causes the conductor's length to change and hence change resistance. A number of temperature compensation techniques have been developed to mitigate the effects of temperature change. If the contact's surface properties are known then one technique is to design the conductor to have approximately the same coefficient of linear expansion as the contact surface. This effectively negates the effect of temperature on the sensor readings. If the contact surface or object is unknown or frequently changes then another method is to bond multiple strain gauges (2 – 4 gauges) at different locations on the sensor. The strain gauges are then connected to different legs of the same Wheatstone bridge with the opposing strain gauge cancelling the effects due to temperature-induced strain. Secondly, bonding strain gauges to curved surfaces can cause problems in certain applications, especially in situations where the sensing structure or contacting object is changing rapidly. This is because the changing surface weakens the strain gauge bond hence giving inaccurate strain and resistance measurements. Thirdly, the size of the strain gauge itself also presents challenges to integrating them into very small sensors since typical sensing areas are less than 10 mm^2. A tactile fingertip by [55]

illustrates a typical example of how strain gauges can be integrated into a proposed robotic fingertip. The tactile sensor is designed to measure forces applied anywhere on a 16.9 × 14.9 mm contact cover which is designed to concentrate the force onto two pairs of strain gauges. The strain gauges are arranged orthogonal to each other to measure both longitudinal and transverse forces and torques. [56].

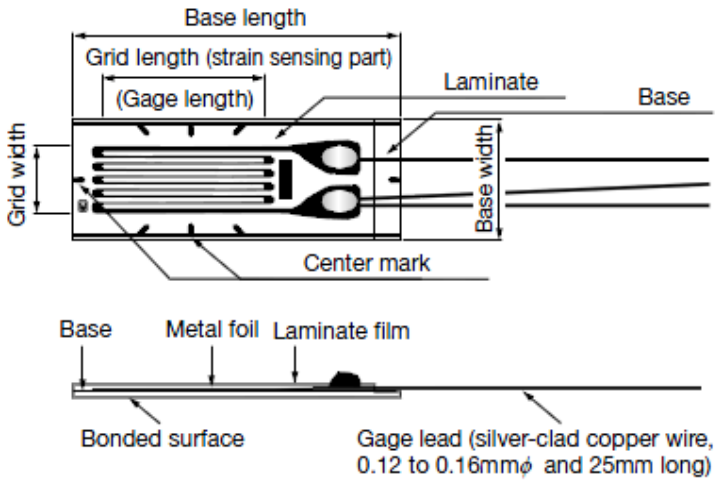

Figure 2-3. The typical strain gauge is usually made as a "waved" pattern to increase the change in resistance due to the applied force [53].

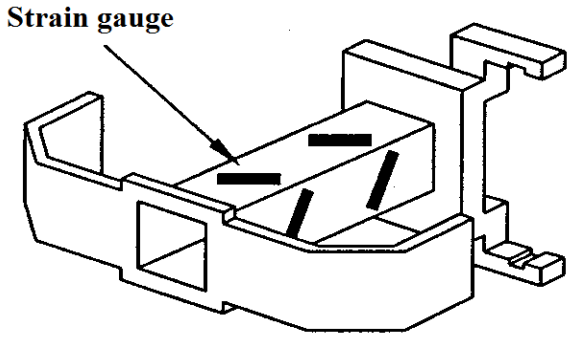

Figure 2-4. The strain gauges are arranged to measure torsional forces applied to the sensing structure [54].

2.2.2 Piezo-based Force Sensing

Piezo-based sensors are mainly semiconductor or MEMS devices that experience a change in resistance or some other property with applied force. Piezo-based sensors are generally divided into two categories: piezoresistive sensors and piezoelectric sensors. Equation 2-1 (Section 2.2.1) indicates that there are two ways by which the applied force can change the resistance of the conductor: by changing the dimensions of the material (length or area) or by changing the resistivity of the material. The first method is used by traditional foil strain gauges presented in Section 2.2.1 to create force sensors however, piezoresistors are made using micromachining technology making them smaller than foil gauges but also more fragile and susceptible to temperature fluctuations. The second method, which is possible with the advent of microfabrication technology, allows temperature compensated strain gauges to be manufactured thereby minimizing the effect of temperature fluctuation on the sensor readings. The sensitivity of piezoelectric material is approximately 100 μV/μm.

Piezoelectric sensors, in contrast to piezoresistive sensors, generate a voltage with the applied force instead of changing the material's resistance. Piezoelectric materials contain charged molecules in either crystalline or long-chain molecule patterns. These charged molecules generate an electric field around the piezoelectric material which establishes an initial voltage level for the unstressed material (see Figure 2-5). Forces applied to the piezo-material change the established voltage level; compressive forces increase the voltage while extensive forces decrease the voltage. The sensitivity of piezo-electric material is around 5 V/μm [58][59][60] and it is well suited for dynamic signal investigation but it is susceptible to temperature induced strain.

A number of sensors have been developed which employ piezo-based materials as the main sensing element. Kattavenos *et al.* [61] developed a sensor-equipped forceps using an array of piezoresistive elements as shown in Figure 2-6. Each array resistor measured 0.5 mm × 0.5 mm and placed with a pitch of 1.0 mm on one side of the forceps. This sensor was able to detect irregularly shaped lumps in a phantom bowel provided the sensor was moved slowly over the phantom. Dargahi *et al*. [62] also created an instrumented forceps but used PVDF (piezoelectric) material to form the sensor array as shown in Figure 2-7. This sensor has similar properties to the one by [61] but the PVDF material exhibits better linearity over a larger force range also the output voltage sensitivity and level are larger than the piezoresistive

sensor. Choi *et al.* [63] utilized the enhanced features of the PVDF material, including its high dynamic range, to design a tactile sensor for the fingertips of the SKKP Hand II anthropomorphic robot hand to investigate stick-slip scenarios when grasping objects. Son *et al.* [64] and Kolesar, Jr. and Dyson [65] used PVDF film to create a tactile fingertip sensor that can also detect local object curvature. Goeger *et al.* [66] also developed a fingertip PVDF slip sensor with multiple contact coverings to investigate the best contact finger texture to detect object slippage. Paredes-Madrid *et al.* [67] used piezoresistive sensors to create a data glove for haptic research. Barsky *et al.* [68] used PVDF sensors to detect and damp exerted forces on a gripper to reduce response time and improve gripper control. Cotton *et al.* [69] combined both piezoresistive and piezoelectric materials to create a 2 mm thick multisensory fingertip for the Southampton Hand (see Figure 2-8).

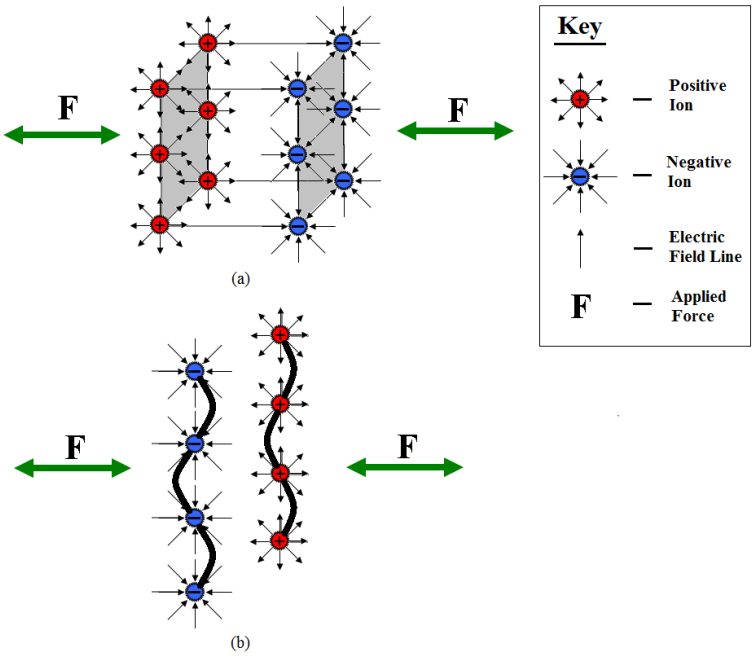

Figure 2-5. The basic structure of a piezoelectric material consists of charged ions on opposing surfaces of the structure thereby forming an electric field around the material. Compressing the opposing surfaces causes the electric field to increase while moving the surfaces apart reduces the electric field. (a) The structure of a crystalline piezoelectric material. (b) The structure of a polymer (long-chain) piezoelectric material.

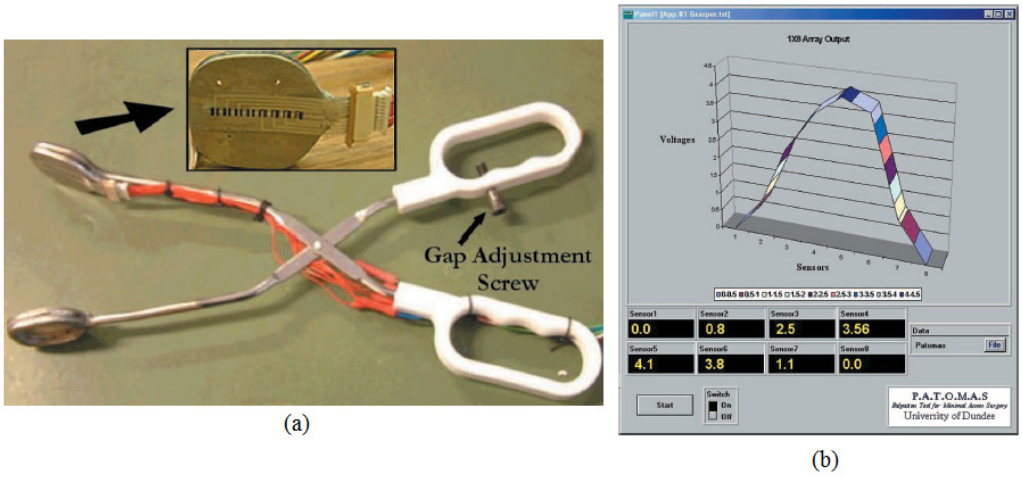

(a) (b)

Figure 2-6. A medical forceps equipped with a piezoresistive sensor array. (a) The array is bonded to one side of the forceps and connected with flexible cables. (b) The output from one element of the array [61].

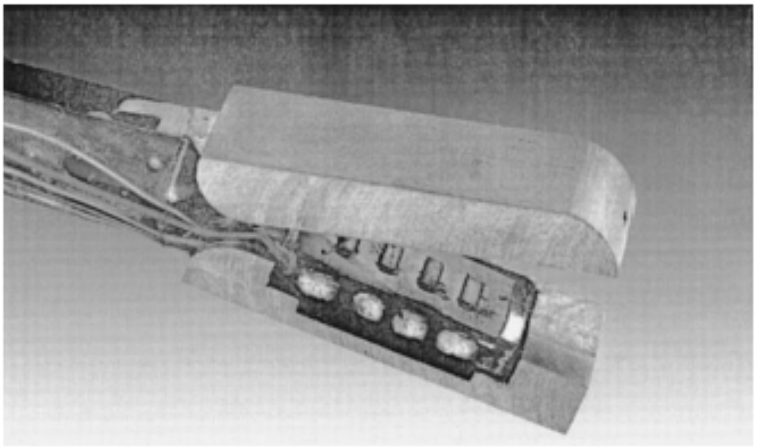

Figure 2-7. A fabricated forceps with an integrated piezoelectric array sensor [62].

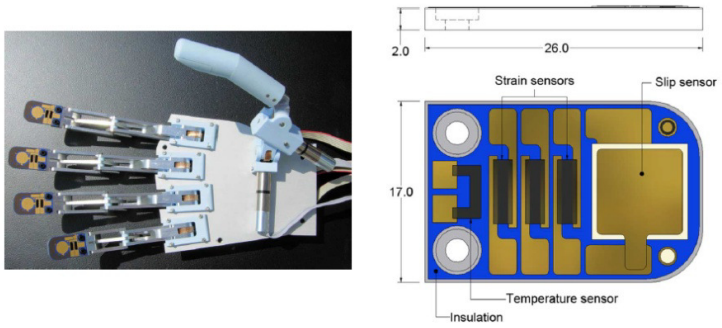

(a)

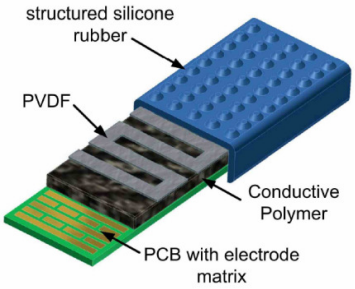

(b)

Figure 2-8. (a) The Southampton Hand with an integrated force and slip sensor by Cotton *et al.* [69]. (b) The fingertip tactile sensor to detect object slippage by Goeger *et al.* [66].

2.2.3 Capacitive Force Sensors

Capacitive sensors experience a change in the value of the capacitance with applied force. The simplest type of capacitor is the parallel plate capacitor which is comprised of a dielectric (insulating) material between two conducting plates (see Figure 2-9a). The equation for a parallel plate capacitor is given by

$$C = \frac{\varepsilon_d A}{d} \qquad \textbf{(2-2)}$$

where $\boldsymbol{A}$ (m^2) is the surface area of the conducting plates, $\boldsymbol{\varepsilon_d}$ (F/m) is the permittivity of the dielectric material, $\boldsymbol{d}$ (m) is the separation distance between the conducting plates and $\boldsymbol{C}$ is the resultant capacitance (F). In general, $\boldsymbol{\varepsilon_d}$ is constant while the applied force varies either **A** or **d**. The voltage across a capacitor is given by

$$V_c(t) = V_0\left(1 - e^{\frac{t}{\tau}}\right) \qquad \textbf{(2-3)}$$

where V_0 is the applied voltage, t is the charging time, τ is the time constant of the circuit (given by the product of resistance, R and capacitance, C) and $V_c(t)$ is the capacitor voltage at time t. Unlike other types of sensors capacitive sensors require a voltage pulse or a changing voltage to charge the capacitor and a current-to-voltage converter the charging current to a measurable voltage. Figure 2-9b shows a simple circuit to measure the change in voltage for a change in capacitance.

Capacitive force sensors have been widely used due to their simple construction and operation. Fearing [72] developed a cylindrical fingertip sensor that can be integrated into the Stanford/JPL dexterous hand. The sensor used an array of eight capacitive sensing elements to improve regrasping operations when handling objects. The sensor gave a good indication of the contact location and centre of pressure at each sensing element but sensing accuracy deteriorated as contact moved away from the sensing element. Success was also achieved in determining the orientation of the grasped object but it was limited by the low sensing element spatial resolution of the sensor. Lee *et al.* [73] designed a tactile array (16 × 16 elements) based on the parallel plate design but encased in PDMS to reduce crosstalk and improve hysteresis (see Figure 2-10). Forces applied to the sensing element change the separation distance of the air gap and hence the capacitance of the element. This basic sensing principle is also used by Chun and Wise [74], Castelli [75] and Chu *et al.* [76]. It is also the basis of the fingertip sensor for the iCub humanoid robot [77].

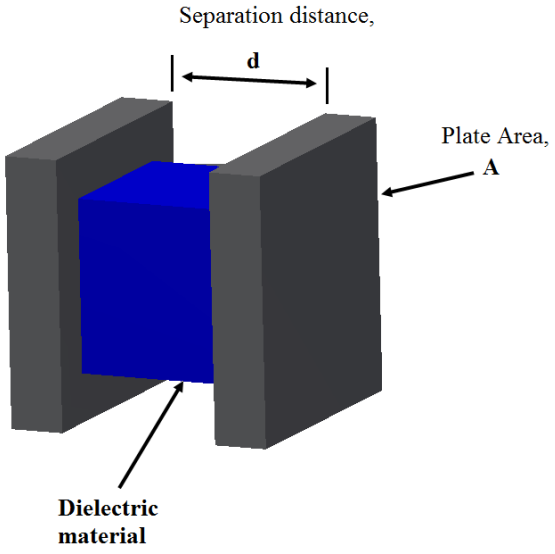

(a)

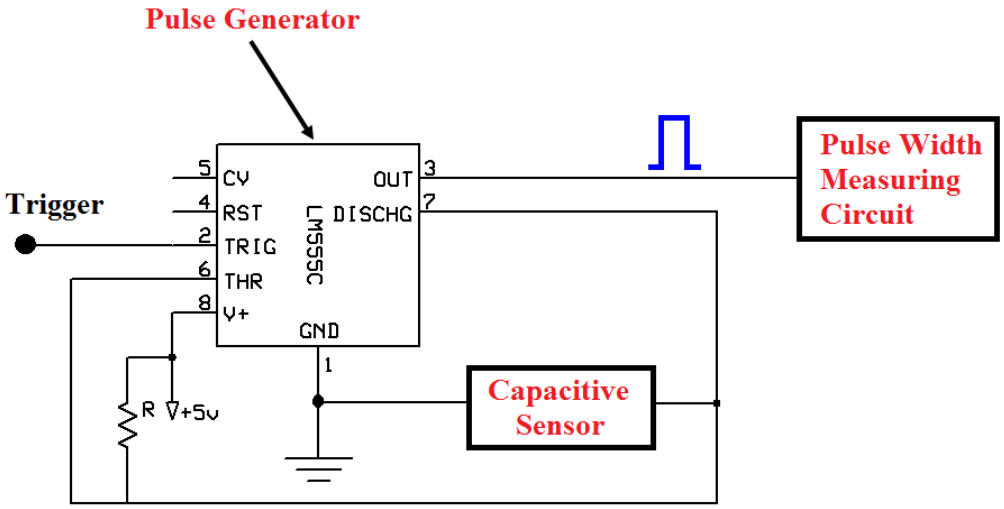

(b)

Figure 2-9. (a) The capacitance of a parallel plate capacitor is based on the area of the conducting plate, *A* and the separation distance, *d* between the two plates. (b) A simple electronic circuit to measure the voltage across a charging capacitor (adapted from [71]).

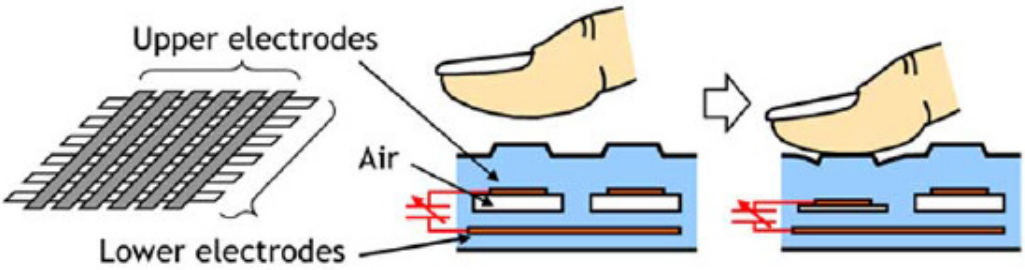

Figure 2-10. An example of the sensing principle of a capacitive sensing element [73].

2.2.4 Optical Force Sensors

Optical force sensors use a change in one of the properties of light to represent a change in applied force. In this discussion light is treated as a repeating sinusoidal wave unless otherwise stated. The general equation for a sinusoidal wave (see Figure 2-11) is given by

$$F = A_m \sin(2\pi ft + \phi) \qquad \textbf{(2-4)}$$

where A_m is the amplitude of the sine wave (in units of meters, voltage, current, etc), f is the frequency of the wave (Hz), ϕ is the phase angle of the wave (radians), t is the time (seconds) and F is the value at a particular time t. The wave description of light presents three general parameters that can be used to create a force sensor: the Amplitude, A_m, the frequency, f and the phase, ϕ. All optical systems require a light source and an optical detector to complete the sensing circuit as shown in Figure 2-12. For situations where it is not feasible or convenient to have the sensor close to the light source or detector then optical fibre cables can be used to extend the distance of the sensor.

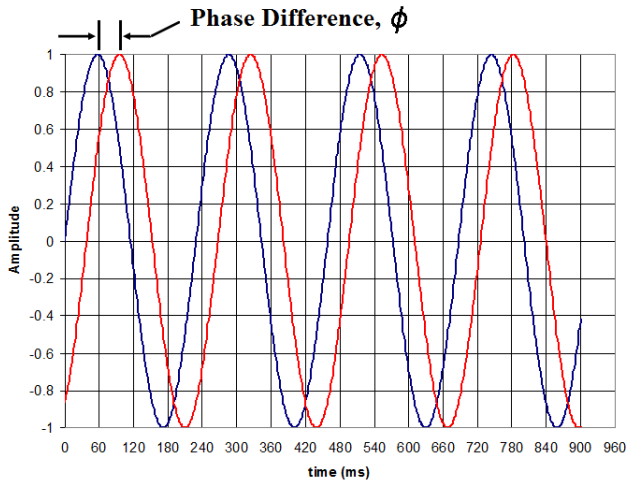

Figure 2-11. The basic characteristics of a sine wave representing a light wave. The two light waves have a phase difference of ϕ between them.

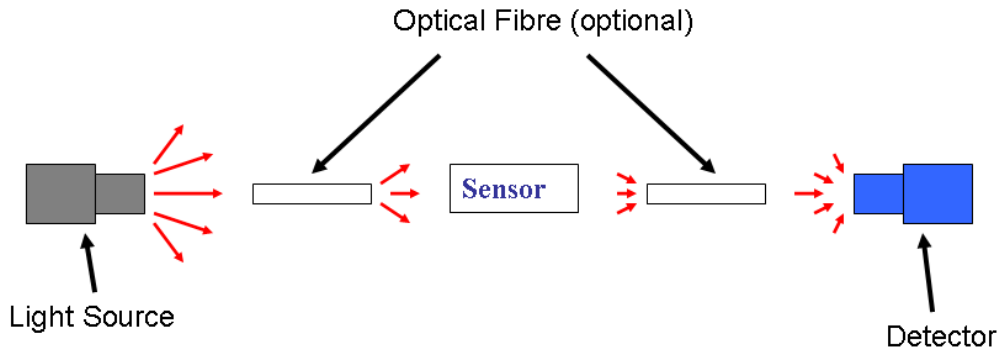

Figure 2-12. The general optical system consists of a light source, a light detector, the optical sensor and (optional) fibre optical cable.

One of the earliest methods of modulating the optical output was to vary the amplitude of the light also called Light Intensity Modulation (LIM). Jeong *et al.* [78]. created a simple 2-DOF fingertip tactile sensor using a single IR (InfraRed) emitter and two orthogonal IR detectors (see Figure 2-13). The orthogonal arrangement of the detectors enabled the sensor to measure both normal and tangential forces while the IR detectors helped to reduce background noise due to visible light. Note that this sensor uses directly coupled light i.e. the light from the light source is directly projected onto the detector so that variations in light intensity are obtained by either partially blocking the light (for normal force measurement) or shifting the emitter and detector out of alignment (for tangential force measurement). The output intensity is

generally nonlinear but can be approximated as linear over a small working range (piecewise linear). Palli and Pirozzi [79] used the misalignment principle to create an optical bend sensor to measure the tendon force on a robotic finger. The sensor was used to improve the robot's force and position control due to the high sensitivity of the misalignment technique. An extension to this misalignment technique deals with using reflected light to increase the sensitivity of the sensor. The basic reflective fibre optic displacement sensor (FODS) consists of a pair of parallel fibre optic cables (transmitter and receiver) and a reflective surface to measure the distance between the transmitting fibre and the reflective surface. The distance can then be used to calculate the applied force the structure provided the elastic properties of the structure are known or the sensor is properly calibrated. The disadvantage of this design is that it is inefficient since only a small portion of the transmitted light is reflected to the receiver. Puangmali et al [80], Buchade and Shaligram [81] and Mazid and Russell [82] used angled or bent-tip fibre to improvement to the design. The bent-tip approach proved superior since more of the reflected light was directed to the receiving fibre (see Figure 2-14). The disadvantage of this technique is that it is only sensitive in a narrow range of operation. An alternative to fibre pairs is to use a fibre optic coupler which allows both the transmitted and reflective light to travel along the same optical fibre. Polygerinos *et al.* [83], Tohyama *et al.* [84], Peirs *et al.* [85] and Kulkarni *et al.* [86] used this method to reduce the size of their sensors while still maintaining good sensitivity.

Another popular LIM technique is that of microbending. Microbending involves bending a length of fibre optic cable beyond its minimum bending radius. Fibre optic cables propagate light using the principle of refraction and total internal reflection (see Figure 2-15). For a straight fibre the light travels within the core of the fibre with minimal intensity loses. If the fibre curves sharply then some of the light rays will escape resulting in reduced received light. Luo *et al.* [87] created a simple microbend sensor using corrugated teeth, with a tooth separation of 3.5 mm, to indent the multimode fibre (see Figure 2-16). The range of the sensor was limited to $300\mu\varepsilon_m$ of strain but a number of sensors could be cascaded to form a distributed sensor. Heo *et al.* [88] extended the basic microbending principle by using multiple orthogonal multimode fibres to form a tactile grid (see Figure 2-17). Applying force on the sensor caused an indenter above the intersection of the fibres to microbend both fibres resulting in reduced light. The applied force is calculated from the received light

intensity while the contact position is determined from the fibre grid. The sensor had a force range of 0 – 15 N and a resolution of 0.05 N. Other microbend sensors include a bend detection sensor by Koch *et al.* [89] which contained slits on one side of the fibre. Bending the fibre inward resulted in less light escaping the firber while bending the fibre outward cause more light to be lost. Depending on the received intensity the direction of the bending force (torque) can be detected. Hetero-core fibres, used by Watanabe et al. [90] and Nishiyama and Watanbe [91], consists of a short length of fusion-spliced single mode optical fibre (Ø 3 – 5 µm) spliced axially between two larger core optical fibres (Ø > 9 µm). The advantage of hetero-core fibres is that the point of microbending can be accurately determined.

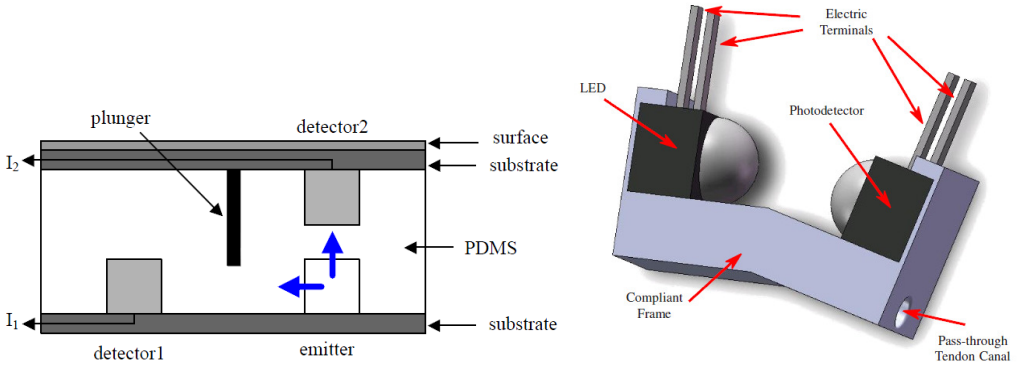

(a) (b)

Figure 2-13. (a) A 2-DOF fingertip sensor based on directly coupled/aligned IR LED light [78]. (b) An optical force sensor to measure the force on a tendon for a robotic hand [79].

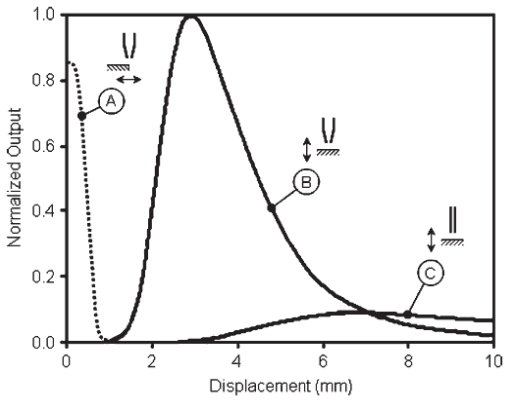

Figure 2-14. The vertical displacement profile of bent-tip fibres (B) has a superior performance to traditional vertical displacement parallel fibres (C) [80].

Fibre optic sensors have also been developed which affect the frequency of the transmitted light. The most popular technique is to use Fibre Bragg Gratings (FBG) to selectively block certain frequencies of the transmitted light. FBGs are optical fibres which have periodic variations in the refractive index of the fibre (see Figure 2-18). The reflected Bragg wavelength is given by

$$\lambda_B = 2n_f \Lambda \qquad \textbf{(2-5)}$$

where n_f is the refractive index of the fibre, Λ is the pitch between Bragg gratings and λ_B is the wavelength of the reflected light [92]. Strain and force sensors can be easily created from FBG because the Bragg wavelength is mainly affected by the pitch of the Bragg gratings so any applied force or strain changes the reflected light. The disadvantage is that FBGs are also susceptible to thermal strain so temperature compensation elements are necessary for FBG sensors. Also, the spectrum analyzer needed to analyze the reflected light as well as the fibres themselves can be expensive. Rajan *et al.* [93] present a typical FBG application where the blades of a robotic scissors were equipped with FBGs to measure the cutting force and as a reference for temperature compensation. The maximum force for this sensor was 30 N with a resolution of 1.1 N and Bragg frequency between 1500 – 1600 nm. Torque on a structure can also be measured depending on the placement of the FBG sensors. Swart *et al.* [94], Kruger et al. [95] and Tian and Tao [96] presented typical examples of a FBG torque sensor for a cylindrical bar where two FBGs were orientation at ±45 ° to the axis of rotation to provide simultaneous tension and compression strains (see Figure 2-19). Torque measurements of up to 200 Nm were capable with these sensors. Another advantage of FBGs is they can be easily multiplexed on the same fibre. Recall that FBGs only reflect a specific wavelength (within a narrow band) while allowing other wavelengths to pass undisturbed. This means that more than one FBG can be written on the same fibre thereby reducing the number of sensing fibres in the system. The disadvantage is that one or more spectrum analyzers must be used to measure the reflected signals.

The final variable parameter is to measure the phase shift of the reflected signal after passing through the sensor. One of the most widely known optical phase

modulation techniques is the Fabry-Perot resonator. As shown in Figure 2-20, this device uses two mirrored surfaces, one partially reflective and the other fully reflective and separated by a distance, *d* (usually in the order of a few micrometres). Changing the distance, *d* generates interference between the reflected light rays which causes a change in the intensity of the reflected light. Totsu and *et al.* [97] designed a Fabry-Perot pressure sensor with a diameter of 125 µm to monitor the pressure within blood vessels and capillaries. The force range was between -13.3 kPa – 53.3 kPa with a resolution of 0.53 kPa for a separation distance between 1600 – 1740 nm. Other sensors by Chang and Sirkis [98], Lee et al. [99] and Kim and Lee [100] present slight variations of this principle by using a combination of single and multimode fibres and optical multiplexing techniques.

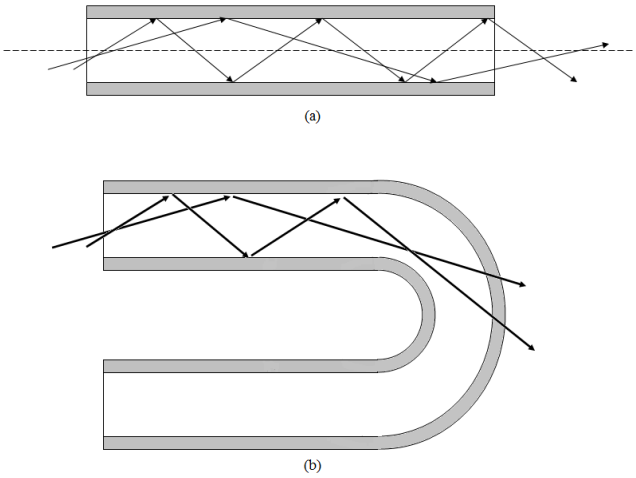

Figure 2-15. (a) Optical rays propagating through a straight optical fibre by total internal reflection. (b) Optical rays lost from an optical fibre that is bent beyond its minimum bending radius as specified by the manufacturer.

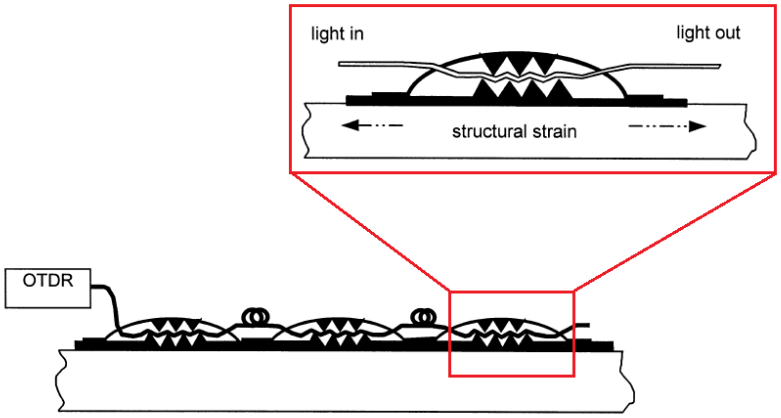

Figure 2-16. Microbending sensors modulate the light by bending the optical fibre beyond its minimum bending radius so that light is lost from the fibre [87]. The light lost is a function of the applied force.

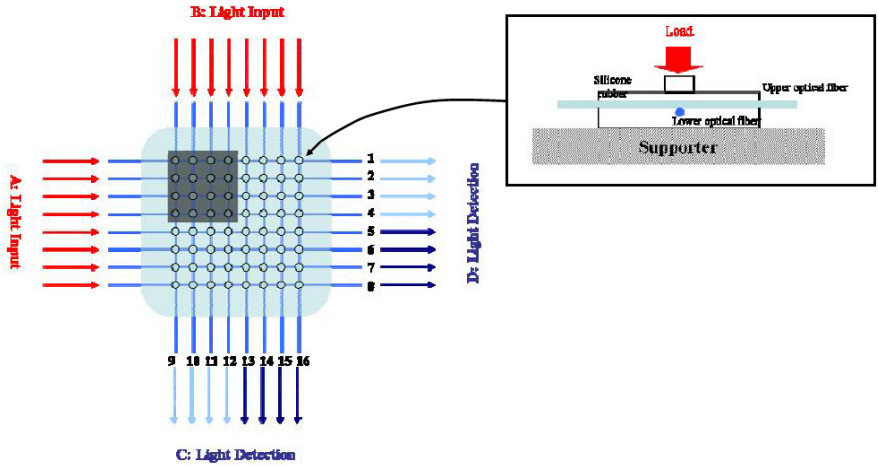

Figure 2-17. A tactile microbending grid array by Heo *et al.* [88].

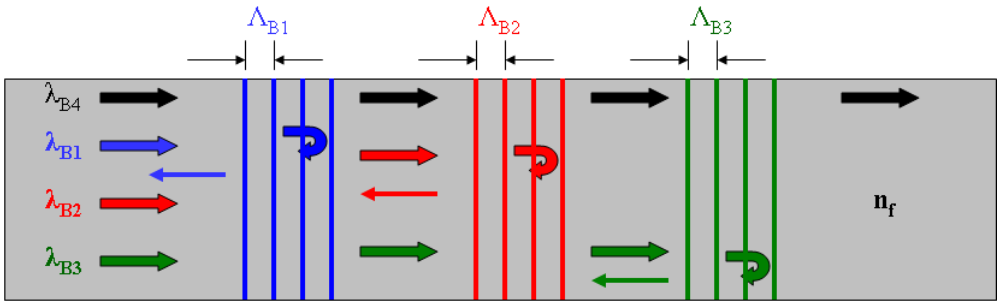

Figure 2-18. A FBG consists of periodic variations in the refractive index of the optical fibre. The periodic variations only reflect that portion of the spectrum which has the same pitch as the periodic variations.

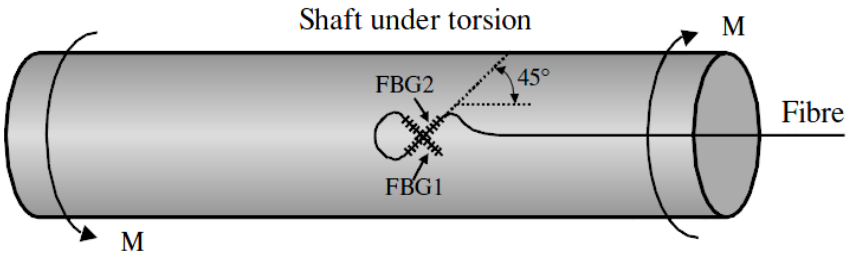

Figure 2-19. A typical fibre optic torque sensor uses two FBGs arranged at 45 ° to the axis of rotation [94].

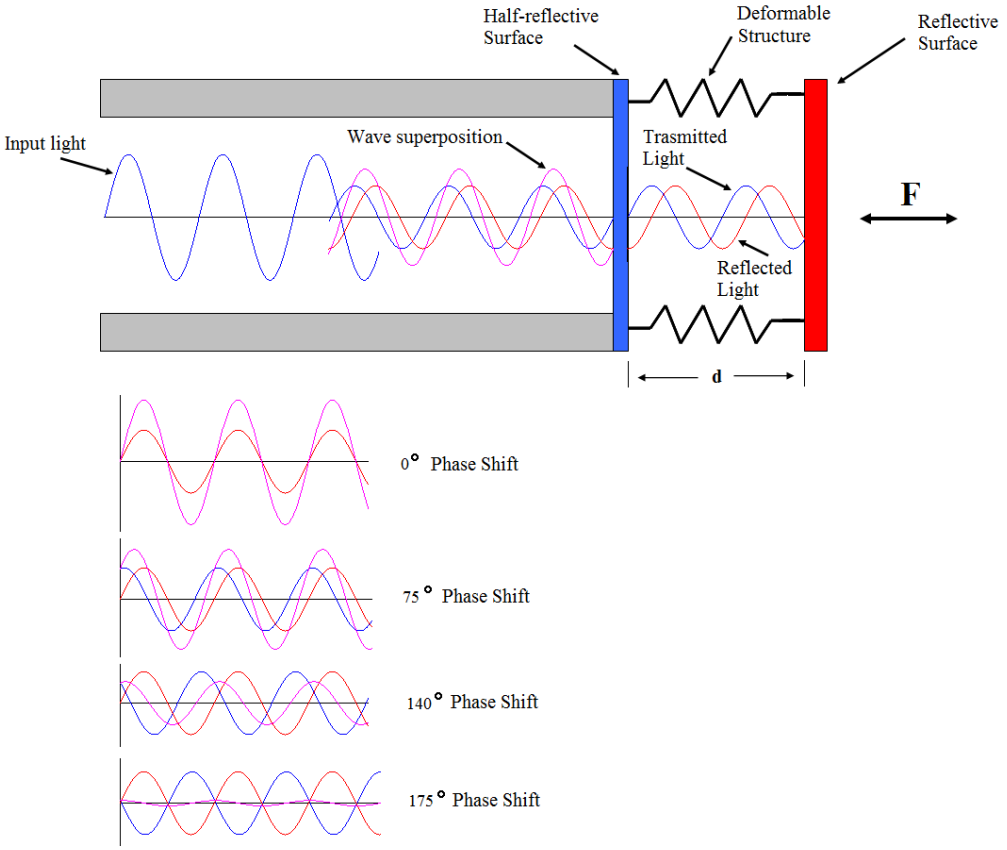

Figure 2-20. The Fabry-Perot sensor uses interference of light waves to measure the applied force. The applied force varies the separation distance between the mirrors causing the transmitted and reflected waves to interfere and change the resultant light intensity.

2.2.5 Other Sensors

The previous sections presented common sensing techniques which have been used to develop force sensors. With the advancement in technology new force sensors have been created which utilize new sensing techniques. One approach investigated was to integrate transistors directly into the sensing fabric. Someya *et al.* [101] created an organic field-effect transistor based tactile sensor that is highly flexible (up to a bend radius of 2 mm) and bonded to a pressure sensitive rubber base. The applied pressure varies the FET's Gate-to-Source voltage and hence changes the drain current. The drain current can then be further amplified by external circuit if desired. Dahiya *et al.* [102] produced a similar sensor but with standard MOSFET materials bonded to piezoelectric material. Another new technology is that of Electrorheological (ER) fluid sensing. ER fluids change viscosity depending on the applied electric field. Voyles Jr. *et al.* [103] proposed an ER-based tactile fingertip where the ER fluid is the dielectric of capacitors embedded within the fingertip. The applied electric field sets the viscosity of the ER fluid while the applied force changes the capacitance of the sensor and hence the capacitor's voltage. The sensor also has the advantage of having variable stiffness since the viscosity of the sensor can be dynamically changed. Wettels *et al.* [104] also presented a fluid-filled sensor but used conductive fluid (propylene glycol/sodium iodide) with a known resistivity as the sensing medium. Applying force to the conductive fluid changes the resistivity of the fluid which can then be measured and used to calibrate the sensor for known forces. Forces between 10 – 18 N were obtained depending on the conductive fluid.

2.3 Multi-axial Sensors

As previously mentioned in Section 1.1, increasing the DOF of a sensor increases the amount of force information that can be measured during a contact event. The previous section (Section 2.2) presented some of the more common types

of sensing techniques which are used in robotic fingertips and for other sensing devices. However, sensing techniques are only one half of the sensing mechanism with the other half of the problem being the sensing structure itself. The sensing structure is in direct contact with the object and experiences some level of structural deformation from the contact forces, thereby producing a change in the measurable quantity. This section presents several multi-axial sensors that have been created using the principles highlighted in the previous section and incorporating them into the proposed sensing structure.

From the literature a number of features have to be considered when designing the sensing structure. These features include: type of material, size of the structure, shape, stress points and degrees of freedom. For example, increasing the DOF of the sensor generally increases the size of the structure and to some extent the shape as well. Any applied force, **F**, can be decomposed into its constitute x-, y- and z-axis forces ($\mathbf{F_x}$, $\mathbf{F_y}$, $\mathbf{F_z}$) and x-, y- and z-axis torque ($\mathbf{M_x}$, $\mathbf{M_y}$, $\mathbf{M_z}$) components (see Figure 2-21), therefore a 6-DOF sensor is capable of measuring any force applied by a robotic gripper. Miniaturizing existing 6-DOF sensors to fit within an anthropomorphic fingertip is still a major challenge. The majority of the multi-axial sensors utilize multiple strain gauge sensors to achieve multi-axial sensors since strain gauges are linear, simple to use and inexpensive but they need to be temperature compensated and are not naturally suited to be bonded to curved surfaces. Kaneko [105] proposed building 6-DOF sensors by combining two 3-DOF sensors provided the resulting calibration matrix is of full rank i.e. it can form 6 independent equations. Berkelman *et al.* [106], [107] developed a 3-DOF force sensor (F_x, F_y, F_z) based on a dual 4-cross design and with integrated silicon strain gauges at the edges of each of the arms of the crosses (see Figure 2-22). The sensor was developed for microsurgical applications with a force range of ±1.0 N, resolution of 0.05 mN and a diameter of 12.5 mm. The 4-cross is a popular sensor design because it is simple, symmetric and the arms easily coincide with the Cartesian coordinate system so the conversion calculations are easier to perform than other designs. The dual 4-corss design has the added benefit of equalizing the axial and non-axial forces to produce more uniform output data. Another important feature of the 4-cross design is the use of stress points/features which determine where the structure will deform. Figure 2-22 shows the locations of the strain gauges which are bonded to the edges of the slim arms.

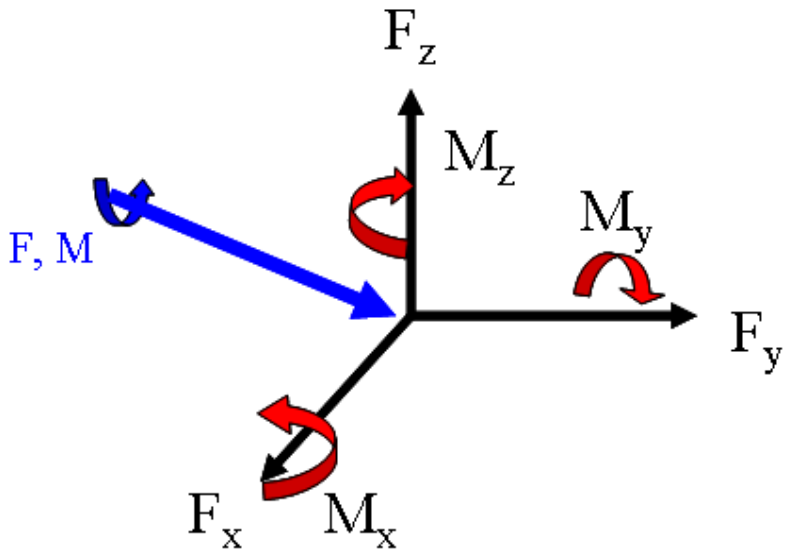

Figure 2-21. Any force, F can be decomposed into one or more of the following components: F_x, F_y, F_x, M_x, M_y and M_z (Cartesian coordinate system).

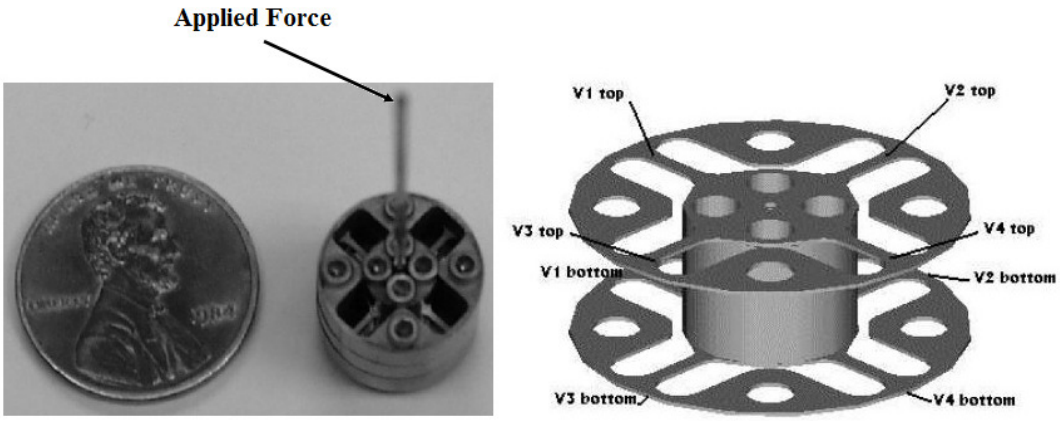

Figure 2-22. The 3-axis sensor (F_x, F_y, F_z) was developed using a dual 4-cross design with integrated strain gauges at the edges of each of the arms of the cross.

The smaller the arms the more sensitive they are to applied forces and placing the strain gauges at the edges increases the deformation due to moment forces. This highlights three areas that must be considered when determining the sensitivity of the sensing structure:

1. The type of sensor to use.

2. The design and properties of the stress features to concentrate the applied forces on the sensing elements.
3. The placement of the sensors on the stress features to maximize the effect of the deformation on the sensor output.

Fujii *et al.* [108] presented an extensive mathematical analysis on designing the arms of the cross so that the measureable force and sensitivity can be tailored to the specific application. A number of 4-cross sensors have been developed, ([109] – [119]) with applications ranging from robotic fingertips ([109]-[112]) to insect leg forces ([113]). Six DOF sensors are also possible depending on the configuration of the sensing elements (see Jin *et al.* [115] and Kim *et al.* [116]). Three-cross sensors have also been developed by Cui *et al.* [120], Butterfab *et al.* [121] and Yamada *et al.* [122]. These sensors reduce the size and weight of the sensor but increase the complexity of resolving the applied forces. Other multi-axial sensors structures include dome-shaped structures ([130]-[136]), capacitive structures ([123]-[129]) and parallel structures ([139]-[141]). Dome-shaped structures are symmetric which provide a more even distribution of contact force to the sensor and reduces the need to orient the sensor in a special configuration to contact an object. The disadvantage is that the dome increases the size of the sensor. Capacitive structures build parallel plate capacitors directly into the structure itself resulting in a more compact design but it can be affected by magnetic interference. Parallel structures have a symmetric arrangement with top and bottom parallel plates connected by moveable arms. One of the more popular parallel designs is the Stewart platform (see Figure 2-23). Parallel designs have high stiffness and a high level of structural redundancy but the structure may have a number of moving parts that introduce friction. Even more complicated sensing structures were created by Park *et al.* [138] who developed a flexible honeycombed-shaped 6-DOF fingertip sensor with five embedded FBG sensors to measure contact forces. The honeycomb shape ensured a light and flexible but yet strong structure with a maximum static force of 12 N and can measure dynamic forces of 10 mN at 20 Hz.

Figure 2-23. A typical Stewart Platform showing the 6-DOF movable contact surface, base and extensible links (adapted from [185]).

2.4 Sensing Principle Selection

The preceding sections in this chapter presented several of the more common sensing technologies including the sensing elements and sensing structures. Section 1.2 presented the two major aims of this research: to develop a 6-DOF force and torque sensor for the fingertip of a dexterous robotic manipulator and to make the sensor MR-compatible so that can be used for medical applications. Table 2.1 presents a comparison between the different types of sensing technologies and the desired aims of the research. The deciding factor in the selection of a sensing technology is the desire for MR compatibility. The best MR-compatible sensing technology is optical fibre which also has the advantage of low signal attenuation and

multiple sensors can be multiplexed on the same fibre with the appropriate equipment. Although optical techniques such as FBGs and Fabry-Perot are viable optical modulation techniques they require more expensive detection instruments and they increase the cost of the sensor. LIM was chosen as the optical modulation technique because it is simple, easy to implement and inexpensive. Chapter 3 presents a 2-DOF sensor based on LIM optical fibre technology and a 4-cross design.

Sensing Principle	**Force/Torque Sensing Aim**	**MR-compatibility Aim**
Strain gauge	√	**X**
Piezo	√	**X**
Capacitance	√	**X**
Optical Fibre	√	√

Table 2.1 Suitability of Sensing Principle to Project Aims

2.5 Chapter Summary

This chapter examined two general aspects of sensor design: the sensing element/transducer which converts the applied force/torque into a measureable quantity (usually current or voltage) and the sensing structure which is in contact with the object. Four general types of force sensing techniques were presented: strain-gauge sensing, piezo-based sensing, capacitance-based sensing and optical-based sensing.

Strain-gauge sensors are based on the principle that an applied force produces a small change in the length and hence resistance of a length of conductor as given by equation 2-1 (Section 2.2.1). Piezo-based sensors generate a voltage in proportion to

the applied force and have higher sensitivity than the strain-gauge type sensors (Section 2.2.2). Capacitance-based sensors experience a change in capacitance with applied force with the capacitance given by equation 2-2. The change in capacitance changes the current flowing through the sensing circuit which can then be measured to give an indication of the applied force (see Section 2.2.3). Optical-based sensors (Section 2.2.4) modulate one of the properties of light (amplitude, frequency or phase) as given by equation 2-4. Light Intensity Modulation (LIM) optical sensors are simple to construct and use but frequency (Fibre Bragg Gratings) and phase modulation (Fabry-Perot) optical sensors have superior sensitivity and performance characteristics. Optical sensors also have desirable characteristics such as immunity to magnetic noise and corrosive environments.

The other area examined was the sensing structure that would be in contact with the object. One of the more popular sensing structures is the "4-cross" design where each arm is perpendicular to each other and the arms can be aligned to the Cartesian coordinate system to simplify force and torque calculations (see Figure 2-22). Another structure examined was the parallel mechanism where the contact surface is supported by extensible legs and the applied load is distributed among the structures legs (See Figure 2-23). The features of the parallel mechanism are that it offers high structural stiffness and redundancy and better load bearing capabilities than serial mechanisms but calculation of the displacement and orientation of the contact platform is more difficult than serial mechanisms.

Given the features of the investigated sensing techniques and the desired application of the sensor to dexterous robotic fingertips and a desire for MR-compatibility, the chosen sensing technique was the light intensity modulation optical sensor due to it magnetic immunity features (MR-compatibility requirement) and a serial sensing structure to simplify the design and reduce the size of the device. Chapter 3 presents a description and model of the developed force and torque sensor based on the optical sensing principle and the developed sensing structure.

CHAPTER 3 – Design and Development of a 2-DOF Force and Torque Sensor

3.1 Introduction

The previous chapter examined several sensing technologies and sensing structures that can be used to create multiaxial sensors. The reviewed sensing technologies were compared with the research aims and objectives with a view of deciding on the best strategy for designing the desired fingertip sensor. From the review process the path chosen was to use Light Intensity Modulation (LIM) with a 4-cross design to the fingertip sensor. Section 2.2.4 presented the basic principles of LIM and the methodologies used to achieve LIM. This chapter presents a novel 2-DOF sensor based on LIM and incorporating linear polarizers for torque measurement. The following sections explain the design and operation of the developed sensor and present a mathematical model of the sensor. Section 3.2.1 discusses the operation and mathematical modelling of the linear force sensor (F_z) while Section 3.2.2 introduces the concept of linear polarizers and their application to torque measurement (M_x).

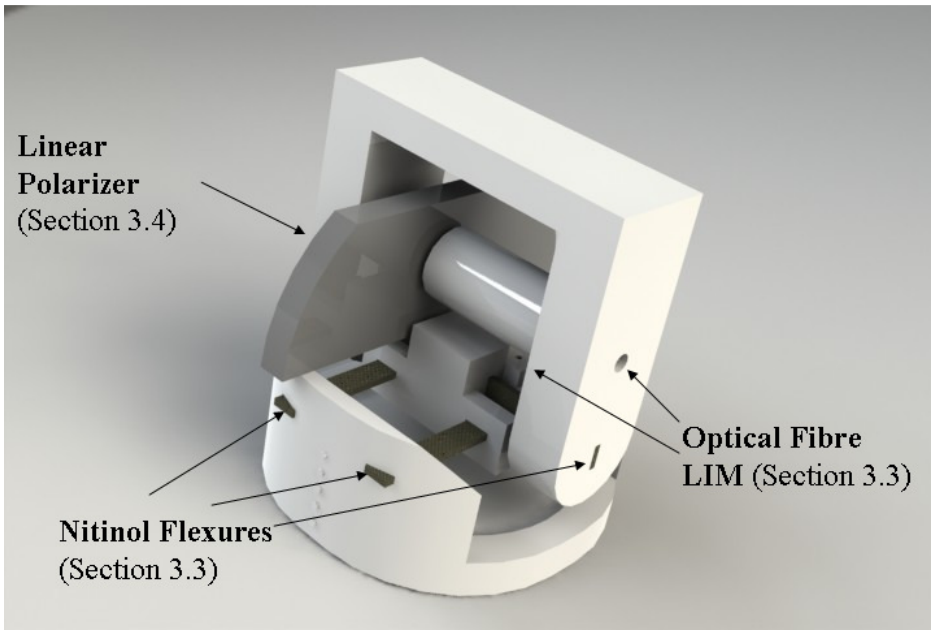

Figure 3-1. A magnified image of the 2-DOF outlining the major sections of the sensor described in this chapter (diameter: 9 mm; height: 10 mm).

3.2 2-Axis Sensor Overview

The proposed 2-DOF sensor was designed to measure two forces (F_z and M_x) simultaneously. The sensor uses two intensity modulation techniques:

— Modulating the intensity by varying the displacement between axially-aligned optical fibres.

— Modulating the intensity by rotating a linear polarizer in the path of linearly polarized light.

The structure of the force sensor is shown in Figure 3.2 and consists of two lengths (approximately 0.6 m each) of 0.25 mm general purpose simplex plastic multimode optical fibre (NA of 0.5) [142], [143]; one length was the receiving fibre and it was embedded within a fixed support to provide a known starting position and the other length was the transmitting fibre and it was embedded within a moveable support for the applied force. The other end of the transmitting fibre was connected to a red superbright LED light source with a centre wavelength of 660 nm. The red light was chosen because it offered less transmission attenuation and better optical coupling for plastic optical fibre than other types of light sources (ideal wavelength would be 650 nm). The receiving fibre was connected to a high sensitivity phototransistor which converted the received light into a corresponding current [144]. The output voltage was further amplified and digitized before being transmitted to a computer for further processing. The initial separation distance between the transmitting and receiving fibres was set at 1.8 mm thereby providing an initial output voltage when no force is applied to the sensor. Referring to Figure 3-2, if a downward force is applied to the moveable contact plate then the transmitting and receiving fibres are moved closer together increasing the coupled light and the phototransistor voltage. Conversely, if an upward force is applied to the moveable contact plate then the transmitting and receiving fibres are moved farther apart decreasing the coupled light and the phototransistor voltage. Therefore, both the magnitude (coupled light intensity) and the direction of the force (increasing or decreasing intensity/voltage) can be determined for the force sensor.

The structure of the torque sensor is shown in Figure 3-3 and is structurally similar to the force sensor but with the following modifications. First this sensor embeds the transmitting and receiving fibres into two fixed supports so there is no relative motion between the fibres. Secondly, the light is intensity modulated by rotating a linear polarizer in the path of the light. The intensity is therefore modulated by varying the angle of rotation of the linear polarizer. Polarization will be further discussed in Section 3.4. The entire sensor was made of ABS plastic and nitinol strips which exhibit little or negligible effects from magnetic fields thus making them suitable for MR environments. A number of other materials were tested prior to selecting nitinol strips for the twisting flexures [186]. Materials such as rubber, cured liquid latex and plastic strips were tried but although they were all MR-compatible the rubber and liquid latex exhibited low stiffness and low load bearing capabilities. Flexures based on these types of materials were very sensitive to pure torque forces but resolving combined force and torque forces proved difficult. The stiffness of the plastic strips was better than the rubber-based materials but the main problem with the plastic strips was that the position of the point of flexing could not be consistently guaranteed thereby affecting the repeatability of the sensor. The rectangular nitinol strips used in the sensors were sample products from Memry Cooperation [187] with a width of 0.5 mm and a thickness of 0.2 mm. The Young's Modulus of Elasticity for the material was approximated to be 5.5 GPa. The advantages of the nitinol were that it was stiffer than the other materials and the small size would help reduce the size of the sensor. In addition, since the nitinol was a metal it had superior elastic properties to the other materials investigated.

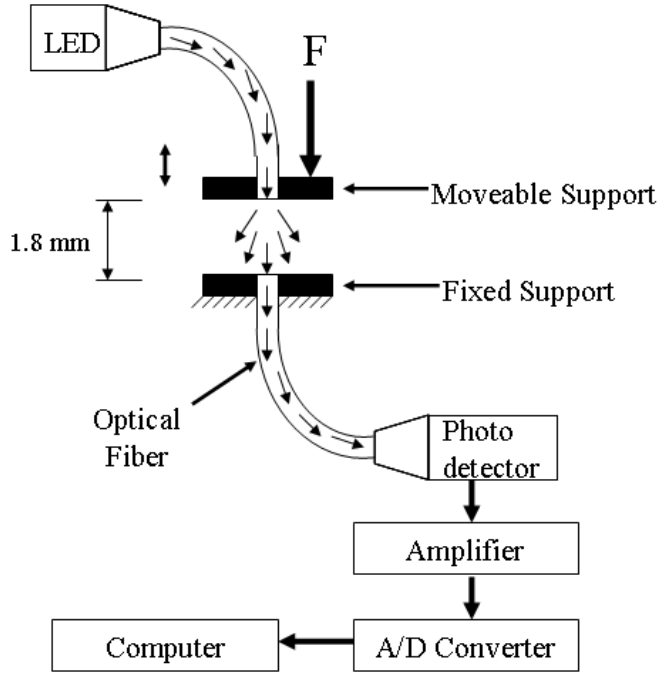

Figure 3-2. General operation of the force sensing component of the 2-DOF sensor.

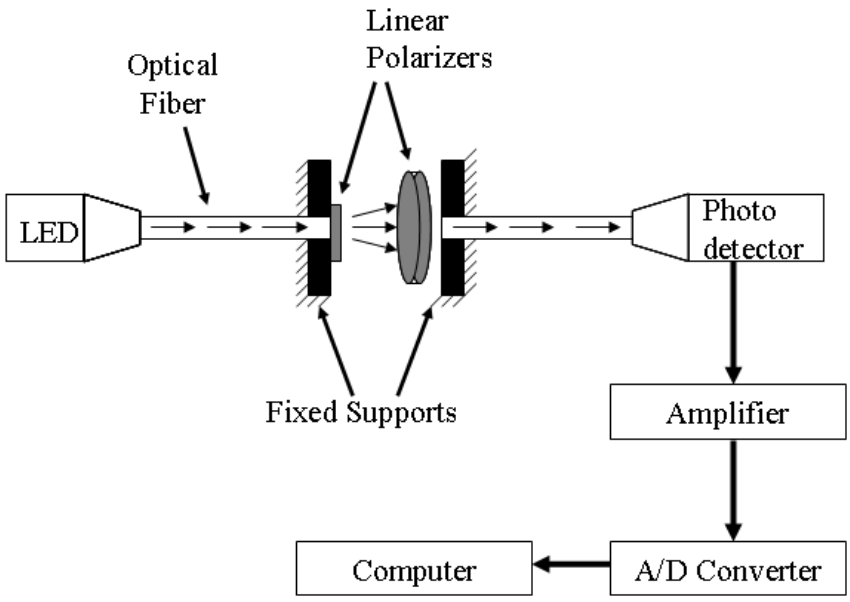

Figure 3-3. General operation of the torque sensing component of the 2-DOF sensor.

3.3 Force Sensor Mathematical Modelling

Section 3.2 presented the general overview of the sensing system. This section concentrates on the force sensing structure and the structural and optical intensity mathematical modelling of the sensor when it is subjected to applied forces. The 2-DOF sensor consists of three main parts: A – C. Components Part B, Part C and Nitinol Strip A form the force sensing (F_z) component of the 2-DOF sensor as shown in Figure 3-4 to Figure 3-7. Note that for this description Nitinol Strip J collectively refers to the two horizontal nitinol strips. The two strips help stabilize the sensor and reduce unwanted coupling between sensing axes. In addition, Part B and Part C contain the holes for the axially-aligned transmitting and receiving fibres. All of the parts of the sensor are rigidly bonded to each other with only the nitinol strips designed to flex or twist under applied forces. The rigid bonding design eliminates frictional forces, increases structural stiffness and reduces maintenance costs.

Consider a single strip J, rigidly fixed at its ends in Part C and embedded in the middle by Part B as shown in Figure 3-8a. If a vertical force is applied to Part B then the strip flexes inwards and moves the transmitter and receiver closer together. Let z_0 be the initial separation distance between the transmitting and receiving fibres. The strip deflection, δz of a uniform rectangular strip, fixed at both ends and subjected to a point load is given by

$$\delta z = \frac{2Fa^3(L-a)^2}{3EI_{xx}(2a+L)^2} \quad \text{(m)} \qquad \textbf{(3-1)}$$

where $\boldsymbol{L}$ is the total length of the strip (m), $\boldsymbol{a}$ is the distance between the applied force and the fixed end (m), $\boldsymbol{E}$ is the Young's Modulus of Elasticity of the material (Pa), $\boldsymbol{F}$ is the applied force (N), $\boldsymbol{I_{xx}}$ is the second moment of inertia for the strip (m^4) and $\boldsymbol{\delta z}$ is the deflection of the strip (m) when loaded as shown in Figure 3-8b [146]. The second moment of inertia of a rectangular beam about the x-axis is given by

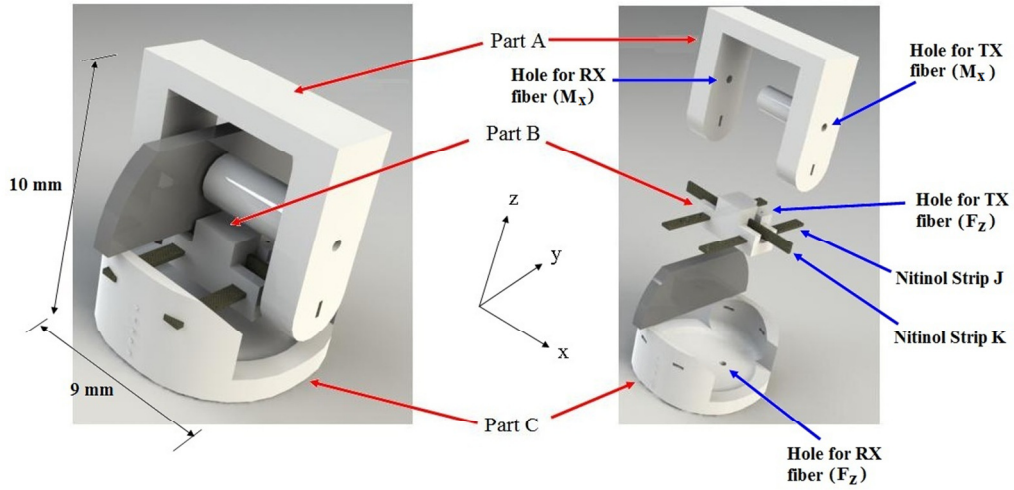

Figure 3-4. The proposed 2-DOF sensor based on LIM using linear polarizers. Part A is connected to the fingertip and Part C makes contact with the object. Part B links Parts A and C and provides the 2-DOF movement with Nitinol Strip K providing rotation movement (M_x component) and Nitinol Strip J providing translational movement (F_z component). The polariser (grey material) intensity modulates the light when Part C is in contact with an object.

Figure 3-5. A photo of the 2-DOF sensor and the dexterous fingertip.

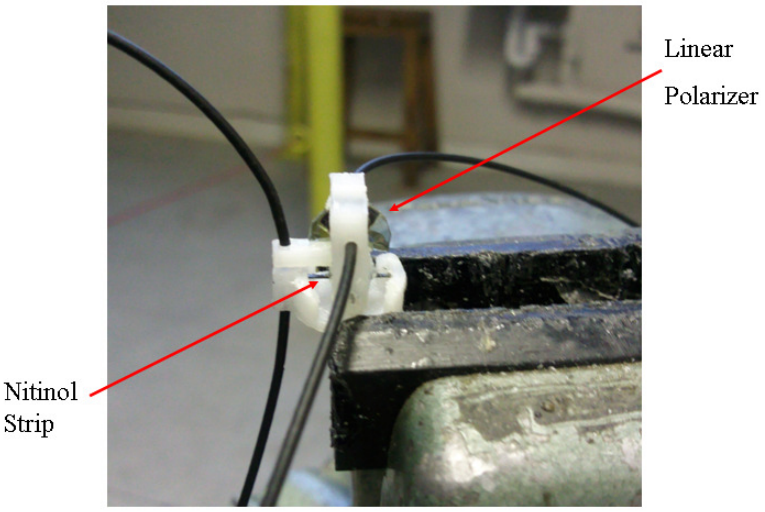

Figure 3-6. The completed 2-DOF before it was integrated into the fingertip.

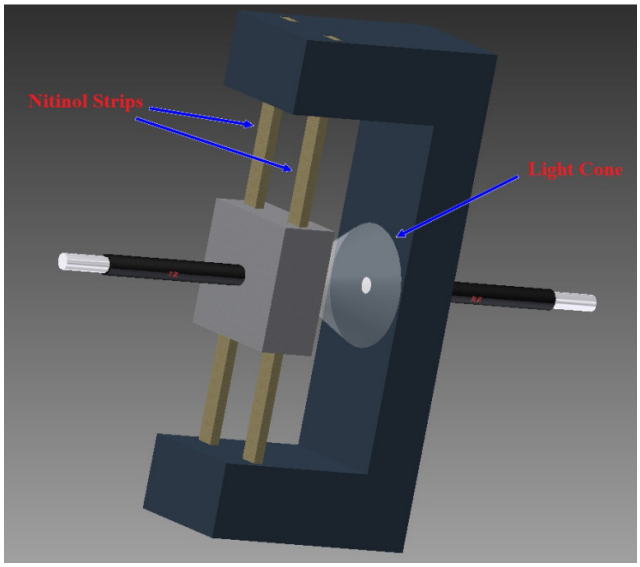

Figure 3-7. Drawing of the force sensing component of the 2-DOF sensor and incorporating an illustration of the light emitted from the transmitting fibre.

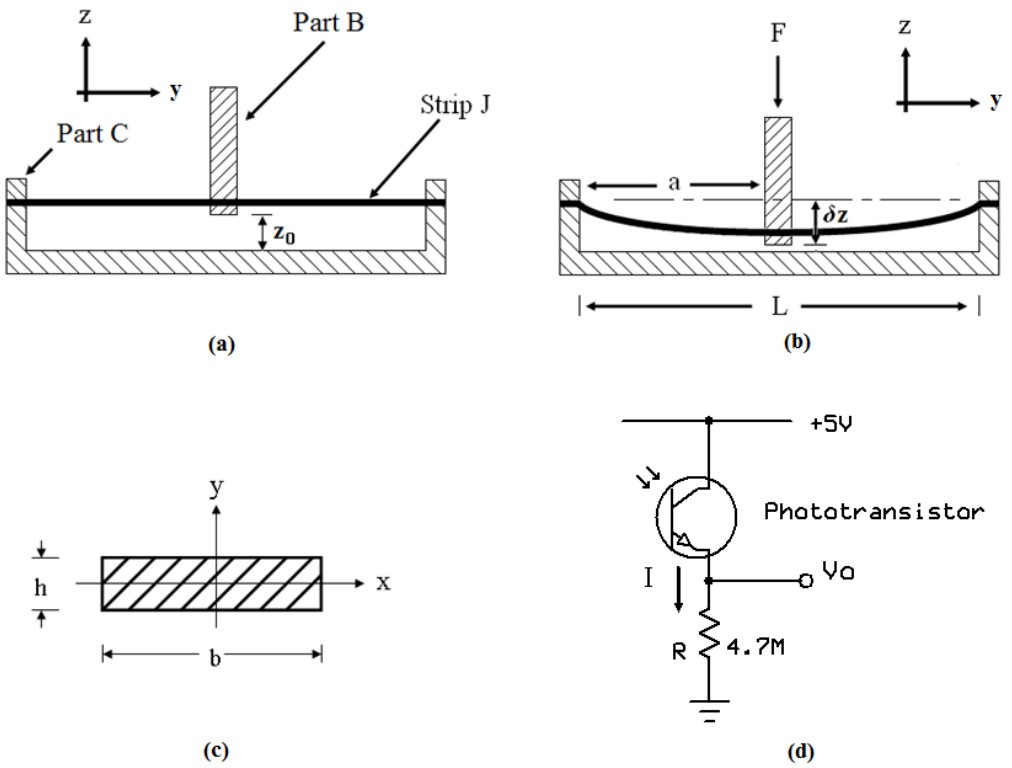

Figure 3-8. Nitinol strip deflection principle. (a) Default position of the unloaded strip. (b) The strip deflecting due to an applied force. (c) The cross-sectional area of the strip. (d) The phototransistor detection circuit.

$$I_{xx} = \frac{bh^3}{12} \quad (\mathrm{m}^4) \tag{3-2}$$

where ***h*** is the thickness perpendicular to the axis (m) and ***b*** is the width of the strip parallel to the axis (m) (see Figure 3-8c). If the deviation is small then the strip deflection is approximately linear and obeys Hooke's Law,

$$F = k\delta z \qquad (\mathrm{N}) \tag{3-3}$$

where ***F*** is the applied force (N), ***k*** is the constant for the strip and ***δx*** (m) is the deflection of the loaded strip. Substituting (3-1) into (3-3) gives the value of ***k*** where,

$$k = \frac{3EI_{xx}(2a+L)^2}{2a^3(L-a)^2} \qquad \text{(N/m).} \qquad \textbf{(3-4)}$$

The transmitting fibre is embedded within the deflecting section (Part B) so as the strip deflects more light is coupled to the receiving fibre in Part C. The light emitted from the fibre generates a Gaussian profile as it propagates away from the fibre. The equation describing the Gaussian profile is given by

$$I(r,z) = I_0\left(\frac{w_0}{w(z)}\right)^2 e^{\left(\frac{-2r^2}{w^2(z)}\right)} \qquad \text{(cd)} \qquad \textbf{(3-5)}$$

where z is the distance propagated from the emitting fibre, r is the radial distance from the centre of the emitting fibre (m), I_0 is the intensity at the centre of the Gaussian beam (cd) , w_0 is the Gaussian beam waist at the emitting fibre (m), $w(z)$ is the beam waist (m) after the light has propagated a distance of z metres and $I(r, z)$ is the intensity at a radial distance r metres after propagating a distance of z metres **[147]**. The beam waist, w_0 (m) is defined as the radial width of the profile at which the intensity falls to $1/e^2$ (13.5%) of its maximum value. The beam waist, w as a function of propagation distance, z is given by

$$w(z) = w_0\left[1+\left(\frac{z\lambda M^2}{\pi w_0^{\,2}}\right)^2\right]^{1/2} \qquad \text{(m)} \qquad \textbf{(3-6)}$$

and

$$z = z_0 + \delta z \qquad \text{(m)} \qquad \textbf{(3-7)}$$

where λ is the wavelength of the transmitted light (nm) and M^2 is the quality factor of the Gaussian beam, $w(z)$ is the beam waist at a propagation of z and z_0 is initial separation between the transmitting and receiving fibres (see Figure 3-8). Figure 3-9d

shows how the Gaussian profile changes with different values of M^2. An ideal Gaussian distribution has a quality factor of 1 which produces a very slender profile while larger values of M^2 produce an increasingly flatter profile [152]. This is because the area under a Gaussian profile is fixed hence as the wave spreads the amplitude of the profile must decrease to maintain the fixed area under the curve. The optical power of the light received by the receiving fibre depends on the size of the core of the receiving fibre and the intensity of the receiving light. The received power is given by

$$P(r,z) = \int_0^r I(r,z) \cdot 2\pi r dr \qquad \textbf{(3-8)}$$

where $2\pi r$ is the circumference of the receiving aperture and $I(r, z)$ is the intensity of the light at the receiving fibre. Substituting equation (3-5) into (3-8) and integrating gives

$$P(r,z) = I_0 \left(\frac{w_0}{w(z)} \right)^2 2\pi \int_0^r r \cdot e^{-\frac{2r^2}{w^2(z)}} dr$$

$$\therefore \qquad P(r,z) = \frac{\pi I_0 {w_0}^2}{2} \left(1 - e^{\frac{-2r^2}{w(z)^2}} \right) \quad \text{(W)}. \qquad \textbf{(3-9)}$$

The photodetetctor produces a current that is proportional to the power of the light being received. The photodetector in this research is a phototransistor which has an intrinsic amplification factor, K_p and it also has a relative spectral sensitivity, S_k to the wavelength of the light used. Both of these parameters were available from the phototransistor's datasheet. The current supplied by the phototransistor is then given by

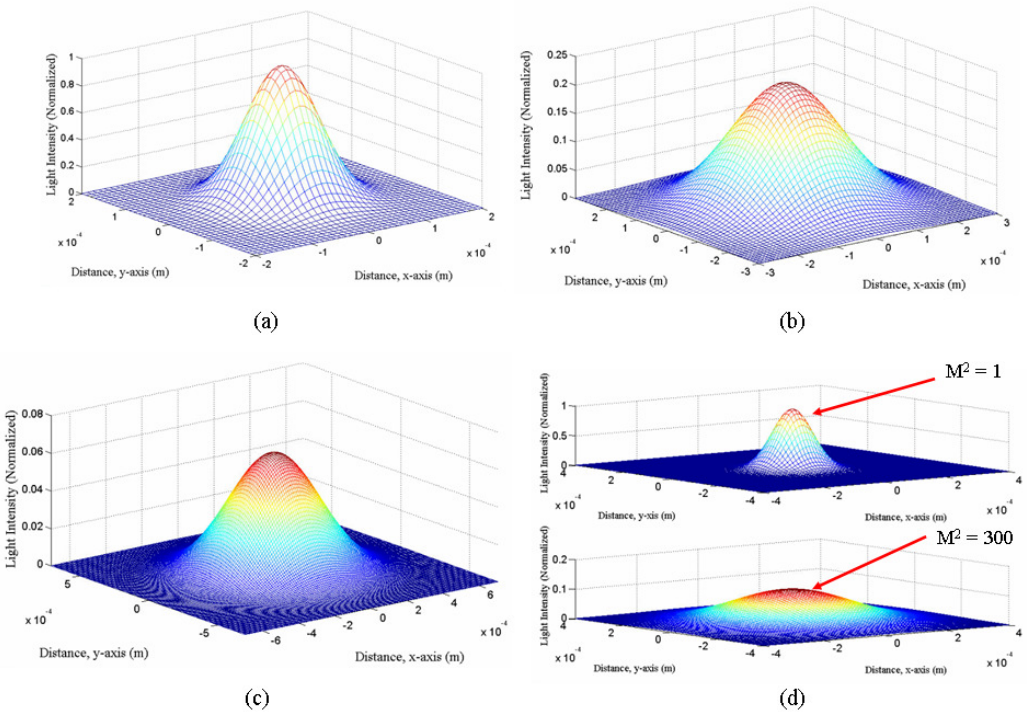

Figure 3-9. The Gaussian waveform decreases in amplitude in order to maintain the constant volume under the curve as it propagates away from the source. (a) The Gaussian light at the emitter of the light source. (b) The Gaussian light at a medium distance (5 mm) from the emitter of the light source. The intensity has fallen to approximately one quarter of the maximum intensity at the emitter. (c) The Gaussian light at a far distance (10 mm) from the emitter of the light source. The intensity has fallen to less than one tenth of the maximum intensity at the emitter. (d) A comparison of the effect of the quality factor, M^2 on the profile of the Gaussian beam.

$$I_R(z) = K_p \cdot S_k \cdot P(r,z)$$

$$I_R(z) = K_p \cdot S_k \cdot \frac{\pi I_0 {w_0}^2}{2}\left(1 - e^{\frac{-2r^2}{w(z)^2}}\right) \qquad \text{(A)} \qquad \textbf{(3-10)}$$

The phototransistor current flows through a resistor ***R*** which converters the current to a representative voltage of the received light. The voltage representation of the change in received light is then given by

$$V_R(z) = I_R \cdot R$$

$$V_R(z) = R \cdot K_p \cdot S_k \cdot \frac{\pi I_0 {w_0}^2}{2}\left(1 - e^{\frac{-2r^2}{w(z)^2}}\right) \quad \text{(V)} \quad \textbf{(3-11)}$$

where $V_R(z)$ is the change in voltage for the change in distance, z (see Figure 3-6). Plotting equation (3-11) for propagation distance, z produces the curve shown in Figure 3-10. The response curve is generally does not have a constant gradient but small displacements about an initial position produce an approximately constant gradient output. The sensor's linear displacement is limited to a maximum travel of ± 1 mm from the initial position (the red line in Figure 3-10). The general equation of the line is given by

$$V_R(z) = q(z - z_0) + V_o \quad \textbf{(3-12)}$$

where q is the gradient of the line, V_o is the initial voltage at the unloaded position, z is the displacement of the deflecting strip and $V_R(z)$ is the voltage at the position z. The value of the gradient, g can be found experimentally during calibration of the sensor. Substituting equation (3-7) into (3-12) and rearranging gives

$$\delta z = z - z_0$$

$$\Rightarrow \quad \delta z = \frac{V_R(z) - V_o}{q} \quad \text{(m)} \quad \textbf{(3-13)}$$

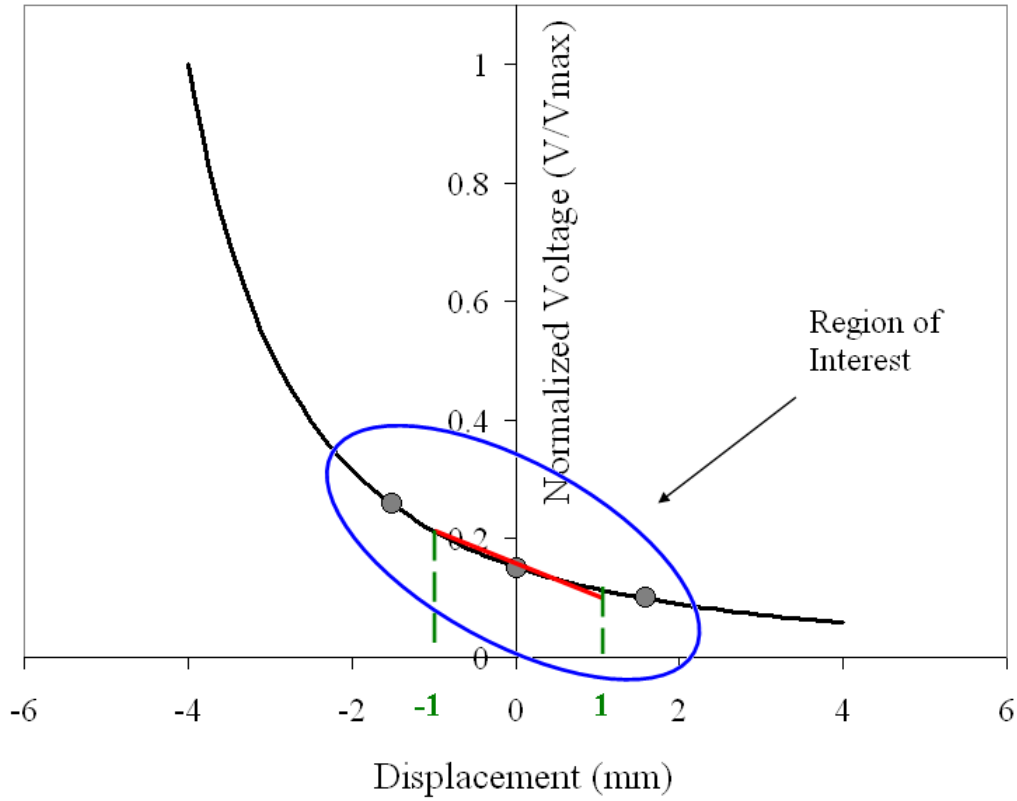

Figure 3-10. Graph of the normalized detector voltage for the displacement of the transmitting fibre.

and substituting equation (3-13) into (3-3) gives

$$F = \frac{k}{q}\left(V_R(z) - V_o\right) \quad \text{(N)} \qquad \textbf{(3-14)}$$

where k is the constant for the strip given by equation 3-4. Equation (3-14) therefore gives the relationship between the applied force and the change in voltage.

Temperature fluctuations affect the diameter of the sensing fibre causing fluctuations in the phototransistor current and the force reading. The radial change due to temperature is given by

$$\Delta r = r_0 \alpha \Delta T \tag{3-15}$$

where r_0 is the initial radius of the fibre, α is the coefficient of linear expansion of the material, ΔT is the change in temperature and Δr is the change in fibre radius. The change in received power due to the change in temperature is given by

$$P(\Delta r, z) = \frac{\pi I_0 {w_0}^2}{2}\left(1 - e^{\frac{-2(r_0 \alpha \Delta T)^2}{w(z)^2}}\right). \tag{3-16}$$

The temperature sensitivity of the voltage with respect to the temperature is given by

$$\frac{\partial V}{\partial T} = R \cdot K_p \cdot S_k \cdot \frac{2\pi I_0 {w_0}^2 {r_0}^2 \alpha^2}{w(z)^2}\left(e^{\frac{-2(r_0 \alpha \Delta T)^2}{w(z)^2}}\right)\Delta T. \tag{3-17}$$

The graph of equation 3-17 is shown in Figure 3-10 where the sensitivity is plotted against the temperature change.

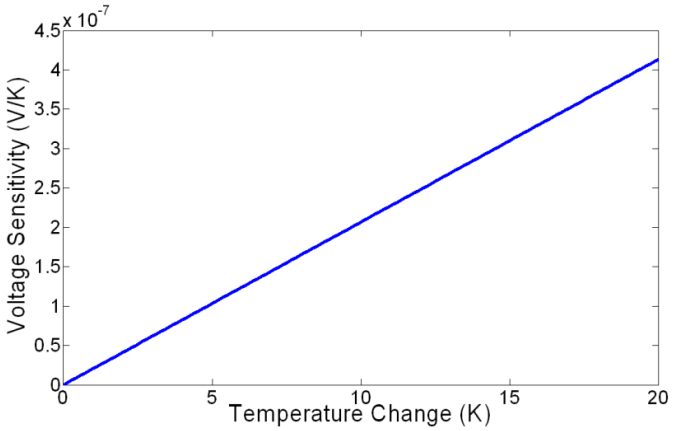

Figure 3-11. Graph of the temperature sensitivity of the sensing fibre for a change in temperature.

3.4 Torque Sensor Mathematical Modelling

The torque sensing component of the sensor is comprised of Part A, Part B and Nitinol Strip K as shown in Figure 3-4. The ends of Nitinol Strip K are rigidly embedded into Part A while the middle of Strip K is bonded to the middle of Part B resulting in the two parts experiencing only rotational movement relative to each other (about the x-axis). Both of the transmitting and receiving fibres are axially-aligned and embedded within Part A at a fixed distance z from each other. This is in contrast to the force sensor which has the fibres axially-aligned but modulates the intensity by moving the fibre towards or away from each other. The torque sensor modulates the light intensity by rotating a linear polarizer in the path of light beam. Linear polarisers commonly consist of long chains of aligned crystalline material embedded within a plastic sheet. Light that is oriented parallel to the crystalline chains passes through the slits unattenuated while all other orientations are attenuated with maximum attenuation occurring at angles perpendicular to the crystalline chains [145]. Figure 3-11 shows two polarisers whose polarization axes are oriented at angles of 0°, 45° and 90° corresponding to full, half and zero intensity respectively. The first polarizer is fixed at zero degrees to produce the linearly polarized light while the second polarizer, also referred to as the analyzer, can rotate freely in the polarized light.

Applications of linear polarisers include glare reduction [150] and investigation of liquid crystals and metametarials [151], [153]. In order to mathematically model the torque sensor consider a beam, fixed at one end and subjected to a torque on the other end as shown in Figure 3-13. The torque required to twist the beam by an angle of θ is given by

$$T = \frac{JG\theta_r}{L} \qquad \textbf{(3-18)}$$

where $\boldsymbol{G}$ is the shear modulus of the material, $\boldsymbol{L}$ is the length of the twisting beam, $\boldsymbol{J}$ is the torsional stiffness of the structure, $\boldsymbol{\theta_r}$ is the angle of twist in radians and $\boldsymbol{T}$ is the required torque.

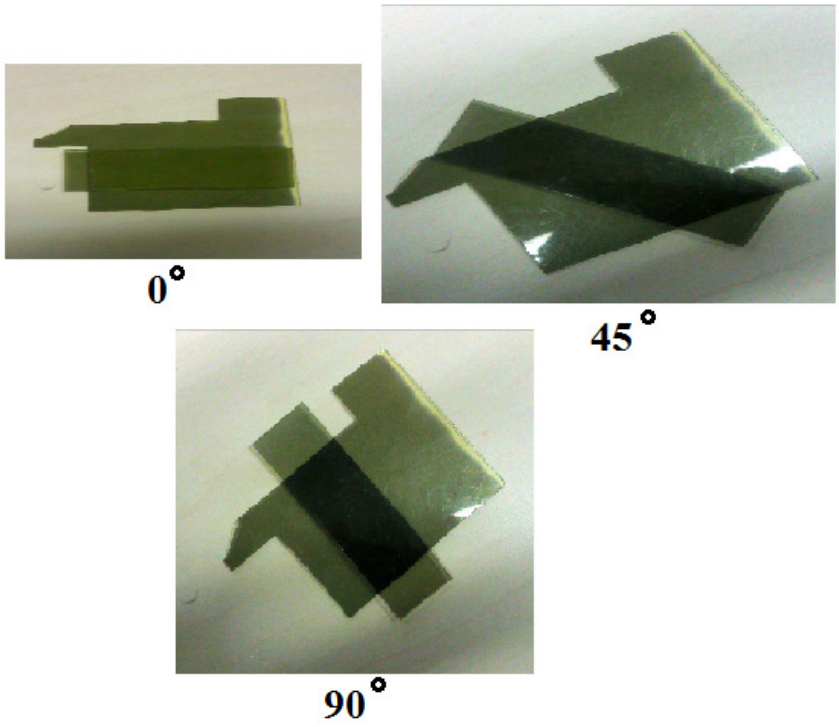

Figure 3-12. The intensity modulation of light at polarization angles of 0°, 45° and 90°.

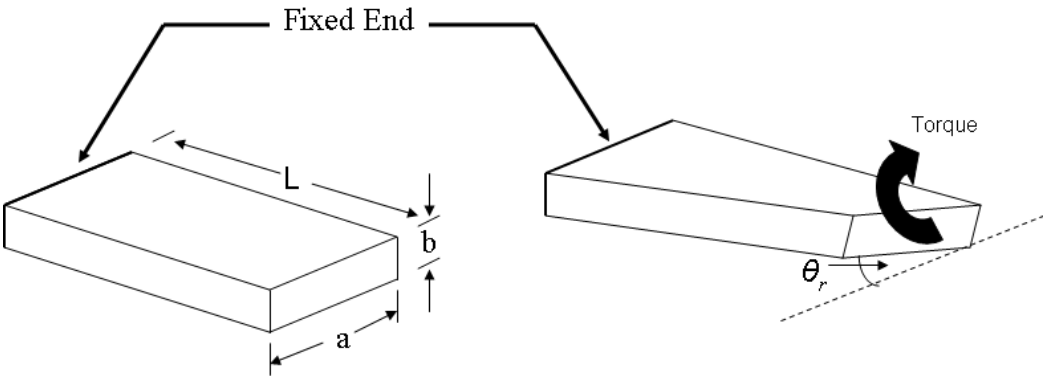

Figure 3-13. Illustration of the twisting of a beam from an applied torque.

The torsional stiffness of a structure is an indication of the torque required to twist a structure. The torsional stiffness of a structure depends on structure's shape and dimensions. Generally, for a rectangular structure with cross-sectional dimensions of ***a*** and ***b*** and length, ***L*** (see Figure 3-13) the torsional stiffness, ***J*** is given by

$$J = ab^3\left[\frac{1}{3} - 0.21\frac{b}{a}\left(1 - \frac{b^4}{12a^4}\right)\right] \qquad (\text{m}^4). \qquad \textbf{(3-19)}$$

One of the design requirements of sensor is the simultaneous measurement of both the applied force and torque, i.e. the DOF should be decoupled. To achieve this result Strip K is oriented perpendicularly (vertical) to the orientation of Strip J (horizontal) thereby presenting the thin edge of the strip to the vertical (F_z) force. From equation (3-2), the vertical orientation decreases the possibility of bending when a vertical force, F_z is applied to the sensor. For example, if ***b*** is 5 units and ***h*** is 2 units in equation (3-2) then the second moment of inertia is over six times larger if the values are reversed.

The light passing through two consecutive linear polarizers is defined by

$$I(\theta) = \eta_p I_0 \cos^2(\theta) \qquad (\text{cd}) \qquad \textbf{(3-20)}$$

where $\boldsymbol{I_0}$ is the maximum light intensity incident on the polarizer, $\boldsymbol{\theta}$ is the angle of rotation, $\boldsymbol{\eta_p}$ is the efficiency of polarizer to transmit light and $\boldsymbol{I(\theta)}$ is the intensity of the transmitted light. One other feature of linear polarizers is that the output intensity is not affected by linear translations only rotations. This feature also helps decouple the force and torque sensors. Plotting equation (3-20) produces a sigmoid curve as shown in Figure 3-14. One of the features of the sigmoid function is that it has a linear region around the midpoint of the curve. This is advantageous for three reasons: firstly the midpoint, at 45° of rotation, represents half of the intensity and is a convenient position for the starting configuration of the device. Secondly, the linear response simplifies the conversion between rotated angle and intensity. Thirdly, the direction of the rotation can be easily determined by the magnitude of the response with respect to the starting position.

The torque sensor transmitting and receiving fibres are both embedded in Part A at a fixed separation distance. Equation (3-5) can modified for a fixed distance, z to give

$$P(\theta) = \frac{\pi I(\theta) {w_0}^2}{2}\left(1 - e^{\frac{-2r^2}{w^2}}\right) \quad \text{(W)} \qquad \textbf{(3-21)}$$

where $\boldsymbol{I(\theta)}$ is the intensity of the transmitted polarized light and $\boldsymbol{P(\theta)}$ is the optical power at angle $\boldsymbol{\theta}$. Substituting equation (3-20) into (3-21) gives

$$P(\theta) = \frac{\pi {w_0}^2 \eta_p I_0 \cos^2(\theta)}{2}\left(1 - e^{\frac{-2r^2}{w^2}}\right) \quad \text{(W).} \qquad \textbf{(3-22)}$$

The output current is given by

$$I_R = K_p \cdot S_k \cdot \frac{\pi {w_0}^2 \eta I_0 \cos^2(\theta)}{2}\left(1 - e^{\frac{-2r^2}{w^2}}\right) \text{(A)} \qquad \textbf{(3-23)}$$

and the corresponding output voltage is given by

$$V_R = R \cdot K_p \cdot S_k \cdot \frac{\pi {w_0}^2 \eta I_0 \cos^2(\theta)}{2}\left(1 - e^{\frac{-2r^2}{w^2}}\right) \quad \text{(V)} \qquad \textbf{(3-24)}$$

where $\boldsymbol{K_p}$ is the intrinsic amplification factor of the phototransistor, $\boldsymbol{S_k}$ is the relative spectral sensitivity of the phototransistor, $\boldsymbol{R}$ is the sensing resistor and V_R is the voltage across the sensing resistor. The temperature sensitivity is given by

$$\frac{\partial V}{\partial T} = 2 \cdot R \cdot K_p \cdot S_k \cdot \frac{\pi {w_0}^2 \eta I_0 \cos^2(\theta) {r_0}^2 \alpha^2}{w^2}\left(e^{\frac{-2(r_0 \alpha \Delta T)^2}{w^2}}\right)\Delta T \quad \text{(V/K).} \qquad \textbf{(3-25)}$$

Equation (3-24) is linear for rotations between 25 ° - 65 ° (45 ± 20 °) about the midpoint.

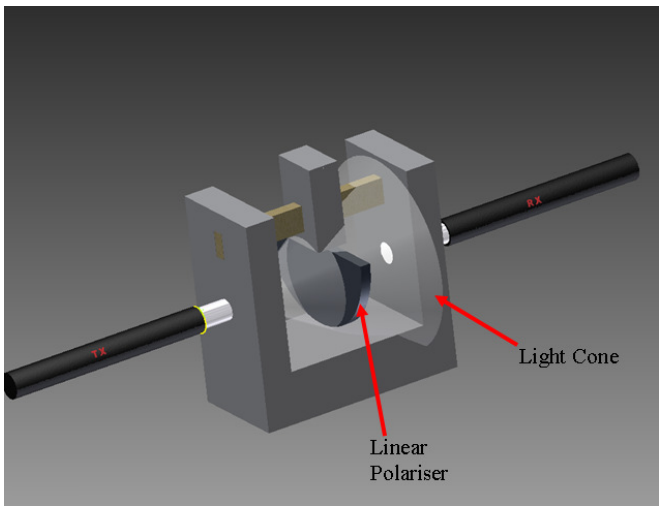

Figure 3-14. The drawing of the torque sensing component of the 2-DOF sensor.

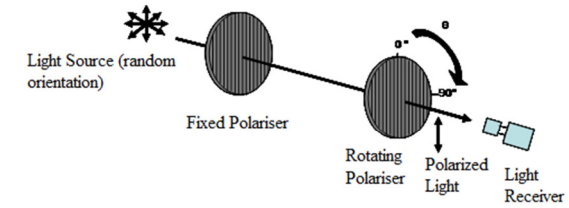

(a)

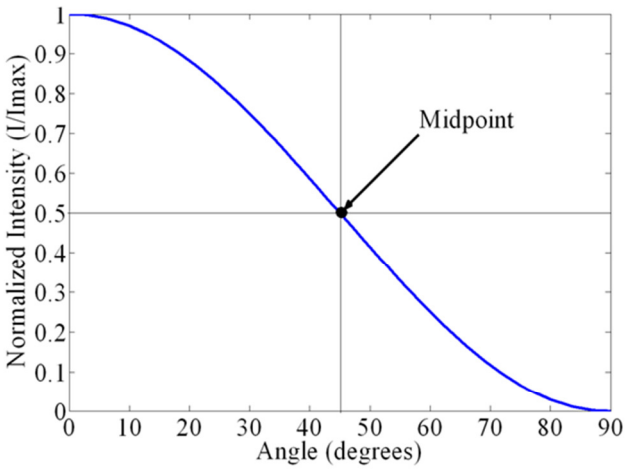

(b)

Figure 3-15. The general principles of linearly polarized light. (a) Unpolarized light is first polarized by passing through a fixed linear polarizer then intensity modulated by an analyzer polarizer. (b) The response curve of transmitted linearly polarized light.

The equation for the linear response can be written in the form

$$V_R(\theta_r) = c\left(\theta_r - \frac{\pi}{4}\right) + V_1 \quad \text{(V)} \qquad \textbf{(3-26)}$$

where c is the gradient of the line, V_1 is the voltage at the midpoint and $V_R(\theta_r)$ is the voltage at angle θ_r (in radians). Substituting (3-26) into (3-18) for θ_r gives

$$T = \frac{JG}{Lc}\left[V_R(\theta_r) - V_1\right] \quad \text{(Nm)} \qquad \textbf{(3-27)}$$

Note that in (3-26) and (3-27) the angle has been expressed in radians. Equations (3-14) and (3-27) therefore present models of the force and torque sensors respectively. Both equations were developed based on small deviations from the initial unloaded position. For equation 3-14 the typical working range is between ± 1 mm from the unloaded position while for equation 3-27 the typical working range is between 45 ± 25° which is within the constant gradient portion of the linear polariser response curve.

3.5 Sensor Simulation

Section 3.3 and Section 3.4 developed mathematical models of the sensor based on the sensor's sensing structure and light intensity modulation techniques. The models provided a correlation between the photodetector voltage and the applied force and torque. This section presents a Finite Element Model (FEM) simulation of the operation of the structure of the sensor to obtain both qualitative data (such as do the flexures deflect as predicted) and quantitative data (such as what is the safe

working range of the sensor). The sensor was drawn and simulated using Autodesk Inventor Professional 2013 [154]. This program only simulates the deformation of the sensor's structure when forces are applied to the contact plate. The light intensity modelling of the aligned optical fibres and the linear polarisers can not be simulated with that particular software package hence a model combining both areas (structure and light intensity) was developed to compare theoretical output of the model with the experimental output of the sensor when subjected to applied forces. Although only the mechanical structure can be simulated with the program it does allow for two important design properties to be examined before the sensor is fully integrated into a dexterous fingertip. The first aim is to examine the deviation of the nitinol flexures since the pieces used were sample material so the flexure response is not documented. In addition, the Young's Modulus of the material is not exactly given by the manufacturer due to confidentiality reasons. The second aim of the simulations is to investigate the safe working range and the maximum working limit before applying large forces to the sensor. Note that the model assumes a constant gradient response for linear displacements of ± 1 mm from the default position therefore knowing the range of forces to maintain the displacement in this range is important. The parameters for the simulation are given in Table 3.1.

Figure 3-16 shows the simulation results of a 5 N force applied to the centre of the sensor to produce a purely linear (z-axis) displacement. The colour bar on the left of the diagram shows the displacement of each portion of the sensor. From the simulation results the nitinol flexures deflected inward producing a displacement of approximately 0.67 mm for Part C for the 5 N applied force while exhibiting negligible twisting. This is within the working range of the model of ± 1 mm. Note also that both horizontal nitinol strips (Strip J) curved gently and uniformly along their lengths indicating the structure is balanced. The maximum simulated force was 7 N before the sensor started to fail (due to breaking) and approach the limit of displacement of the model (± 1 mm). Figure 3-16b also shows the vertical Strip K which is designed to resist bending under maximum vertical (F_z) force. Note that this strip does not experience any bending (no colour change) hence changing the orientation and thereby the second moment of inertia (equation 3-2) of the strip can determine which flexures deform under difference forces. Given the values in Table

3.1 the vertical nitinol strip in the torque sensor had over twelve times more resistant to bending when a linear force (F_z) was applied to the sensor.

Figure 3-17 shows the simulated results for a 1 N force applied at the edge of the sensor to produce a purely rotational (x-axis) movement. The colour bar on the left of the diagrams shows the displacement of each portion of the sensor under load. Note that in Figure 3-17a the nitinol Strip J is pratically straight which indicates that the force and torque sections of the sensor are generally decoupled so the force and torque outputs can be separated. The simulations results showed that the 4.5 mNm torque produced a twist of approximately 20 ° which is within the linear range of the linear polarisers. The maximum applied torque was simulated to be 5 mNm to remain within the ± 25 ° constant gradient region of the linear polariser.

Symbol	Parameter	Value
E	Young's Modulus of Elasticity	5.5 GPa
ν	Poisson's Ratio	0.33
G	Shear Modulus	$G = \frac{E}{2(1+\nu)}$ = 2.068 GPa
D	Sensor Diameter	9×10^{-3} m
H	Sensor Height	10×10^{-3} m
a	Strip Width	0.7×10^{-3} m
b	Strip thickness	0.2×10^{-3} m
L_1	Length of Strip J	8×10^{-3} m
L_2	Length of Strip K	2×10^{-3} m
J	Torsional Stiffness	1.53×10^{-15} (from eqn 3-19)

Table 3.1. Table of model parameters and their associated values.

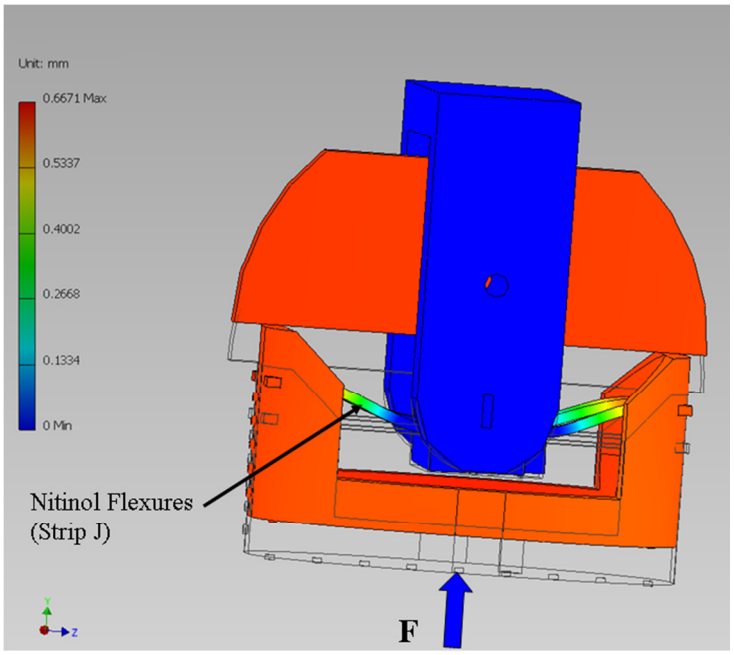

(a)

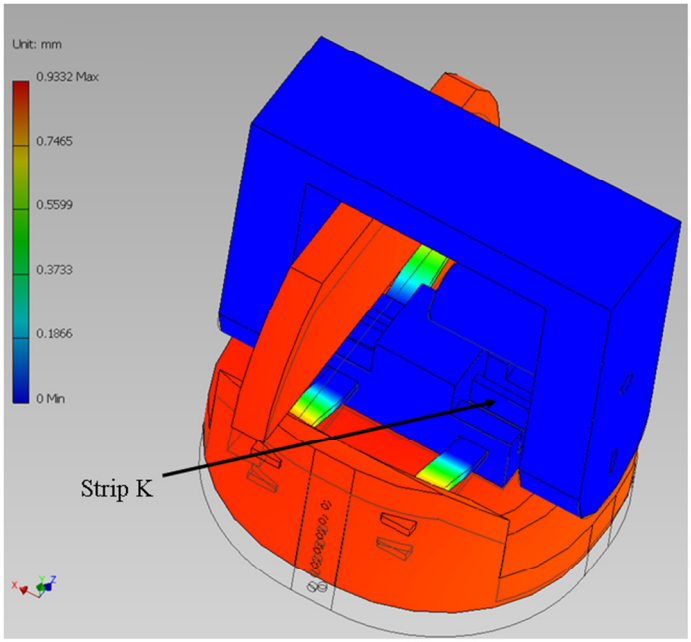

(b)

Figure 3-16. Simulation of a vertical force applied to the centre of the sensor. (a) The displacement of the contact plate under a 5 N vertical force. Note that the nitinol flexures flex inward as required. (b) The vertical Strip K is oriented to resist bending under vertical forces hence there is no colour change with the maximum applied force of 7 N.

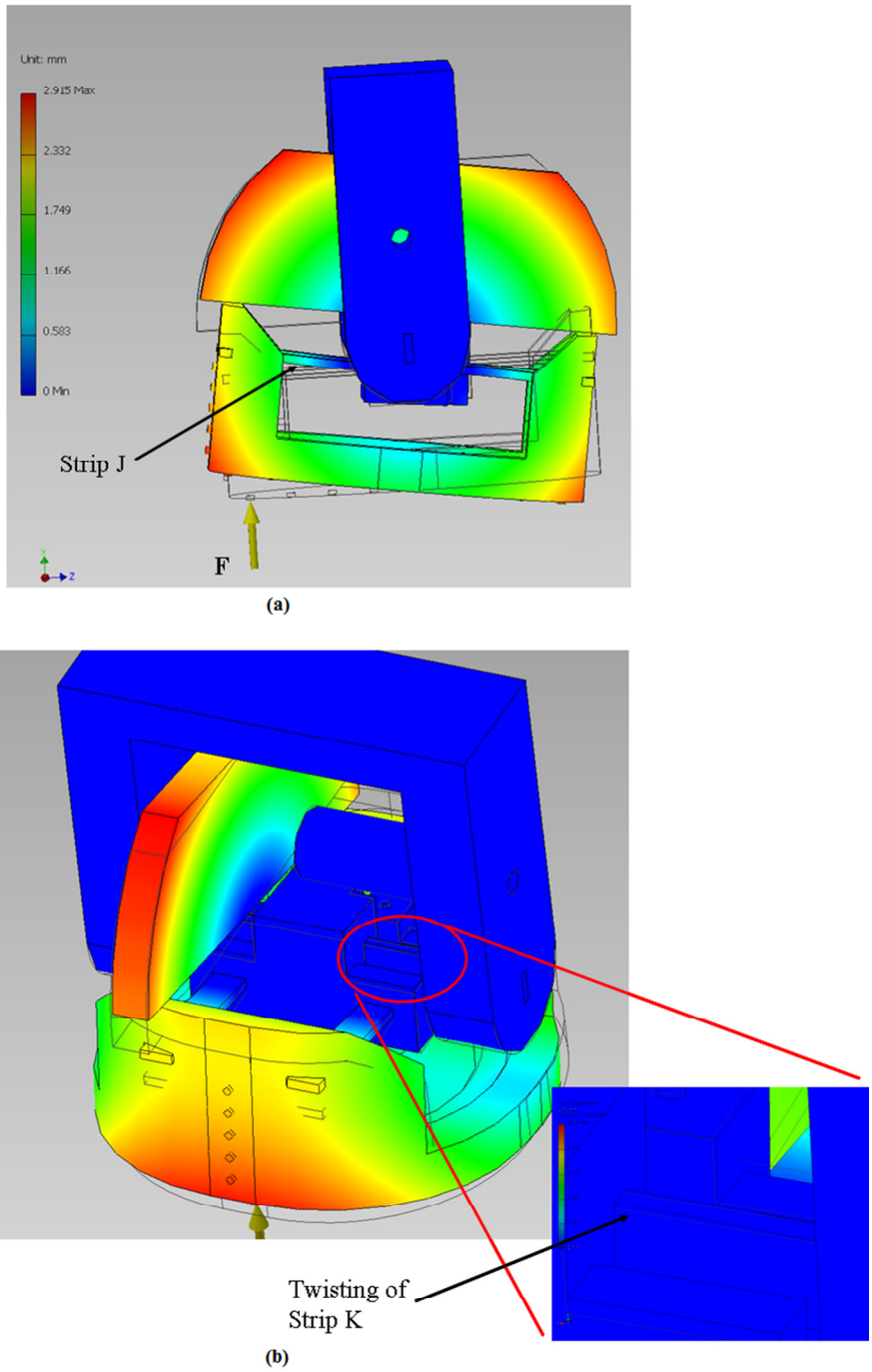

Figure 3-17. Simulation of a torque on the sensor. (a) Side view of a 1 N forces being applied to the edge of a sensor. (b) Twisting of Strip K with the applied torque.

3.6 Chapter Summary

This chapter focused on developing a mathematical model of the proposed 2-DOF sensor in order to predict the expected response of the sensor to applied forces. The 2-DOF sensor used two sensing principles to measure the applied force (F_z) and torque (M_x):

1) Modulating the intensity by varying the displacement between axially-aligned optical fibres (Section 3.3).
2) Modulating the intensity by rotating a linear polarizer in the path of linearly polarized light (Section 3.4).

The two methods necessitated the use of two separate equations to model the behaviour of the 2-DOF sensor. For the first method equation (3-11) expressed the fibre separation distance, z as a change in phototransistor voltage, V. The graph of this function (Figure 3-9) is generally nonlinear, however for small displacements about the initial (undeflected) position the graph can be considered piecewise linear in that region and obeys Hooke's Law (equation (3-3)). With these assumptions equation (3-14) establishes a linear relationship between the applied force and the photodetector voltage provided the displacement around the initial position is small. Simulations of the force sensor (Section 3-5) indicated that the sensing structure did flex as designed and it had a predicted maximum applied force of 5 N before damage occurred.

The torque sensing component of the sensor was designed to be decoupled from the force sensor so that both the force and torque can be measured simultaneously. Two techniques were used to achieve this result. The first technique was to orient the nitinol strip so that its thin edge was presented to the applied F_z force. This change resulted in the strip being twelve times stiffer under vertical (z-axis) forces than a horizontal strip (e.g Nitinol Strip J in Figure 3-4). The second technique was to use linear polarizers to measure the angle of twisting. The linear polarizers have very attractive features that can be applied to sensing applications including:

- It is a commercial product so it can be easily purchased.

- The transmitted intensity is mathematically defined by equation (3-20).
- The output intensity is dependent only on the angle of rotation thereby making the output invariant under translations (refer to equation (3-20)).
- The intensity is half of the maximum intensity at 45 ° of rotation (see Figure 3-15).

Equation (3-24) establishes a linear relationship between the angle of twist and the photodetector voltage provided the angle of twist is between 25 ° – 65 °. The measured torque can then be determined from equation (3-27) establishing a linear relationship between the photodetector voltage and applied torque provided the angle of twist is between 25 ° – 65 °. Simulations of the torque sensor (Section 3.5) indicated that the maximum applied torque of 20mNm is within the required range. Chapter 4 presents experiments where the 2-DOF is integrated into the fingertip of a dexterous manipulator and grasping experiments conducted in order to compare the theoretical and practical results.

CHAPTER 4 – Testing and Evaluation of the 2-DOF Sensor

4.1 Introduction

Chapter 3 presented mathematical models of the 2-DOF sensor that described its operation as well as simulations to estimate the limits of the 2-DOF design. This chapter presents the results of experiments conducted with the 2-DOF sensor and compares and contrasts the actual results with the theoretical projections. The sensor was first calibrated using a commercial force/torque sensor in order to compare the actual and theoretical values. The 2-DOF sensor was then integrated into the fingertip of a Barrett Hand dexterous manipulator and grasping of different objects conducted in order to evaluate the sensor's response to an object's shape, rigidity and curvature. The following sections present the experiments conducted and discussions of those results. Finally, improvements to the sensor are presented based on the experimented results.

4.2 Sensor Calibration Experiments

A number of experiments were conducted on the 2-DOF sensor to investigate such features as temperature variations on the sensor readings, the sensor's response to flat, curved and deformable objects and the sensor's hysteresis. The following sections describe the experiments conducted and examine the results from each of the experiments.

4.2.1 Temperature Sensitivity Experiment

Section 2.2.4 presented common optical modulation techniques for force sensors. One of the common techniques is FBGs which offer high sensitivity and accuracy but is adversely affected by temperature fluctuations. The temperature sensitivity experiment investigates how variations in temperature affect the sensor's readings, specifically if the photodetector's voltages are significantly and adversely affected by temperature fluctuations. The sensor was baked in a GENLAB General

Purpose oven (Model: OV/50/DIG) [157] and the torque sensor photodetector voltage measured at seven intervals between 24 °C (297.15 K) to 44 °C (317.15 K). The maximum temperature was limited to 44 °C to prevent the ABS plastic from plasticizing and causing the fibres to shift out of alignment. The torque sensor was used because the maximum voltage was small enough to use with the most sensitive setting of the voltmeter. The results of the test are shown in Figure 4-1 where the photodetector voltage increases linearly with increasing temperature. The maximum voltage change over the temperature range was approximately 1.5 mV. The data acquisition circuit uses a 10-bit A/D converter and a 5 V supply giving a voltage resolution of 4.88 mV which is above the voltage change for the temperature range. For a 12-bit A/D converter the resolution is 1.22 mV which is about the same as the voltage change and within the error range of the A/D converter (± 1 bit) therefore small temperature fluctuates do not adversely affect the sensor output.

4.2.2 Sensor Calibration

The sensor must first be calibrated so that the voltage output can be correlated to a known force. Section 3.3 and Section 3.4 developed equations that mathematically describe the force and torque components of the sensor however these equations and the values in Table 3.1 can also be used to theoretically calibrate the sensor. The photodetector voltage can be expressed as a function of displacement, z for the force sensor. Assuming small deviations about the initial position then equation 3-3 gives

$$\delta z = \frac{F}{k}$$

and substituting for k from equation 3-4 gives

$$\delta z = \frac{2a^3 F(L-a)^2}{3EI_{xx}(2a+L)^2} \qquad \textbf{(m)} \qquad \textbf{(4-1)}$$

The distance between the transmitter and receiving fibres is then given by equation 3-7 and the change in beam waist as a function of distance, z is given by equation 3-6.

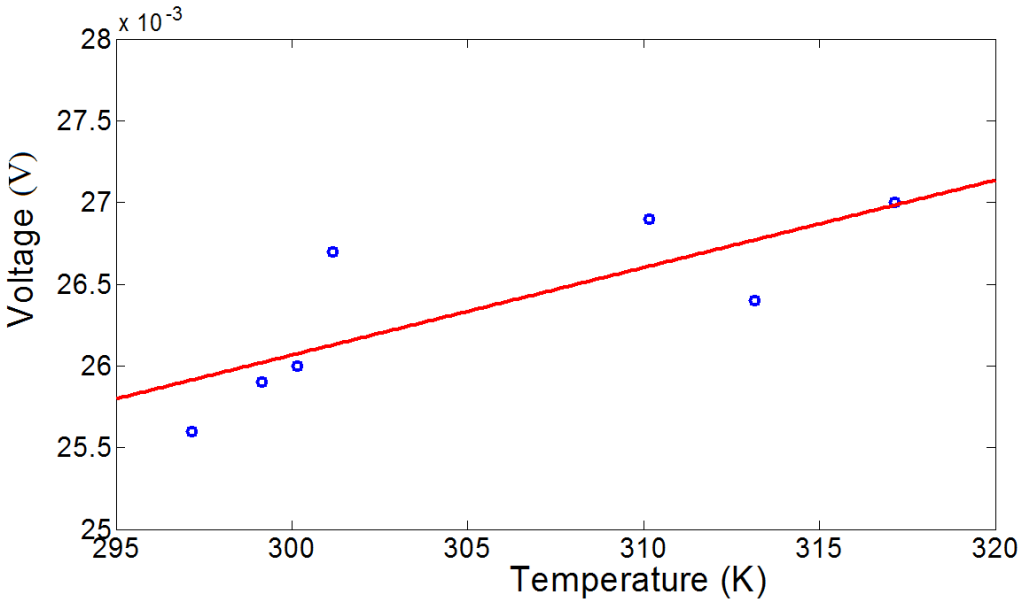

Figure 4-1. The results from the temperature sensitivity test show that the change in voltage with temperature change is generally constant.

The photodetector voltage can also be expressed as a function of the applied torque. The torque due to twisting a material by an angle of θ_r (radians) is given by equation 3-18. For consecutive linear polarisers the amplitude of the intensity-modulated light depends on the angle between the polarization axes of the two linear polarisers (equation 3-20). For the angle θ_r (in degrees) the corresponding output voltage is given by equation 3-24. Therefore for an applied torque the corresponding output voltage can be given by the model. The theoretical calibration curves for 2-DOF sensor are shown in Figure 4-2 and Figure 4-3. The MATLAB code for the calibration curves is given in Appendix F.

The physical calibration of the 2-DOF sensor was performed using a commercial 6-DOF force/torque sensor (ATI, Mini40) and a 6-DOF robotic arm (Mitsubishi, MELFA RV-6SL) as shown in Figure 4-4. The force sensor component was calibrated by loading and unloading the middle of the sensor in steps of 0.1 mm, up to a limit of 0.8 mm and recording the force required for each displacement step. Table 4.1 shows the values of the parameters used in the theoretical model.

Symbol	Parameter	Value
R	Photodetector Resistor	4.7×10^{6} Ω
S_k	Relative Spectral Sensitivity	0.6
K_p	Photodetector Amplification Factor	7.4
d	Fibre diameter	0.25×10^{-3} m
w_0	Beam waist	$0.42 \times d = 0.105 \times 10^{-3}$ m
M^2	Beam Quality	73
λ	Light wavelength	660 nm (red)
E	Young's Modulus of Elasticity	5.5 GPa
I_0	Light Intensity	600 mcd
D	Sensor Diameter	9×10^{-3} m
H	Sensor Height	10×10^{-3} m
a	Strip Width	0.7×10^{-3} m
b	Strip thickness	0.2×10^{-3} m
L_1	Length of Strip J	8×10^{-3} m
L_2	Length of Strip K	2×10^{-3} m
J	Torsional Stiffness	1.53×10^{-15} (from eqn 3-19)
η_p	Polarizer transmission efficiency	0.22

Table 4.1. Table of the parameters and associated values for sensor theoretical model.

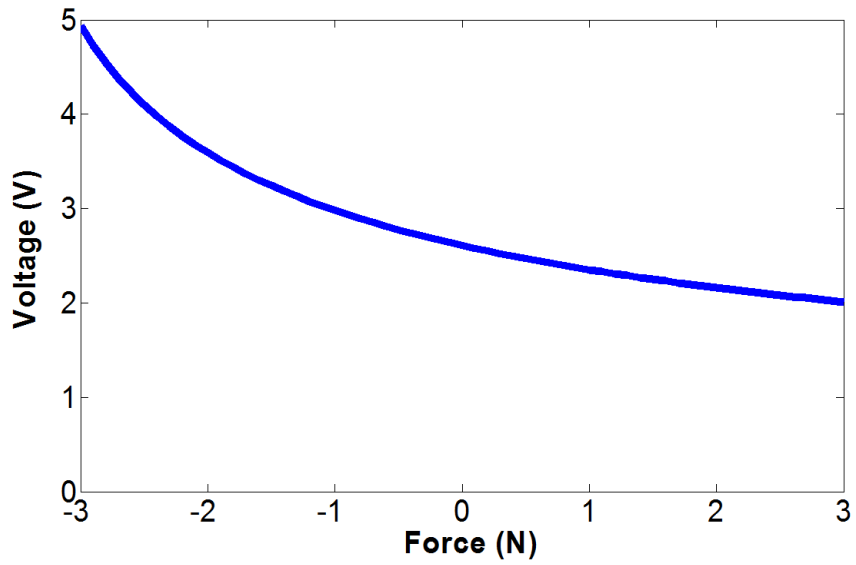

Figure 4-2. Theoretical calibration curve of the sensor based on equations 3-1 to 3-11.

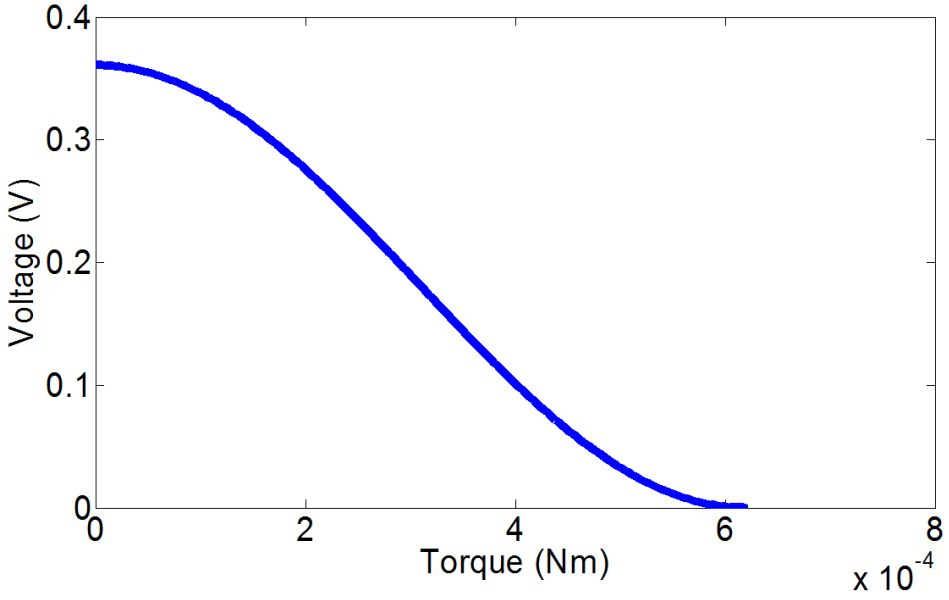

Figure 4-3. Theoretical calibration curve of the sensor for given input torque values.

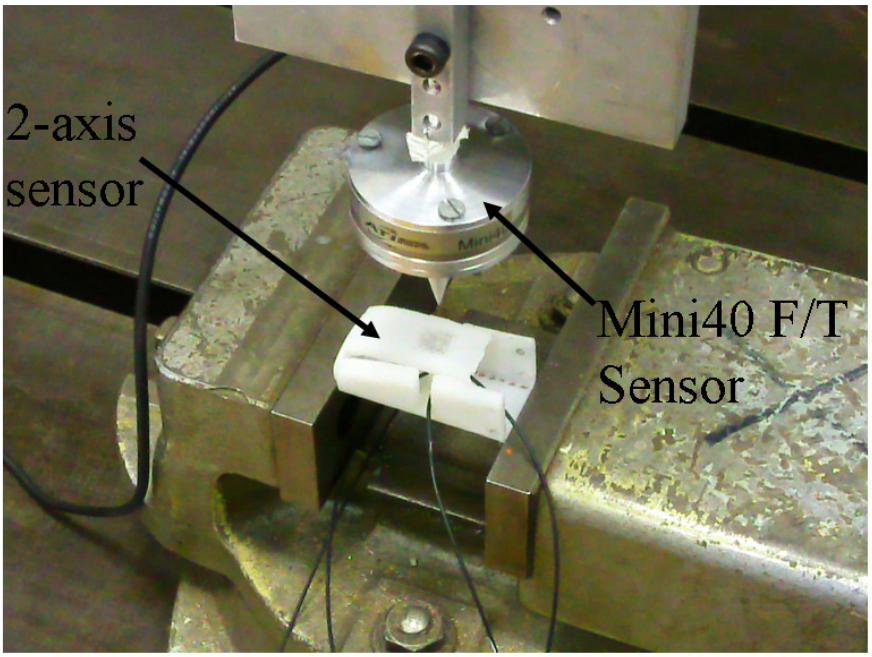

Figure 4-4. The 2-DOF sensor was calibrated using a Mini40 Force/Torque sensor.

Figure 4-5a shows the output photodetector voltage with applied displacement where the diamonds (red) denote the loading points and the squares (blue) denote the unloading points for the nitinol strips. The loading and unloading curves are identical indicating good repeatability, low hysteresis were the hysteresis is given by

$$hysteresis(\%) = \left| \frac{F_{load\,(i)} - F_{unload\,(i)}}{F_{scale}} \right| \times 100\% \qquad \textbf{(4-2)}$$

where $\boldsymbol{F_{load(i)}}$ is the loading force at point $\boldsymbol{i}$, $\boldsymbol{F_{unload(i)}}$ is the unloading force at point $\boldsymbol{i}$ and $\boldsymbol{F_{scale}}$ is the measurable range. The typical hysteresis was approximate 1% with a maximum hysteresis value of 5%. In addition, the loading and unloading curves are linear which is consistent with the assumption that small displacements obey Hooke's Law for equation (3-3). Figure 4-5b shows the comparison between the actual and theoretical photodetector voltage for the applied force. Note that the hysteresis is also

very low (about 2%) and the theoretical and actual curves are identical. This indicates that the output of the force model (equation (3-14)) is indeed correct. The maximum force was limited to 2.66 N to prevent damage to the sensor and the senor's resolution was 11 mN given the A/D voltage resolution was 4.88 mV.

The torque component of the sensor was calibrated by applying forces along the length of the fingertip at 2 mm intervals, up to a limit of 10 mm and recording the applied force, torque and voltage readings at individual contact points. A protractor was also used to measure the angle of twist of the linear polarizer elements. Figure 4-6a shows the output of the linear polarizer when the force component of the sensor was being calibrated. In this case the hysteresis is also low however the shape of the curve is not constant as expected. Recall from Section 3.6 that one of the features of the linear polarizer is that the intensity of the transmitted light is invariant under translations so the output voltage should be constant. There are two possible reasons for this discrepancy. Firstly, the orientation for the polarizer may not be centred at the 45 ° midpoint as desired resulting in the shift of the response to the curved portion of the polarizer graph. Secondly, the applied calibration force is not centred exactly at the centre of the sensor resulting in a combination of linear force and torque during calibration. Figure 4-6b shows the comparison of the theoretical polarizer voltage and the actual polarizer photodetector voltage for the given angular displacement. Note that the shapes of the two curves are similar but the actual response is shifted to the right by approximately 22 ° which validates the first assumption about the shape of Figure 4-6a. Figure 4-7 shows the corrected graph of Figure 4-6b where the actual values were shifted to the left by 22 °.

Figure 4-8 illustrates the effect of applying a centred and an off-centred force on the sensor. A force, $\boldsymbol{F}$ applied to the centre of sensor produces a linear displacement, δx and a linear force, $\boldsymbol{F}_v$. Figure 4-9 (blue dots) shows the response of the sensor to a purely linear force. If the force, $\boldsymbol{F}$ is applied at a point $\boldsymbol{P}$, distance $\boldsymbol{x}$ from the centre of the sensor then the sensor experiences both linear and torque forces.

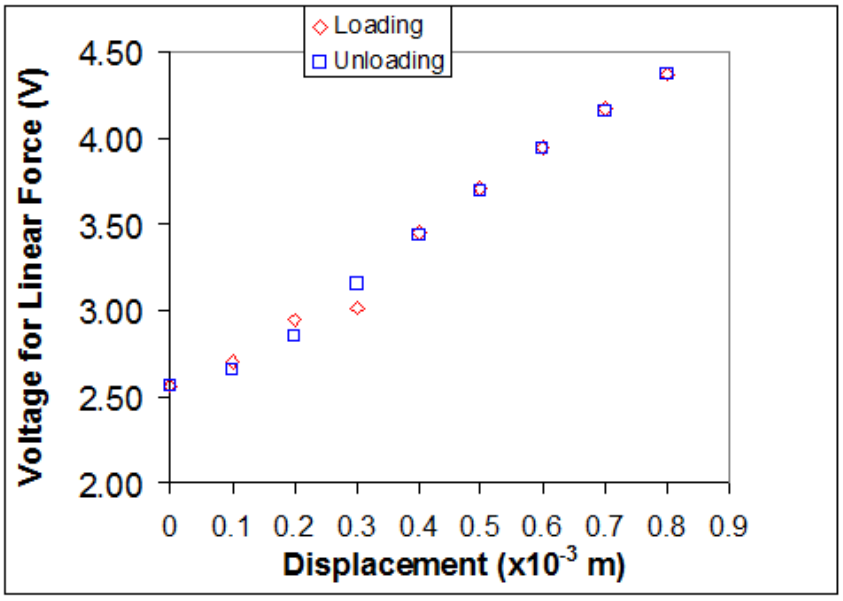

(a)

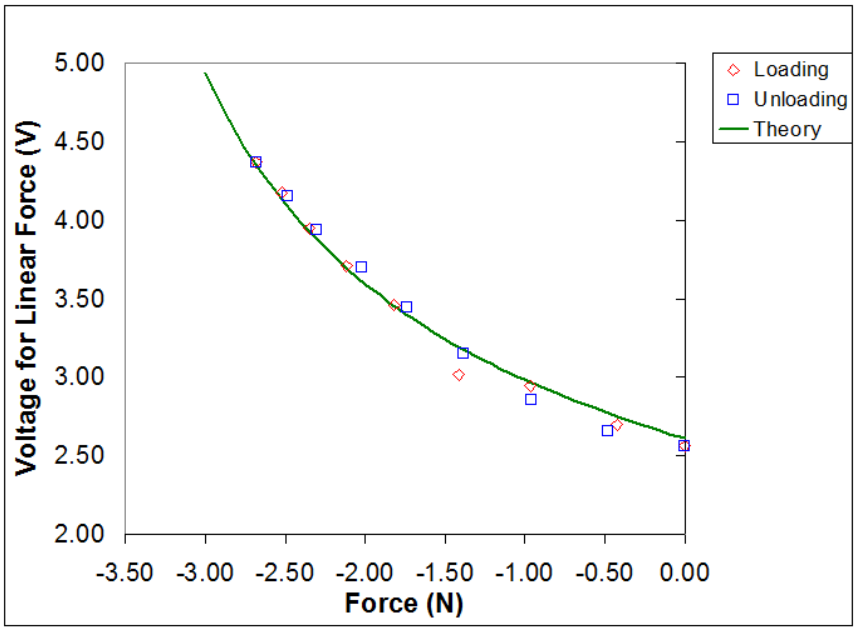

(b)

Figure 4-5. Calibration graphs for the force component of the 2-DOF sensor. (a) The loading and unloading characteristics of the sensor. (b) Comparison of the actual and theoretical photodetector voltage for the sensor.

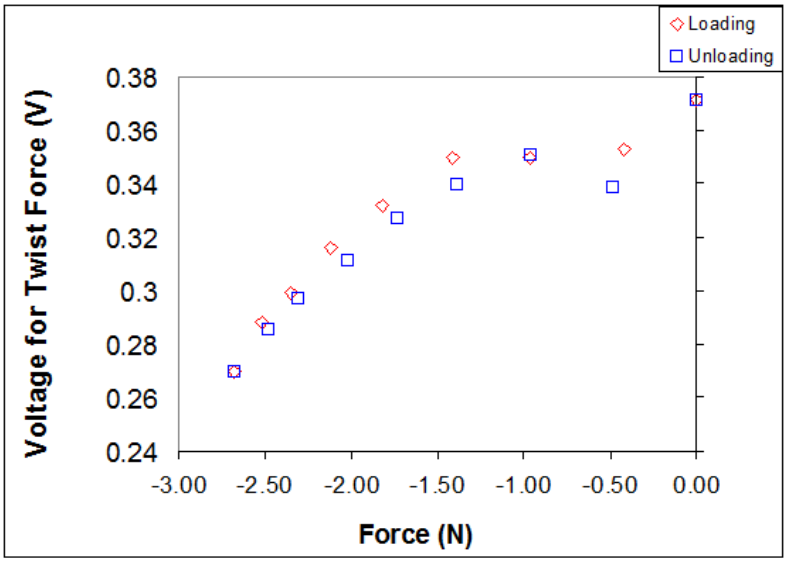

(a)

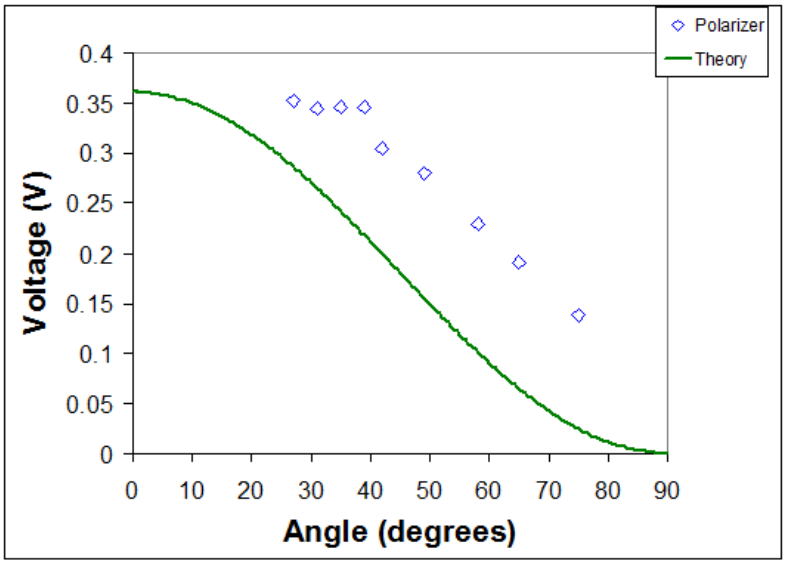

(b)

Figure 4-6. Calibration graphs for the torque component of the 2-DOF sensor. (a) The loading and unloading characteristics of linear polarizer voltage when the force component of the sensor was being calibrated with a vertical force. (b) The output of the linear polarizer as a function of the angle of twist during the torque calibration procedure.

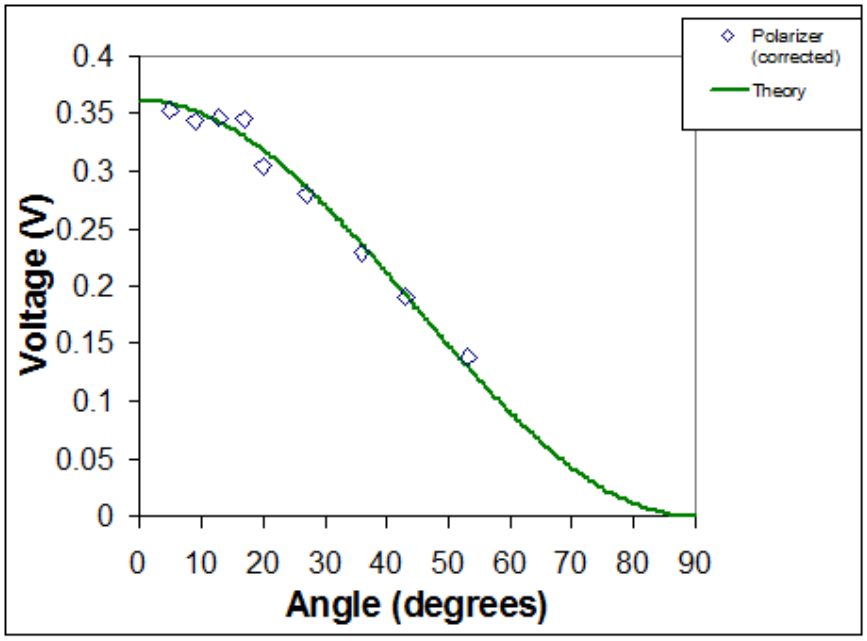

Figure 4-7. The graph of the corrected output of the polarizer voltage.

Assuming that no slippage occurs and the contact point itself does not deform then the applied force produces both normal, F_B and tangential forces, F_A on the surface of the sensor. The torque produced by the off-centred force is balanced by the torque from the twisting nitinol strip and the angle of twist, θ can be measured by the linear polarizer. Parameter, f is the frictional force from the contact surface. The component of the applied force, F that causes linear displacement, δx is given by

$$F_v = F\cos^2\theta \tag{4-3}$$

the tangential force is given by

$$F_A = F\sin\theta \tag{4-4}$$

and the maximum angle before slipping occurs is given by

$$\theta_s = \tan^{-1}(\mu) \tag{4-5}$$

where F is the applied force, θ is the angle of twist, μ is the coefficient of friction, θ_s is the maximum angle before slipping occurs, F_A is the tangential force and F_v is the linear force measured by the sensor. Figure 4-9 (green triangles) shows the corrected force curve when the twisting angle is taken into account in the force calculations. Note that for small angular displacements both graphs are identical but as the applied force moves away from the centre the corrected curve reaches a limiting angle at which slipping occurs. Therefore if the grasped object's contact point is near then sensor's centre then the correction is not required.

Figure 4-10 shows the calibration of the torque sensor. The actual torque values are shown as blue diamonds while the theoretical torque is shown as the solid green line. Note that there is some dissimilarity between these two curves which is mainly due to construction inaccuracies. The effect of the construction inaccuracies can be investigated by considering equation (3-18). Taking the partial derivative of equation (3-18) with respect to both θ_t and L gives

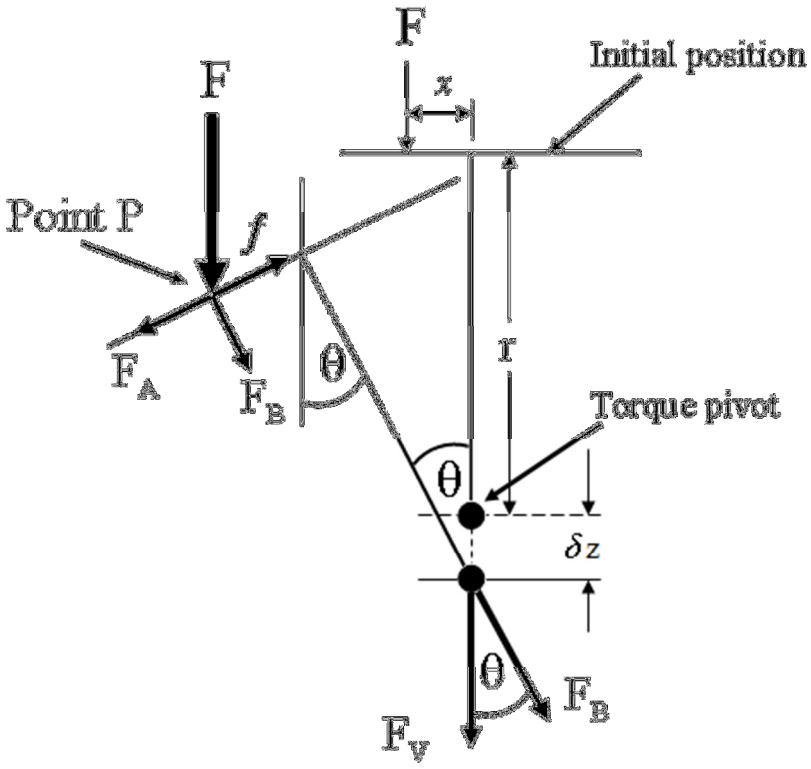

Figure 4-8. Illustration of the sensor experiencing a combination of both torque and linear force.

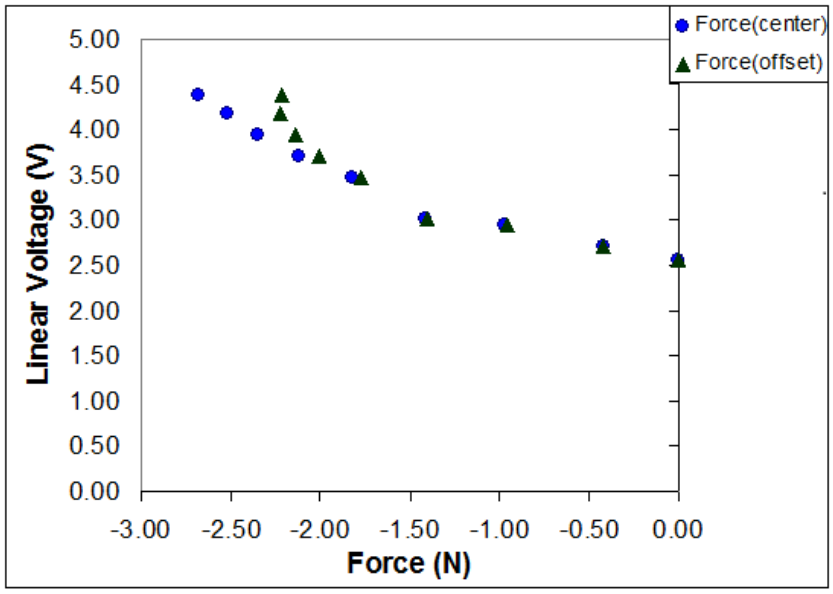

Figure 4-9. The comparison of the sensor experiencing a purely linear force and a combination of linear and torque forces.

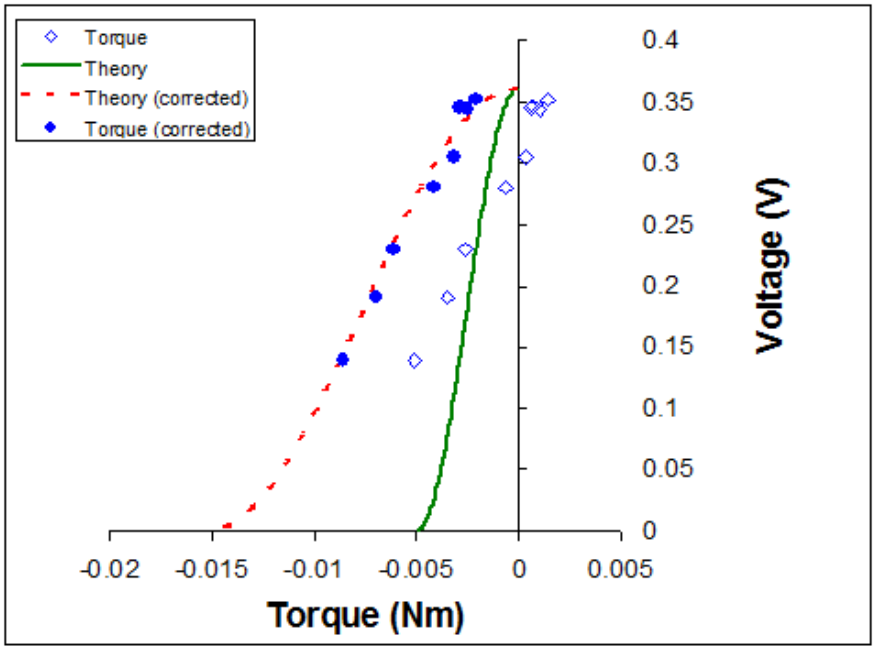

Figure 4-10. The graph of the calibration curve for the torque sensor with corrected values.

$$\frac{dT}{d\theta_r} = \frac{\partial T}{\partial \theta_r} + \frac{\partial T}{\partial L}\frac{dL}{d\theta_r} \quad \textbf{(4-6)}$$

and

$$\frac{dT}{dL} = \frac{\partial T}{\partial L} + \frac{\partial T}{\partial \theta_r}\frac{d\theta_r}{dL} \quad \textbf{(4-7)}$$

respectively. Parameters ***G*** and ***J*** are constants while the twisting length, ***L*** and angle, $\boldsymbol{\theta}$ are independent of each other so $\frac{dL}{d\theta_r}$ and $\frac{d\theta_r}{dL}$ are both zero hence

$$\frac{dT}{d\theta_r} = \frac{JG}{L} \quad \textbf{(4-8)}$$

and

$$\frac{dT}{dL} = -\frac{JG\theta_r}{L^2}. \quad \textbf{(4-9)}$$

Equation (4-6) shows that the sensitivity of torque with respect to θ is linear while equation (4-7) shows that the sensitivity of torque with respect to L is nonlinear and inversely proportional to the square of the twistable length. This indicates that the torque is more sensitive to the length of the twisting material than the angle so this parameter should be investigate first as the main cause of any torque inaccuracies. Careful inspection of the sensor indicated that the epoxy used to bond the sensor's components had reduced the twistable length from 2 mm to 1 mm. This had the effect of increasing the torque required to twist the sensor by an angle, θ. Figure 4-8 shows the final corrected torque curves (red dashed line and blue dots) were the measured values were offset by 3.5 mNm to correct for the reduction in twistable length.

4.3 Sensor Grasping Experiments

The main aim of the experiments conducted in this section was to investigate the response of the 2-DOF sensor to a number of objects that a robot might interact with and utilize in a human environment. If the robot can identify certain affordances of an object by touch alone then it can optimize grasping forces to minimize power consumption, execution time or some other performance metric. Three general purpose objects were chosen for these experiments: a power adapter (a flat, rigid object), a partially-filled plastic bottle (a deformable object) and a paper punch (rigid and curved object). Each object was grasped by a dexterous manipulator embedded with first the 2-DOF sensor and then the Nano17. The dexterous manipulator used throughout these experiments was the Barrett Hand by Barrett Technology Inc which is a three-fingered, 4-DOF dexterous manipulator. Two features of the Barrett Hand which must be taken into account when using the manipulator are that the S1 and S2 sections of the fingers are fixed at 45 ° to each other and there is only one motor per finger. These two features limit the dexterity of the manipulator and can introduce unwanted movements when grasping objects. Figure 4-11 shows the Barrett Hand grasping a block in its palm. If the fingers are incrementally closed then the block experiences a shear force instead of a purely vertical force. This behaviour should be observed and corrected in the grasping experiments.

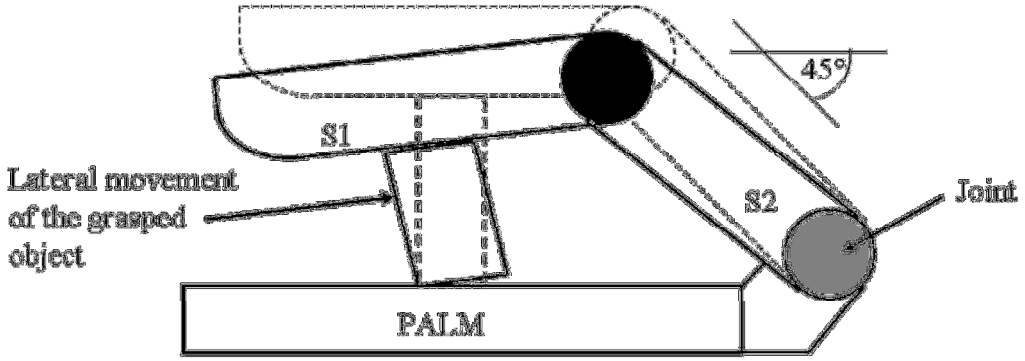

Figure 4-11. Illustration of one of the fingers of the Barrett Hand. Fingers S1 and S2 are fixed at 45 ° to each other resulting in lateral movement of any gripped object when performing a grasping operation.

4.3.1 Hard, Rigid Object Experiment

The first experiment conducted was to grasp a flat rectangular power adapter and apply forces to one side to investigate the response of the sensor to a hard, flat surface. The sensor was integrated into the F1 finger of the Barrett Hand and the adapter was held rigidly in the palm of the Barrett Hand by the F2 and F3 fingers (see Figure 4-12 and Figure 4-13). The results from the grasping experiment are shown in Figure 4-14. Each graph is divided into two sections: Section A which is the initial loading phase and Section B which is the steady-contact phase. The initial loading phase corresponds to the period where contact is made between the object and the fingertip but full/stable grasping force has not yet been reached. The steady-contact phase corresponds to the period where a stable grasp has been achieved so that the object is rigidly held by the Barrett Hand. The point of stable grasp is indicated by the vertical line at 600 seconds in Figure 4-14. The time before 300 seconds also shows the sensor output when the grasp was tested for stability. Notice that in Section B the contact response has a small gradient. This is caused by the Barrett Hand producing the shear force as highlighted in Section 4.3 and Figure 4-11. Also note in this section that there is a decline in the force and torque responses due to a limitation of the Barrett Hand that disables the drive mechanism if too much force is applied when grasping an object.

Figure 4-14b represents the change in the angle of the contact plate when grasping the power adapter. Equation 3-20 gives the intensity of emitted light after passing through two consecutive linear polarisers. The intensity of the light can be converted into a voltage by equation 3-24 to give

$$V(\theta) = V_0 \cos^2(\theta) \quad \text{(V)} \qquad \textbf{(4-10)}$$

where V_0 is the maximum voltage across the sensing resistor, $V(\theta)$ is the output voltage corresponding to the angle of rotation of the rotating polariser and θ is the angle of rotation of the rotating polariser. Recall from Section 3.4 that the torque sensor uses two parallel linear polarisers, one fixed and the other rotatable.

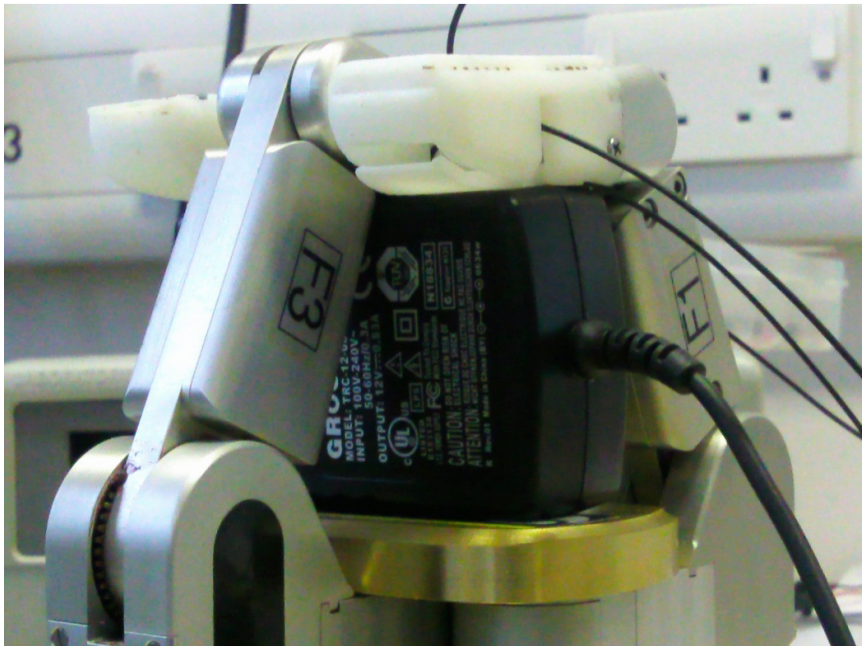

Figure 4-12. Photo of the Barrett Hand with integrated 2-DOF sensor grasping a power adapter.

The rotatable polariser is fixed to the contact plate so as it rotates the polarization angle relative to the fixed polariser changes which therefore modulates the light intensity and output voltage (see Figure 4-13). Solving equation 4-10 for θ gives

$$\theta = \cos^{-1}\sqrt{\frac{V(\theta)}{V_0}}\,. \qquad \textbf{(4-11)}$$

Therefore as different sections of the contact plate make contact with the adapter the angle changes until full contact is made at which point the angle stablizes.

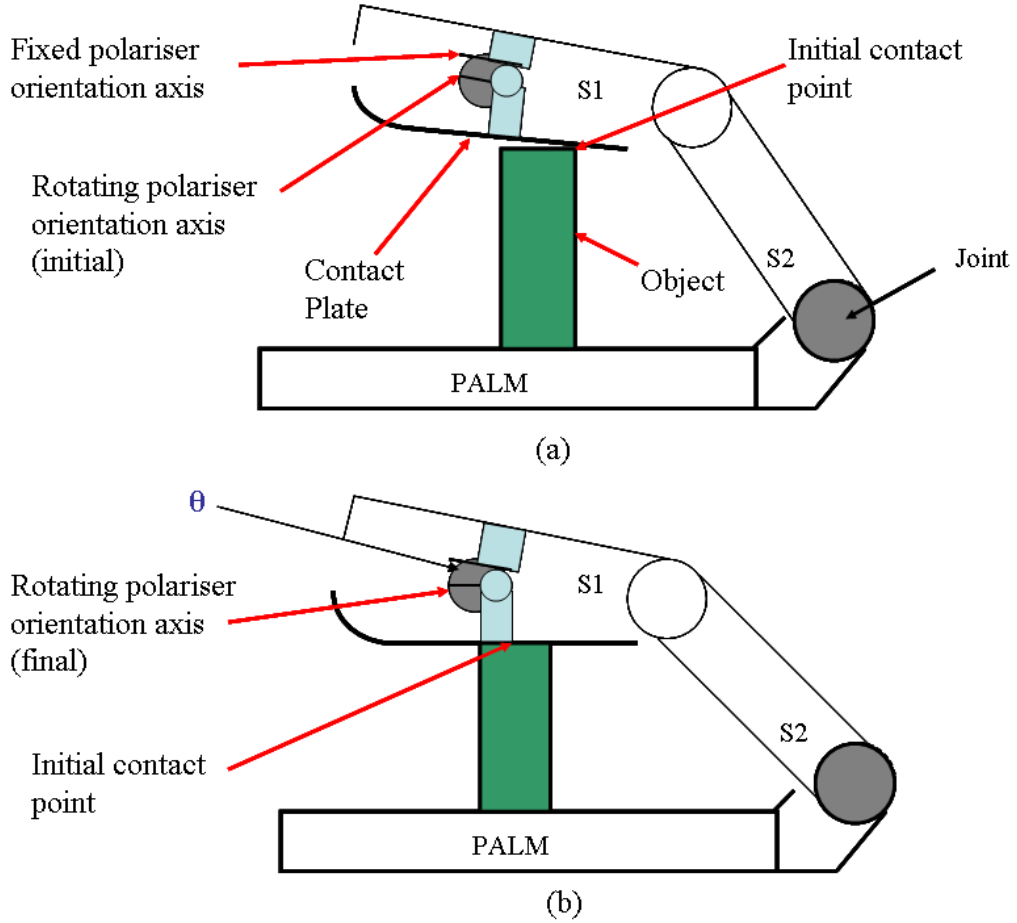

Figure 4-13. An Illustration of the 2-DOF sensor twisting on contact with an object. (a) The pre-contact orientation where the fixed and rotating polarization axes are parallel. (b) Full contact with an object where the contact plate has rotated by an angle of θ.

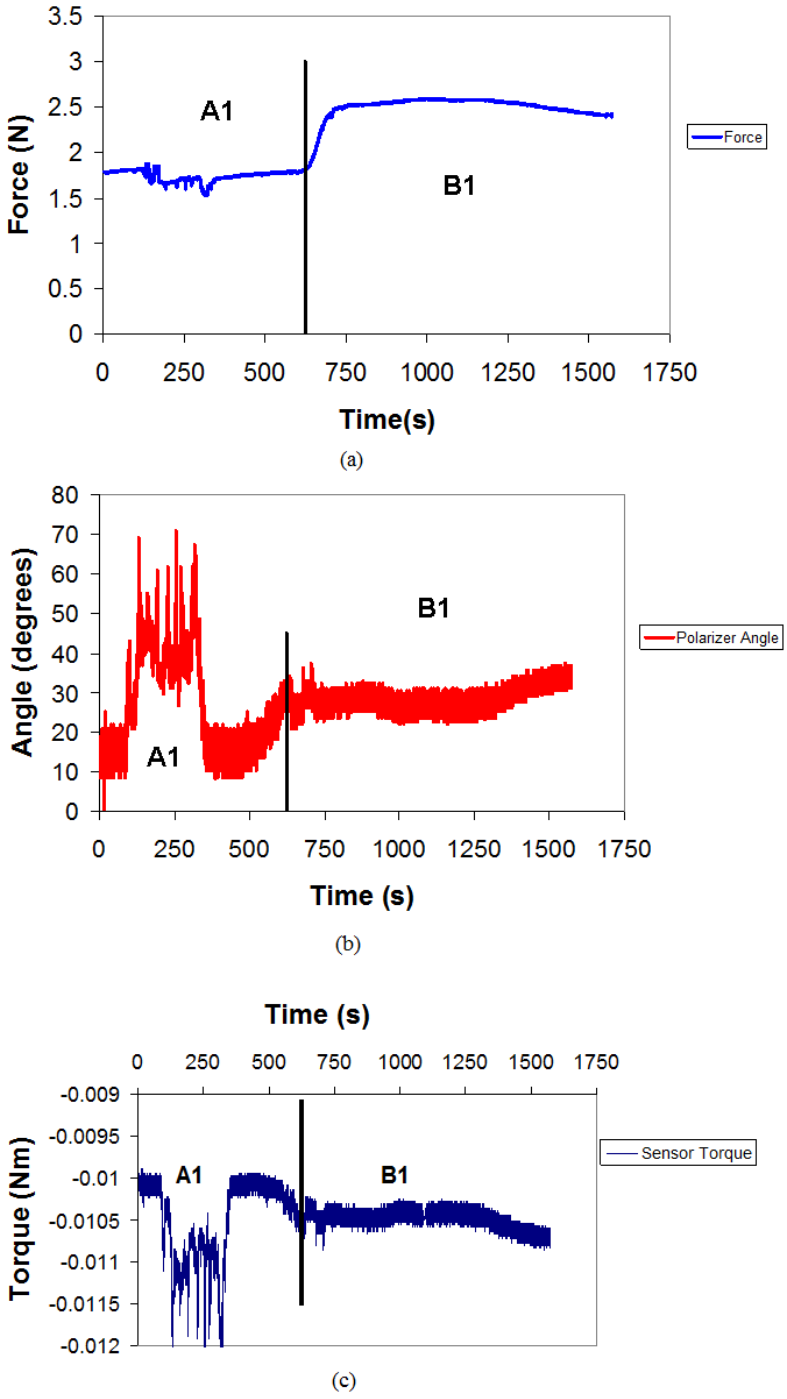

Figure 4-14. Graphs of the response of the 2-DOF sensor to contact with a rigid, flat surface. (a) The response of the force component of the sensor. (b) The change in polarizer orientation as the grasping force is being applied. (c) The torque experienced by the sensor.

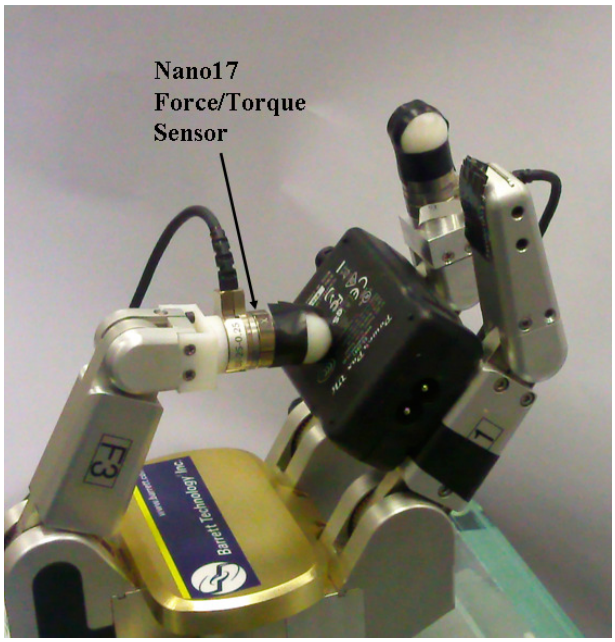

Figure 4-15. Photo the Barrett Hand with integrated Nano17 force/torque sensor grasping a power adapter.

Figure 4-15 shows the grasping experiment repeated using a Nano17 force/torque sensor instead of the 2-DOF sensor. The Nano17 was integrated into the F3 fingertip since this was the only fingertip that could provide effective contact with the power adapter. Another change from the previous experiment was that power adapter was fixed to the F1 and F2 fingers instead of the palm to enable the Nano17 to make contact with the power adapter. Figure 4-16 shows the response of the Nano17 to the power adapter. Section A1 shows the force and torque of the initial contact while B1 shows the response after full contact had been made.

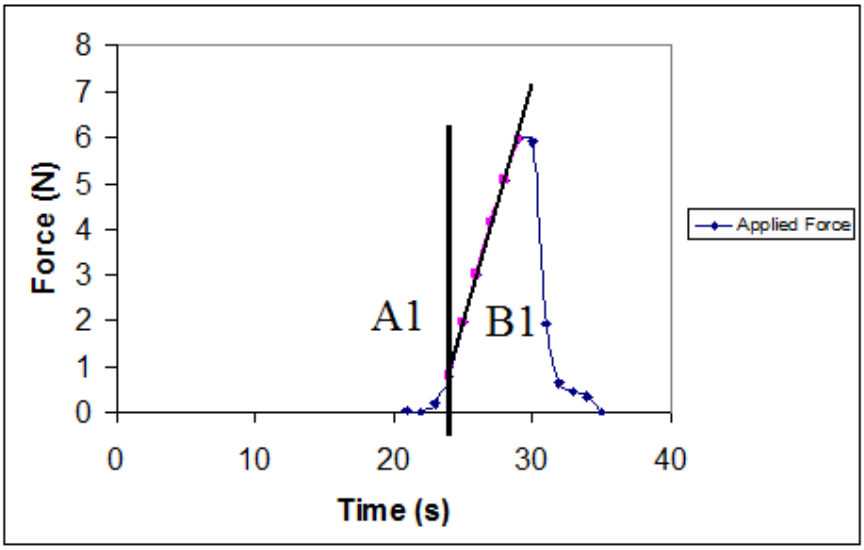

(a)

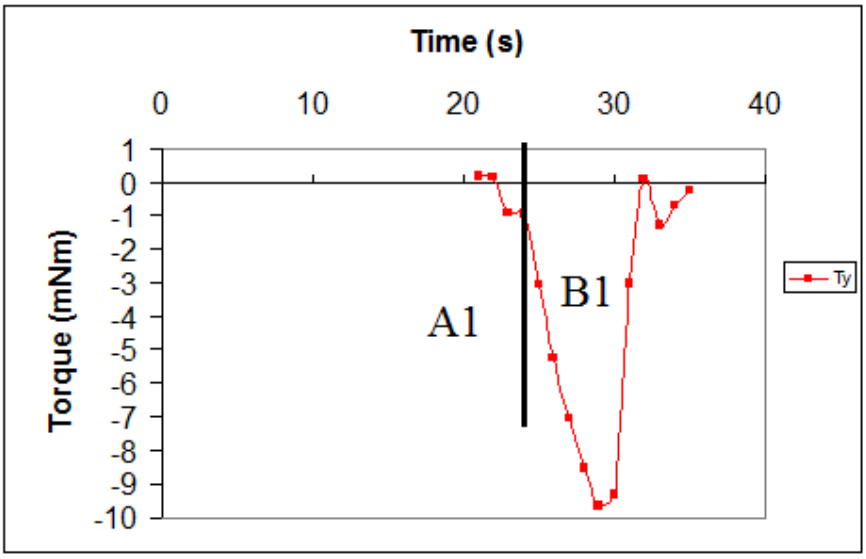

(b)

Figure 4-16. The response of the Nano17 when it was integrated into the Fingertip of the Barrett Hand in place of the 2-DOF sensor. (a) The measured force on the adapter. (b) The measured torque during contact.

4.3.2 Deformable Object Experiment

The next experiment conducted was to grasp a deformable object in order to investigate the response of the 2-DOF sensor to situations where the grasped object may unexpectedly change shape. The deformable object used in this experiment was a partially filled (approximately a third full) bottle of cleaning gel which was firmly held in the palm of the Barrett Hand by the F2 and F3 fingers (see Figure 4-17). The F1 finger then applied increasing grasping forces until the bottle deformed. Figure 4-18 shows the results of these experiments where each graph is divided into two general sections, A and B that define the initial and stable grasps. The incremental increases in grasping force are clearly seen in Section A2 and show how the force changes between incremental increases in force. In this case the force is not constant during incremental increases but decreases slightly between forces increments. Note also that the gradient of the slope is not constant during force increments but decreases to zero as the force approaches the limit for the bottle material. During this phase of the grasp the torque and polarizer angle are constant indicating no change in the surface of the bottle. The force increments continued until the bottle just deformed which was indicated by the change in polarizer angle and torque. Section B2 shows the response of the sensor after the bottle had deformed showing the force decreasing with further closing grasps.

The grasping experiment was also repeated using a Nano17 force/torque sensor to compare the results with the output of the 2-DOF sensor. The Nano17 was attached to the F3 finger since the size of the sensor prohibited it from being installed on the other fingers (see Figure 4-19). Figure 4-20 shows the response of the Nano17 when it is in contact with the partially filled plastic bottle. The curve is initially linear but starts to deviate from the straight line after the bottle begins to deform. Note also that the torque reading remains constant even after the bottle has deformed which is in contrast to the 2-DOF sensor.

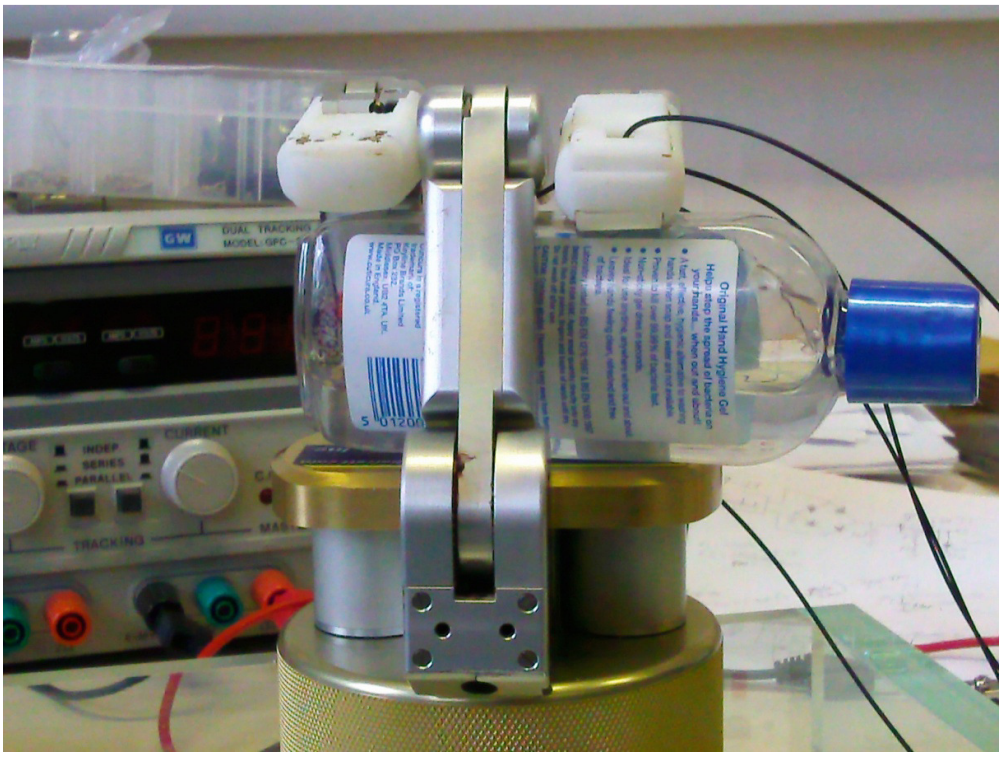

Figure 4-17. Photo of the Barrett Hand grasping a partially filled plastic bottle (deformable object).

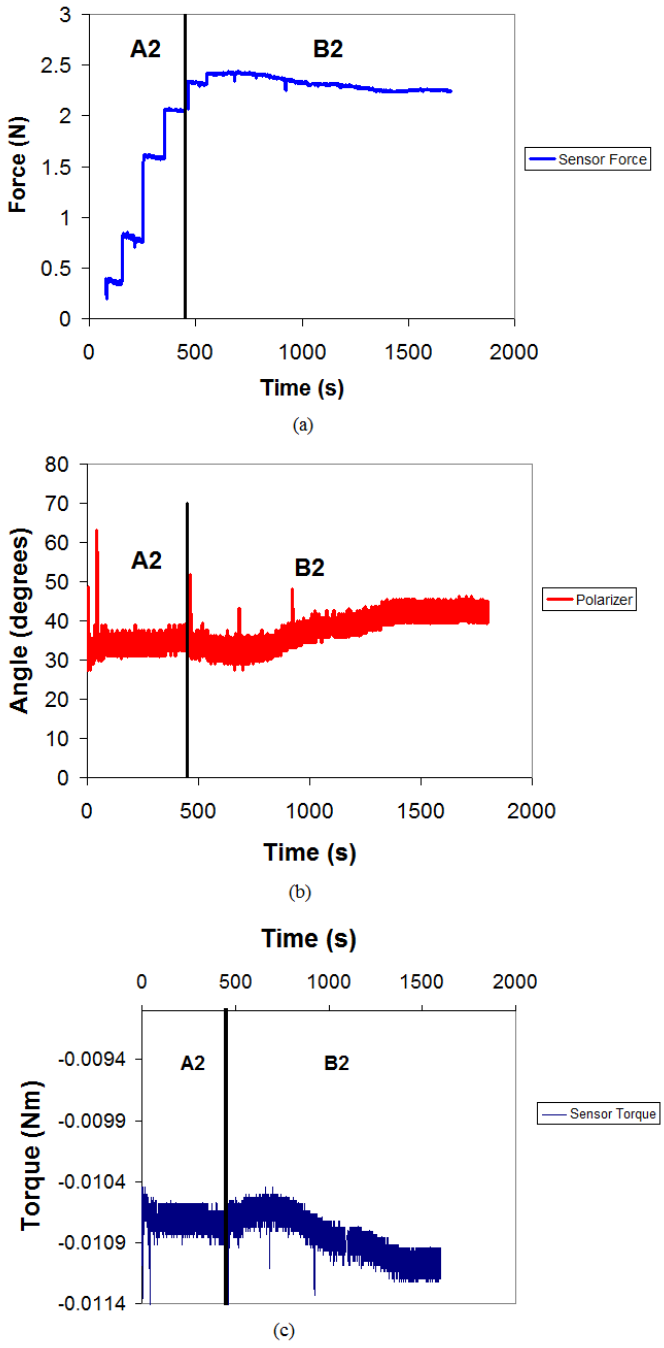

Figure 4-18. Results of the response of the 2-DOF sensor when in contact with a deformable object. (a) Response of the force component of the sensor. (b) The change in orientation of the contact surface during grasping. (c) The variation in torque of during grasping.

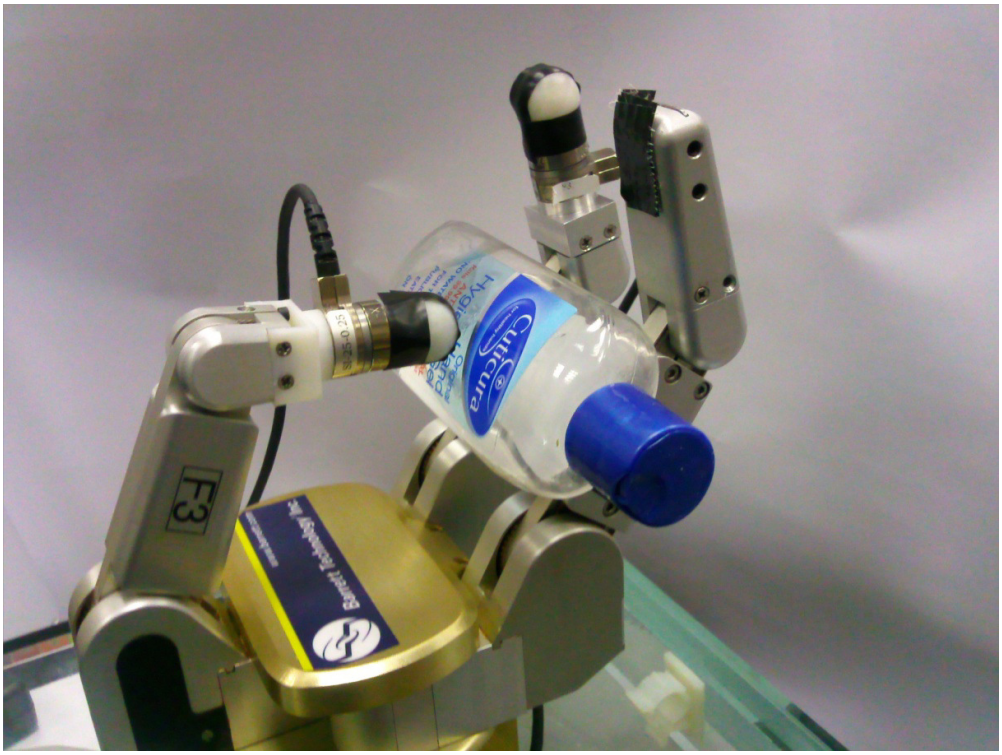

Figure 4-19. Photo of the Barrett Hand and Nano17 force/torque sensor as it applies force to a partially-filled plastic bottle.

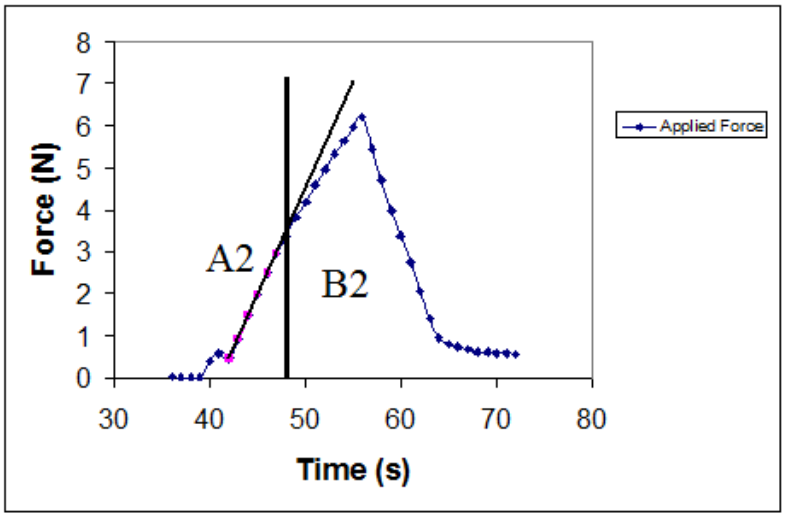

(a)

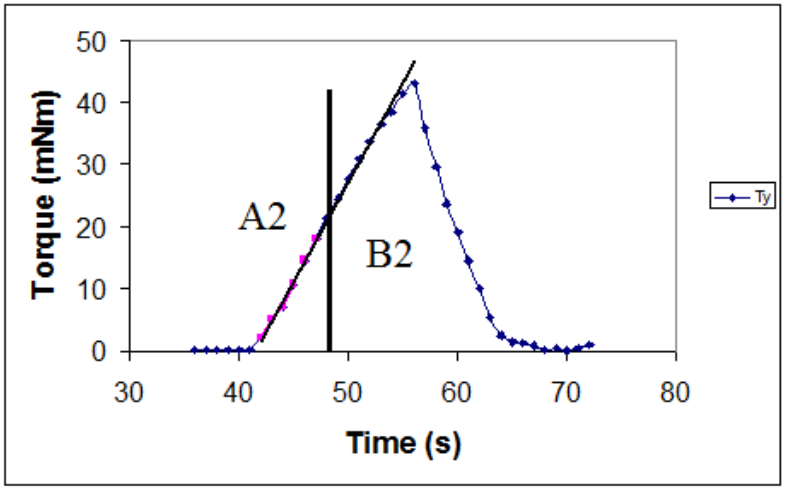

(b)

Figure 4-20. The response of the Nano17 when used to grasp the partially filled plastic bottle (deformable object).

4.3.3 Rigid, Curved Object Experiment

The final experiment conducted was to investigate the response of the 2-DOF sensor to forces not aligned to any of its sensing axes. This experiment used a curved paper punch because it had curves along all axes which made it easier to grasp with the Barrett Hand. The paper punch was held firmly in the palm of the Barrett Hand by the F2 and F3 fingers and grasping forces applied with the F1 finger as shown in Figure 4-21. The results of the grasping experiment are shown in Figure 4-22. The force response decreased with increased grasping in both sections of the graph in Figure 4-22a. This response is unlike the previous experiments where the force reading increased with incremental movements. The reason for change is because the 2-DOF now experienced a torque about the y-axis (M_y) which it was not designed to measure. The result is that the axially-aligned optical fibres are no longer aligned thereby reducing the received light and photodetector voltage (see Figure 3-2 and Section 3.3). Figure 4-22b shows the sensor being twisted outside of its normal working workspace. The torque response however was unaffected by the undesired twisting since the change in curvature of the paper punch is approximately 40°.

The experiment was also repeated using the Nano17 sensor attached to the F3 finger as shown in Figure 4-23 and the results are shown in Figure 4-24. Generally, the results of this experiment are similar to the results from the power adapter even though there is curvature in the shape of the object. More about these results will be discussed in the following section.

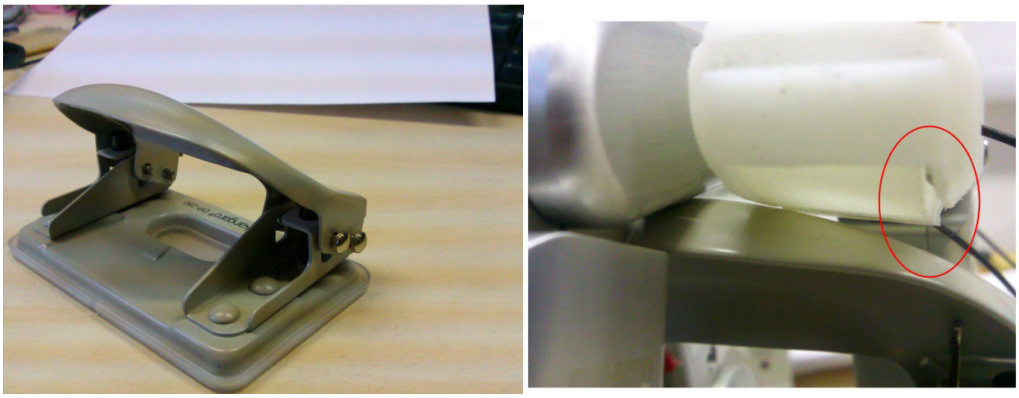

(a) (b)

Figure 4-21. (a) Photo of the rigid and curved paper punch. (b) The 2-DOF sensor fingertip in contact with the paper punch. The deviation of the sensor is highlighted.

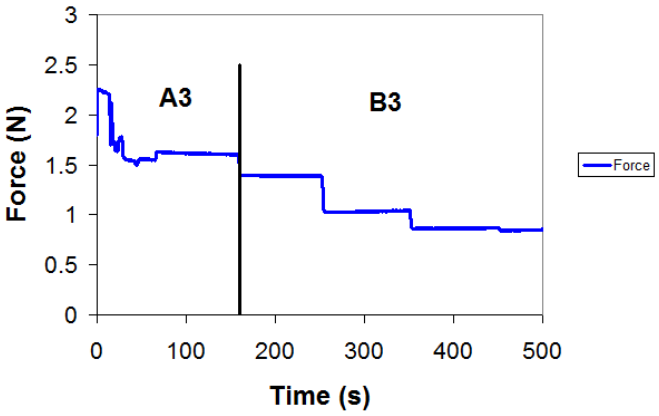

(a)

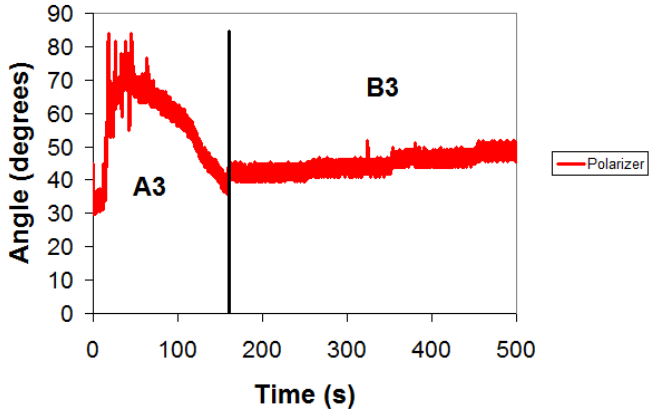

(b)

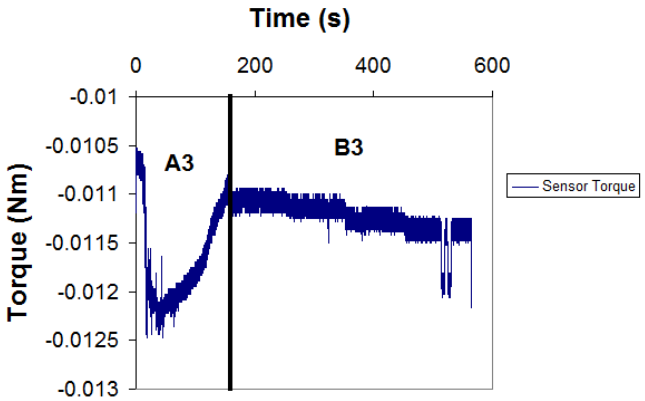

(c)

Figure 4-22. Response of the 2-DOF to contact with a curved, rigid object. (a) The force response of the sensor. (b) The change in orientation during grasping. (c) The change in torque during grasping.

Figure 4-23. Photo of the Nano17 installed on the F3 finger during testing of the paper punch.

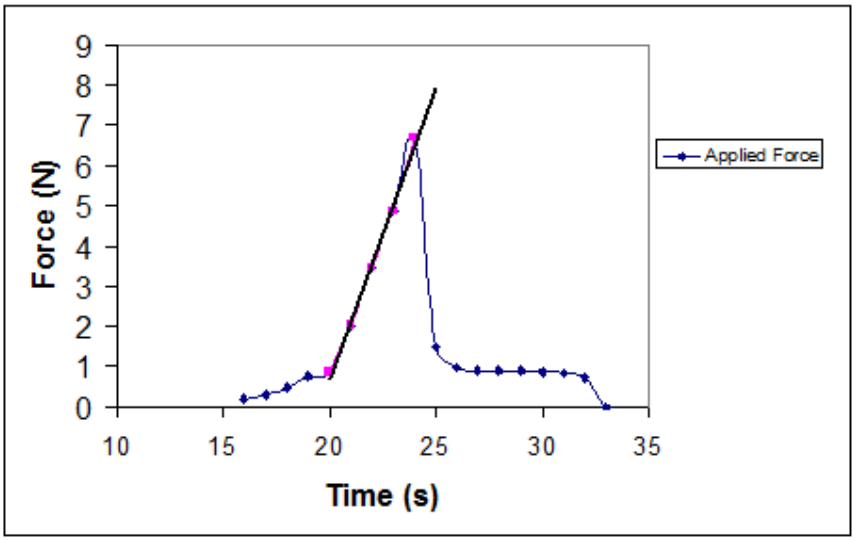

(a)

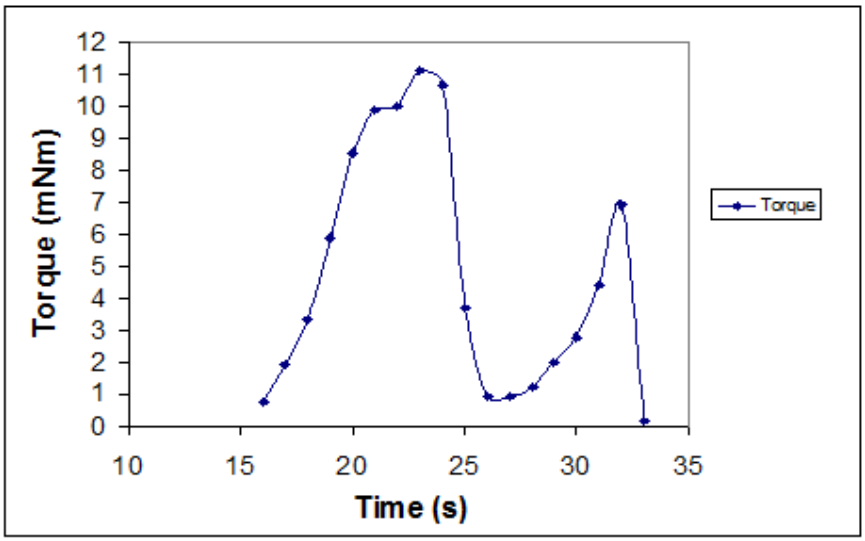

(b)

Figure 4-24. Response of the Nano17 to incremental contact with the curved paper punch. (a) Force response of the Nano17. (b) Torque response of the Nano17.

4.4 Discussion and Conclusion

This section discusses the experimental results presented in Section 4.3 and looks at the performance of the 2-DOF sensor compared to the Nano17 when conducting grasping experiments with the Barrett Hand. Due to the size of the Nano17 both sensors could not be fitted to the Barrett Hand on the same finger and at the same time so the magnitude of the results were different but the general trend was consistent for each sensor. The first experiment conducted was grasping the power adapter which was a hard (non-deformable) and rigid (unmoving) object. For such an object the force and torque should be constant or the rate of increase should be linear with increasing applied force. The purpose of this experiment was to verify that the 2-DOF sensor followed this trend and worked as expected. Figure 4-14 and Figure 4-16 showed the results of the 2-DOF sensor and the Nano17 respectively. The Nano17 response is constant as expected producing a linear response with increasing applied force and torque (section B1). The 2-DOF sensor also produced a linear response curve but reached a peak force of 2.5 N before falling to 2.4 N. This occurred because the Barrett Hand contains a limiting device that disables the drive mechanism if damage may occur. Also note the configurations of the 2-DOF sensor in Figure 4-12 and the Nano17 in Figure 4-15. The Barrett Hand cannot provide more force to the 2-DOF sensor than 2.5 N because of the limitations highlighted in Section 4.3 and Figure 4-11. In contrast the Nano17 attached to the F3 finger has more freedom and hence greater capacity to exert more force on the power adapter. This also explains why the Nano17 experienced a higher than expected torque (Figure 4-14c vs Figure 4-16b) since the closing force from the Barrett Hand causes the Nano17 to slip upward along the flat side of the power adapter. The 2-DOF sensor would not have contacted the power adapter if it was placed on the F3 finger.

Unlike the Nano17 the 2-DOF has a flexible structure that allows it to twist when subjected to a torque providing not only the applied torque but also the orientation of the surface under contact. The torque results from the 2-DOF sensor indicate that the sensor experiences very little change in torque (approximately 0.2 mNm) which is consistent with a flat surface as expected. The small change in torque also corresponds to a small change in contact angle. This is also consistent with the Barrett Hand because it produced a small shear force when contacting objects in the

palm of its hand as shown in Figure 4-11. The angle detection property of the 2-DOF sensor is therefore a novel and informative property of the sensor since it provides information that can not be easily obtained from rigid devices such as the Nano17.

The next experiment conducted was to grasp a partially-filled plastic bottle and apply incremental forces until it deformed. Unlike the previous experiment with the hard power adapter the deformable plastic bottle presents an interesting grasping object because it is initially a hard object until the structural limit of the material has been reached then it has a lower stiffness if further manipulated. Figure 4-18 and Figure 4-20 present the results for the 2-DOF sensor and the Nano17 respectively. The force on the Nano17 is initially linear up to a time of 48 seconds then it starts to deviate from the linear curve. In contrast the torque experienced by the Nano17 remains linear as more force is applied to the plastic bottle. The Nano17 force and torque results indicate that the point at which the bottle deforms can be determined from the force graph but information about the local deformation is not available. Local deformation information is important because it may indicate damage to the object or features that can be used to improve grasp stability or dexterity. The 2-DOF sensor force results are similar to the Nano17's force results except there was a longer pause between force increments. During each pause there was a slight reduction in measure force resulting in a gradient instead of a flat line as expected for a constant force. The gradient also appeared to approach zero (constant) as the force was incremented. This result can be attributed to the pressure inside of the bottle increasing with increased grasping force.

Another observation in the 2-DOF results is that there is a variation in the polarizer angle and torque just before the material deforms which is not present in the Nano17 results. The maximum change in orientation also corresponded to the maximum change in force. The linear polarizer therefore provides information on the local deformation of the bottle which is unavailable from only force data.

The final experiment involved grasping a hard, curved paper punch to investigate the response of the 2-DOF sensor to torques in the *x*- and *y*-axes simultaneously (see Figure 4-21). The force from the Nano17 is shown in Figure 4-24 and gives similar results to the power adapter experiment. The 2-DOF sensor results however are different from the power adapter, especially for the force value as shown in Figure 4-22. In this case the force values decrease with incremental increases in

grasping force. This occurs because the optical fibres for the force sensor are moving out of axial alignment with each other resulting in less light being coupled to the receiver (see Section 3.3 for further details). This disadvantage is caused by the limited number of degrees of freedom of the sensor thereby limiting the application of the sensor to all objects. The advantage of the misalignment is that the manipulator can easily determine if it had grasped an object in a position that will affect the sensor data or if it is in contact with a 2-dimensional curved object. In contrast to the force data the torque data is unaffected by the misalignment since it continues to provide accurate angle and torque readings. The paper punch has a change in curvature of approximately 40 ° which is consistent with the change in angle for the torque sensor. This indicates that the linear polarizers are unaffected by small deviations perpendicular to the polarization axis of the polarizer.

The results presented for the grasping experiments showed that the 2-DOF sensor performed as designed but can be improved. The main advantages of the sensor were its ability to identify the local deformation of an area due to the operation of the linear polarisers modulating the transmitted light intensity when the contact area changed. The other advantage was that the torque sensor was not affected by small misalignments of sensor. The main disadvantage was that the force sensor did not provide accurate results when subjected to torques about the y-axis of the sensor. Improvements to the sensing structure are therefore necessary to improve the sensor's response to 2-dimensional curved surfaces.

4.5 Chapter Summary

This chapter presented the results of testing and calibrating the 2-DOF sensor and the results of three grasping experiments aimed at testing the response of the 2-DOF sensor to common objects that can be found in a human environment. The first test was a temperature test to determine if temperature fluctuations significantly affected the output of the sensor (Section 4.2.1). The results showed that small temperature fluctuations did not affect the sensor output. The sensor was then calibrated using a Mini40 force/torque sensor and a 6-DOF robotic arm (Section 4.2.2). The calibration tests showed that the sensor had low hysteresis (typically 2%) and the length of the twisting strip had the largest impact on torque sensitivity. The force resolution was 11 mN and a tested range of 0 – 2.66 N. The torque resolution was 0.15 mNm with a range of 15 mNm.

Three experiments were conducted to investigate the response of the sensor to contact with objects. The first experiment conducted was grasping a power adapter to test the sensor's response to a hard, rigid object (Section 4.3.1). The result was that the applied force was linear with little deviation in read torque (see Figure 4-14). The second experiment conducted was to grasp a partially-filled plastic bottle to test the sensor's response to a deformable object (Section 4.3.2). The result was that the sensor detected the local deformation of the object under test by the change in torque which was not detectable by the Nano17 sensor (see Figure 4-18). The final experiment conducted was to grasp a curved paper punch to investigate the sensor's response to a hard, curved object (Section 4.3.3). The result was that the torque sensor detected the correct surface curvature (approximately 40°) however the force sensor had reduced values due to the optical fibres being misaligned resulting in reduced light being coupled between the optical fibres (see Figure 4-22). The 2-DOF sensor thus performed well for objects that are aligned to the sensing axes of the sensor but fails for other axes. Improvements to the sensing structure are therefore needed so that forces applied in all axes can be measured. Improvements to the sensor are discussed in the next chapter.

CHAPTER 5 – Design and Development of a 6-DOF Force and Torque Sensor

5.1 Introduction

Chapter 3 presented the design and development to of a 2-DOF force and torque sensor (F_z and M_x) based on light intensity modulation (LIM). The structure of the sensor is based on a 4-cross design with bonded nitinol flexures to provide a flexible and strong structure (Section 3.2). The sensor used two methods of LIM: the first method used axially-aligned optical fibres which modulated the light intensity by varying the separation distance between the transmitting and receiving fibres (Section 3.3). The second method used linear polarizers which modulated the light by rotating a linear polarizer in the path of linearly polarized light (Section 3.4). Chapter 4 presented three experiments to investigate the response of the developed sensor to grasping forces by a Barrett Hand dexterous manipulator. The first experiment investigated the sensor's response to grasping a hard, flat object which was a power adapter (Section 4.3.1). The second experiment investigated the sensor's response to a deformable object which was a partially-filled (sealed) plastic bottle (Section 4.3.2). The third experiment investigated the sensor's response to a hard, curved object which was a paper punch (Section 4.3.3). The results showed that the 2-DOF sensor performed as expected producing a linear response for the hard objects (first and third experiments) and provided an indication of the point at which deformation occurs in the partially-filled plastic bottle (second experiment). The second experiment also showed that sensor can detect local deformation in the contact position as indicated by the change in the light intensity of the linear polarizer/torque component. The main disadvantage of the 2-DOF sensor was that large force errors occurred if the sensor contacted a 2-dimensional curved object (axial fibre misalignment) but the torque component (linear polariser fibre) was unaffected by the contact.

This chapter presents an improved sensing structure that enables full 6-DOF sensing thereby eliminating the problems of axial fibre misalignment inherent with the previous 2-DOF sensor. The improved sensor uses only linear polarisers thereby simplifying the force and torque calculations since only one type of equation (linear polariser) is used instead of two (aligned fibre and linear polariser) in the 2-DOF sensor. The improved sensor also uses a novel approach to reduce output drift. Figure

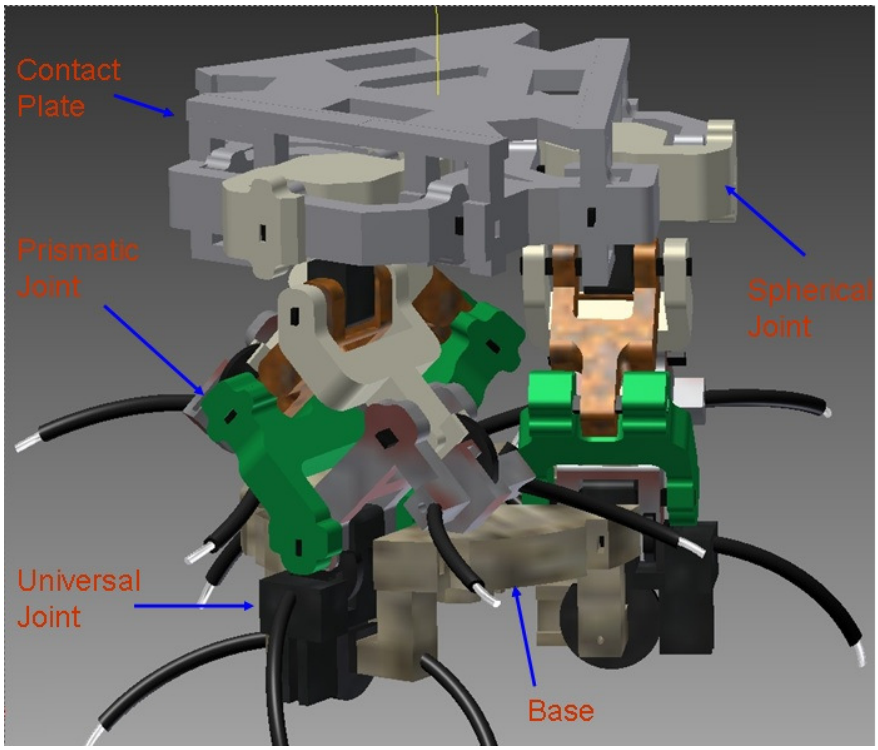

Figure 5-1. Image of the 3-UPS 6-DOF force and torque sensor.

5-1 shows an illustration of the 6-DOF sensor. The remainder of this chapter presents the description and mathematical model of the improved sensor.

5.2 Sensor Overview

The improved sensor is a full 6-DOF sensor that can measure all applied forces and torques (F_x, F_y, F_z, M_x, M_y, M_z). One of the design improvements is that the 6-DOF sensing structure has been replaced with a parallel mechanism. Parallel mechanisms have high stiffness, high positional accuracy and they offer a redundancy in the event of a structural failure. Parallel mechanisms have been used in underwater exploration [162], medical applications [163]-[167] and force/torque sensing [168]-[173]. One of the more common types of parallel mechanisms is the Stewart Platform

which is a 6-UPS mechanism consisting of two parallel plates connected by six prismatic legs, universal joints and spherical joints as shown in Figure 5-2. This mechanism has very good load balancing structures since the applied load is spread among the six legs. Two main problems arise if this mechanism is directly applied as a fingertip sensor for a dexterous manipulator. Firstly, the components must be minimized in order to fit within the fingertip of the manipulator. The problem with this approach is that the components can only be miniaturized to a certain limit before size and cost became an issue. Secondly, the universal and spherical joints need to be adequately lubricated to prevent friction impeding the operation of the joints. If the joints are too small then the joints may not be adequately lubricated. The solution to these problems is to use flexural joints which deform rather than move and they help reduce the size of the mechanism [172], [174].

The developed 6-DOF sensor has a diameter of 16 mm, height of 15.50 mm and mass of 1 gram and uses the flexural joint approach to reduce the size of the fingertip sensor and also increase the sensor's stiffness by bonding the flexures to the sensing structure. The number of prismatic legs has also been reduced from six to three to further reduce the sensor's size without severely compromising the sensor's loading bearing properties. The reduced mass of the sensor is very advantageous because heavy sensors at the fingertip of a dexterous manipulator can affect the dynamic properties of the dexterous manipulator.

The sensor can be modelled as two flat, rigid plates connected by three legs each placed at 120° intervals around the plates [176]-[179]. Each leg is comprised of three main parts:

- A 2-DOF universal joint located in the base of the sensor.
- A 3-DOF spherical joint located in the top plate of the sensor.
- A 1-DOF prismatic joint connecting the universal and spherical joints.

Figure 5-3a illustrates the basic principle of an ideal universal joint which is comprised of two orthogonal arms in the same plane and with bearings to provide smooth rotation. This configuration gives the joint two degrees of rotational freedom (one about the x-axis and one about the y-axis). The 6-DOF sensor uses a modified

universal joint (see Figure 5-3b) where the arms remain orthogonal to each other but are not in the same plane since one arm is raised 0.65 mm above the other. This modification was necessary because the small size of the components prevented both arms from being embedded securely into the structure with the result that one arm would break away from the joint when subjected to load. Figure 5-3c shows the modified universal joint undergoing twisting.

An ideal spherical joint is shown in Figure 5-4a which is comprised of a ball-and-socket which provides three rotational degrees of freedom. Unfortunately, problems arise when miniaturizing a ball-and-socket joint since all surfaces must remain smooth and there is also a problem with effectively lubricating the surfaces to reduce friction. There is also the requirement that the sensor be MR-compatible thereby limiting the types of materials that can be used in the sensor. A modified spherical joint is shown in Figure 5-4b which uses three pairs of revolute flexures to form the spherical joint. The spherical joint is based on the design by Zhang *et al.* [175] but modified so that the joint is flat to reduce its profile.

The final component is the prismatic joint which has a single linear degree of freedom and links the universal and spherical joints (see Figure 5-5a for the ideal case). The ideal prismatic joint was modified into a four-bar mechanism (see Figure 5-5b) where the rigid links are connected by flexural rotational joints thereby limiting the mechanism to only linear movement as required.

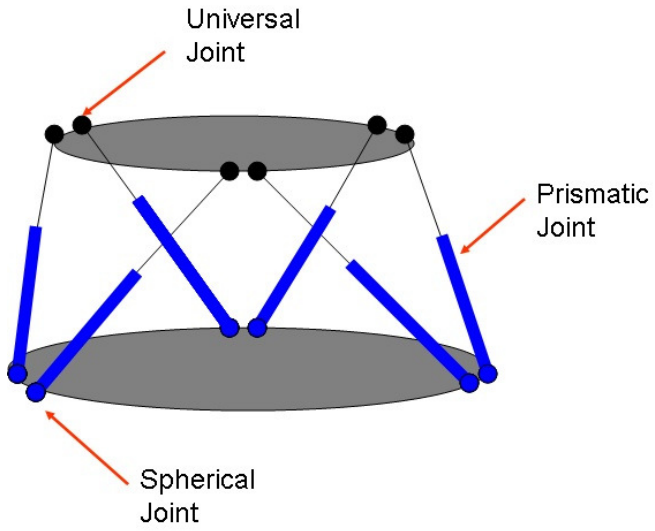

Figure 5-2. Illustration of a Stewart Platform.

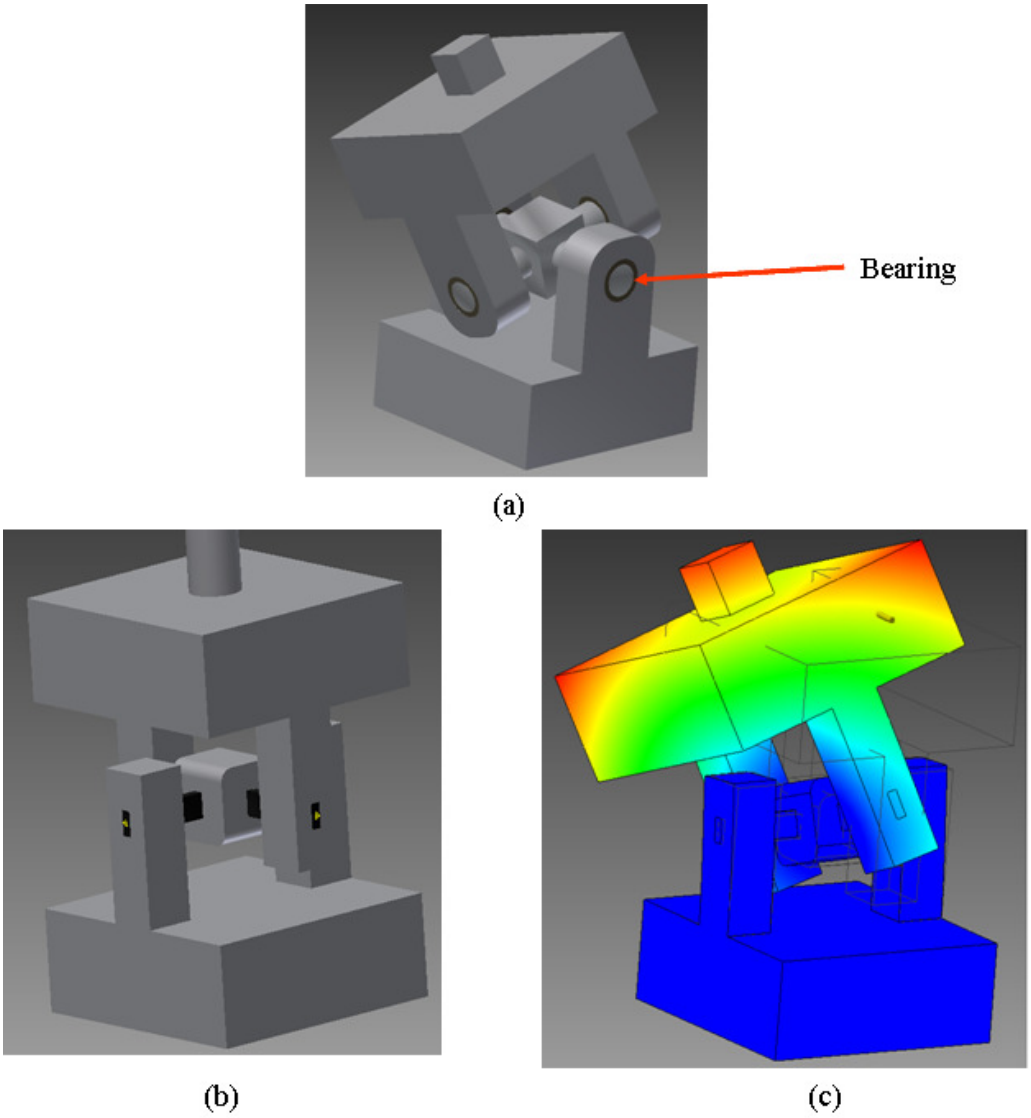

Figure 5-3. Operation of a universal joint. (a) An ideal universal joint uses bearings to provide smooth rotation. (b) The modified universal joint using flexures instead of bearings. (c) The modified universal joint being twisted.

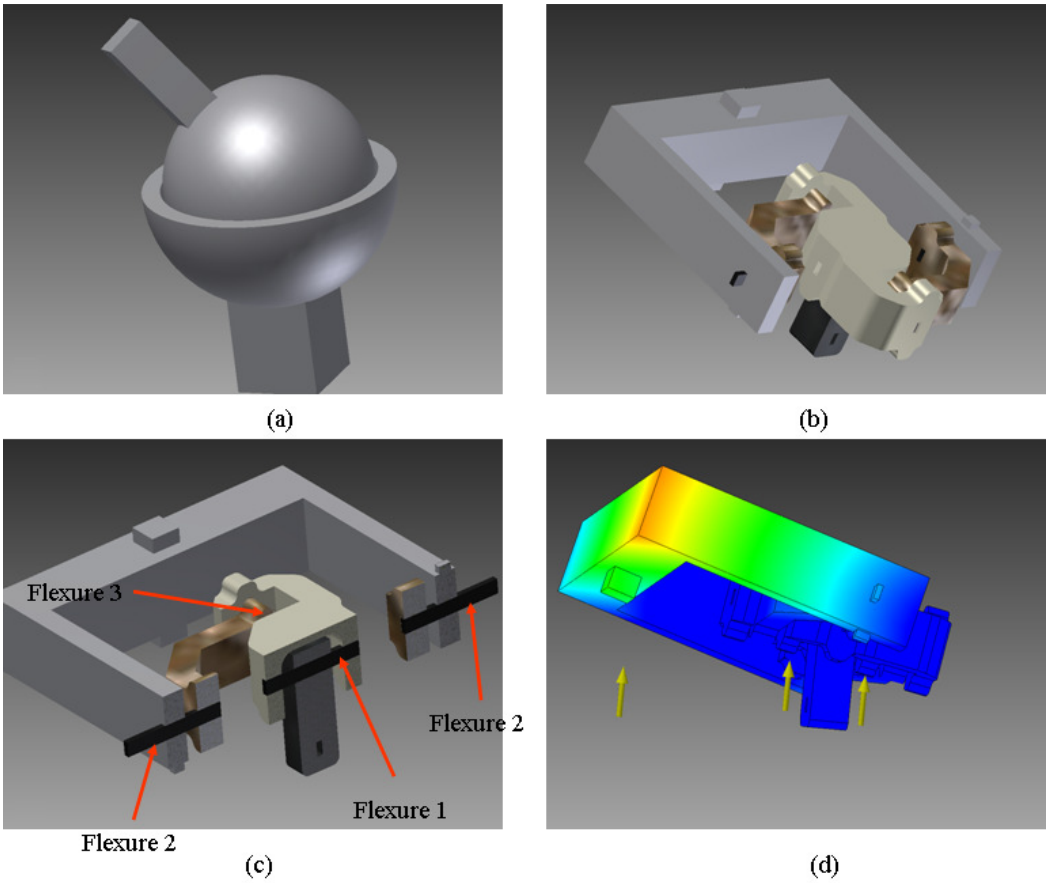

Figure 5-4. Illustrations of spherical joint configurations. (a) An ideal spherical joint comprised of a ball-and-socket combination. (b) The spherical joint used in the 6-DOF sensor comprised of flexural joints instead of bearings. (c) A half-section of the spherical joint showing the interior components. (d) A view of the modified spherical joint in (b) showing the movement of the components.

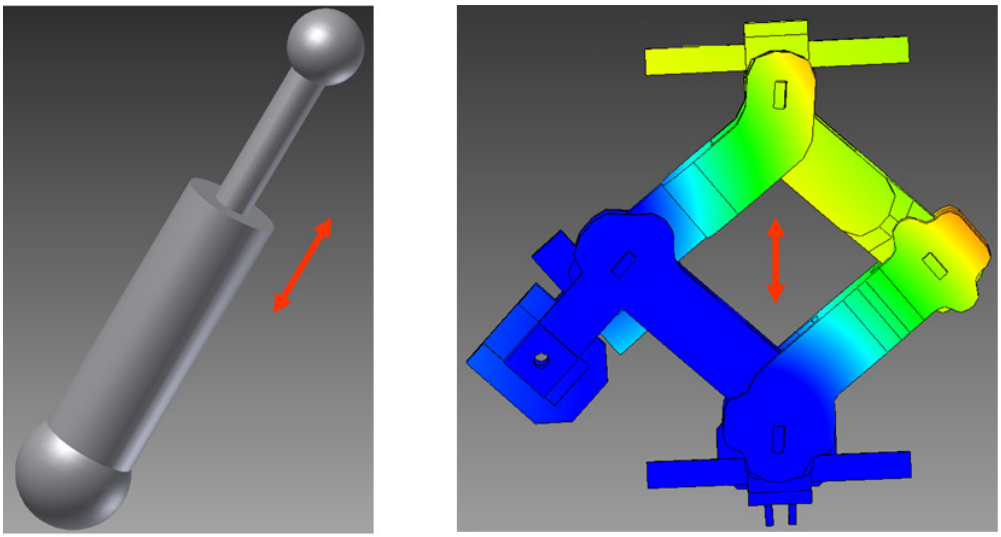

Figure 5-5. A comparison of a typical prismatic joint and the modified prismatic joint. The arrows indicate the direction of travel. (a) A typical prismatic joint consisting of two axially-aligned cylinders moving along a common axis. (b) The modified prismatic joint consisting of four rigid links connected by flexible rotational joints.

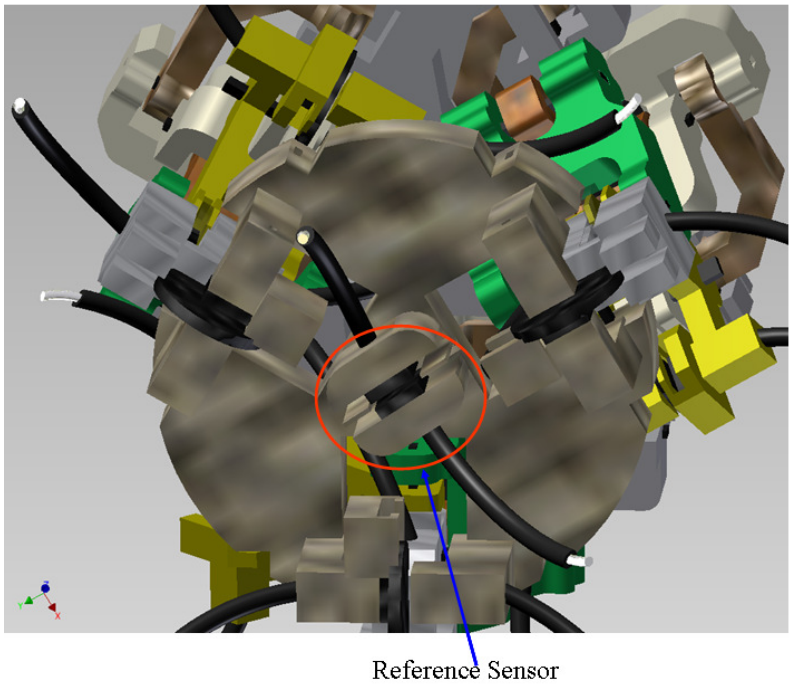

Figure 5-6. An image of the bottom of the sensor showing the location of the reference fibre.

Figure 5-6 shows an image of the reference sensor at the bottom of the sensor which is used to provide a reference signal to properly calibrate the readings from the leg sensors. The sensor consists of a pair of linear polarisers, separated by 0.75 mm and oriented with parallel polarisation axes so that the maximum light is transmitted between the transmitting and receiving fibres. Since all of the transmitting fibres are connected to the same light source any change in light intensity is mirrored in all transmitting fibres.

Forces applied to the contact plate are balanced by restoring forces from the flexural joints. The force on each leg of the sensor depends on the position of the applied force. Linear polarizers are embedded within the revolute joints to provide the angle of twist for the flexures. Three pairs of optical fibre are embedded within each leg of the sensing structure: one pair in the prismatic link and two pairs in the universal joint. There is also an additional pair of fibres embedded within the base plate to provide a reference signal for the sensing data. The next section develops a mathematical model of the sensor based on the deformation of the sensing structure and the LIM of the linear polarizers.

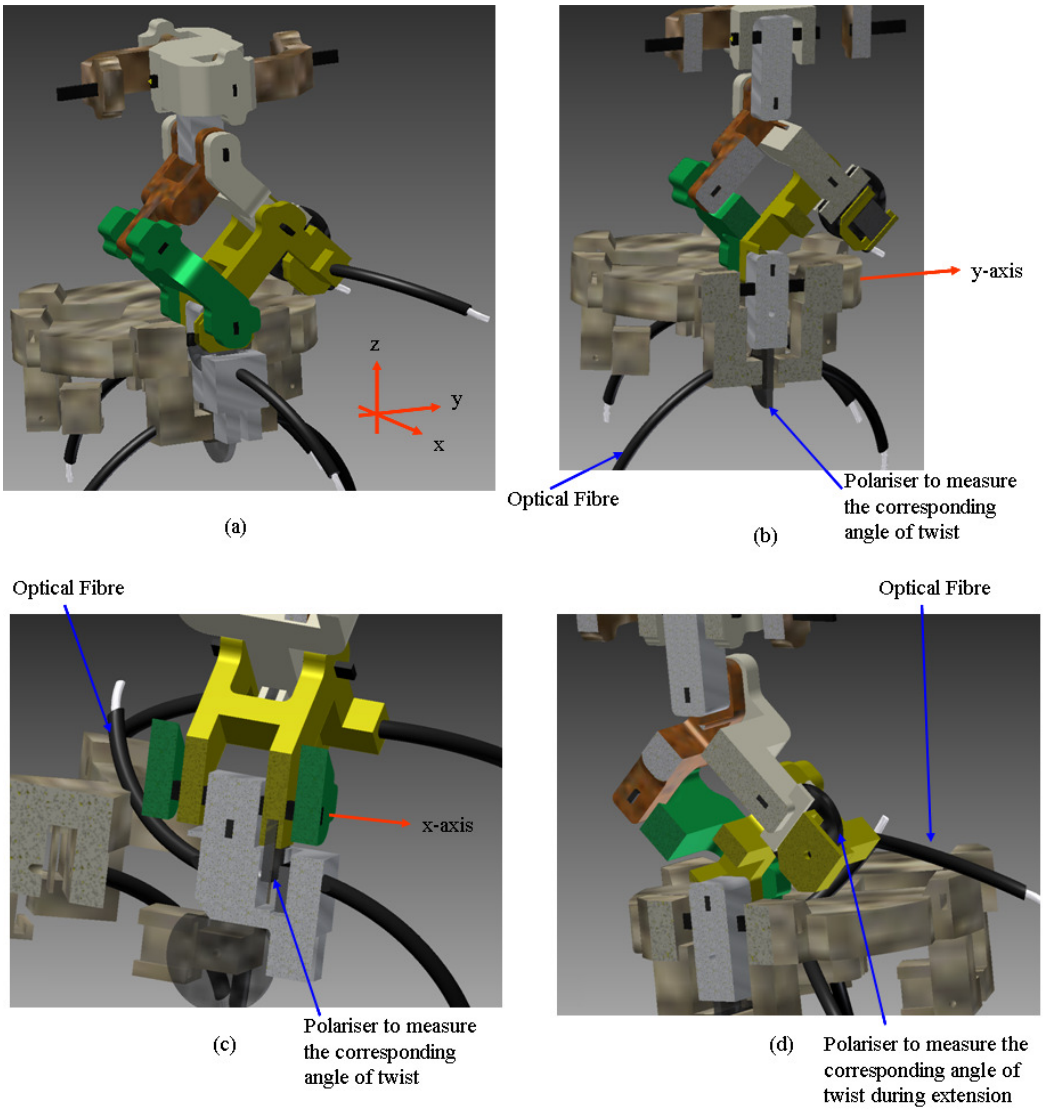

Figure 5-7. Sectional views of one of the leg of the 6-DOF sensor. (a) One leg of the 6-DOF sensor and the local coordinate system. (b) Half-section of one of the legs (y-axis) showing the positions of the optical fibres and linear polarisers.

5.3 Sensor Modelling

The mathematical modelling of the sensor is divided into two sections: the sensor displacement and orientation model and the force and torque model. The first section develops a model for the movement and orientation of the contact plate with applied force. This is because unlike purely rigid force/torque sensors the proposed 6-DOF sensor deforms under applied forces therefore the displacement and orientation of the contact plate changes depending on the applied force vector. The second section develops a model to determine the applied force and torque based on the movement of the contact plate and the angle of the twisting flexures.

5.3.1 Sensor Displacement and Orientation Model

This section develops a model of the movement of the contact plate with applied force. A number of constraints can be applied to the design to ensure correct modelling of the sensor and to simplify the calculations. These constraints are:

1. All universal and spherical joints are spaced at 120 ° intervals around the base and contact plates.
2. All universal joints lie in the same plane.
3. All spherical joints lie in the same plane.

Figure 5-8 shows a simplified model of the 6-DOF sensor that can considered for the purpose of this analysis as two flats, rigid surfaces connected by extensible legs. Consider a single leg as shown in Figure 5-9 where the contact plate (top) is translated horizontally while the base plate is fixed. Let R_C and R_B be the radius of the contact and base plates respectively. The displacement of the point Q_i can be expressed as

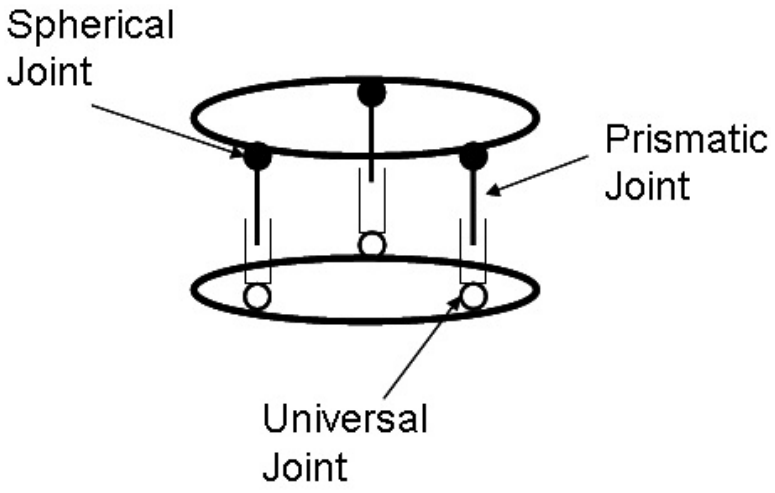

Figure 5-8. A simplfied model of the 6-DOF sensor based on a 3-UPS design.

$$\vec{q} = \vec{p} + [T]\vec{a} \tag{5-1}$$

or

$$\vec{q} = \vec{b} + \vec{s} \tag{5-2}$$

where ***q*** is the displacement of the leg of the sensor, ***p*** is the distance between the centres of the contact and base plates, ***b*** is the position of the universal joint on the base plate, ***s*** is the displacement of the leg, ***a*** is the position of the spherical joint on the contact plate and *[T]* is the transformation matrix to convert the coordinates on the contact plate to coordinates on the base plate. Equating (5-1) and (5-2) and solving for ***p*** gives,

$$p = \vec{b} + \vec{s} - [T]\vec{a} \,. \tag{5-3}$$

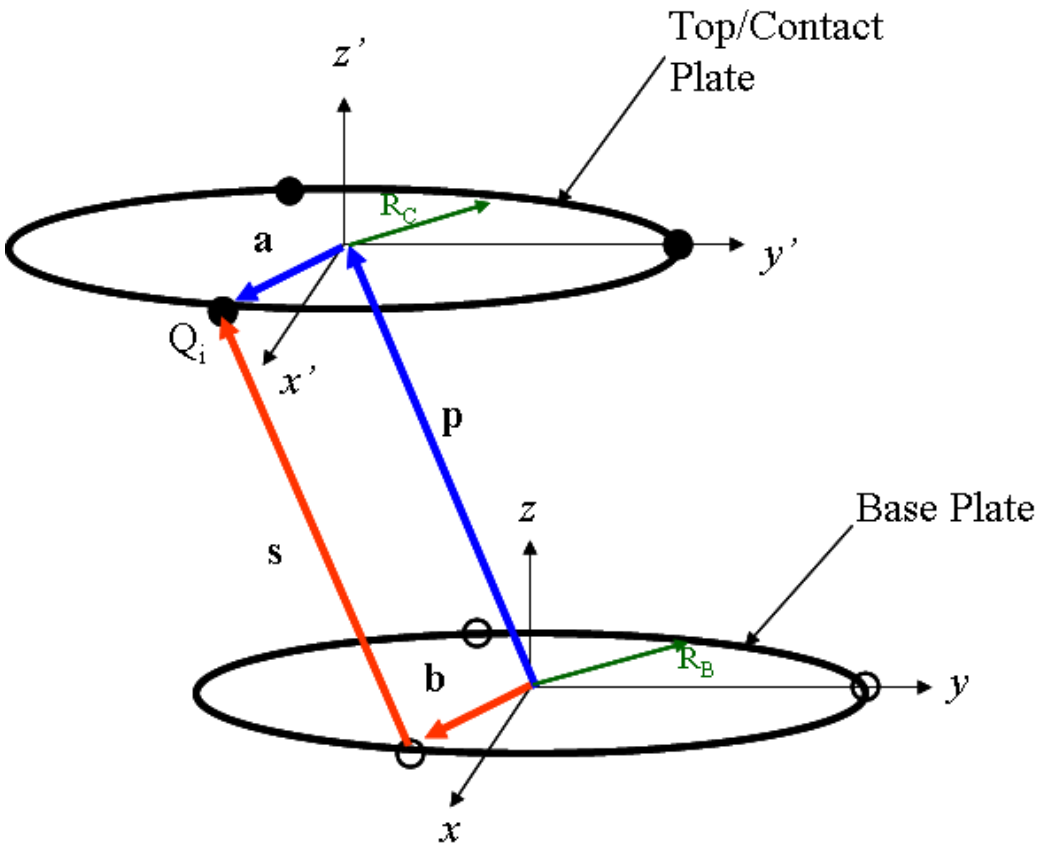

Figure 5-9. Modelling of one of the legs of the 3-UPS sensor.

Parameters ***b*** and ***a*** are at constants positions on the base and contact plates respectively and ***s*** is the displacement vector of the prismatic link. Figure 5-10 shows a simplified model of the prismatic link comprised of four equal arms of length, L. The magnitude of the distance between joints A and B can be calculated from the Cosine Rule to give

$$s = 2L_p\sqrt{1-\cos^2\gamma} \qquad \textbf{(5-4)}$$

where γ is the angle between the arms of the link of the leg of the structure, L_p is the length of each arm and s is the magnitude of the extension of the prismatic link. The locations of the universal and spherical joints on each plane are fixed and equidistant from each other.

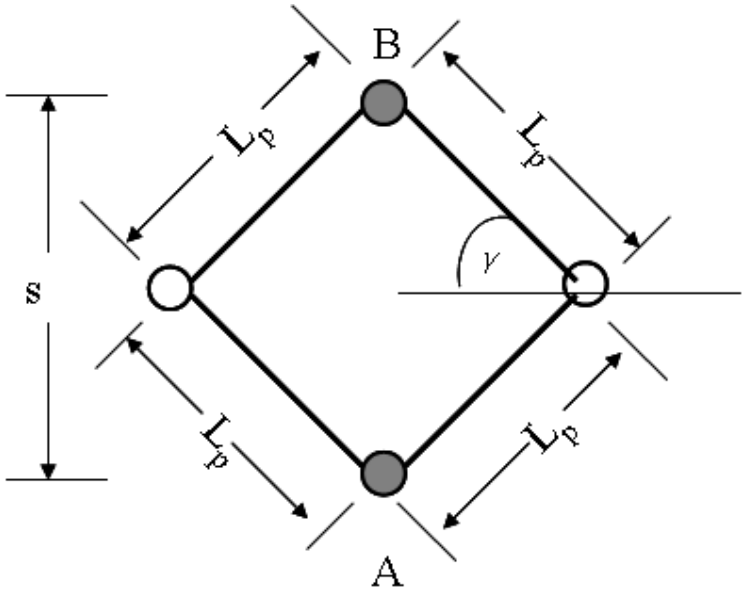

Figure 5-10. A simplified model of the prismatic link for the 3-UPS structure.

Figure 5-11 shows an illustration of the coordinate systems used in the sensor. The global coordinate system (X, Y, Z) is oriented to pass through one of the universal joints in the base plane to simplify the calculations. For the local coordinate system (x, y, z) the x-axis is defined as the axis parallel to the vector from the centre of the base plate and passing through the centre position of the base universal joint. The other axes are defined by the right-hand rule as shown in Figure 5-11 where the axes are superimposed on the universal joint. The positions of the base coordinate frames are

$$\vec{B}_1 = R_B\hat{i} \quad \text{(m)} \tag{5-5}$$

$$\vec{B}_2 = \frac{R_B}{2}\left(-\hat{i} + \sqrt{3}\hat{j}\right) \quad \text{(m)} \tag{5-6}$$

$$\vec{B}_3 = -\frac{R_B}{2}\left(\hat{i} + \sqrt{3}\hat{j}\right) \quad \text{(m)} \tag{5-7}$$

For the sensor only the universal joints and prismatic links contain polarisers to measure the angle of rotation. Figure 5-12 shows a representation of one of the legs

of the sensor. The default configuration of the sensor is that all of the legs are initially vertical. The position of the spherical joint in the universal joint frame can be expressed by resolving the position in the y-z plane (See Figure 5-13). Let $\vec{Q}$ be the position vector in the universal joint plane then

$$\vec{Q} = \begin{pmatrix} 0 \\ s\cos\beta \\ s\sin\beta \end{pmatrix} \text{ (m)} \qquad \textbf{(5-8)}$$

Let $\vec{E}$ be the position vector of the spherical joint in local reference frame (x', y', z'). $\vec{E}$ can be expressed as a rotation about the y-axis then

$$\vec{E} = R(y,\alpha)\cdot\vec{Q} \qquad \textbf{(5-9)}$$

where ***R*** is the rotation matrix for each axis and ***Q*** is the initial position of the spherical joint in the universal joint reference frame (x", y", z"). This gives

$$\Rightarrow \quad \vec{E} = \begin{pmatrix} \cos\alpha & 0 & \sin\alpha \\ 0 & 1 & 0 \\ -\sin\alpha & 0 & \cos\alpha \end{pmatrix} \begin{pmatrix} 0 \\ s\cos\beta \\ s\sin\beta \end{pmatrix}$$

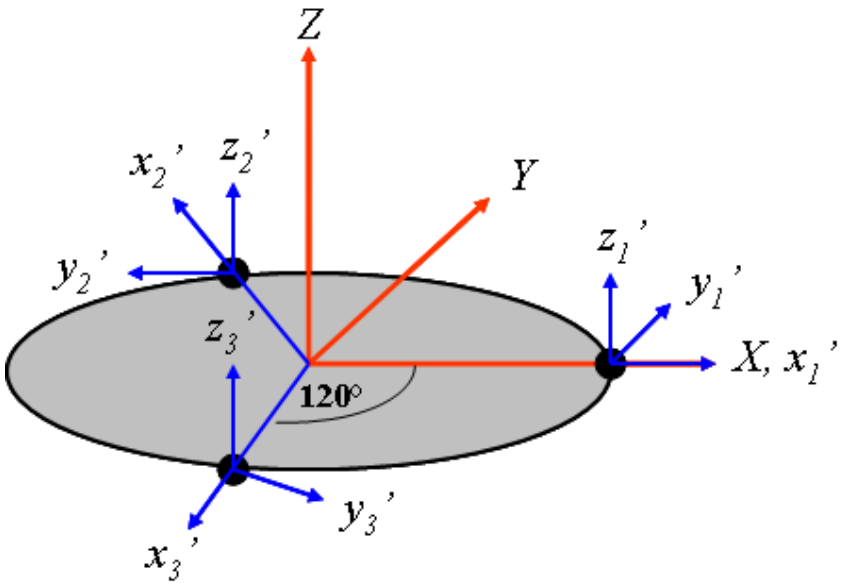

Figure 5-11. An illustration of the global (X, Y, Z) and local (x, y, z) coordinate systems.

$$\Rightarrow \qquad \vec{E} = \begin{pmatrix} s\sin\alpha\sin\beta \\ s\cos\beta \\ s\cos\alpha\sin\beta \end{pmatrix} \text{ (m)} \qquad \textbf{(5-10)}$$

Substituting 5-4 into 5-10 gives

$$E = \begin{pmatrix} 2L_p\sin\gamma\sin\alpha\sin\beta \\ 2L_p\sin\gamma\cos\beta \\ 2L_p\sin\gamma\cos\alpha\sin\beta \end{pmatrix} \text{ (m)} \qquad \textbf{(5-11)}$$

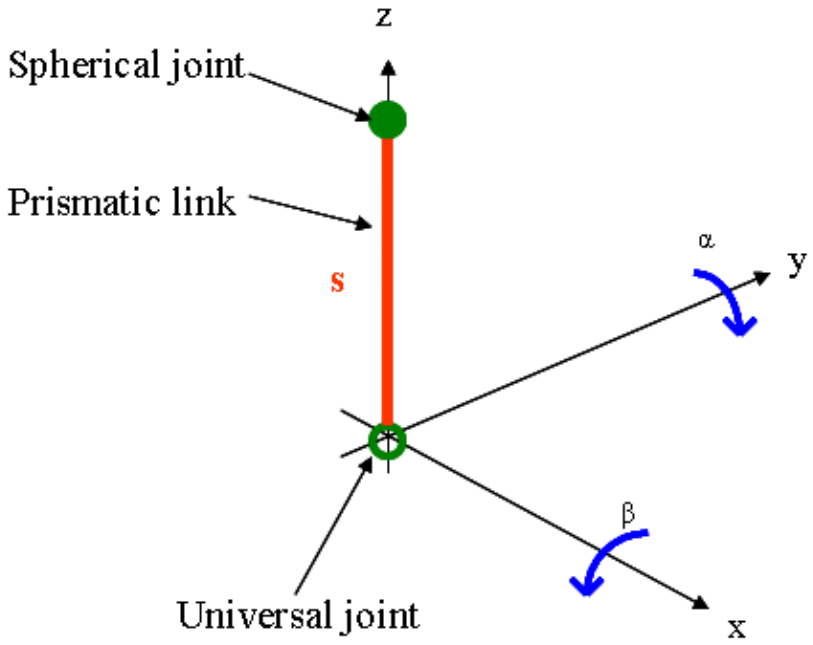

Figure 5-12. Illustration of a single leg and universal joint. α represents the rotation about the y-axis and β represents the rotation about the x-axis.

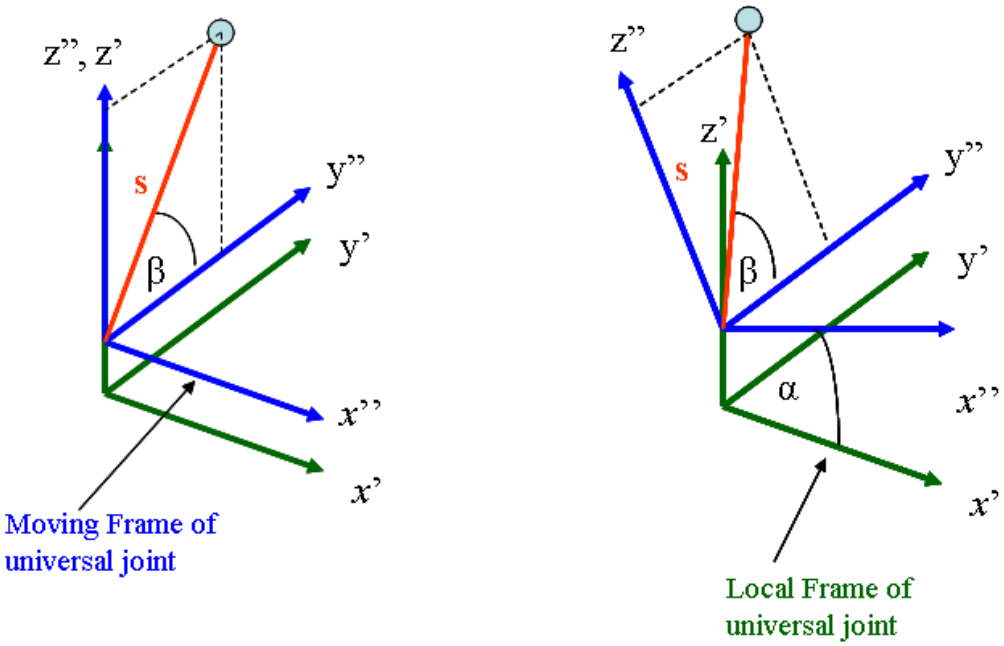

Figure 5-13. Coordinate transformation of the universal joint into the local coordinate system. The prismatic link, ***s*** is first resolved into components (***β***) in the universal joint frame (x'', y'', z'') and the coordinate system rotated by angle, ***α***.

Equation 5-11 represents the position of each spherical joint in the local base frame (x', y', z') of each leg. The next task is to convert the local coordinates into global base frame coordinates (X, Y, Z). Each local frame in Figure 5-11 is located at a fixed distance from the centre of the base plate and at 120° intervals around the base. Note that the z-axis is common for both local and global reference frames. The local reference frames can therefore be converted into the global reference frame by translating and rotating (about the common z-axis) the local frames into the global frame. The rotation matrix about the z-axis, R(z, ψ) is given by

$$R(z,\psi) = \begin{pmatrix} \cos\psi & -\sin\psi & 0 \\ \sin\psi & \cos\psi & 0 \\ 0 & 0 & 1 \end{pmatrix} \qquad \textbf{(5-12)}$$

and the translational matrix for each local frame, T(x,y) is given by

$$T(x, y) = \begin{pmatrix} R_B \cos\psi \\ R_B \sin\psi \\ 0 \end{pmatrix} \qquad \textbf{(5-13)}$$

where $\boldsymbol{R_B}$ be the radius of the base circle on which the base universal joints lie and $\boldsymbol{\psi}$ is the angular position of each universal joint. Expressing the rotation and translation matrices as affine transformation matrices (4×4) the resulting transformation matrix, A is given by

$$A = T(x, y)R(z,\psi) \qquad \textbf{(5-14)}$$

$$\Rightarrow \quad A = \begin{pmatrix} 1 & 0 & 0 & R_B\cos\psi \\ 0 & 1 & 0 & R_B\sin\psi \\ 0 & 0 & 1 & 0 \\ 0 & 0 & 0 & 1 \end{pmatrix} \begin{pmatrix} \cos\psi & -\sin\psi & 0 & 0 \\ \sin\psi & \cos\psi & 0 & 0 \\ 0 & 0 & 1 & 0 \\ 0 & 0 & 0 & 1 \end{pmatrix}$$

$$\Rightarrow \qquad A = \begin{pmatrix} \cos\psi & -\sin\psi & 0 & R_B\cos\psi \\ \sin\psi & \cos\psi & 0 & R_B\sin\psi \\ 0 & 0 & 1 & 0 \\ 0 & 0 & 0 & 1 \end{pmatrix} \qquad \textbf{(5-15)}$$

The position vector of the spherical joint in the base frame, $\vec{P}$ is then given by

$$\vec{P} = \vec{A}\vec{E}$$

$$\Rightarrow \qquad \vec{P} = \begin{pmatrix} \cos\psi & -\sin\psi & 0 & R_B\cos\psi \\ \sin\psi & \cos\psi & 0 & R_B\sin\psi \\ 0 & 0 & 1 & 0 \\ 0 & 0 & 0 & 1 \end{pmatrix} \begin{pmatrix} 2L_p\sin\gamma\sin\alpha \\ -2L_p\sin\gamma\cos\alpha\sin\beta \\ 2L_p\sin\gamma\cos\alpha\cos\beta \\ 1 \end{pmatrix}$$

$$\Rightarrow \qquad \vec{P} = \begin{pmatrix} 2L_p\sin\gamma(\sin\alpha\sin\beta\cos\psi - \cos\beta\sin\psi) + R_B\cos\psi \\ 2L_p\sin\gamma(\sin\alpha\sin\beta\sin\psi + \cos\beta\cos\psi) + R_B\sin\psi \\ 2L_p\sin\gamma\cos\alpha\sin\beta \\ 1 \end{pmatrix} \qquad \textbf{(5-16)}$$

Let ***m*** represent the sensor's leg of interest then the position, $\vec{P}$ of the *m*th leg is given by

$$\vec{P}_m = \begin{pmatrix} 2L_p\sin\gamma_m(\sin\alpha_m\sin\beta_m\cos\psi_m - \cos\beta_m\sin\psi_m) + R_B\cos\psi_m \\ 2L_p\sin\gamma_m(\sin\alpha_m\sin\beta_m\sin\psi_m + \cos\beta_m\cos\psi_m) + R_B\sin\psi_m \\ 2L_p\sin\gamma_m\cos\alpha_m\sin\beta_m \\ 1 \end{pmatrix} \qquad \textbf{(5-17)}$$

where only the x, y and z components are considered.

The position of each spherical joint can be verified by considering the diagram in Figure 5-14. Since all of the spherical joints lie in the same plane, without loss of generality, the vertical height can be taken as constant (in the plane) and the distance between the spherical joints is given by the cosine rule

$$c^2 = {R_B}^2 + {R_B}^2 - 2{R_B}^2 \cos\psi$$

$$\Rightarrow \quad c^2 = 2{R_B}^2(1-\cos\psi)$$

But the angular separation between any pair of spherical joints in the contact plane, ψ = 120º for the sensor,

$$\Rightarrow \quad c^2 = 2{R_B}^2\left(1-\left(-\frac{1}{2}\right)\right)$$

$$\Rightarrow \quad c = \sqrt{3}R_B \qquad \textbf{(5-18)}$$

or

$$c = \sqrt{(P_{3x}-P_{2x})^2 + (P_{3y}-P_{2y})^2 + (P_{3z}-P_{2z})^2}$$

as shown in Figure 5-14.

Unlike the universal joints and prismatic links the spherical joints do not contain linear polarisers to measure the angle of rotation. However, the contact plate can be viewed as a plane and the spherical joints as points embedded in the plane. Given the position of the three points on the plane both the normal vector and equation of the plane can be calculated from the cross product of any two vectors in the plane. The normal vector to the plane is given by

$$\vec{n} = \left(\vec{P}_2 - \vec{P}_1\right)\times\left(\vec{P}_3 - \vec{P}_1\right) \qquad \textbf{(5-19)}$$

where $\vec{P}_1$, $\vec{P}_2$ and $\vec{P}_3$ are the points of the spherical joints in the base frame. The corresponding values of ψ for each leg m=1, 2, 3 are given in Table 5.1. Expanding 5-17 and substituting the values of ψ for each leg m gives

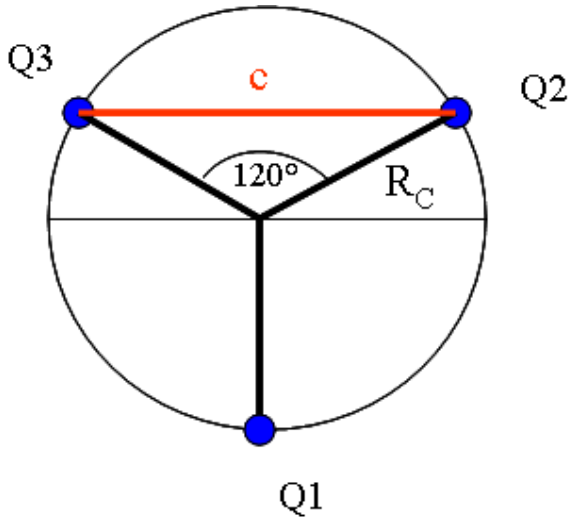

Figure 5-14. The spherical joints are positioned at 120° intervals around a base circle of radius R_C. The magnitude of the separation distance, c between any pair of spherical joints is therefore constant at $\sqrt{3}R_C$.

Leg #	Angle, ψ (°)
1	0
2	120
3	240

Table 5.1. Table of angular positions, ψ for each leg of the sensor.

$$P_1 = \begin{pmatrix} 2L_p \sin\gamma_1 \sin\beta_1 + R_B \\ 2L_p \sin\gamma_1 \cos\beta_1 \\ 2L_p \sin\gamma_1 \cos\alpha_1 \sin\beta_1 \end{pmatrix} \quad \textbf{(5-20)}$$

$$P_2 = \begin{pmatrix} -L_p \sin\gamma_2\left(\sin\alpha_2 \sin\beta_2 + \sqrt{3}\cos\beta_2\right) - \dfrac{R_B}{2} \\ L_p \sin\gamma_2\left(\sqrt{3}\sin\alpha_2 \sin\beta_2 - \cos\beta_2\right) + \dfrac{\sqrt{3}R_B}{2} \\ 2L_p \sin\gamma_2 \cos\alpha_2 \sin\beta_2 \end{pmatrix} \quad \textbf{(5-21)}$$

and

$$P_3 = \begin{pmatrix} L_p \sin\gamma_3\left(-\sin\alpha_3 \sin\beta_3 + \sqrt{3}\cos\beta_3\right) - \dfrac{R_B}{2} \\ -L_p \sin\gamma_3\left(\sqrt{3}\sin\alpha_3 \sin\beta + \cos\beta_3\right) - \dfrac{\sqrt{3}R_B}{2} \\ 2L_p \sin\gamma_3 \cos\alpha_3 \sin\beta_3 \end{pmatrix} \quad \textbf{(5-22)}$$

Equation 5-19 now becomes

$$\begin{aligned} \vec{n} = &\left[\left(P_{2x} - P_{1x}\right)\hat{i} + \left(P_{2y} - P_{1y}\right)\hat{j} + \left(P_{2z} - P_{1z}\right)\hat{k}\right] \\ &\times\left[\left(P_{3x} - P_{1x}\right)\hat{i} + \left(P_{3y} - P_{1y}\right)\hat{j} + \left(P_{3z} - P_{1z}\right)\hat{k}\right] \end{aligned} \quad \textbf{(5-23)}$$

$$\Rightarrow \qquad \vec{n} = \begin{vmatrix} \hat{i} & \hat{j} & \hat{k} \\ \left(P_{2x} - P_{1x}\right) & \left(P_{2y} - P_{1y}\right) & \left(P_{2z} - P_{1z}\right) \\ \left(P_{3x} - P_{1x}\right) & \left(P_{3y} - P_{1y}\right) & \left(P_{3z} - P_{1z}\right) \end{vmatrix}$$

$$\Rightarrow \qquad \begin{aligned} \vec{n} = &\left[\left(P_{2y} - P_{1y}\right)\left(P_{3z} - P_{1z}\right) - \left(P_{2z} - P_{1z}\right)\left(P_{3y} - P_{1y}\right)\right] \\ &-\left[\left(P_{2x} - P_{1x}\right)\left(P_{3z} - P_{1z}\right) - \left(P_{2z} - P_{1z}\right)\left(P_{3x} - P_{1x}\right)\right]\hat{j} \\ &+\left[\left(P_{2x} - P_{1x}\right)\left(P_{3y} - P_{1y}\right) - \left(P_{2y} - P_{1y}\right)\left(P_{3x} - P_{1x}\right)\right]\hat{k} \end{aligned} . \quad \text{(5-24)}$$

The displacement of the sensor can calculated from the displacement of the centre of the contact plate. Generally, the centre of a circle can be calculated from any 2 vectors in the plane and the normal vector to the plane. Let the points $\vec{P}_1$, $\vec{P}_2$, and $\vec{P}_3$ be the positions of the spherical joints in the base frame. The cross product of any vector in

the plane and the normal vector, $\vec{n}$ produces a bisector vector perpendicular to both vectors and embedded in the plane. Let $\vec{a}$ be the vector from point $\vec{P}_1$ to point $\vec{P}_2$ and $\vec{b}$ be the vector from point $\vec{P}_1$ to point $\vec{P}_3$. This gives

$$\vec{a} = \vec{P}_2 - \vec{P}_1$$

and

$$\vec{b} = \vec{P}_3 - \vec{P}_1$$

The bisector line for vector $\vec{a}$ is given by

$$\vec{L}_1 = \vec{a} \times \vec{n}$$

$$\Rightarrow \quad \vec{L}_1 = \begin{vmatrix} \hat{i} & \hat{j} & \hat{k} \\ a_x & a_y & a_z \\ n_x & n_y & n_z \end{vmatrix}$$

$$\Rightarrow \quad \vec{L}_1 = (a_y n_z - a_z n_y)\hat{i} - (a_x n_z - a_z n_x)\hat{j} + (a_x n_y - a_y n_x)\hat{k} \qquad \textbf{(5-25)}$$

and the bisector line for vector $\vec{b}$ is given by

$$\vec{L}_2 = \vec{b} \times \vec{n}$$

$$\Rightarrow \quad \vec{L}_2 = \begin{vmatrix} \hat{i} & \hat{j} & \hat{k} \\ b_x & b_y & b_z \\ n_x & n_y & n_z \end{vmatrix}$$

$$\Rightarrow \qquad \vec{L}_2 = (b_y n_z - b_z n_y)\hat{i} - (b_x n_z - b_z n_x)\hat{j} + (b_x n_y - b_y n_x)\hat{k} \qquad \textbf{(5-26)}$$

where a_x, a_y, a_z and b_x, b_y, b_z are the x, y and z components of the a and b vectors respectively while n_x, n_y and n_z are the x, y and z components of the normal vector in 5-24. If L_1 and L_2 start at the midpoint of vectors $\vec{a}$ and $\vec{b}$ respectively then the point of intersection of L_1 and L_2 gives the centre position of the contact plate. Let L_{M1} and L_{M2} be the midpoints of vectors $\vec{a}$ and $\vec{b}$ respectively then,

$$\vec{L}_{M1} = \frac{\vec{P}_2 + \vec{P}_1}{2}$$

$$\Rightarrow \qquad \vec{L}_{M1} = \frac{(P_{2x} + P_{1x})}{2}\hat{i} + \frac{(P_{2y} - P_{1y})}{2}\hat{j} + \frac{(P_{2z} - P_{1z}))}{2}\hat{k} \qquad \textbf{(5-27)}$$

and

$$\vec{L}_{M2} = \frac{\vec{P}_3 + \vec{P}_1}{2}$$

$$\Rightarrow \qquad \vec{L}_{M2} = \frac{(P_{3x} + P_{1x})}{2}\hat{i} + \frac{(P_{3y} - P_{1y})}{2}\hat{j} + \frac{(P_{3z} - P_{1z}))}{2}\hat{k} \qquad \textbf{(5-28)}$$

The bisector lines can be written in parametric form to take advantage of the bisector equations. Referring to Figure 5-15b, the position vector of the centre of the contact plane, $\vec{r}_c$ can be written as

$$\vec{r}_c = \vec{L}_{M1} + \vec{L}_1 t \qquad \textbf{(5-29)}$$

or

$$\vec{r}_c = \vec{L}_{M2} + \vec{L}_2 k \qquad \textbf{(5-30)}$$

where $\vec{L}_{M1}$ and $\vec{L}_{M2}$ are given by 5-27 and 5-28 respectively, $\vec{L}_1$ and $\vec{L}_2$ given by 5-25 and 5-26 respectively and ***t*** and ***k*** are coefficients of the vectors. Equating 5-29 and 5-30 and simplifying gives

$$\vec{L}_2 k - \vec{L}_1 t = \vec{L}_{M1} - \vec{L}_{M2} \qquad \textbf{(5-31)}$$

which can be expanded into x, y and z components to give

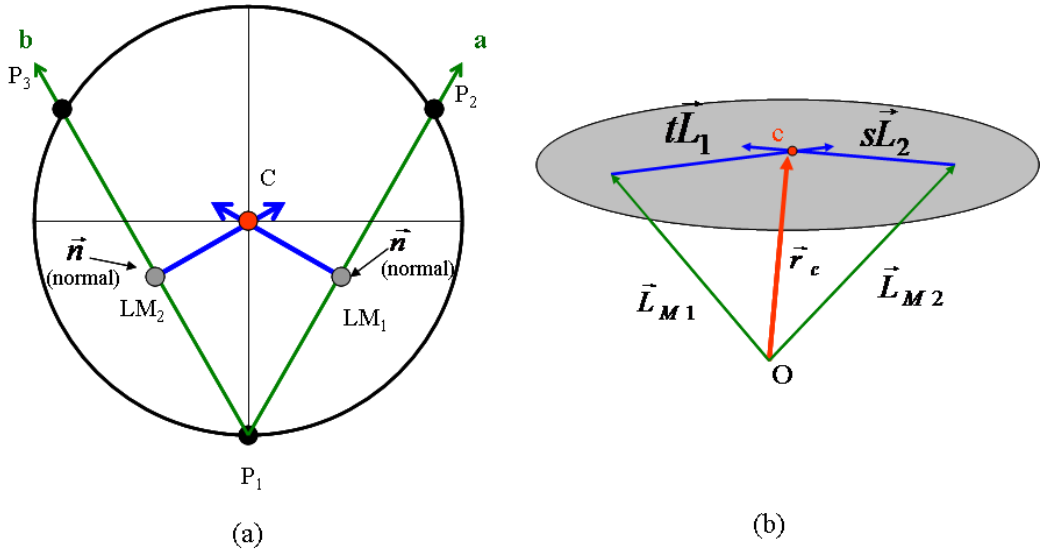

Figure 5-15. The calculation of the centre of a circle from any two vectors in the plane of the circle and the normal to the circle. (a) The intersection of the perpendicular vectors from the midpoint of vectors $\vec{a}$ and $\vec{b}$ gives the centre of the circle. (b) The centre of the circle, $\vec{r}_c$ can also be expressed in parametric form as the sum of vectors $\vec{L}_{M1}$ and $t\vec{L}_1$ or the sum of $\vec{L}_{M2}$ and $k\vec{L}_2$.

$$\vec{L}_{2x}k - \vec{L}_{1x}t = \vec{L}_{M1x} - \vec{L}_{M2x} \qquad \textbf{(5-32)}$$

$$\vec{L}_{2y}k - \vec{L}_{1y}t = \vec{L}_{M1y} - \vec{L}_{M2y} \qquad \textbf{(5-33)}$$

$$\vec{L}_{2z}k - \vec{L}_{1z}t = \vec{L}_{M1z} - \vec{L}_{M2z}\,. \qquad \textbf{(5-34)}$$

Equations 5-32 to 5-34 form a system of equations with only two unknowns hence only two the three equations are needed. Expressing 5-32 and 5-33 in matrix form gives

$$\begin{pmatrix} L_{2x} & -L_{1x} \\ L_{2y} & -L_{1y} \end{pmatrix}\begin{pmatrix} k \\ t \end{pmatrix} = \begin{pmatrix} L_{M1x} - L_{M2x} \\ L_{M1y} - L_{M2y} \end{pmatrix} \qquad \textbf{(5-35)}$$

and solving by Cramer's Rule

$$k = \frac{L_{1x}\left(L_{M1y} - L_{M2y}\right) - L_{1y}\left(L_{M1x} - L_{M2x}\right)}{L_{2y}L_{1x} - L_{1y}L_{2x}} \tag{5-36}$$

and

$$t = \frac{L_{2x}\left(L_{M1y} - L_{M2y}\right) - L_{2y}\left(L_{M1x} - L_{M2x}\right)}{L_{2y}L_{1x} - L_{1y}L_{2x}}. \tag{5-37}$$

Substituting 5-37 into 5-29 and expanding components gives the position of the centre of the contact plate where

$$r_{cx} = L_{M1x} + L_{1x}\left(\frac{L_{2x}\left(L_{M1y} - L_{M2y}\right) - L_{2y}\left(L_{M1x} - L_{M2x}\right)}{L_{2y}L_{1x} - L_{1y}L_{2x}}\right) \tag{5-38}$$

$$r_{cy} = L_{M1y} + L_{1y}\left(\frac{L_{2x}\left(L_{M1y} - L_{M2y}\right) - L_{2y}\left(L_{M1x} - L_{M2x}\right)}{L_{2y}L_{1x} - L_{1y}L_{2x}}\right) \tag{5-39}$$

$$r_{cz} = L_{M1z} + L_{1z}\left(\frac{L_{2x}\left(L_{M1y} - L_{M2y}\right) - L_{2y}\left(L_{M1x} - L_{M2x}\right)}{L_{2y}L_{1x} - L_{1y}L_{2x}}\right) \tag{5-40}$$

Equations 5-38 to 5-40 give the displacement of the centre of the contact plate. The orientation of the contact plate can be calculated from the dihedral angle of the contact plane normal vector and the base frame (see Figure 5-16). Taking the dot product of the normal vectors gives

$$\vec{n}_c \bullet \vec{n}_b = \left|n_c\right|\left|n_b\right|\cos\chi \tag{5-41}$$

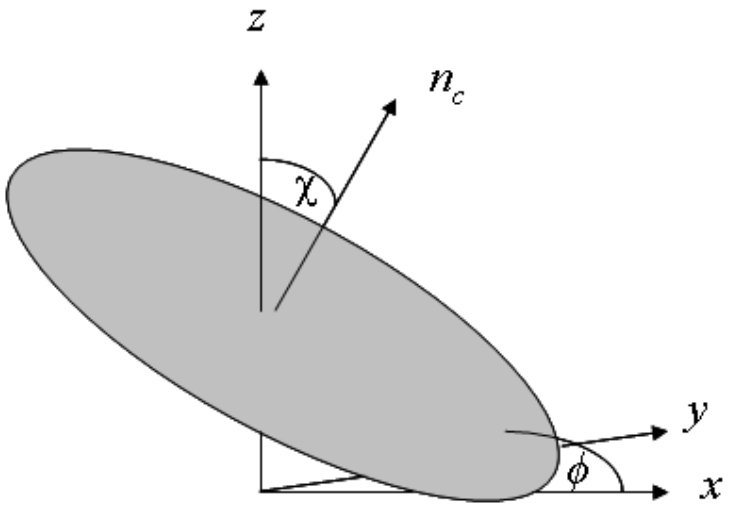

Figure 5-16. The dihedral angle, χ between the plane-normal vector, $\vec{n}_c$ and the base normal, $\vec{n}_b$. The angle ϕ is the angel between the plane and the x-axis.

where n_c is the normal vector to the contact plate, n_b is the normal vector to the required plane, $|n_c|$ is the magnitude of the normal vector to the contact plate, $|n_b|$ is the magnitude of the normal vector of the plane and χ is the angle between the two normals. The base frame has three planes: z-y, x-z, and x-y planes corresponding to unit normals pointing along the x-, y-, and z- axes respectively. The angles between the normal and the x-, y- and z- axes are given by

$$\chi_x = \cos^{-1} \frac{n_{cx}}{\sqrt{{n_{cx}}^2 + {n_{cy}}^2 + {n_{cz}}^2}} \quad \textbf{(5-42)}$$

$$\chi_y = \cos^{-1} \frac{n_{cy}}{\sqrt{{n_{cx}}^2 + {n_{cy}}^2 + {n_{cz}}^2}} \quad \textbf{(5-43)}$$

and

$$\chi_z = \cos^{-1} \frac{n_{cz}}{\sqrt{{n_{cx}}^2 + {n_{cy}}^2 + {n_{cz}}^2}} \quad \textbf{(5-44)}$$

where the components of the normal, n_x, n_y and n_z are taken from 5-24 and the magnitude of the unit vector is one. Since the plane-normal vector and the plane are perpendicular to each other the angle of the contact plane to the base frame is given by

$$\phi = \chi_x - 90° = \left(\cos^{-1} \frac{n_{cx}}{\sqrt{{n_{cx}}^2 + {n_{cy}}^2 + {n_{cz}}^2}} \right) - 90° \qquad \textbf{(5-45)}$$

$$\delta = \chi_y - 90° = \left(\cos^{-1} \frac{n_{cy}}{\sqrt{{n_{cx}}^2 + {n_{cy}}^2 + {n_{cz}}^2}} \right) - 90° \qquad \textbf{(5-46)}$$

$$\psi = \chi_z = \left(\cos^{-1} \frac{n_{cz}}{\sqrt{{n_{cx}}^2 + {n_{cy}}^2 + {n_{cz}}^2}} \right) \qquad \textbf{(5-47)}$$

where χ_x, χ_y and χ_z are given by equations 5-42 to 5-44 respectively. Note that 90 ° is not subtracted from ψ (the angle with respect to the z-axis) since in the default position (no deviation) the base and plate normal vectors are parallel. Therefore equations 5-38 to 5-40 give the displacement of the contact plate while equations 5-45 to 5-47 give the orientation of the contact plate.

A model of the mechanical structure was created to test the mathematical model of the displacement and orientation calculations as shown in Figure 5-17. Table 5.2 shows the comparison between the theoretical results from the mathematical model and the actual measured results from the mechanical model. Displacement measurements were taken with a ruler with an error of ± 1 mm and a protractor for angular measurements with an error of ± 1 °. The results show that the model results are very close (taking manufacturing errors into account) the measured results. Appendix E.1 shows a sample calculation for one investigated configuration.

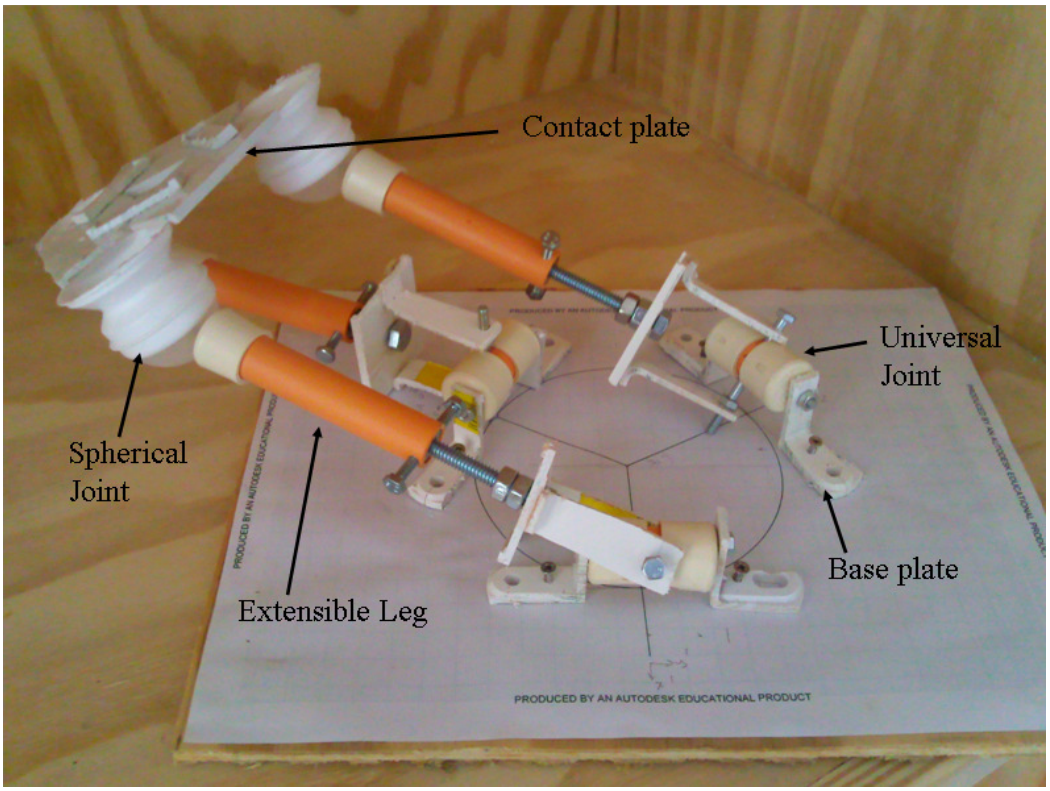

Figure 5-17. A photo of the apparatus used to test the mathematical model for the displacement and orientation of the contact plate.

Leg#	**Angle(°)**	**Position (m) (calculated)**	**Position (m) (measured)**	**Displacement (m) (calculated)**	**Displacement (m) (measured)**	**Orientation (°) (calculated)**	**Orientation (°) (measured)**
1	α=69 β=144 γ=47	P_x = -0.041 P_y = -0.142 P_z = 0.037	P_x = -0.04 P_y = -0.14 P_z = 0.035	C_x = -0.079	C_x = -0.075	ϕ = 22	ϕ = 20
2	α=80 β=34 γ=49	P_x = -0.108 P_y = -0.114 P_z = 0.018	P_x = -0.105 P_y = -0.115 P_z = 0.020	C_y = -0.144	C_y = -0.149	δ = 16	δ = 15
3	α=-89 β=88 γ=38	P_x = -0.097 P_y = -0.178 P_z = 0.003	P_x = -0.100 P_y = -0.175 P_z = 0.005	C_z = -0.02	C_z = -0.023	ψ = -63	ψ = -61

Table 5.2. A comparison between the results of the mathematical model and measure values of the displacement of the contact plate of the 6-DOF sensor.

5.3.2 Force and Torque Modelling

This section develops a model of the applied force and torque based on the displacement of the contact plate and the properties of the flexures used. For static balancing the applied force must be balanced by the restoring force for the flexural joints,

$$\sum_{m=1}^{3} F_m - F_{ext} = 0 \qquad \textbf{(5-48)}$$

and

$$\sum_{m=1}^{3} M_m - M_{ext} = 0 \qquad \textbf{(5-49)}$$

where F_{ext} is the applied external force, F_i is the force from the ith leg of the sensor, M_{ext} is the applied external torque and M_i is the torque from the ith leg. Expanding equation (5-48) gives

$$\vec{F}_1 + \vec{F}_2 + \vec{F}_3 = \vec{F}_{ext} \qquad \textbf{(5-50)}$$

where F_1, F_2 and F_3 are the forces directed along legs 1, 2 and 3 respectively.
Recall that the torque required to twist a rectangular beam by an angle of θ_r is given by equation (3-18), i.e.

$$T = k_T \theta_r \qquad \textbf{(5-51)}$$

where $k_T = \dfrac{JG}{L}$.

The required torque can also be expressed in vector form

$$\vec{T} = \vec{d} \times \vec{F} \tag{5-52}$$

or in magnitude form

$$T = |d||F|\sin\phi \tag{5-53}$$

where T is the torque produced by a force, F at a distance d from a pivot point and ϕ is the angle between r and F. Consider the local coordinate system for one leg as shown in Figure 5-11. Each universal joint has two degrees of rotational freedom resulting in two torque components per joint

$$T_x = k_T \beta_r \tag{5-54}$$

and

$$T_y = k_T \alpha_r \tag{5-55}$$

where β and α are the angles of twist about the x- and y- axes respectively. Expanding the cross product in 5-52 for the leg vector, $\vec{E}$ gives

$$\vec{T} = \begin{vmatrix} \hat{i} & \hat{j} & \hat{k} \\ E_x & E_y & E_z \\ F_x & F_y & F_z \end{vmatrix}$$

$$T = (E_y F_z - E_z F_y)\hat{i} - (E_x F_z - E_z F_x)\hat{j} + (E_x F_y - E_y F_x)\hat{k} \tag{5-56}$$

Note that the cross product assumes that the force and distance are perpendicular to each other. Equating x-components of 5-54 and 5-56 gives

$$k_T \beta_r = E_y F_z - E_z F_y \tag{5-57}$$

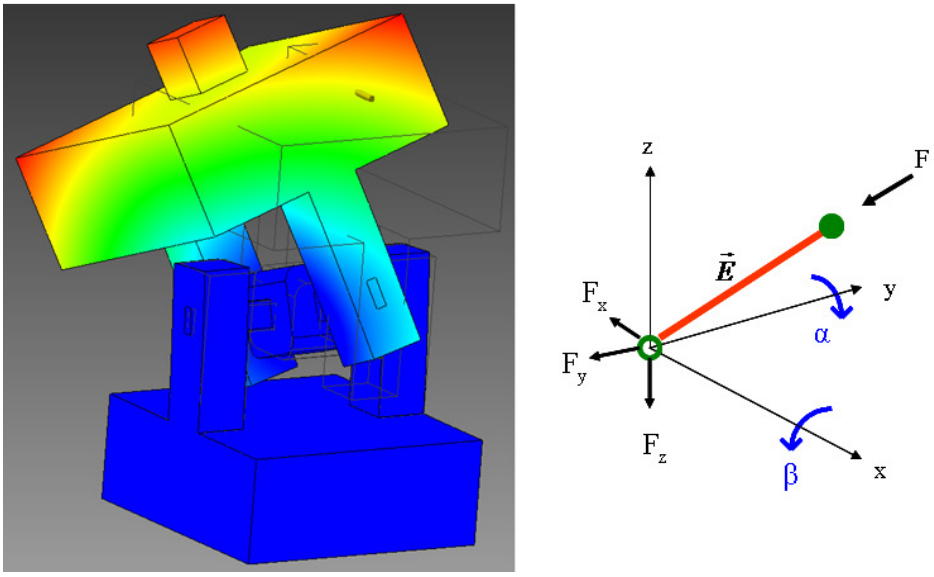

Figure 5-18. Deformation of one of the universal joints when under load.

and the torque about the y-axis is given by

$$k_T \alpha_r = E_z F_x - E_x F_z \,. \tag{5-58}$$

The applied force is directed along the prismatic joint in the direction of the unit vector for that leg (see Figures 5-18 and 5-19). The unit vector for each leg, $\hat{e}$ is given by

$$\hat{e} = \frac{\vec{E}}{\left|\vec{E}\right|} \tag{5-59}$$

where $\vec{E}$ is the vector given by 5-11. The magnitude of $\vec{E}$ is also the extension of the prismatic link which is given by 5-4. Therefore, equation 5-59 becomes

$$\hat{e} = \frac{\vec{E}}{2L_p\sqrt{1-\cos^2\gamma}} \tag{5-60}$$

Equating 5-51 and 5-53 for the magnitude of the torque gives

$$k_T \gamma_r = L_p F_p \sin\left(90° - \gamma\right)$$

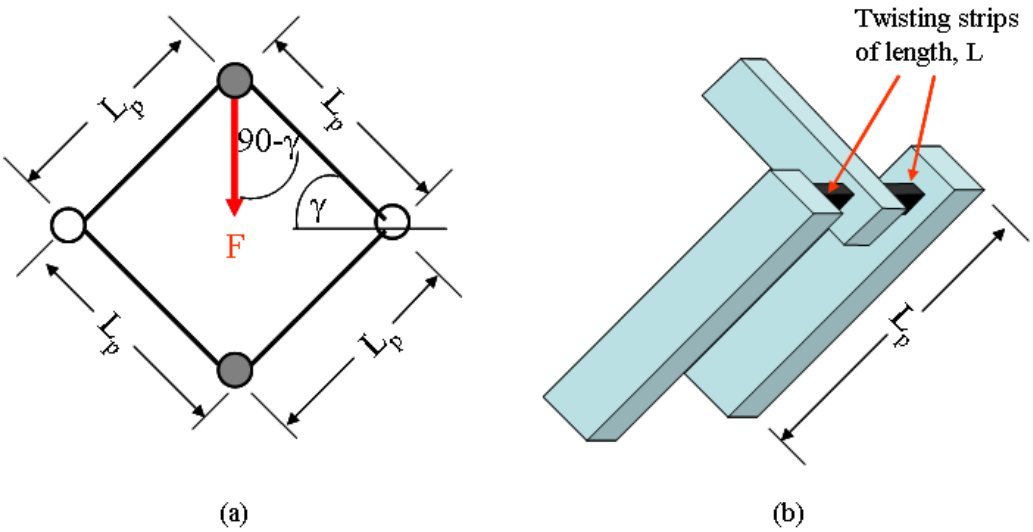

Figure 5-19. The applied force, F causes the joint to move in one direction and change the angle γ between the applied force and the link. (a) Illustration of the force being applied to the prismatic joint. (b) Diagram of one link of the prismatic joint showing one of the twisting strips.

$$\Rightarrow \qquad F_p = \frac{k_T \gamma_r}{L_p \cos\gamma} \qquad \textbf{(5-61)}$$

where L_p is the length of the twisting bar, γ is the angle between the applied force and bar, γ_r is the value of γ in radians and F_p is the magnitude of the force applied to the prismatic joint. Equation 5-61 represents one of the four joints in the prismatic link where each joint consists of two twisting sections as shown in Figure 5-19b. Therefore, the magnitude of the total force from the prismatic link is given by

$$F_{pT} = \frac{8k_T \gamma_r}{L_p \cos\gamma} \qquad \textbf{(5-62)}$$

and hence the force vector is given by

$$\vec{F} = F_{pT} \bullet \hat{e}$$

$$\vec{F} = \frac{8k_T\gamma_r}{L_p\cos\gamma} \bullet \hat{e} \tag{5-63}$$

where the unit vector, $\hat{e}$ is given by 5-59. The z-component of the force vector, F_z is given by

$$F_z = \vec{F} \bullet \hat{k} = \frac{8k_T\gamma_r}{L_p\cos\gamma}\left(\frac{E_z}{2L_p\sqrt{1-\cos^2\gamma}}\right) \tag{5-64}$$

The linear polarisers are used to measure the angle of twist where the intensity of transmitted light is given by (3-20). Without loss of generality the transmitted light can be converted into a voltage to give

$$V = V_m\cos^2\gamma \tag{5-65}$$

where V is the output voltage, V_m is the maximum transmission voltage and θ is the rotation angle of the polarizer. Substituting 5-64 into 5-63 gives

$$F_z = \frac{8k_T\gamma_r}{L_p\cos\gamma}\left(\frac{E_z}{2L_p\sqrt{1-\frac{V}{V_m}}}\right) \tag{5-66}$$

Substituting 5-66 into 5-57 and 5-58 gives

$$F_y = \frac{E_yF_z - k_T\beta_r}{E_z} \tag{5-67}$$

and

$$F_x = \frac{k_T\alpha_r + E_xF_z}{E_z} \tag{5-68}$$

where 5-66 to 5-68 are the force components on each leg in the local coordinate frame. To convert to the local coordinate frame to the global frame apply the rotation matrix in 5-11 to give

$$\vec{F}_{mT} = R(z,\psi_m)\cdot\vec{F}_m$$

$$\vec{F}_{mT} = \begin{pmatrix} \cos\psi_m & -\sin\psi_m & 0 \\ \sin\psi_m & \cos\psi_m & 0 \\ 0 & 0 & 1 \end{pmatrix}\begin{pmatrix} F_{mx} \\ F_{my} \\ F_{mz} \end{pmatrix}$$

$$\begin{aligned}\vec{F}_{mT} &= \left(F_{mx}\cos\psi_m - F_{my}\sin\psi_i\right)\hat{i} \\ &\quad + \left(F_{mx}\sin\psi_m + F_{my}\cos\psi_m\right)\hat{j} + F_{mz}\hat{k}\end{aligned} \qquad \textbf{(5-69)}$$

where m=1,2,3 represents on of the three legs of the sensor, ψ_m is the angle given in Table 5.1 and F_{mT} is the force for the mth leg of the sensor. The applied force is balanced by the total force from the sensor legs. Therefore,

$$\vec{F}_{1T} + \vec{F}_{2T} + \vec{F}_{3T} = \vec{F}_{ext} \qquad \textbf{(5-70)}$$

Expanding 5-70 into components gives

$$F_{extx} = F_{1Tx} + F_{2Tx} + F_{3Tx} \qquad \textbf{(5-71)}$$

$$F_{exty} = F_{1Ty} + F_{2Ty} + F_{3Ty} \qquad \textbf{(5-72)}$$

$$F_{extz} = F_{1Tz} + F_{2Tz} + F_{3Tz} \qquad \textbf{(5-73)}$$

The torque for a given leg is given by

$$\vec{M} = \vec{p}\times\vec{F} \qquad \textbf{(5-74)}$$

where $\vec{p}$ is direction vector of the leg, $\vec{F}$ is the force on the leg in the global coordinate frame and $\vec{M}$ is the torque in the global coordinate frame. Expanding 5-74 into components for the mth leg gives

$$\vec{M}_m = \left(p_{my}F_{mz} - p_{mz}F_{my}\right)\hat{i} - \left(p_{mx}F_{mz} - p_{mz}F_{mx}\right)\hat{j} + \left(p_{mx}F_{my} - p_{my}F_{mx}\right)\hat{k} \quad \textbf{(5-75)}$$

The total externally applied torque is then the sum of the torques of each leg

$$\vec{M}_{ext} = \sum_{m=1}^{3} \vec{M}_m = \vec{M}_1 + \vec{M}_2 + \vec{M}_3$$

and expanding into components gives

$$M_{extx} = \left(p_{1y}F_{1z} - p_{1z}F_{1y}\right) + \left(p_{2y}F_{2z} - p_{2z}F_{2y}\right) + \left(p_{3y}F_{3z} - p_{3z}F_{3y}\right) \quad \textbf{(5-76)}$$

$$M_{exty} = -\left[\left(p_{1x}F_{1z} - p_{1z}F_{1x}\right) + \left(p_{2x}F_{2z} - p_{2z}F_{2x}\right) + \left(p_{3x}F_{3z} - p_{3z}F_{3x}\right)\right] \quad \textbf{(5-77)}$$

$$M_{extz} = \left(p_{1x}F_{1y} - p_{1y}F_{1x}\right) + \left(p_{2x}F_{2y} - p_{2y}F_{2x}\right) + \left(p_{3x}F_{3y} - p_{3y}F_{3x}\right) \quad \textbf{(5-78)}$$

Equations 5-76 to 5-78 give the components of the torques on the 6-DOF sensor.

5.4 Sensor Simulations

Force and torque simulations on the 6-DOF were performed in Autodesk Inventor 2012 to investigate the likely response of the sensor to applied forces and the working range of the sensor. The aim of the simulations is to investigate the displacement and orientation of the contact plate with applied forces. The simulator only uses Finite Element Analysis (FEA) to simulate the movement of the structure but it cannot model the properties of the linear polarisers or of the polarised light.

Figure 5-20 shows the simulation of a 10 N vertical force (F_z) applied to the centre of the contact plate. In this simulation the sensor experienced purely linear displacement of approximately 0.2 mm. The prismatic link also operates as designed by compressing inward with the applied force. Figure 5-21 shows the response of the sensor to a 5 N horizontal force, F_x parallel to the x-axis of the sensor. The simulation

shows the contact plate displaced by approximately 0.3 mm and the prismatic links extending as designed. Figure 5-22 shows a simulated 2 Nmm torque about the z-axis. In this case the torque causes each prismatic link to extend by equal amounts (less than one degree) to ensure pure rotation of the contact plate. The final simulation is shown in Figure 5-23 where an 8 N vertical force was applied at a radius of 3 mm from the centre of the sensor and midway between two legs of the structure. The results show that the contact plate tilts downward producing a torque about the x- and y-axis. From the simulated results the estimated maximum values of the sensor are shown in Table 5.3. These results were based on the simulations and the maximum extension/compression of the prismatic joints where are constrained to work within the linear region of the linear polarizers. These limits are within the desired range as highlighted with the aims of the device in Section 1.2.

Force	**Limit**
$\mathbf{F_z}$	20 N
$\mathbf{F_x}$	10 N
$\mathbf{F_y}$	10 N
$\mathbf{M_x}$	20 Nmm
$\mathbf{M_y}$	20 Nmm
$\mathbf{M_z}$	40 Nmm

Table 5.3. Table of the maximum estimated forces for the 6-DOF, 3-UPS sensor.

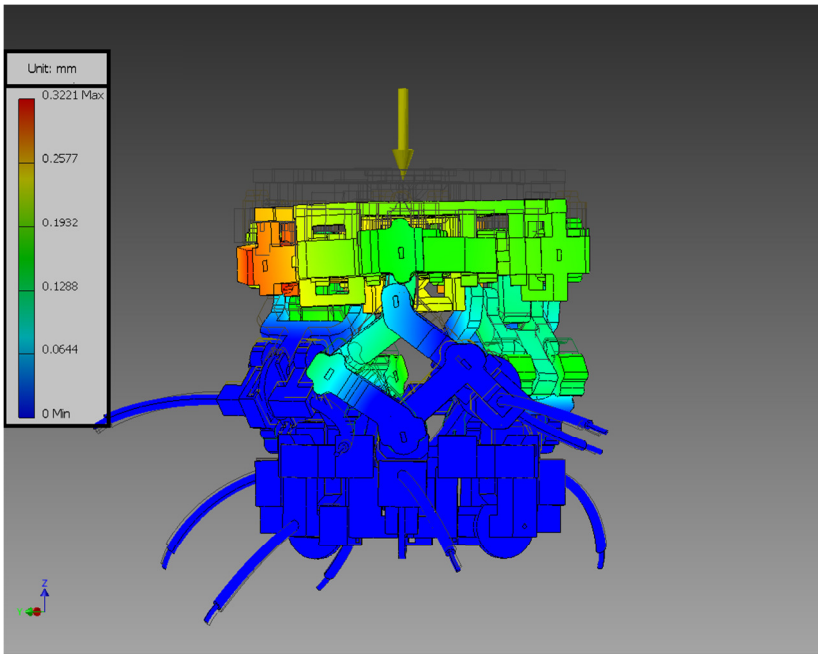

Figure 5-20. Simulation of the 6-DOF, 3-UPS sensor experiencing a 10 N force applied parallel to the z-axis. (The displacement range is from 0 mm (Blue) to 0.32 mm (Red)).

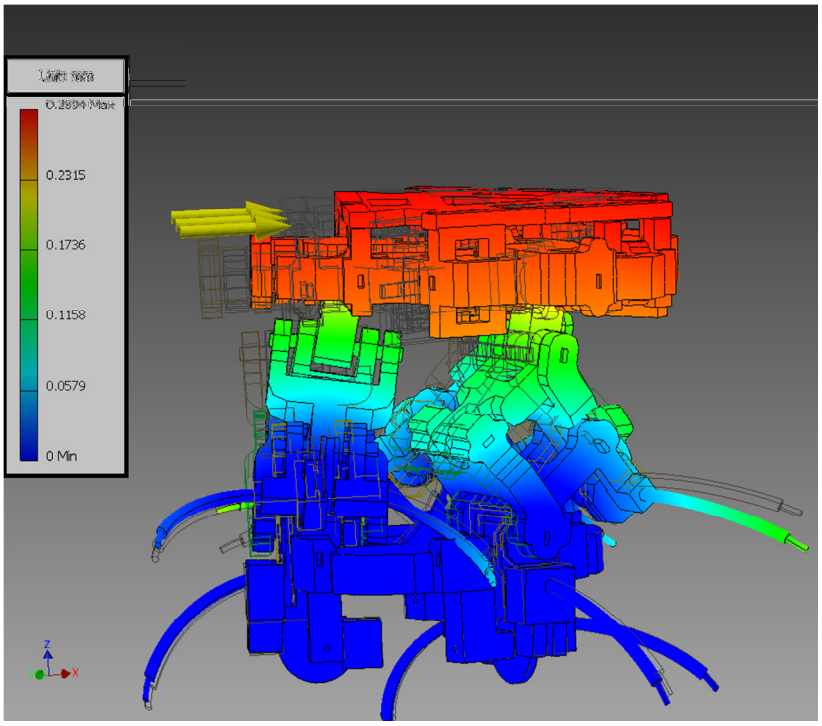

Figure 5-21. Simulation of the 6-DOF 3-UPS sensor experiencing a 5 N force along the x-axis. (The displacement range is from 0 mm (Blue) to 0.29 mm (Red)).

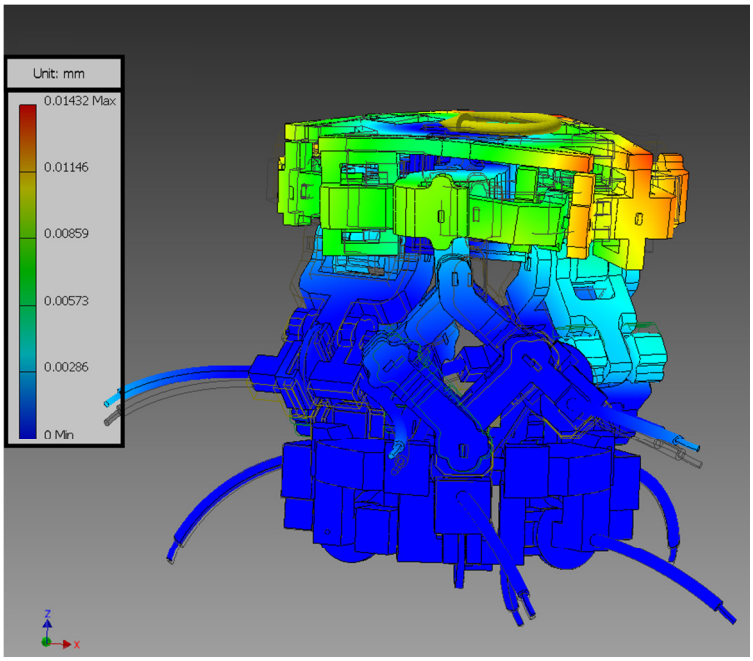

Figure 5-22. Simulation of the 6-DOF, 3-UPS sensor experiencing a 2 mNm force about the z-axis. (The displacement range is from 0 mm (Blue) to 0.014 mm (Red)).

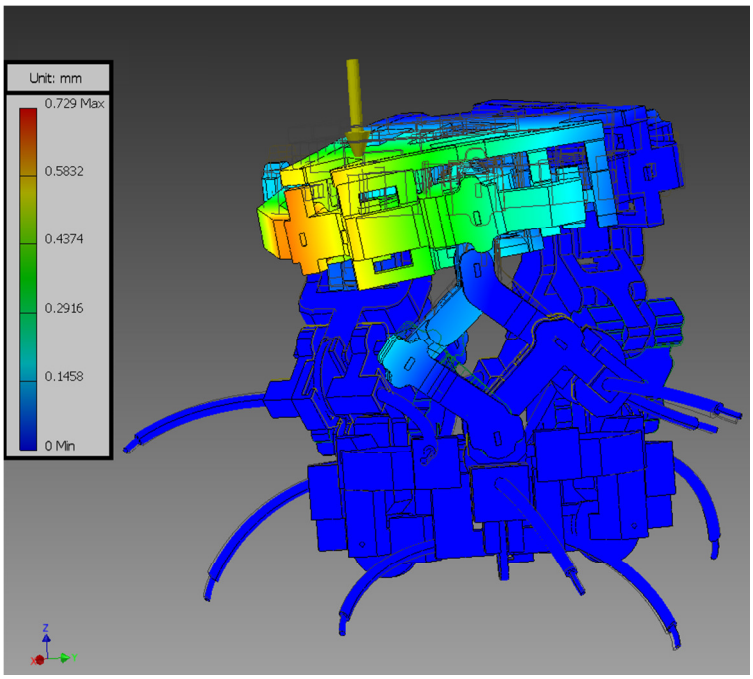

Figure 5-23. Simulation of the 6-DOF 3-UPS sensor experiencing an 8 N force at a radius of 3 mm from the centre of the sensor. (The displacement range is from 0 mm (Blue) to 0.73 mm (Red)).

5.5 Sensor Drift Reduction

Sensor drift can be defined as the increasing deviation of a parameter from a preset value over time. Optical sensor drift can occur for a number of reasons including temperature fluctuations, power supply fluctuations, aging components and light intensity fluctuations. The main indication of sensor drift is a gradually deviation of the sensor's output value when it is unloaded. The effect of sensor drift is that the sensor gradually loses accuracy over time compromising the integrity of the test results. This can have detrimental effects if a dexterous manipulator is grasping a fragile object. Figure 5-24 shows a comparison of a sensor with and without drift where the output voltage increases as time passes. Hardware solutions have been proposed to reduce the effects of drift such as using temperature insensitive materials, increasing the stability of the power supply components and controlling the working environment of the sensor. However, pursuing these options is not always possible so software options have also been pursued. Peirs *et al.* [180] proposed modulating the light source with a 5 kHz sine wave in order to reduce the heat build up that can occur if the power source is on continuously.

The drift reduction technique proposed in this research is based on the principles of a lock-in amplifier but simplifies the calculations to maintain a constant sensor output even if the sensor drifts radically. Lock-in amplifiers generate a high frequency reference signal and compare all read signals with the reference signal to retrieve the modulated signal even if the signal-to-noise ratio is very low. This is similar in many respects to the phase modulation techniques highlighted in (Section 2.2.4). The high frequency reference signal helps reduce the noise signal and improve the signal-to-noise ratio [181]-[183]. Hardware-based lock-in amplifiers are very expensive due to their high precision but software alternatives have been developed that can still perform well [184].

The method used in this research is to drive the LED light source with a sinusoidal waveform which keeps the LED operating within the linear region and prevents excessive heating of the LED thereby causing sensor drift. The sinusoidal waveform is internally generated by a dsPIC33FJ256GP710A microcontroller and a

digital potentiometer. All of the transmitting optical fibres of the sensor are connected to the same light source so that any fluctuations affect all detectors and hence can be compensated. All of the sensor's photodetectors are locked to the generating frequency and are read before generating the next voltage step. Two complete sinusoidal waves per sensing fibre are generated for each processing cycle to improve sensor performance. In addition to the nine sensing fibres (three per leg) there is an extra pair of fibres to provide a reference voltage for the system. The data from each sensing fibre is then shifted by 90° and subtracted from the reference data. Figure 5-25 shows a sample calculation for the algorithm. The reference (blue) and sensing (red) voltages have a voltage range of 2.5 ± 0.8 V. The data for the reference and sensing voltages are shown in "Voltage" and "Shifted Angle Voltage" columns respectively. The "Differential Voltage" column shows the difference between the reference voltage and the sensing fibre voltage. Notice that in the last column the alternate values are always the same. Figure 5-26 shows a simulated sensor drift where the input (green), output (blue) and shifted wave (red) all drift from the set value of 1.3 V but the differential voltage (brown) is constant at 1.1 V. Using the alternate samples thus provides a constant output value even if the sensor drift is large which is a highly desirable feature.

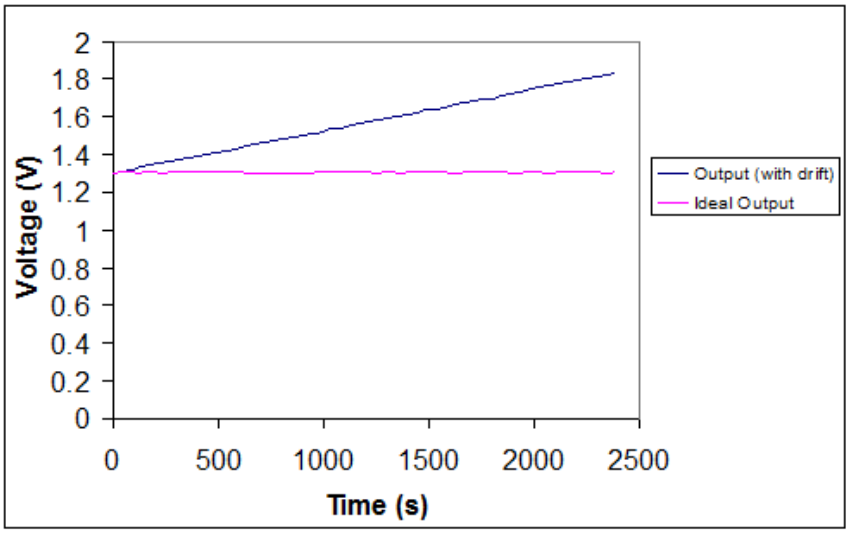

Figure 5-24. Simulation of sensor drift.

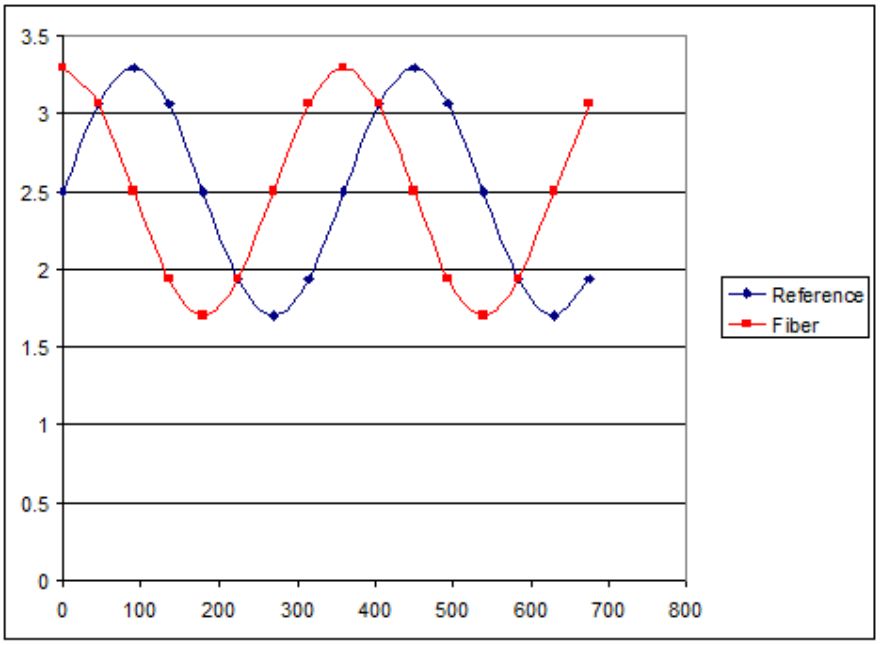

(a)

Sample No.	Angle (Continuous)	Voltage	Shifted Angle Voltage	Differential Voltages
0	0	2.5	3.3	0.8
1	45	3.06568542	3.065685425	4.44089E-16
2	90	3.3	2.5	0.8
3	135	3.06568542	1.934314575	1.13137085
4	180	2.5	1.7	0.8
5	225	1.93431458	1.934314575	2.22045E-16
6	270	1.7	2.5	0.8
7	315	1.93431458	3.065685425	1.13137085
8	360	2.5	3.3	0.8
9	405	3.06568542	3.065685425	4.44089E-16
10	450	3.3	2.5	0.8
11	495	3.06568542	1.934314575	1.13137085
12	540	2.5	1.7	0.8
13	585	1.93431458	1.934314575	2.22045E-16
14	630	1.7	2.5	0.8
15	675	1.93431458	3.065685425	1.13137085

(b)

Figure 5-25. Sample calculation for drift reduction algorithm. (a) Generated sine waves. (b) Algorithm calculations.

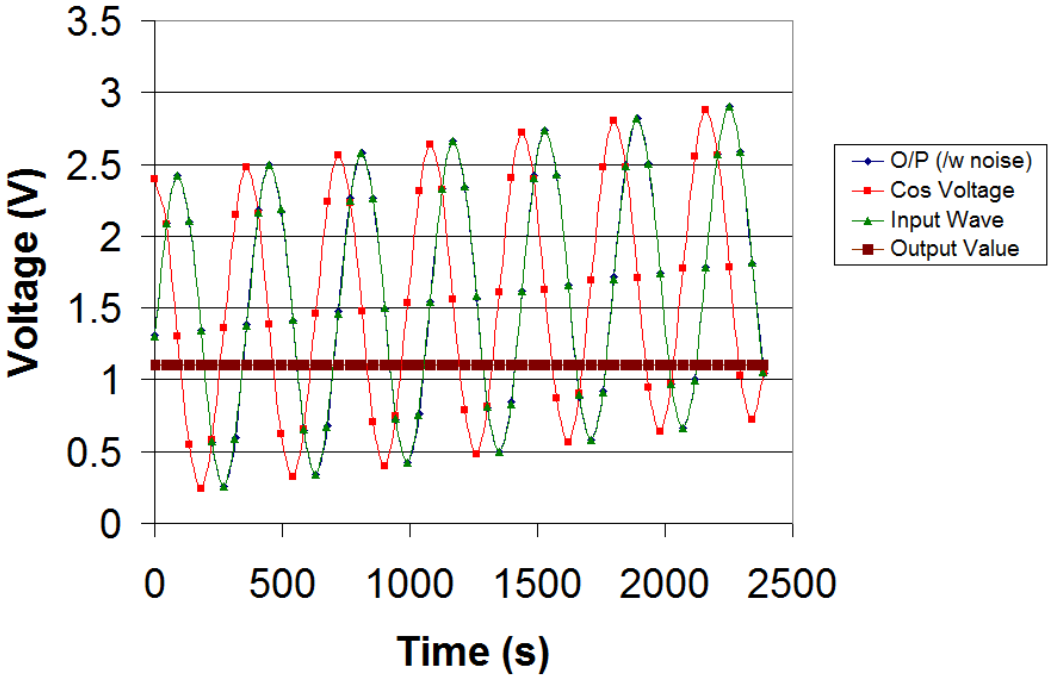

Figure 5-26. A simulation of the output value (straight line) when subjected to a drifting input.

5.6 Chapter Summary

This chapter presented a 6-DOF sensor based on a 3-UPS design and LIM based on linear polarizers. All of the joints of the new sensor are based on revolute joints so that the applied force changes the polarization angle of the polarizers hence modulation the light intensity. A mathematical model of the sensor was also developed (Section 5.3) where the applied force (equation 5-18) and torque (equation 5-26) can be calculated from the linear polarizer voltages in each of the three legs of the sensing structure. The use of the linear polarizers helped simplify the sensor's design since only one LIM equation is required to measure both force and torque and

the equation describing the linear polarizer intensity is defined. Simulations of the sensor (Section 5.4) showed that the sensor performed as expected under simulated forces and torques. Estimated maximum forces and torques were also determined from the simulation results so that a safe working range could be used when using the sensor for grasping experiments. This chapter also presented a simple and quick software method to reduce sensor drift by using the interference of sine and cosine waves. This method produced alternating output of constant value which is free of the effects of drift. The next chapter presents grasping experiments using the 6-DOF sensor to compare the expected (simulated) results with the actual sensor data.

CHAPTER 6 – Testing and Evaluation of the 6-DOF Force and Torque Sensor

6.1 Introduction

This chapter presents experiments conducted using the 6-DOF sensor (Ø 16 mm × 15.50 mm) and a Barrett Hand dexterous manipulator. The sensor was first calibrated using the Nano17 force/torque sensor and a 6-DOF Fanuc M-6iB robotic arm then integrated into the fingertip of the Barrett Hand for the grasping experiments. All of the components of the sensor were created by a Projet 3D printer (HD 3000*Plus*, Projet). The following sections describe the experiments conducted and an analysis of results.

6.2 Sensor Calibration

The first test was to verify that the microcontroller was generating the desired frequency of 2 kHz. All of the sensor's transmitting fibres are connected to the same LED light source to prevent variation between individual transmitting fibres. Figure 6-1 shows the custom fibre holder which houses all of the transmitting fibres and a wide angle red LED light source. Figure 6-2 shows the modulating waveform that drives the common LED light source. Figure 6-2a shows the raw output from the digital potentiometers while Figure 6-2b shows the smoothed output, centred at 2.5 V that drives the LED. The smoothed output is preferable to the raw potentiometer since the smoothed waveform reduces sudden changes in current which can damage the LED.

The calibrating procedure for the 6-DOF sensor is similar to the procedure for the 2-DOF sensor (2-DOF calibration) but applied to all six axes. To adequately calibrate the sensor a sensor holder had to be made to rigidly hold the sensor while it was being twisted as shown in Figure 6-3. Figure 6-3 shows the completed calibration setup. The sensor holder consists of two parts: a Bottom Segment which is rigidly fixed to the base of the sensor and a Top Segment which is rigidly fixed to the contact plate. The Nano17 F/T is rigidly connected to the Top Segment of the sensor holder

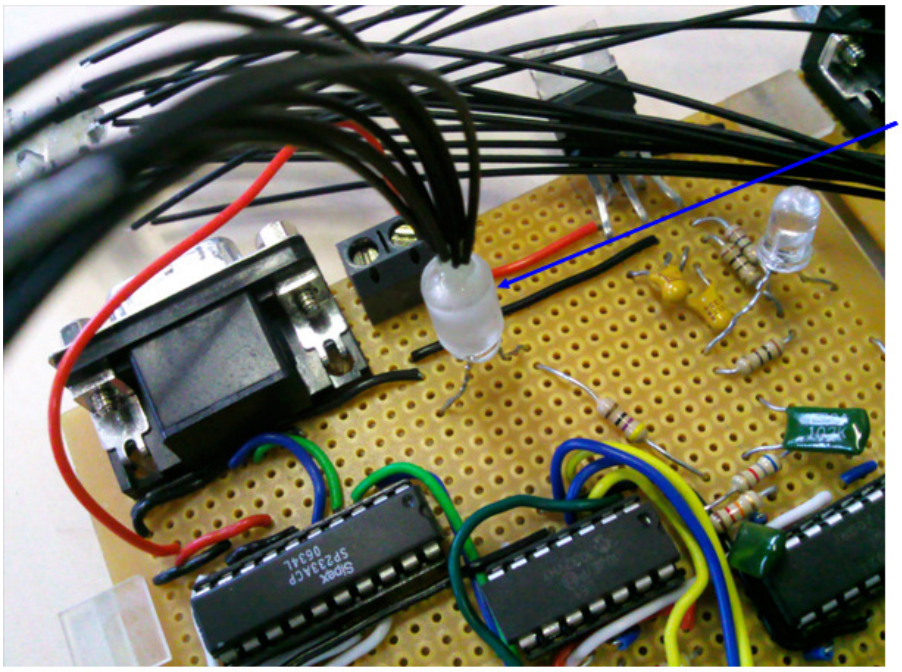

Figure 6-1. A single LED drives all of the transmitting fibres of the sensor.

and the Fanuc robot arm. The Bottom Segment of the sensor holder is rigidly held in a vice to prevent movement.

The calibration procedure is split into two parts: calibration of the force sensor and calibration of the torque sensor. The force sensor is calibrated by translating the Top Segment 1 mm forward and backward in steps of 0.25 mm. This procedure was repeated five times per axis and the average value taken per step. The torque sensor was calibrated by rotating the Top Segment 2 degrees clockwise and anticlockwise in steps of 0.5 degrees. This procedure was repeated five times and the average value take per step.

Figure 6-5 shows the results from the vertical force, F_z calibration where the output is linear with the applied force and Figure 6-6 shows the data for the calibration experiment. Figure 6-5 shows that the θ_1 and θ_2 angles for each leg are horizontal indicating no movement for these angles with applied force while the prismatic link angles change with increasing force. This result is expected for a purely vertical force since the

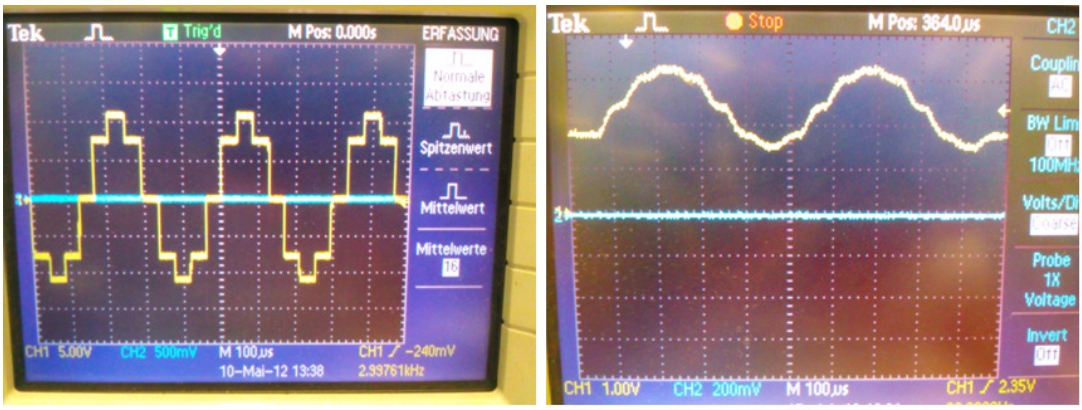

(a) (b)

Figure 6-2. Microcontroller generated waves. (a) Raw output from the digital potentiometers. (b) The smoothed output presented to the LED.

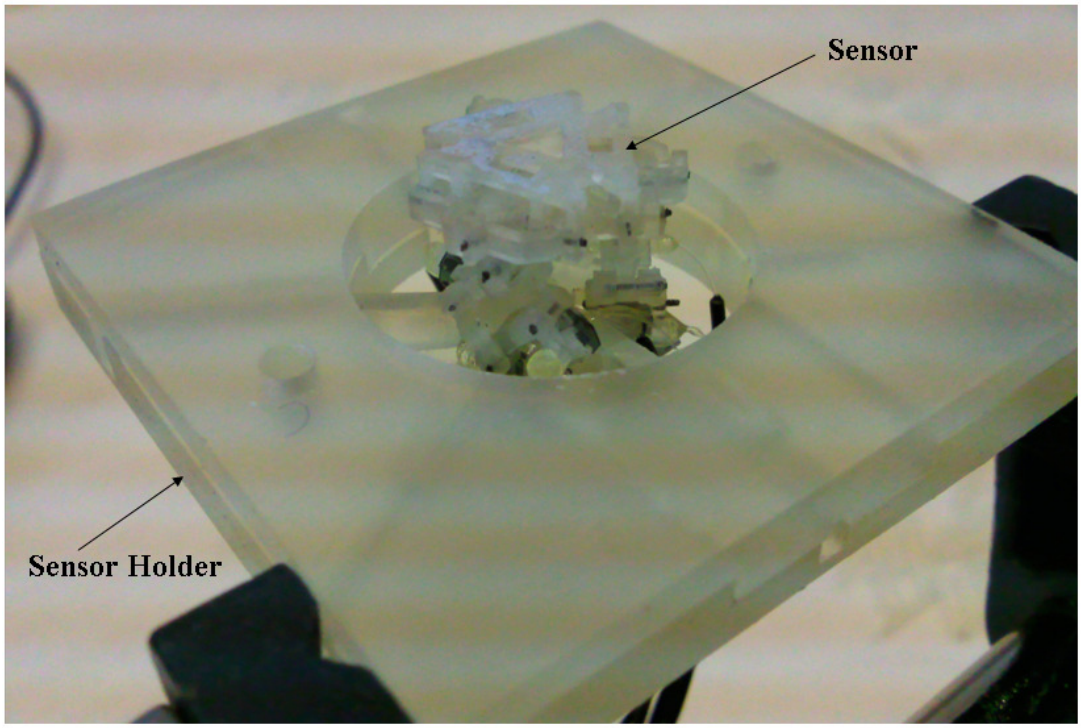

Figure 6-3. Sensor in calibration holder prior to being calibrated.

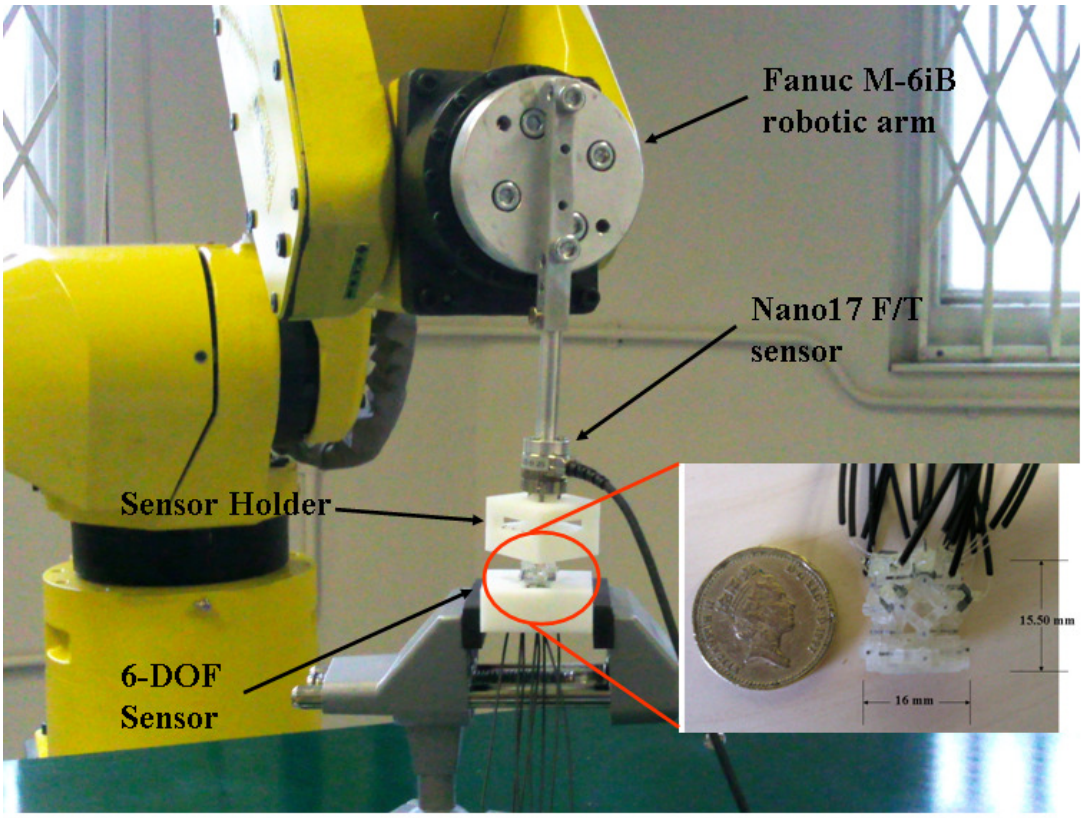

Figure 6-4. 6-DOF undergoing calibration.

universal joints should not bend when a force is applied along the thin edge of the nitinol strips (recall Section 3-4 and equation 3-2). The gradient of each line is given in Figure 6-6 where the gradients of the first two legs are approximately the same (0.0126 and 0.0131 respectively) while the gradient of the three leg is higher (0.0145). This suggests that the third leg is experiencing more force that the other legs indicating that the applied force may not be at the exact centre of the sensor as expected. In addition, the model of the senor in the previous chapter assumed that each polarizer is initially at an orientation of 45 ° to give half of the maximum transmitted light. Figure 6-6 shows the calculated initial angles of each leg using equation 5-17 and a maximum voltage of 0.095 V. These results show that the polarizers are slightly offset from their desired positions but can be corrected by including an offset into the calculations. Figure 6-5a also shows that there is some undesired compliance in the sensing structure since a minimum amount of force must be applied to the sensor to affect the prismatic link angles. This effect can be attributed to manufacturing inaccuracies that decrease the stiffness of the sensor.

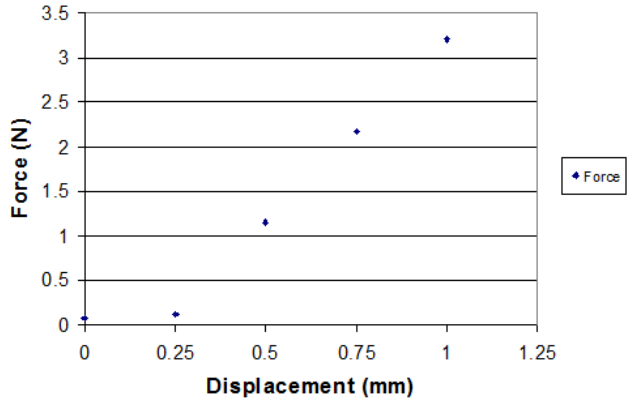

(a)

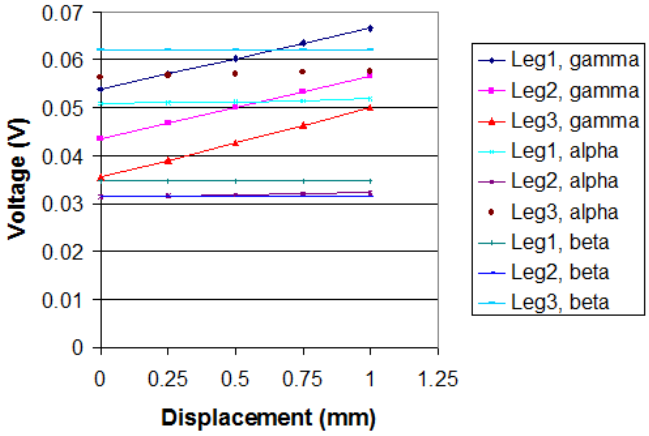

(b)

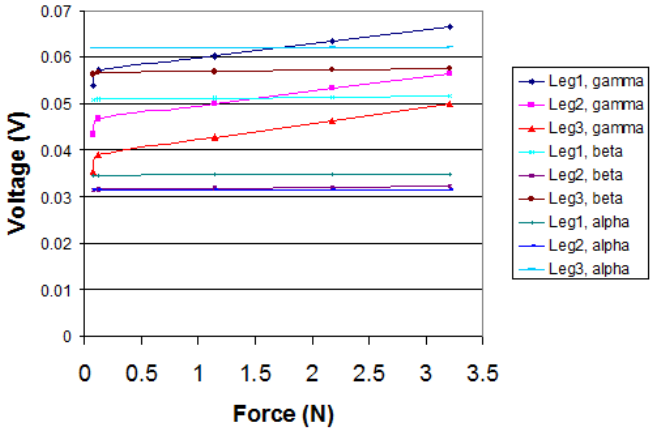

(c)

Figure 6-5. Results of the force (F_z) calibration. (a) Force-Displacement graph. (b) Voltage-Displacement graph. (c) Force-Voltage graph.

Leg No.	Reference Voltage (V)	Voltage (V)	Angle (Desired) (°)	Angle (°)	Required Offset (°)
1	0.095	$V_\alpha = 0.054$ $V_\beta = 0.044$ $V_\gamma = 0.035$	45	41 47 52	4 -2 -7
2		$V_\alpha = 0.051$ $V_\beta = 0.031$ $V_\gamma = 0.056$		43 55 40	2 -10 5
3		$V_\alpha = 0.035$ $V_\beta = 0.031$ $V_\gamma = 0.062$		53 55 36	-8 -10 9

Table 6.1. Data for the vertical force, F_z calibration experiment. The third column gives the voltage measured from each leg polariser sensor. The fifth column gives the corresponding angle for the voltage and the sixth column gives the required offset needed to adjust individual leg sensor readings.

Figure 6-6 shows a comparison of the readings from an undamaged (Figure 6-6a) and damaged (Figure6-6b) sensor respectively. For the undamaged sensor (Figure 6-6a) the separation distance between pairs of spherical joints, *c* (fifth column) is constant at 0.008227 m since the spherical joints are at fixed positions in the contact plane of radius 0.00475 m. For the damaged sensor (Figure 6-6b) the separation distance between pairs of spherical joints, *c* (fifth column) is constant between joint pairs P_2-P_1 and P_3-P_2 but incorrect between joints P_3-P_1. There are two possible causes for the damage to the sensor:

1. The third leg of the sensor is physically broken

2. The optical fibres have been broken.

In this case the latter reason caused the sensor to malfunction during earlier tests with the result that the readings from Leg 3 did not change during testing but the structure reminded intact.

Leg No.	Angle(°)	Position (m) (calculated)	Position (m) (measured)	Distance (c, calculated) (m)	Distance (c, measured) (m)
1	α=69 β=144 γ=47	$P_x = 0.00475$ $P_y = 0$ $P_z = 0.00391$	$P_x = 0.00475$ $P_y = 0$ $P_z = 0.0039$	P_2-P_1 = 0.008227	P_2-P_1 = 0.0082
2	α=80 β=34 γ=49	$P_x = -0.002375$ $P_y = 0.004114$ $P_z = 0.0039$	$P_x = -0.00238$ $P_y = 0.00411$ $P_z = 0.0039$	P_3-P_1 = 0.008227	P_3-P_1 = 0.0082
3	α=-89 β=88 γ=38	$P_x = -0.002375$ $P_y = -0.004114$ $P_z = 0.0039133$	$P_x = -0.00238$ $P_y = -0.00411$ $P_z = 0.0039$	P_3-P_2 = 0.008227	P_3-P_2 = 0.0082

(a)

Leg No.	Angle(°)	Position (m) (calculated)	Position (m) (measured)	Distance (c, calculated) (m)	Distance (c, measured) (m)
1	α=10 β=90 γ=43	$P_x = 0.00417$ $P_y = 0$ $P_z = 0.003291$	$P_x = 0.00415$ $P_y = 0$ $P_z = 0.0033$	P_2-P_1 = 0.008227	P_2-P_1 = 0.0082
2	α=-20 β=119 γ=57	$P_x = -0.001264$ $P_y = 0.006174$ $P_z = 0.003377$	$P_x = -0.00127$ $P_y = 0.00615$ $P_z = 0.0034$	P_3-P_1 = 0.008227	P_3-P_1 = 0.0063
3	α=32 β=98 γ=54	$P_x = -0.001813$ $P_y = -0.002036$ $P_z = 0.003329$	$P_x = -0.0018$ $P_y = -0.002$ $P_z = 0.0033$	P_3-P_2 = 0.008227	P_3-P_2 = 0.0082

(b)

Figure 6-6. Comparison of the spherical joint position information from two instances of using the developed 6-DOF sensor. (a) For the undamaged sensor, the separation distance, *c* (5th column) between pairs of spherical joints is constant at $\sqrt{3}R_C$ (0.008227 m). (b) For the damaged sensor, the separation distance, *c* (5th column) between pairs of spherical joints is constant between joints pairs P_2-P_1 and P_3-P_2 but incorrect between pairs P_3-P_1.

6.3 Grasping Experiments

The 6-DOF sensor was integrated into the fingertip of a Barrett Hand and used to grasp a rectangular power adapter and a plastic egg as shown in Figure 6-7 to Figure 6-10. The power adapter was placed in the palm of the Barrett Hand and held rigidly in place by the F2 and F3 fingertips. The sensor was integrated into the F1 fingertip of the Barrett Hand and the finger closed until it contacted the edge of the power adapter. The power adapter was used because it had both a flat surface and a curved edge therefore the sensor's response to both surfaces can be investigated. The results from the grasping experiment showed that the sensor deformed at the edge of the power adapter so that the contact plate was almost tangential to the point of contact. This deformation presented another interesting feature of the sensor since the tangent to the curvature may be calculated given the angles of the universal joints and the prismatic link as predicted by equation (5-9). Figure 6-8 shows the Nano17 in contact with the edge of the power adapter. The result is that the Nano17 records a torque and begins to slip off of the edge of the power adapter.

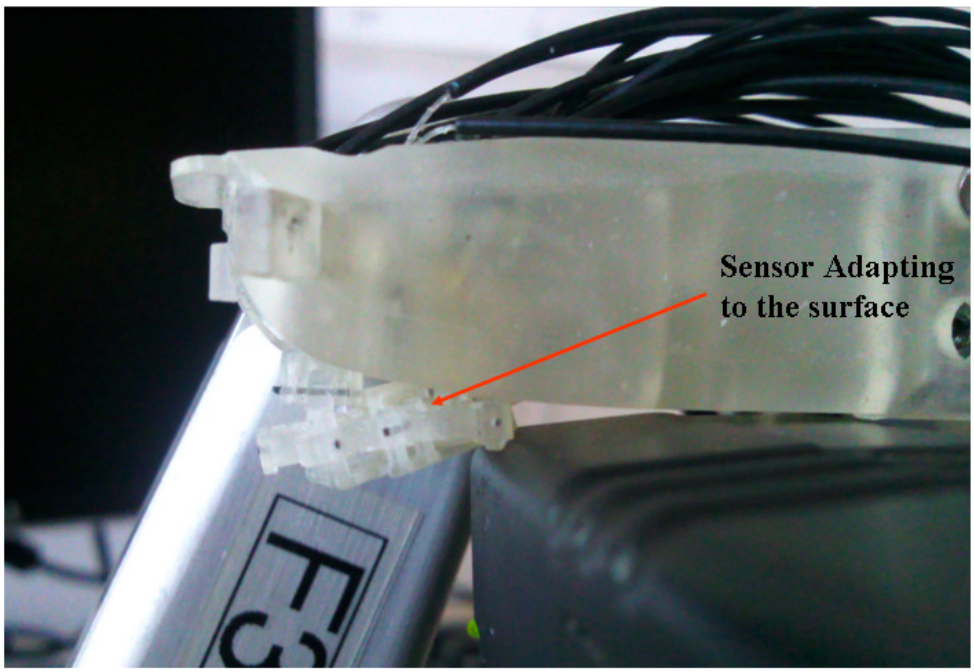

Figure 6-7. Photo of the 6-DOF sensor grasping a power adapter.

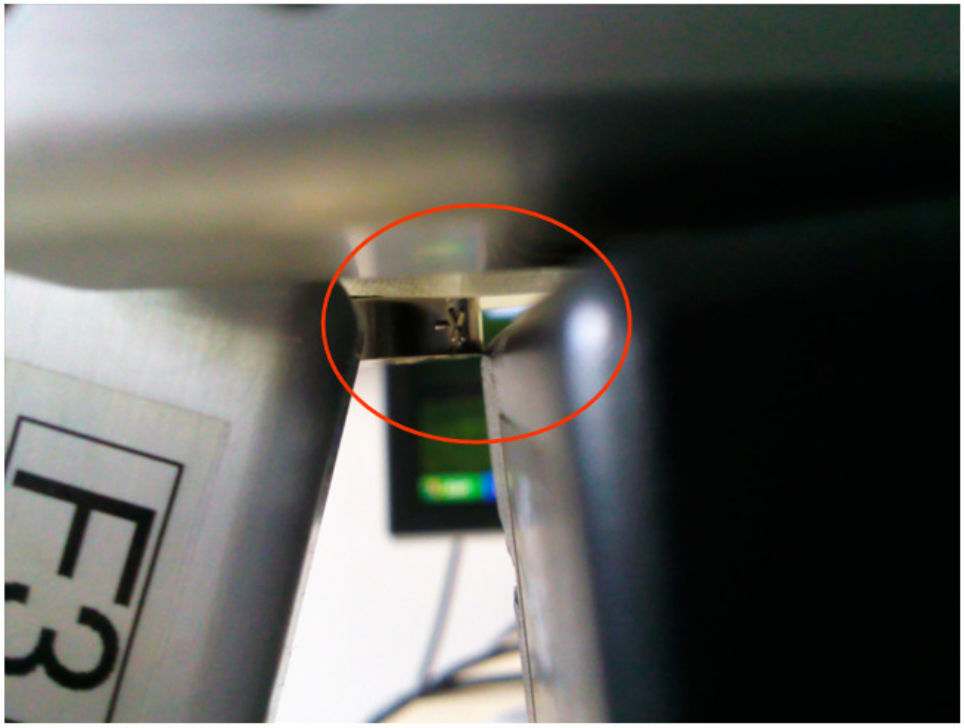

Figure 6-8. The Nano17 experiences a torque before slipping off the edge of the power adapter.

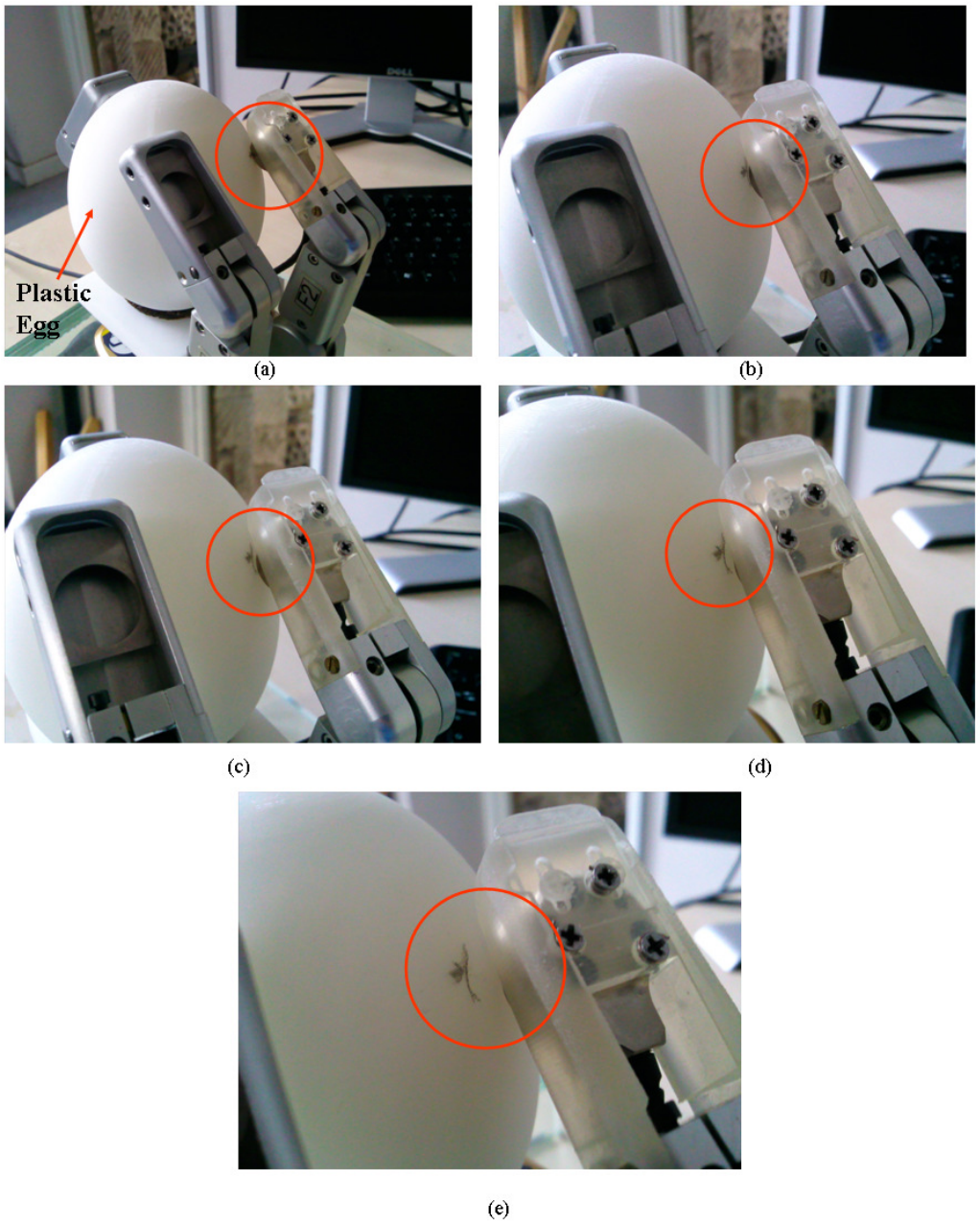

Figure 6-9. A time-elapsed photograph of the Barrett Hand grasping a plastic egg with a Nano17 integrated into one of the fingertips.

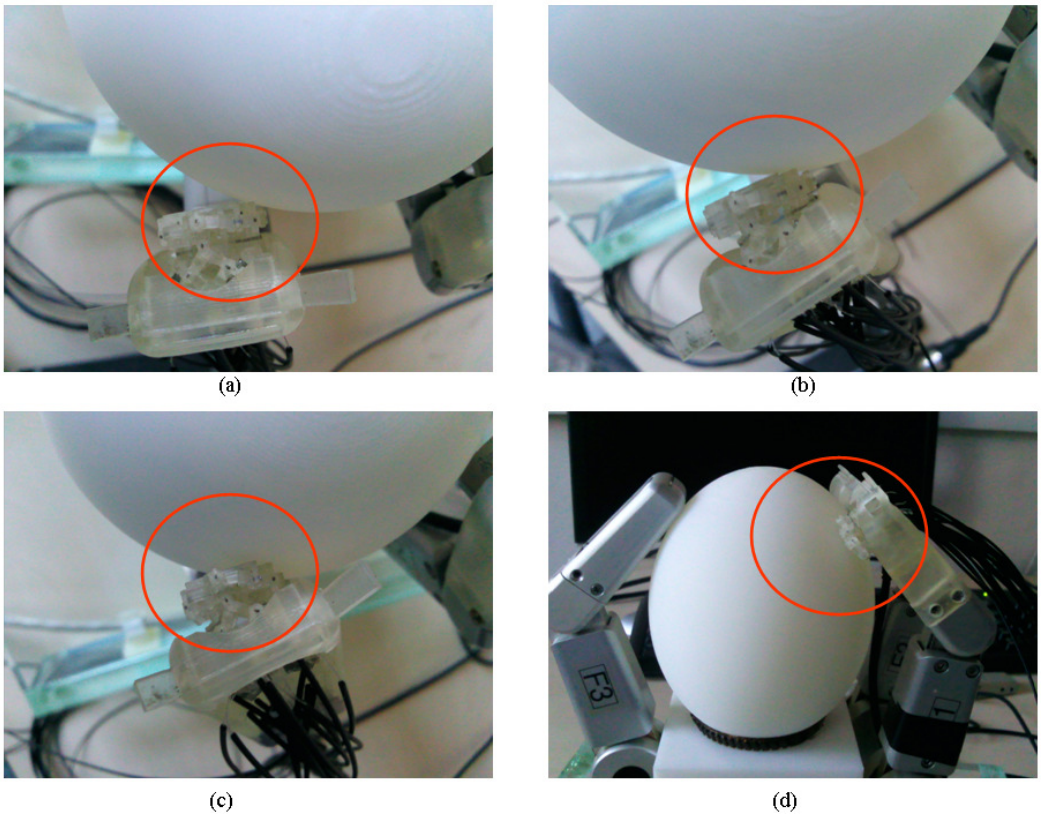

Figure 6-10. Time-elapsed photographs of the Barrett Hand grasping a plastic egg with the integrated 6-DOF sensor.

Figure 6-9 and Figure 6-10 show the results of the Barrett Hand grasping a large custom-made plastic egg. The plastic egg was chosen because it had a large 2-dimensional curved surface and a known curvature so the contact orientation could be easily calulated. The Nano17 was integrated into the F2 fingertip and used to grasp the egg while the Barrett Hand was incrementally closed. In this case the egg could not be fully constrained by the F1 and F3 fingertips because of the egg's shape and size. The result was that the egg continually moved when more force was applied to the egg during the closing action. Figure 6-9 shows the incremental progression of the marker as the closing force was increased. In contrast to the Nano17 the 6-DOF sensor did not move the grasped egg during the incremental closure. Instead, at first contact, the 6-DOF twisted so that the top plate was tangential to the 2-D curved surface. The result was that there was very little force to push the grasped egg unlike

the hard Nano17. This can be a very advantageous feature when grasping delicate objects.

An additional experiment was conducted to further investigate the curvature of a 2-dimensioanl object. The experiment, shown in Figure 6-11, consists of placing a computer mouse with its curved face against the 6-DOF sensor and applying known weights on the flat side of the mouse. Table 6.2 shows the results of the experiment where 1 N, 2 N and 4 N weights were applied to the flat side of the mouse and the signals from the sensor recorded and converted to force and torque readings using the equations in Section 5.4. Figure 6-12 shows the graphs of the force and torque response of the contact experiment.

Columns 2 and 3 in Table 6.2 show the change in position and orientation of the sensor for the applied forces. For the 1 N load the position of the sensor (column 2) was unchanged however the orientation of the platform (column) started to change based on the initial contact. Increasing the load to 4 N caused the sensor to shift mainly along the positive y-axis. The axes are shown on the mouse in Figure 6-11(a) but when the tests were conducted the mouse was upside down so the axes shown correspond to the sensor's axes. Column 3 for the 4 N force also shows that most of the twisting is concentrated about the x-axis ($\phi = 8\ ^\circ$) compared to the y-axis ($\delta = 6\ ^\circ$). Note also that there is no twisting of the sensor since the angle about the z-axis (ψ) is zero.

Columns 4 and 5 give the force and torque respectively on the sensor with the applied forces. For the 1 N applied force the force experienced by the sensor is zero and a small torque. This is in agreement with the position and orientation information in columns 2 and 3 since no displacement indicates no net applied force and the small torque indicates some twisting is being experienced by the sensor. For the 4 N applied force the sensor reading was less than expected because the sensor was contacting a curved surface and experiencing both force and torque instead of a purely vertical force. There is also the possibility that slippage between the sensor and the contacted surface may have occurred which helped contribute the lateral forces observed. This generally indicates that for small forces the torque is the dominant type of force while for large forces the linear force is the dominant component (provided there is no slipping at the contact point). This result is similar to the discussion of Figures 4-8

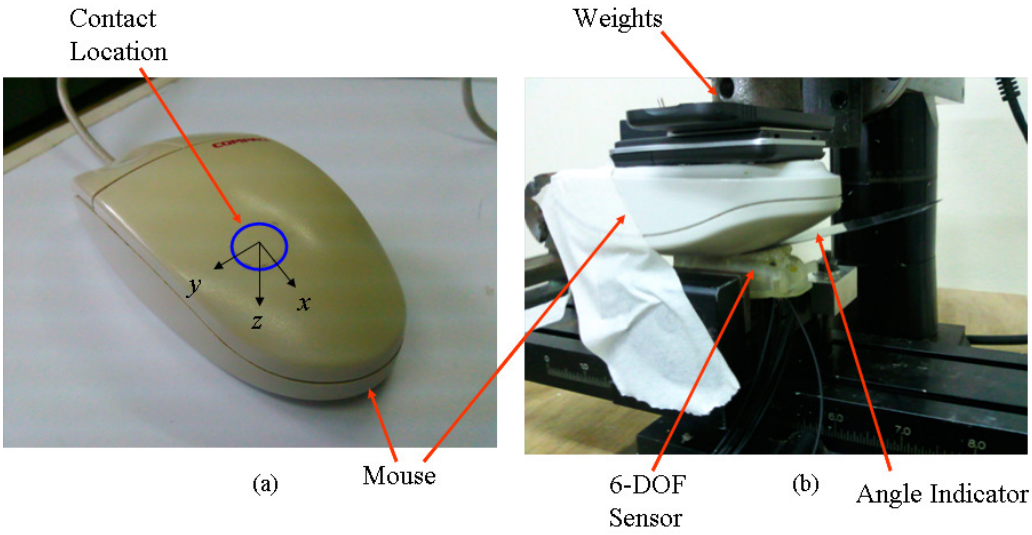

Figure 6-11. 6-DOF sensor in contact with a computer mouse. (a) The contact location on the curved surface of the mouse. (b) The sensor in contact with the mouse while a purely vertical force is applied to the bottom of the mouse.

Vertical Force (N)	Sensor Position (m)	Sensor Orientation (°)	Sensor Force (N)	Sensor Torque (Nm)
1	x = 0 y = 0 z = 0	$\phi = 1$ $\delta = 1$ $\psi = 0$	Fx = 0 Fy = 0 Fz = 0	Mx = 0.004 My = 0.004 Mz = 0
2	x = 0.0001 y = 0.00012 z = 0.0002	$\phi = 3$ $\delta = 2$ $\psi = 0$	Fx = 0.25 Fy = 0.34 Fz = 0.6	Mx = 0.008 My = 0.007 Mz = 0
4	x = 0.0003 y = 0.00032 z = 0.0006	$\phi = 8$ $\delta = 6$ $\psi = 0$	Fx = 1 Fy = 1.3 Fz = 2.8	Mx = 0.011 My = 0.009 Mz = 0

Table 6.2. Table of the force and moment data from contact with a computer mouse.

and 4-9 which illustrate the force/torque relationship depending on the position of the applied force.

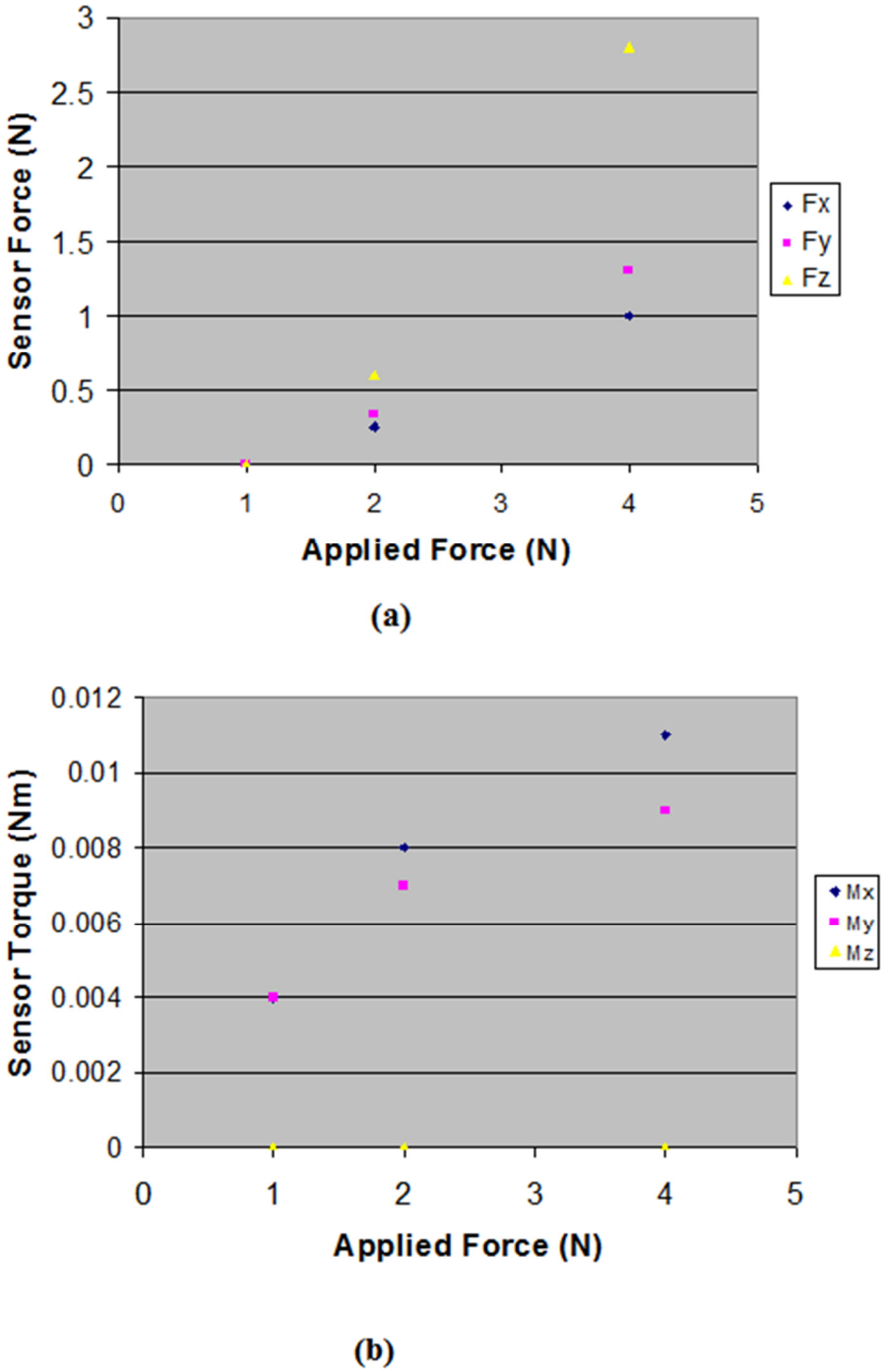

Figure 6-12. Graphs of the response of the 6-DOF sensor to contact with a computer mouse. (a) Comparison of the applied force (linear) and the sensor response. (b) Comparison of the applied force (linear) and the torque response.

6.4 Chapter Summary

This chapter presented the calibration and testing of the developed 6-DOF sensor based on a 3-UPS design. The sensor was first calibrated with a FANUC 6-DOF robot arm and a Nano17 force/torque sensor then integrated into the fingertip of a Barrett Hand. Grasping experiments were then conducted on a rectangular power adapter and a large custom-made plastic egg using both the Nano17 and the 6-DOF sensor. For both experiments the Nano17 slipped on the contact surface and generally pushed the plastic egg with each incremental closing grasp. The 6-DOF sensor generally twisted so that the contact plate was tangential to the point of contact. This resulted in gentler application of force since most of the initial applied contact force was torque until the full contact was made (recall Figure 4-8 and Figure 4-9).

A further experiment was conducted where the sensor was held stationary and a computer mouse placed upside down on the sensor so that the curved portion of the mouse rested on the sensor and forces applied to the flat side of the mouse (see Figure 6-11). The results from this experiment (see Table 6.2 and Figure 6-12) confirmed that for contact with any curved shape the 6-DOF sensor responses with first a change in orientation/torque and then a change in position/force. The 6-DOF sensor was also able to measure the angle of twisting about all of the axes which gives the orientation of the current contact point.

The next chapter presents a short review and conclusion of the work conducted and then presents future work for this research.

CHAPTER 7 – Conclusions and Future Work

7.1 Introduction and Thesis Review

The aim of this thesis was to develop a 6-DOF force and torque sensor that can be integrated into a dexterous manipulator in order to measure the force and torque applied to an object during grasping manoeuvres. Another requirement was that the sensor should be MR-compatible so that it can operate in magnetic environments. Optical sensing techniques were found to be most suitable to magnetic environments since the components are usually made from plastic or glass, they are immune to magnetic interference and the sensing information can be transmitted over long distances with minimal signal attenuation. This research focused on Light Intensity Modulation (LIM) because it is simple to implement and the required materials and equipment are inexpensive. However, problems such as light interference and sensor drift can affect the accuracy of the sensor readings. The other factor is the sensing structure that is in contact with the object. This structure should be able to measure all of the desired forces but should not interfere with the operation of the device that it is connected to.

The first sensor created was a 2-DOF sensor to measure one force, F_z and one torque, M_x. The sensor was created from plastic and nitinol strips in order to maintain the MR-compatibility requirement. The sensing structure was based on a "4-cross" design with two LIM techniques: axially-aligned optical fibre displacement where the applied force, F_z, varied the separation distance between the transmitting and receiving fibres thereby modulating the light intensity and linear polarizer pairs where the applied torque, M_x, varied the orientation between the polarizers thereby modulating the light intensity. The experiments conducted showed that the calibrated sensor produced results that are similar to those of a commercial force/torque sensor (Nano17, ATI) but with an additional advantage of being able to identify the local contact deformation at the point of contact. The major disadvantage of the 2-DOF sensor was the limited number of degrees of freedom when contacting a 2-dimensional curved surface. For this case the force sensor produced indeterminate results while the torque sensor continued to produce the correct results.

The second sensor sought to correct the problems highlighted by the 2-DOF sensor while preserving its advantages. The improved sensor increased the number of degrees of freedom to six to a full 6-DOF force/torque sensor (F_x, F_y, F_z, M_x, M_y, M_z) by changing the sensing structure to a parallel 3-UPS design. Another improvement is that the 6-DOF only uses linear polarizers due to their improved LIM characteristics and fault tolerance. The results from conducted grasping experiments showed that the 6-DOF sensor performed as expected and also maintained the ability to conform to the surface. Table 7.1 presents a comparison of the force and torque sensors used throughout this research. A novel approach is also presented to reduce drift in the sensor readings by using sine and cosine waves to maintain a constant sensor output.

	Device		
Attribute	**Nano17**	**2-DOF**	**6-DOF**
Diameter	17 mm	9 mm	16 mm
Height	15 mm	10 mm	15.50 mm
Mass	9.07 g	0.4 g	1.0 g
Sensing Technique	Silicon Strain Gauge	Fibre Optic	Fibre Optic
Resolution (Fx)	1/320 N	NA	0.08 N
Resolution (Fy)	1/320 N	NA	0.08 N
Resolution (Fz)	1/320 N	0.011 N	0.08 N
Resolution (Mx)	1/64 Nmm	0.15 Nmm	0.001 Nmm
Resolution (My)	1/64 Nmm	NA	0.001 Nmm
Resolution (Mz)	1/64 Nmm	NA	0.001 Nmm
MR-compatible	No	Yes	Yes

Table 7.1. Comparison of the developed sensor to the Nano17 F/T sensor. NA – Not Applicable

7.2 List of Contributions

The main aim of this research was to develop a 6-DOF force and torque sensor that can be embedded into the fingertip of a dexterous robotic manipulator. The second aim of the research was to make the sensor MR-compatible so that it can be used in MR-applications. In this regard a light intensity modulation technique (optical-based sensing) was used as the main sensing technique to measure the applied force and torque on the sensor. The contributions this research has made to the field of force and torque sensor development are listed below.

Firstly, this research presented the application of linear polarisers into the field of force and torque sensing. Traditional uses of linear polarisers include liquid crystal research and photograph but this is the first time (to the author's knowledge) that linear polarisers have been used as the main sensing element of a force/torque sensor. The linear polarisers are made of plastic so they are MR-compatible and are very inexpensive compared to other optical sensing materials. Another benefit is that the output light intensity of linear polarisers is invariant under translations so small deviations in the sensor's construction do not adversely affect the sensor's measurements. Also, linear polarisers are thin (0.3 mm in thickness for the type used in this research) and can be cut into any required shape hence making them very versatile and help to reduce the size and weight of the sensor so that it can fit within the dexterous fingertip.

Secondly, mathematical models of the propagation of light from an optical fibre, light intensity modulation of linear polarizer light and the force and torque output based on the variation in photodetector voltage as a function of separation distance and orientation angle were developed. The importance of the models is they link the modulation of the light with the physical movement of the sensing structure. This linkage is generally not available in commercial simulation packages which either use FEA/FEM to model the movement of the structure or model the general dispersion of light in a room but not specifically for sensing applications. The developed models were primarily designed to provide the force or torque given the change in light intensity but they can also be used to simulate calibration of the sensor where the light intensity can be estimated given specific values of force or torque. This last feature was not discovered in simulation packages investigated.

Thirdly, a 2-DOF sensor (Ø 9 mm × 10 mm) based on two LIM techniques (axially-aligned optical fibres and linear polarisers) was created in order to compare the results between the traditional method and the linear polarizer method. Another feature of the sensor is that the entire structure is MR-compatible by using ABS plastic and nitinol strips. The nitinol strips allow the sensor's contact surface to twist with when in contact with an object. This feature is unique for force and torque sensors since most other sensors are rigid structures and the deformation is small (in the order of μm). The added advantage observed with the deformable nature of the sensor is that changes in the local contact point can be detected when grasping an object. Also, the linear polarizer method had superior performance due to its rigid optical alignment setup, mathematically defined intensity modulation output and tolerance for small deviations tangential to the rotation of the linear polarizer pair.

Fourthly, a force-torque model of a 6-DOF sensor that incorporated the polarizer LIM model and a 3-UPS parallel structure was also created. The unique part of the parallel structure design is that all of the joints were made of revolute nitinol flexures which were bonded to the plastic links thereby providing a strong yet light MR-compatible structure as outlined in the aims and objectives of the research. The importance of this model is that it combines the light intensity modulation and structural deformation into a single model which is not available in many commercial simulation software packages. The 6-DOF force-torque model showed that it is possible to model the applied force and torque based on the modulated polarizer voltage and the characteristics of the parallel sensing structure.

Fifthly, a 6-DOF (Ø 16 mm × 15.50 mm) sensor based on linear polarisers embedded within a parallel 3-UPS sensing structure was created. The design comprised of rigid links made of ABS plastic and nitinol flexural joints to fully exploit the advantages of the linear polarizer and the developed linear polarizer LIM model yet maintain MR-compatibility. The deformable parallel design allows more force to be applied to the sensor since it is balanced by the three legs of the sensor and the deformable nature of the structure allows the sensor to measure the local contact deformation of the grasped object.

7.3 Conclusions, Improvements and Future Work

The sensors developed during this research achieved the main aims of measuring applied force and torque, capable of being integrated into the fingertip of a dexterous manipulator and being MR-compatible. The linear polarizer method of LIM proved to be better than axially-aligned optical fibres or reflective LIM since the intensity output is mathematically defined, the device is a commercial product and the inaccuracies due to fibre misalignment are greatly reduced. However, some improvements to the sensor can be made to enhance its effectiveness for future experiments. These are:

- **Improved Sensor Rigidity** – The rigidity of the sensing structure can be improved by:
    - Improving the bonding between the nitinol strips and the plastic structure.
    - Introduce limits on the sensor travel to prevent unwanted bending at high loads.
- **Sensor Miniaturization** – The size of the sensor can be further miniaturized in the following ways:
    - By using MEMs technology to fabricate the sensing structure.
    - By using smaller optical fibres (125 μm or less) and/or fibre bundles.

- By using polarization maintaining fibres thereby eliminating one of the linear polarisers per sensing axis. Polarized light would then be generated at the light source instead of at the sensing structure.

- **Improved Sensing Electronics** – The sensing electronics can be improved in the following ways:

  - By replacing the hardware lowpass filters with programmable lowpass filters to allow more flexible control of the data collection process.

  - The data transmission speeds can also be improved by using a protocol such as USB instead of the serial port (RS-232) as is currently being used.

  - More amplification of the received signal is required to increase the signal-to-noise ratio.

  - The resolution of the sensor can be improved by limiting the A/D converter to only the maximum change in received voltage instead of the entire supply voltage range.

Future applications of the sensor include:

- **Local Curvature Calculation** – Further work can be conducted in the ability of the sensor to indentify and calculate the local curvature of a contacted object. This would eliminate the need to estimate the object curvature by using the joint position information of the manipulator which may not be completely accurate.

- **Palm Sensor Array** – The research can be further expanded to have arrays of 6-DOF sensors that can be integrated into the palm or fingertip to form a sensing skin (see Figure 7-1). The advantage is that the skin would be hard

thus preventing damage while still flexible due to the sensing structure of the sensor.

- **Underwater Sensing** – This involves using the sensor in underwater environments which are currently prohibitive for conventional force/torque sensors. Since the sensor can operate effectively in clean aqueous environments it does not need special protective coverings which reduce the performance of the sensor.

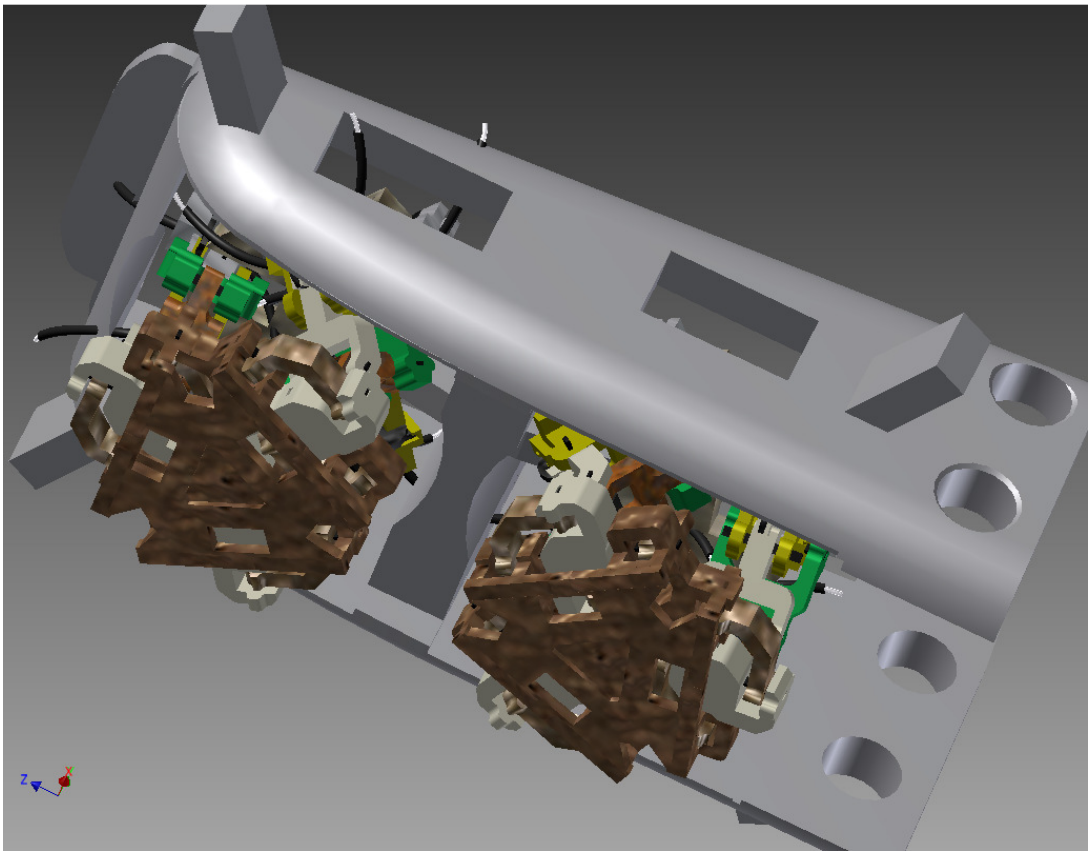

Figure 7-1. Illustration of a 2-senosr array 6-DOF sensors.

APPENDIX A – 2-DOF CAD Drawings

ALL dimensions are in mm unless otherwise stated.

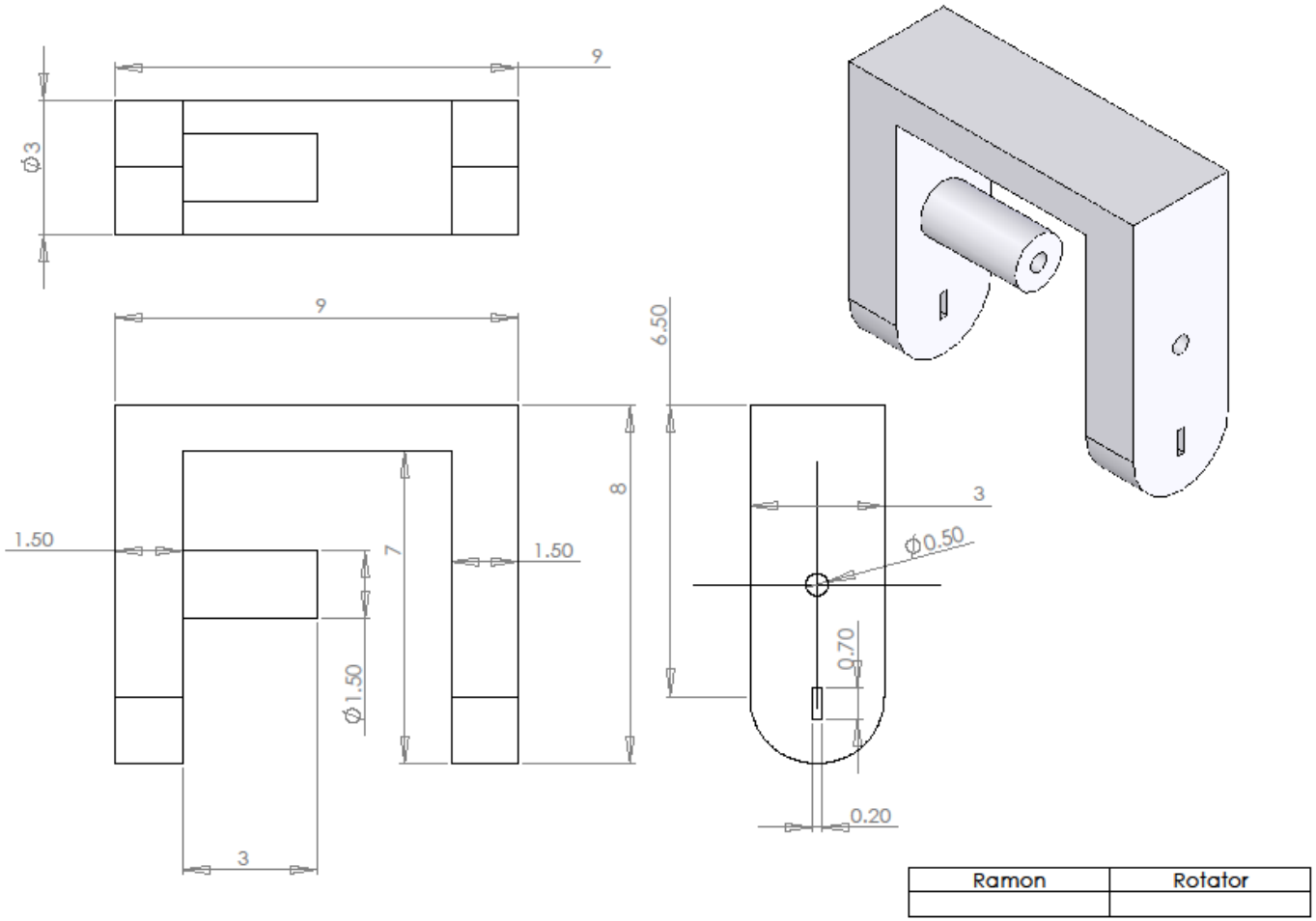

Figure A-1. CAD Drawing of the Rotator of the 2-DOF sensor.

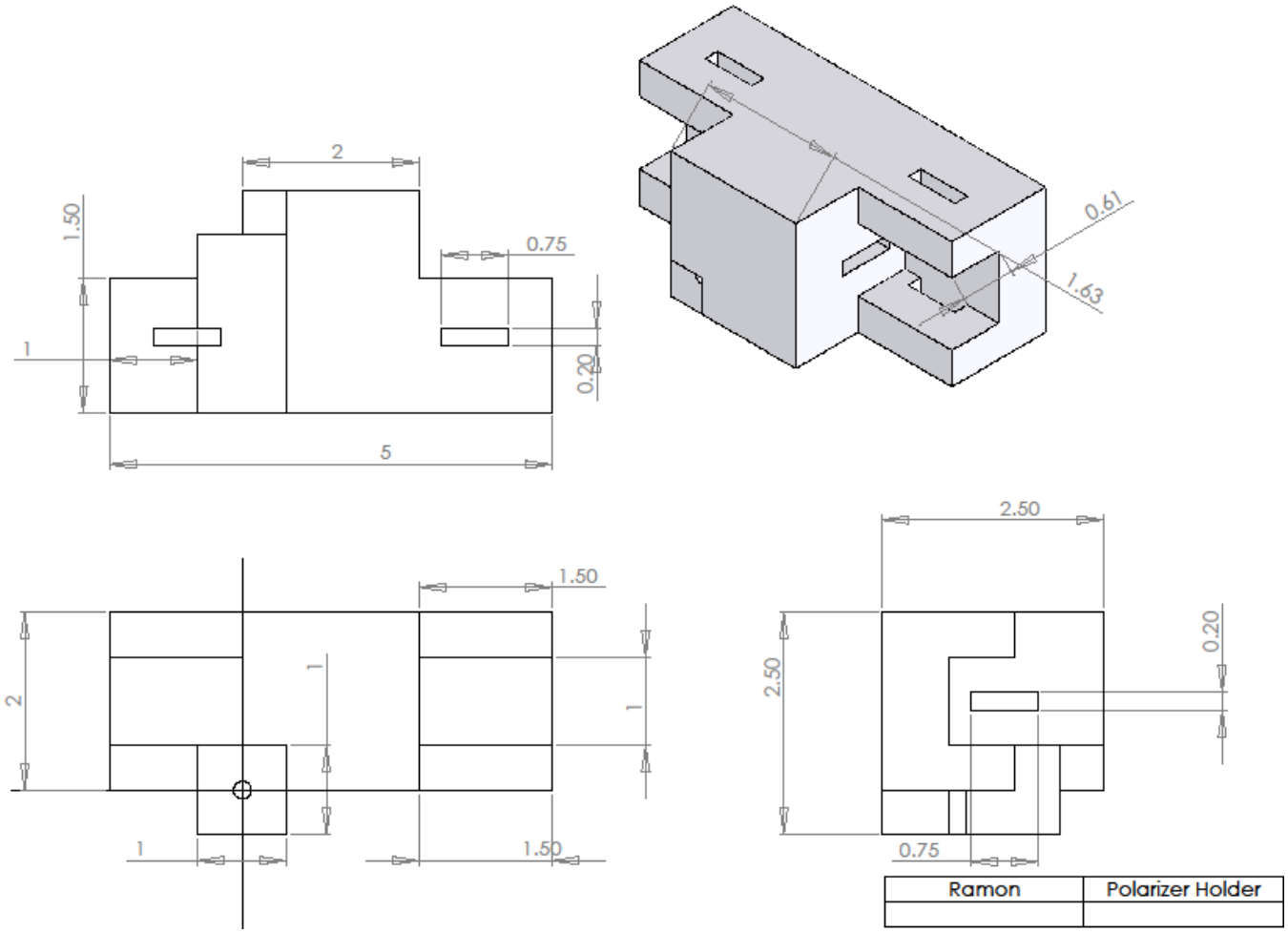

Figure A-2. CAD drawing of the Polarizer Holder of the 2-DOF sensor.

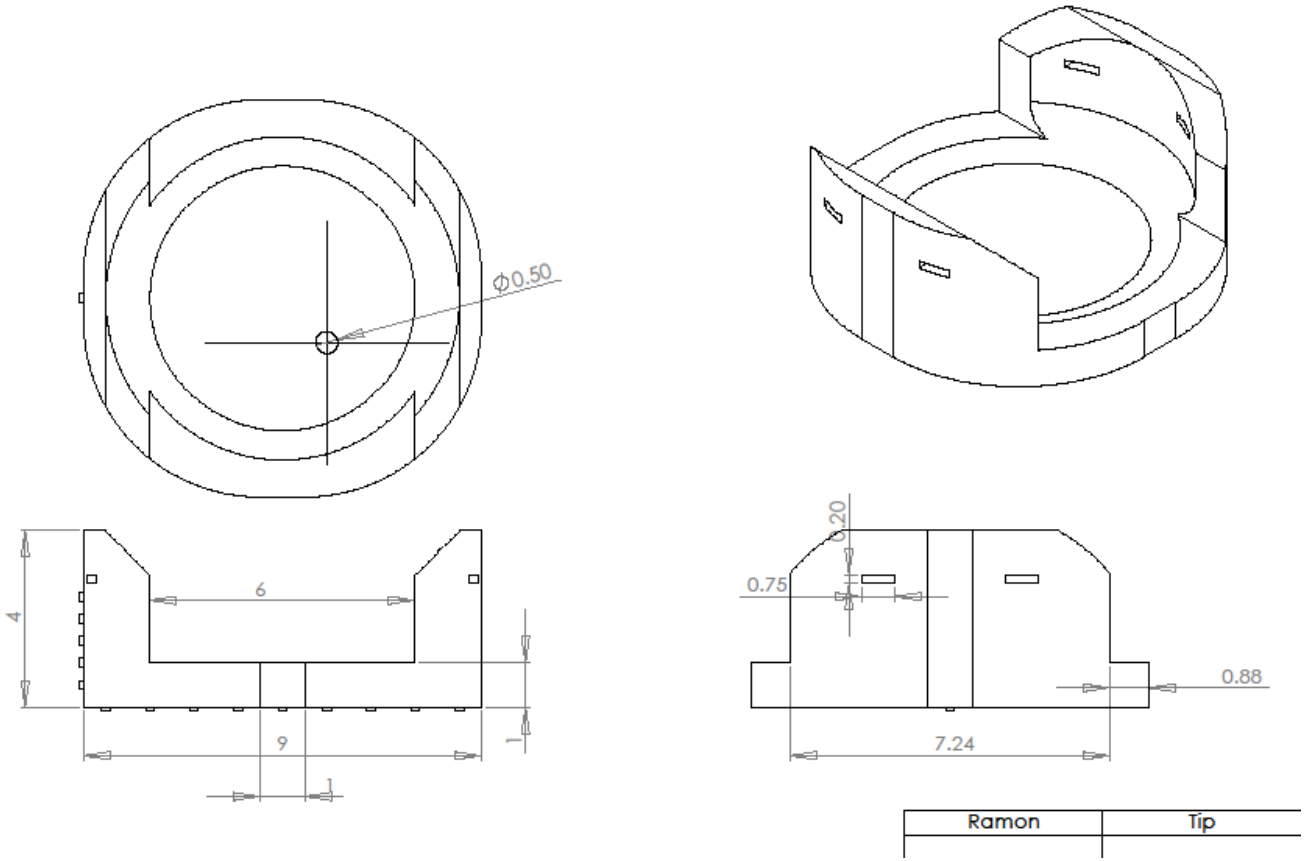

Figure A-3. CAD drawing of the Tip of the 2-DOF sensor.

APPENDIX B – 6-DOF CAD Drawings

All dimensions are in mm unless otherwise stated.

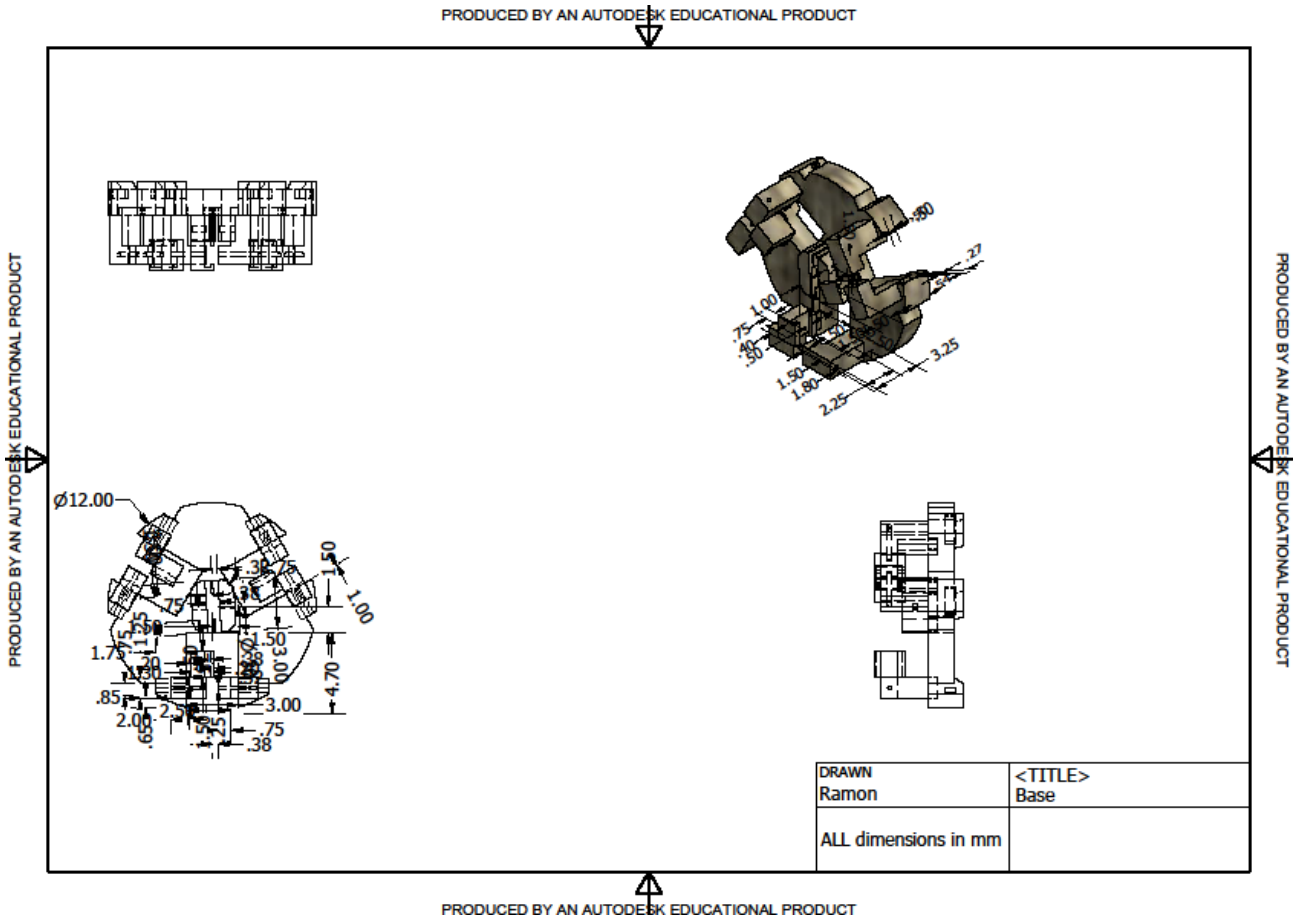

Figure B-1. CAD drawing of the Base of the 6-DOF sensor.

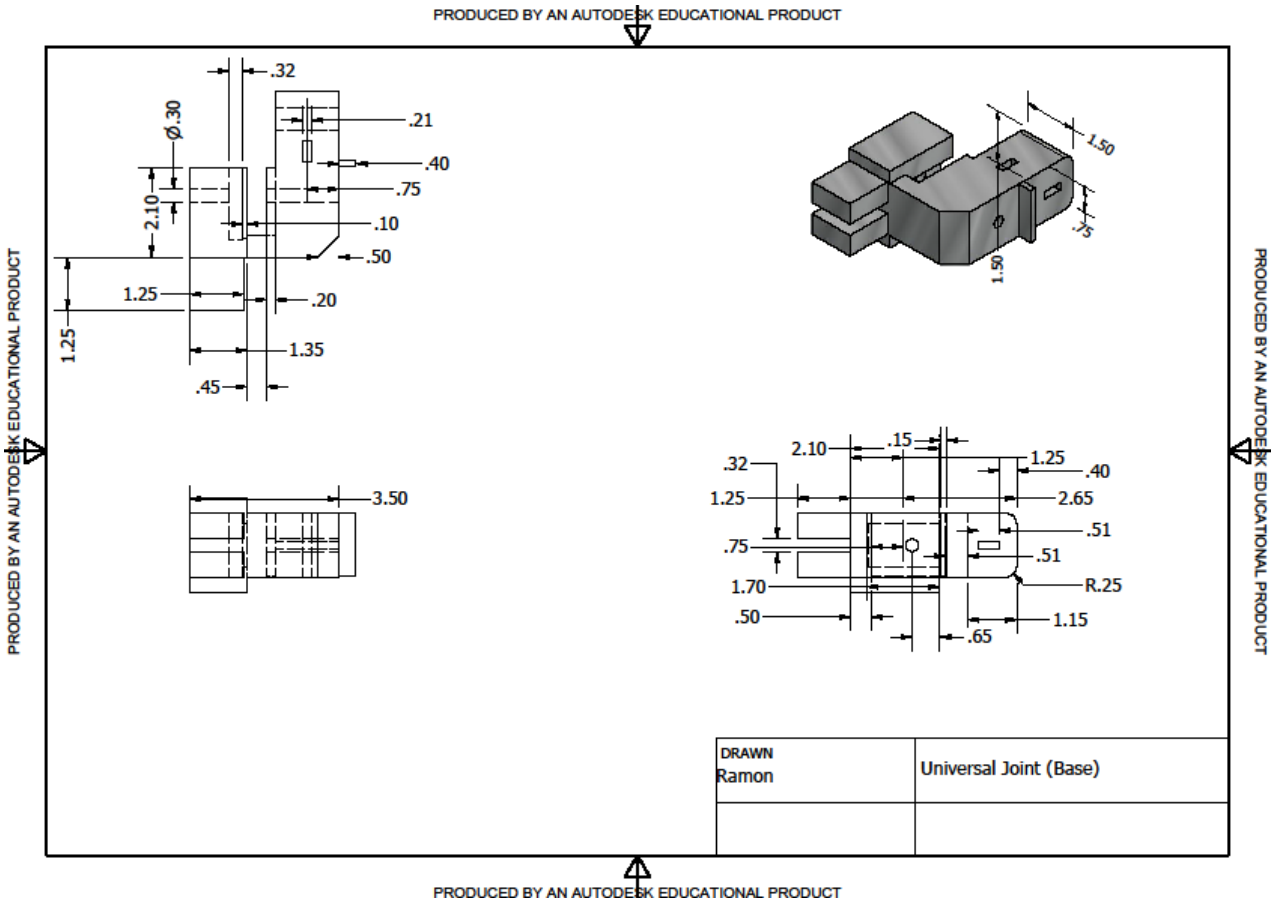

Figure B-2. CAD drawing of the Universal Joint (Base) of the 6-DOF sensor.

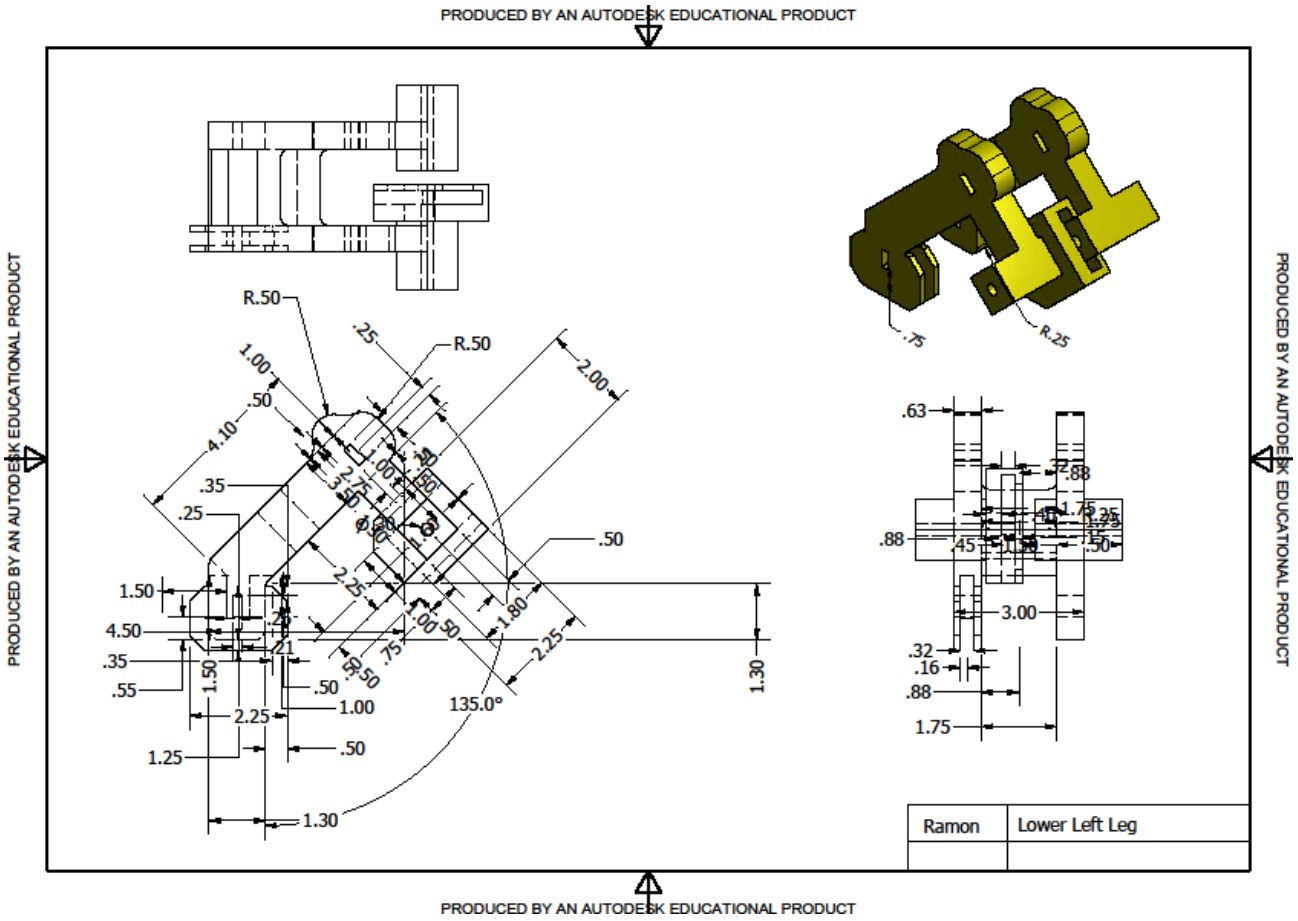

Figure B-3. CAD drawing of the Lower Left Leg of the 6-DOF sensor.

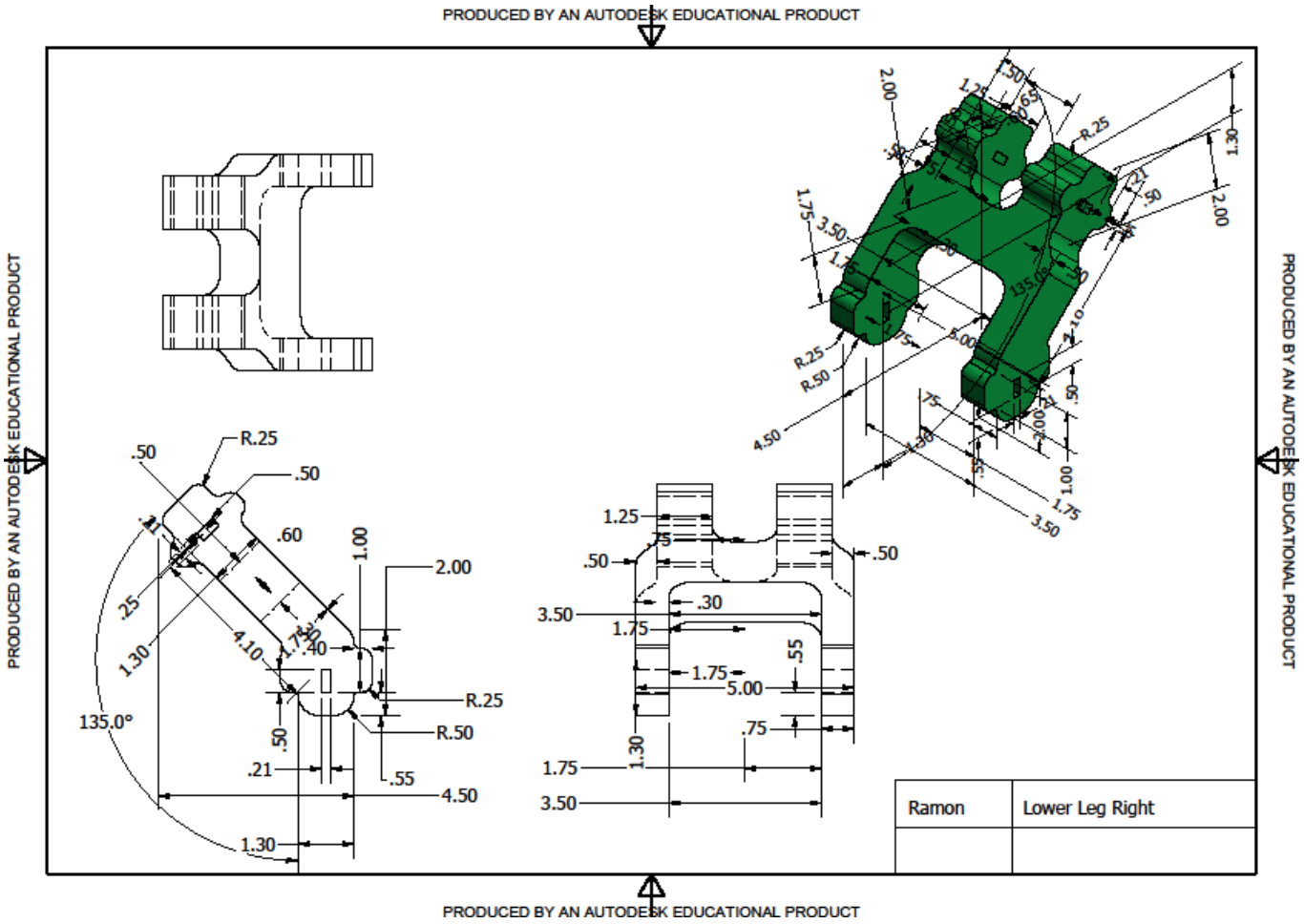

Figure B-4. CAD drawing of the Lower Right Leg of the 6-DOF sensor.

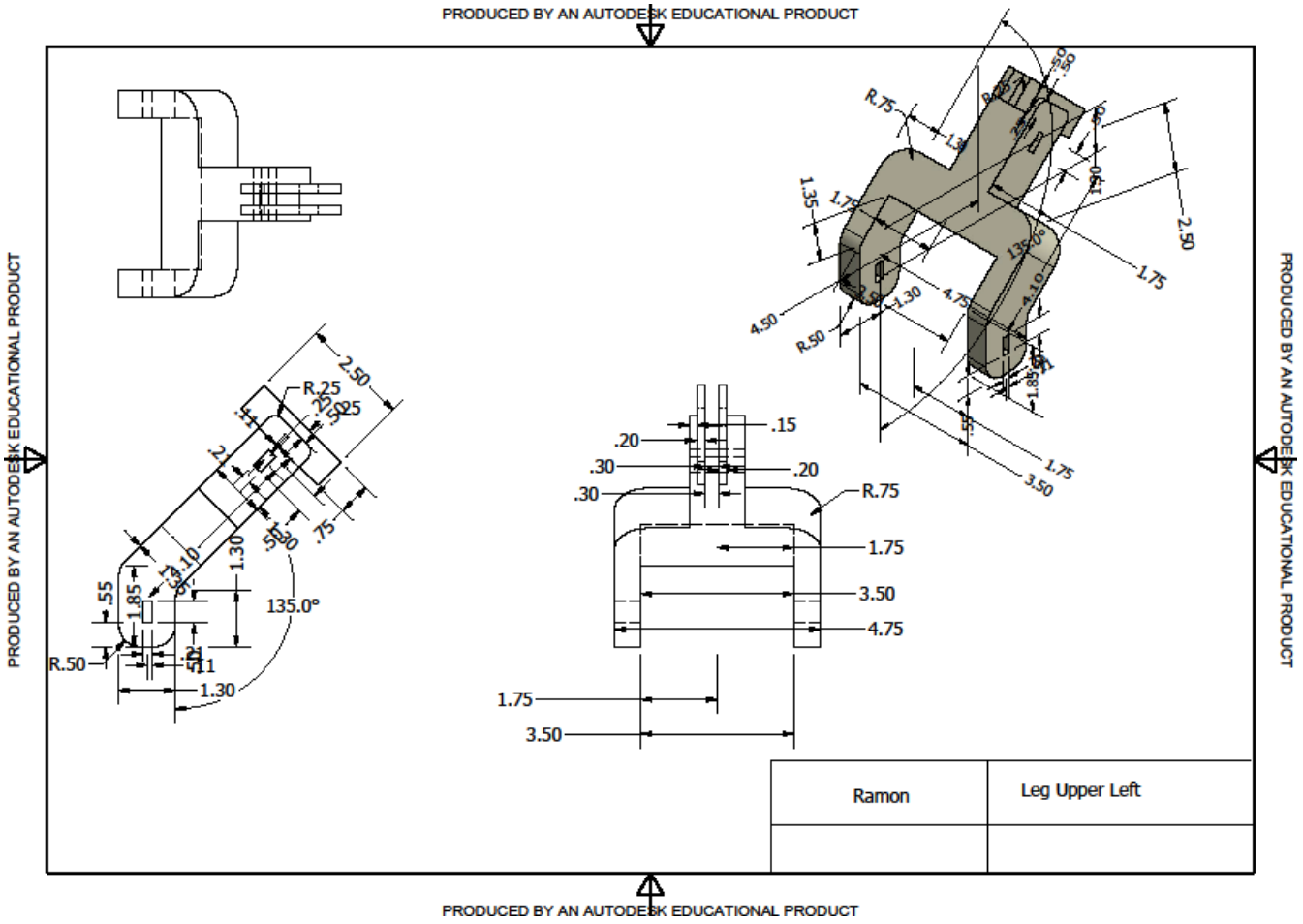

Figure B-5. CAD drawing of the Upper Left Leg of the 6-DOF sensor.

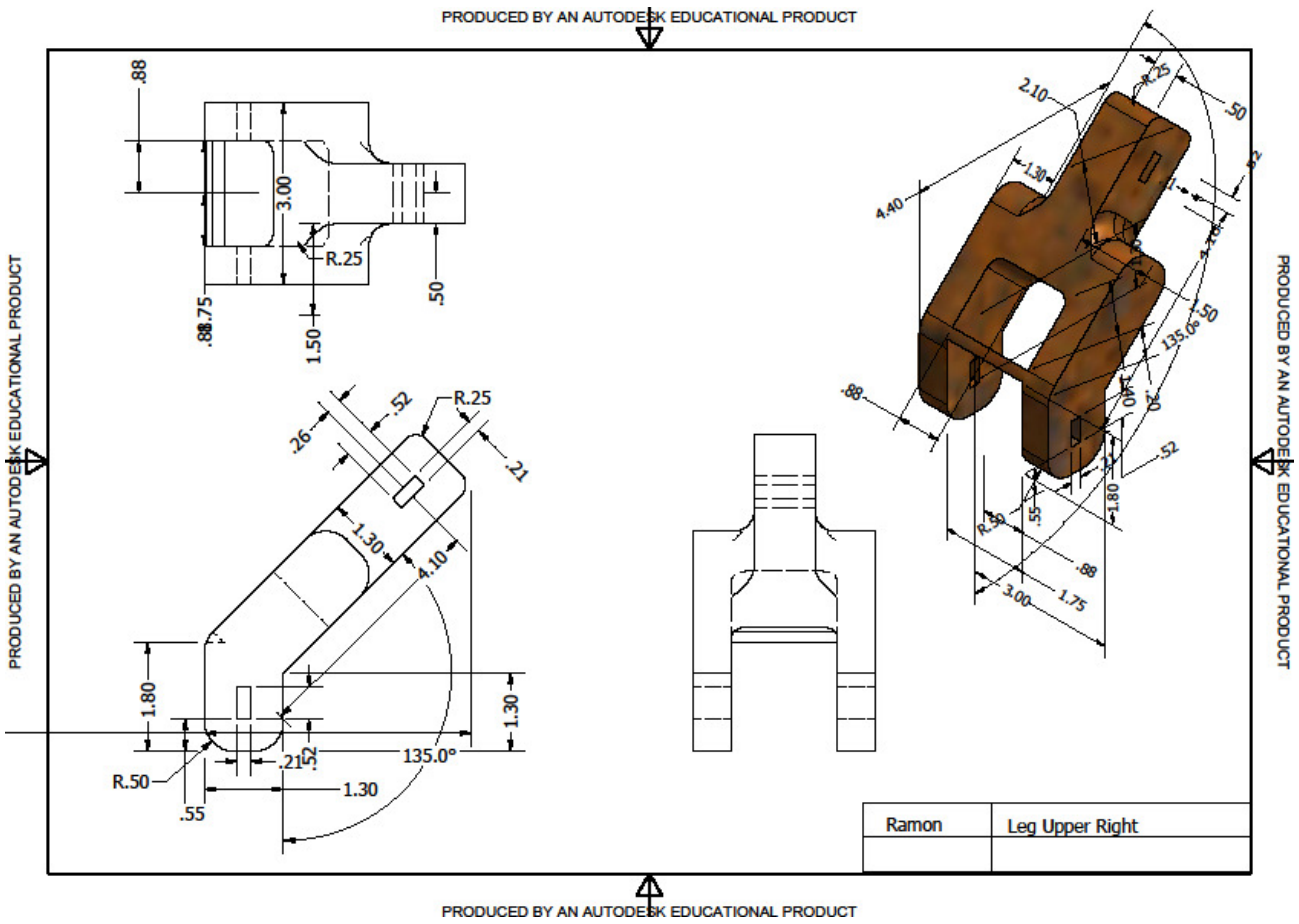

Figure B-6. CAD drawing of the Upper Right Leg of the 6-DOF sensor.

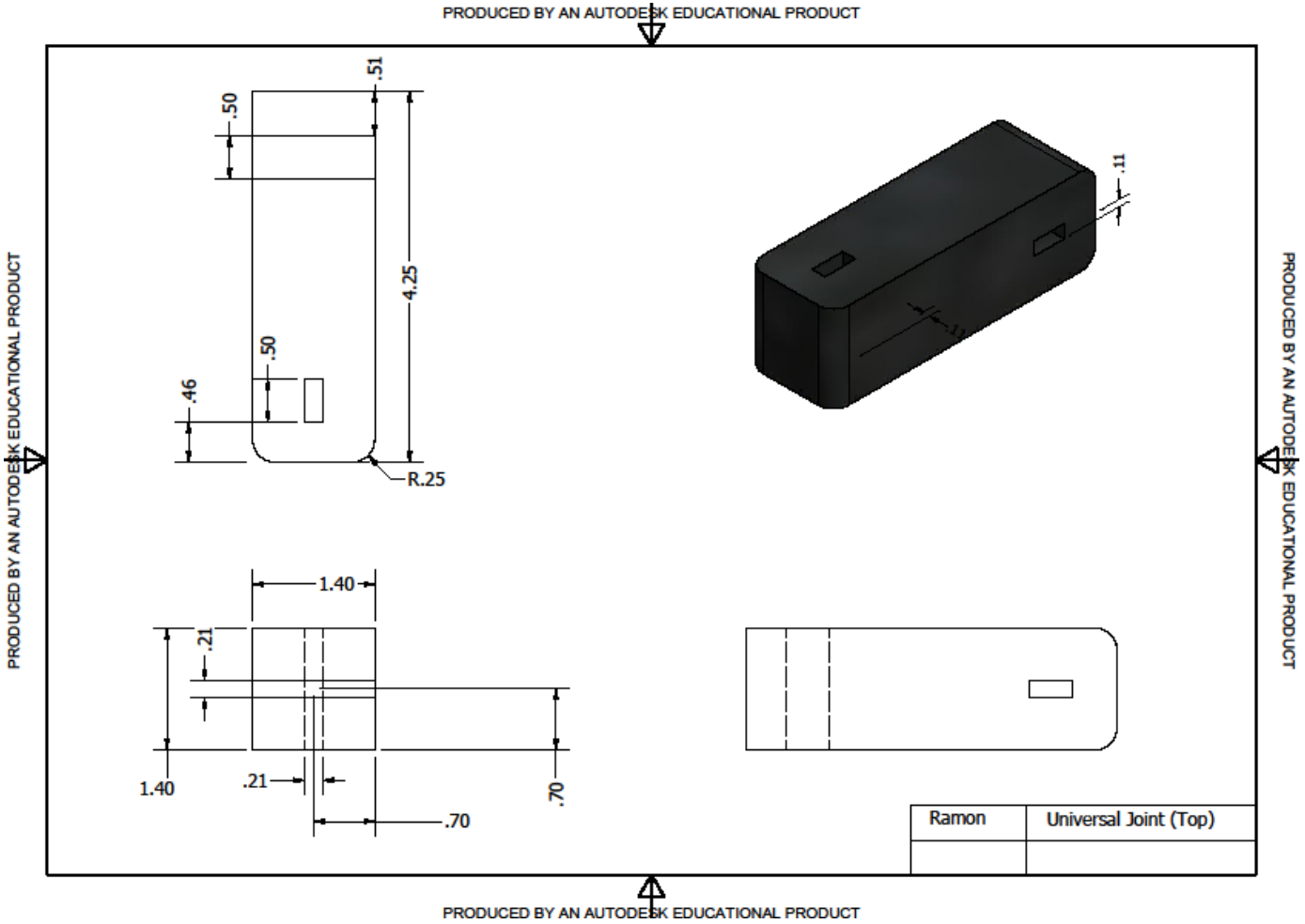

Figure B-7. CAD drawing of the Universal Joint (Top) 6-DOF sensor.

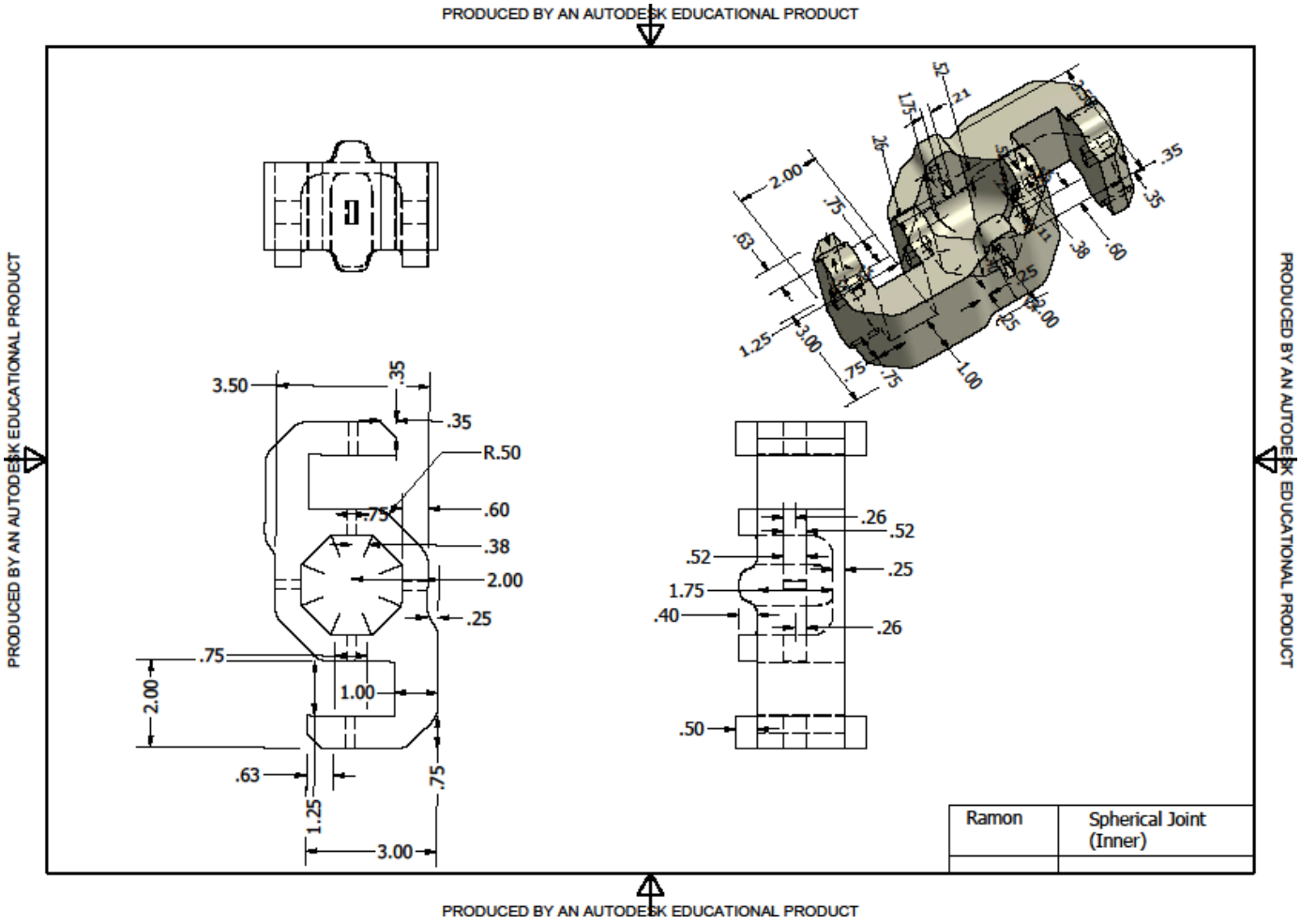

Figure B-8. CAD drawing of the Spherical Joint (Inner) 6-DOF sensor.

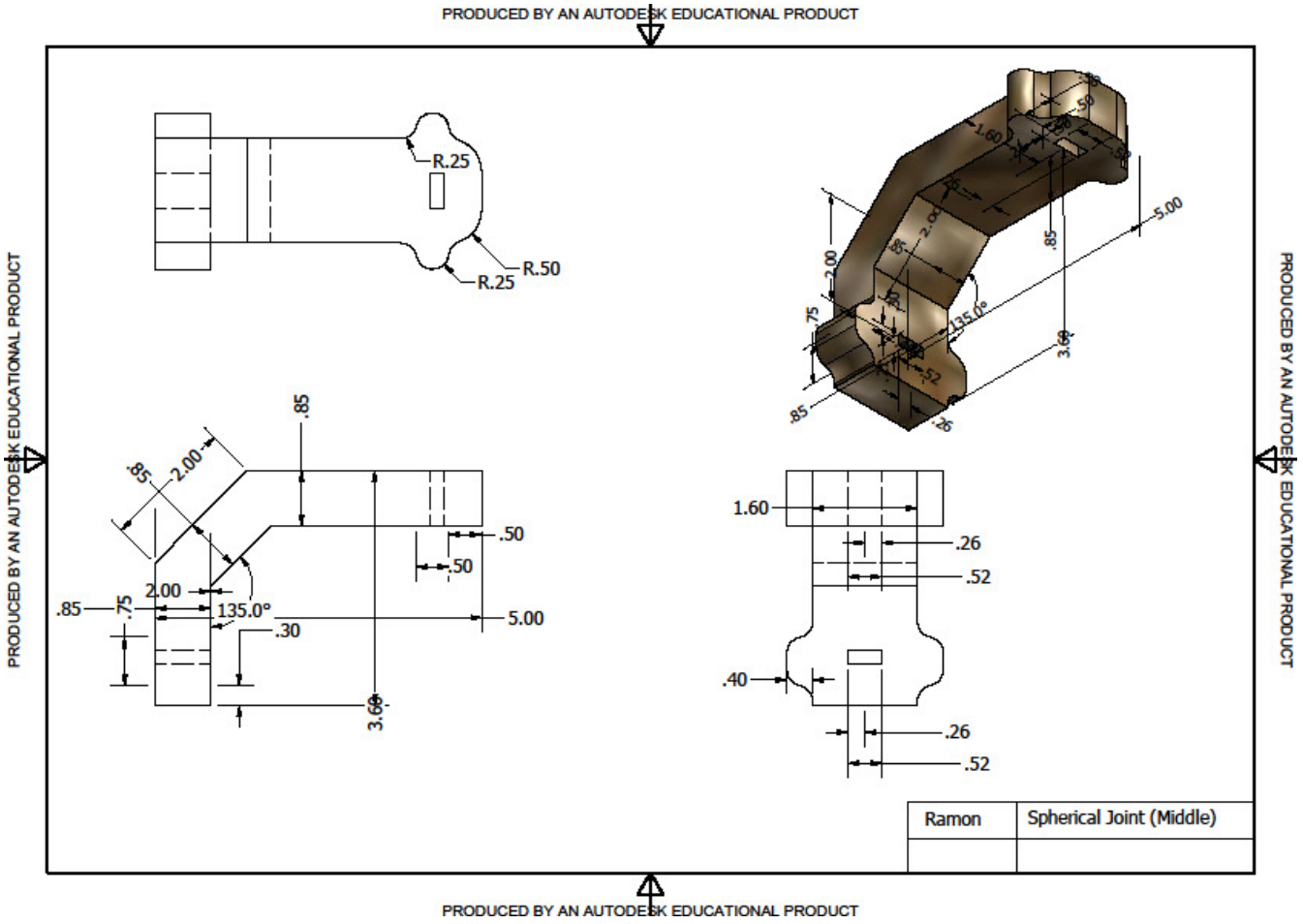

Figure B-9. CAD drawing of the Spherical Joint (Middle) 6-DOF sensor.

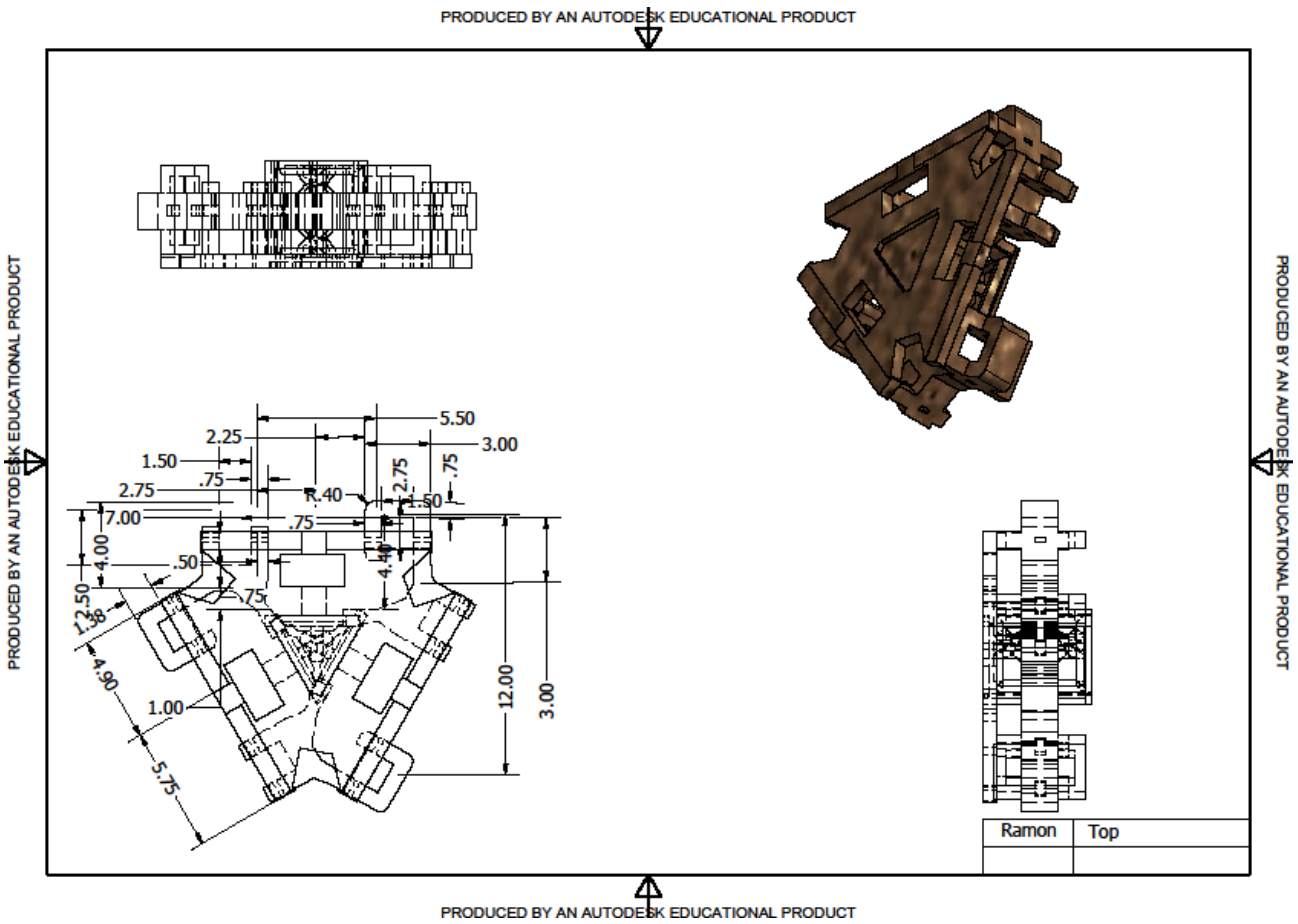

Figure B-10. CAD drawing of the Top of the 6-DOF sensor.

APPENDIX C – FANUC Calibration Code

Calibration Program

```
LBL[30000]
P[50] 100mm/sec FINE
P[51] 100mm/sec FINE
R[1] = 4                ;# of steps/cycle
R[3] = 0.25             ;linear increment
R[4] = 5                ;# of cycles
R[5] = R[4]
R[6] = 0.5              ;angular increment
;----------------------------------------- z-axis (Linear) ----------------------------------------
----
LBL[1000]
IF R[5]=0, JMP LBL[2999]
R[2] = R[1]
PR[2] = P[51]
PR[1, 1] = 0
PR[1, 2] = 0
PR[1, 3] = R[3]
PR[1, 4] = 0
PR[1, 5] = 0
PR[1, 6] = 0
LBL[1001]
IF R[2]<>0, JMP LBL[1002]
JMP LBL[1003]
LBL[1002]
R[2]=R[2]-1
PR[2]=PR[2]+PR[1]
PR[2] 100mm/sec FINE
JMP LBL[1001]

LBL[1003]
R[2]=R[1]
LBL[1004]
```

```
IF R[2]<>0, JMP LBL[1005]
JMP LBL[1006]
LBL[1005]
R[2] = R[2] – 1
PR[2] = PR[2] – PR[1]
PR[2] 100mm/sec FINE
JMP LBL[1004]

LBL[1006]
R[5] = R[5] – 1
JMP LBL[1000]
;---------------------------------------- x-axis (Linear ) ----------------------------------------
LBL[2999]
R[5] = R[4]
LBL[2000]
IF R[5]=0, JMP LBL[3999]
R[2] = R[1]
PR[2]=P[51]
PR[1, 1] = R[3]
PR[1, 2] = 0
PR[1, 3] = 0
PR[1, 4] = 0
PR[1, 5] = 0
PR[1, 6] = 0
LBL[2001]
IF R[2]<>0, JMP LBL[2002]
JMP LBL[2003]
LBL[2002]
R[2]=R[2]-1
PR[2] = PR[2] + PR[1]
PR[2] 100mm/sec FINE
JMP LBL[2001]

LBL[2003]
```

```
R[2]=R[1]
LBL[2004]
IF R[2]<>0, JMP LBL[2005]
JMP LBL[2006]
LBL[2005]
R[2] = R[2] – 1
PR[2] = PR[2] – PR[1]
PR[2] 100mm/sec FINE
JMP LBL[2004]

LBL[2006]
R[5] = R[5] – 1
JMP LBL[2000]
;---------------------------------------- y-axis (Linear) ----------------------------------
LBL[3999]
R[5] = R[4]
LBL[3000]
IF R[5]=0, JMP LBL[4999]
R[2] = R[1]
PR[2]=P[51]
PR[1, 1] = 0
PR[1, 2] = R[3]
PR[1, 3] = 0
PR[1, 4] = 0
PR[1, 5] = 0
PR[1, 6] = 0
LBL[3001]
IF R[2]<>0, JMP LBL[3002]
JMP LBL[3003]
LBL[3002]
R[2]=R[2]-1
PR[2] = PR[2] + PR[1]
PR[2] 100mm/sec FINE
JMP LBL[3001]
```

```
LBL[3003]
R[2]=R[1]
LBL[3004]
IF R[2]<>0, JMP LBL[3005]
JMP LBL[3006]
LBL[3005]
R[2] = R[2] – 1
PR[2] = PR[2] – PR[1]
PR[2] 100mm/sec FINE
JMP LBL[3004]

LBL[3006]
R[5] = R[5] – 1
JMP LBL[3000]
;---------- z-axis (Angle) ----------
LBL[4999]
R[5] = R[4]
LBL[4000]
IF R[5]=0, JMP LBL[5999]
R[2] = R[1]
PR[2]=P[51]
PR[1, 1] = 0
PR[1, 2] = 0
PR[1, 3] = 0
PR[1, 4] = 0
PR[1, 5] = 0
PR[1, 6] = R[6]
LBL[4001]
IF R[2]<>0, JMP LBL[4002]
JMP LBL[4003]
LBL[4002]
R[2]=R[2]-1
PR[2] = PR[2] + PR[1]
```

```
PR[2] 100mm/sec FINE
JMP LBL[4001]

LBL[4003]
R[2]=R[1]
LBL[4004]
IF R[2]<>0, JMP LBL[4005]
JMP LBL[4006]
LBL[4005]
R[2] = R[2] – 1
PR[2] = PR[2] – PR[1]
PR[2] 100mm/sec FINE
JMP LBL[4004]

LBL[4006]
R[5] = R[5] – 1
JMP LBL[4000]
;---------------------------------------- y-axis (Angle) ------------------------------------
LBL[5999]
R[5] = R[4]
LBL[5000]
IF R[5]=0, JMP LBL[6999]
R[2] = R[1]
PR[2]=P[51]
PR[1, 1] = 0
PR[1, 2] = 0
PR[1, 3] = 0
PR[1, 4] = 0
PR[1, 5] = R[6]
PR[1, 6] = 0
LBL[5001]
IF R[2]<>0, JMP LBL[5002]
JMP LBL[5003]
LBL[5002]
```

```
R[2]=R[2]-1
PR[2] = PR[2] + PR[1]
PR[2] 100mm/sec FINE
JMP LBL[5001]

LBL[5003]
R[2]=R[1]
LBL[5004]
IF R[2]<>0, JMP LBL[5005]
JMP LBL[5006]
LBL[5005]
R[2] = R[2] – 1
PR[2] = PR[2] – PR[1]
PR[2] 100mm/sec FINE
JMP LBL[5004]

LBL[5006]
R[5] = R[5] – 1
JMP LBL[5000]
;---------------------------------------- x-axis (Angle) ------------------------------------
LBL[6999]
R[5] = R[4]
LBL[6000]
IF R[5]=0, JMP LBL[30000]                    ;loop if at end of program
R[2] = R[1]
PR[2]=P[51]
PR[1, 1] = 0
PR[1, 2] = 0
PR[1, 3] = 0
PR[1, 4] = R[6]
PR[1, 5] = 0
PR[1, 6] = 0
LBL[6001]
IF R[2]<>0, JMP LBL[6002]
```

```
JMP LBL[6003]
LBL[6002]
R[2]=R[2]-1
PR[2] = PR[2] + PR[1]
PR[2] 100mm/sec FINE
JMP LBL[6001]

LBL[6003]
R[2]=R[1]
LBL[6004]
IF R[2]<>0, JMP LBL[6005]
JMP LBL[6006]
LBL[6005]
R[2] = R[2] – 1
PR[2] = PR[2] – PR[1]
PR[2] 100mm/sec FINE
JMP LBL[6004]

LBL[6006]
R[5] = R[5] – 1
JMP LBL[6000]
```

APPENDIX D – Electronics Schematics

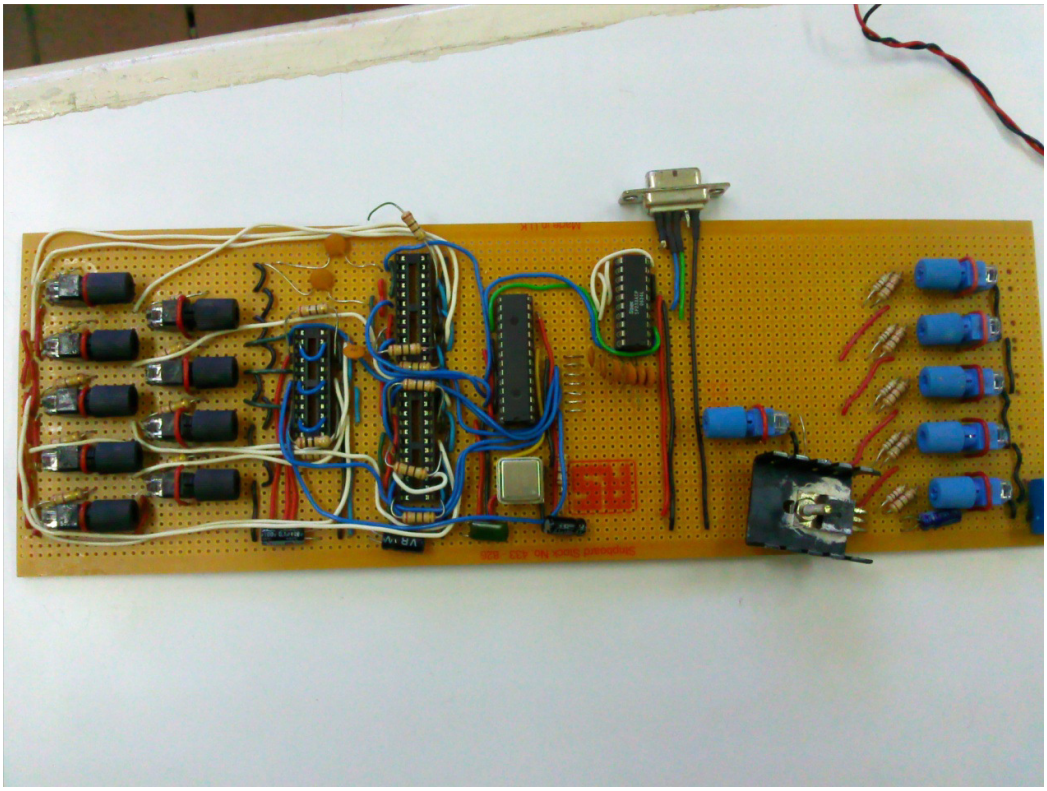

Figure D-1. Photo of the custom-made data acquisition board.

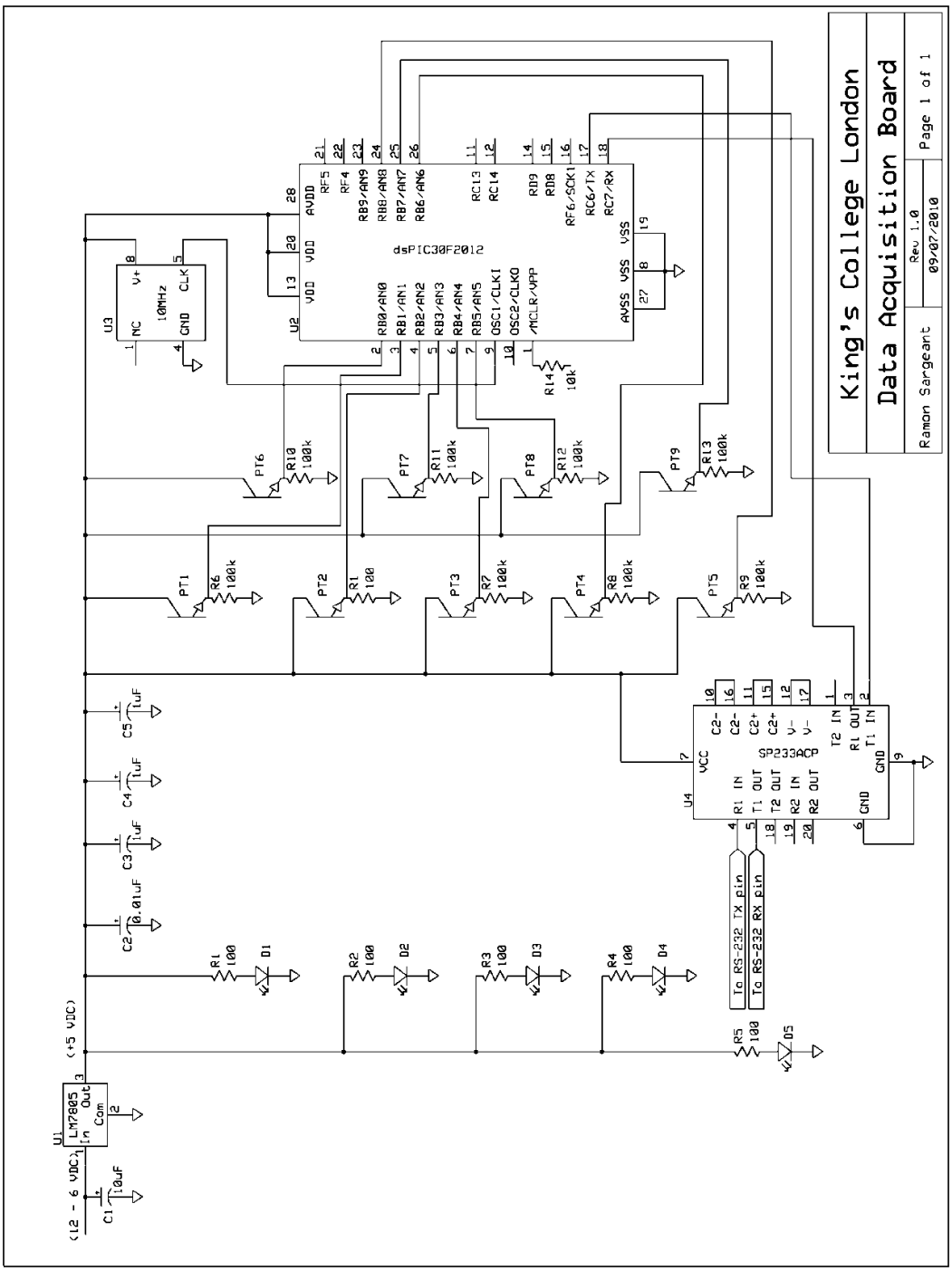

Figure D-2. Schematic diagram of the custom-made data acquisition board.

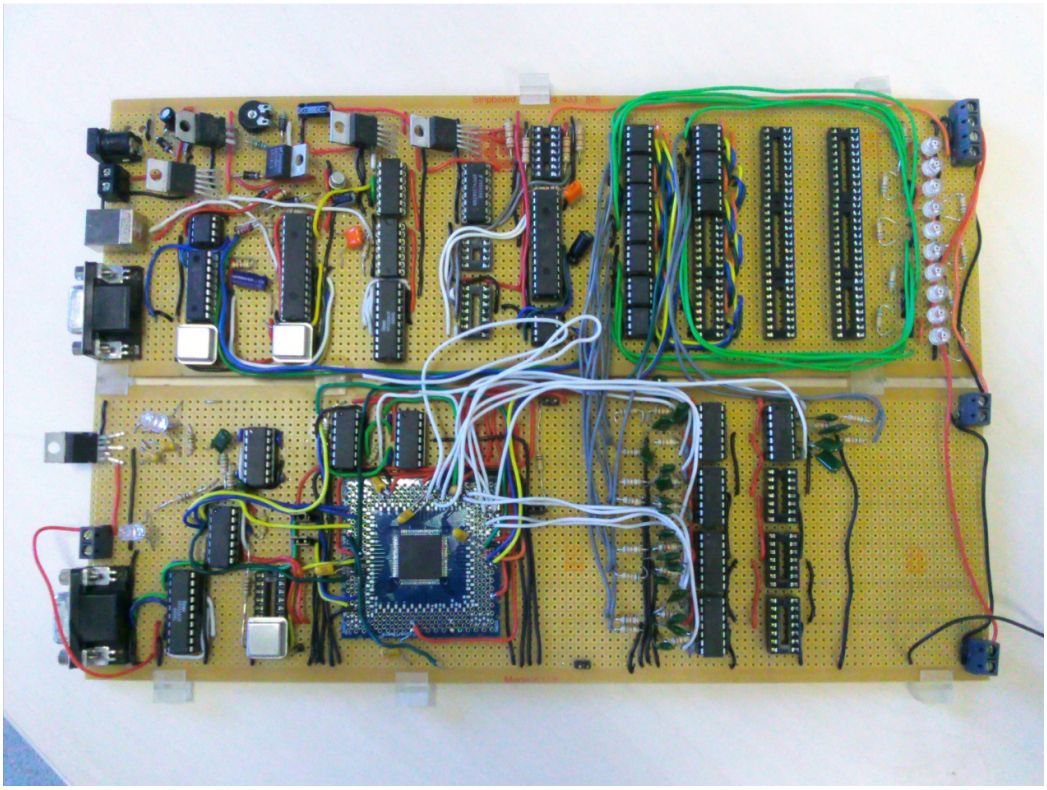

Figure D-3. Photo of the updated data acquisition board incorporating reduced drift technique.

APPENDIX E –
Mathematical Formulae

E.1 Displacement and Orientation Mathematical Model Calculation

This section presents a sample calculation of the displacement and orientation of the 6-DOF sensor. Table E.1 lists the values of the parameters used in the calculations.

Parameter	Description	Value
L_p	Length of one link of the prismatic joint	0.12 m
R_B	Radius of the base circle on which the universal joints lie	0.11 m
ψ_1	Angular position of the first leg	0 °
ψ_2	Angular position of the second leg	120 °
ψ_3	Angular position of the third leg	240 °
α_1	Rotation about the y-axis of leg 1	69 °
β_1	Rotation about the x-axis of leg 1	144 °
γ_1	Rotation about the z-axis of leg 1	47 °
α_2	Rotation about the y-axis of leg 2	80 °
β_2	Rotation about the x-axis of leg 2	34 °
γ_2	Rotation about the z-axis of leg 2	49 °
α_3	Rotation about the y-axis of leg 3	-89 °
β_3	Rotation about the x-axis of leg 3	88 °
γ_3	Rotation about the z-axis of leg 3	38 °

Table E.1. List of values used for a large scale model of the 6-DOF sensor.

The locations of the spherical joints in the local reference frame are given by equation 5-11, therefore the individual spherical locations in the universal joint frame are given by

$$\vec{E}_m = \begin{pmatrix} 2L_p \sin\gamma_m \sin\alpha_m \sin\beta_m \\ 2L_p \sin\gamma_m \cos\beta_m \\ 2L_p \sin\gamma_m \cos\alpha_m \sin\beta_m \end{pmatrix} \qquad \textbf{(E-1)}$$

Substituting the values of Table E.1 for m = 1, 2, 3 into E-1 gives

$$\vec{E}_1 = \begin{pmatrix} 2L_p \sin\gamma_1 \sin\alpha_1 \sin\beta_1 \\ 2L_p \sin\gamma_1 \cos\beta_1 \\ 2L_p \sin\gamma_1 \cos\alpha_1 \sin\beta_1 \end{pmatrix}$$

$$\Rightarrow \qquad \vec{E}_1 = \begin{pmatrix} 2\times 0.12\times \sin 47° \sin 69° \sin 144° \\ 2\times 0.12\times \sin 47° \cos 144° \\ 2\times 0.12\times \sin 47° \cos 69° \sin 144° \end{pmatrix}$$

$$\Rightarrow \qquad \vec{E}_1 = -0.096\hat{i} - 0.142\,\hat{j} + 0.037\hat{k} \quad \text{(m)} \qquad \text{(E-2)}$$

For the second leg

$$\vec{E}_2 = \begin{pmatrix} 2L_p \sin\gamma_2 \sin\alpha_2 \sin\beta_2 \\ 2L_p \sin\gamma_2 \cos\beta_2 \\ 2L_p \sin\gamma_2 \cos\alpha_2 \sin\beta_2 \end{pmatrix}$$

$$\Rightarrow \qquad \vec{E}_2 = \begin{pmatrix} 2\times 0.12\times \sin 49° \sin 80° \sin 34° \\ 2\times 0.12\times \sin 49° \cos 34° \\ 2\times 0.12\times \sin 49° \cos 80° \sin 34° \end{pmatrix}$$

$$\Rightarrow \qquad \vec{E}_2 = -0.1\hat{i} + 0.15\,\hat{j} + 0.018\hat{k} \quad \text{(m)} \qquad \text{(E-3)}$$

For the third leg

$$\vec{E}_3 = \begin{pmatrix} 2L_p \sin\gamma_3 \sin\alpha_3 \sin\beta_3 \\ 2L_p \sin\gamma_3 \cos\beta_3 \\ 2L_p \sin\gamma_3 \cos\alpha_3 \sin\beta_3 \end{pmatrix}$$

$$\Rightarrow \qquad \vec{E}_1 = \begin{pmatrix} 2\times 0.12\times \sin 38°\sin -89°\sin 88° \\ 2\times 0.12\times \sin 38°\cos 88° \\ 2\times 0.12\times \sin 38°\cos -89°\sin 88° \end{pmatrix}$$

$$\Rightarrow \qquad \vec{E}_1 = 0.148\hat{i} + 0.005\,\hat{j} + 0.003\hat{k} \text{ (m)} \qquad \text{(E-4)}$$

The locations of the spherical joints in the global frame are given by equations 5-20 to 5-22. Substituting the values of Table E.1 in these equations give

For the first leg

$$P_1 = \begin{pmatrix} 2L_p \sin\gamma_1 \sin\beta_1 + R_B \\ 2L_p \sin\gamma_1 \cos\beta_1 \\ 2L_p \sin\gamma_1 \cos\alpha_1 \sin\beta_1 \end{pmatrix}$$

$$\Rightarrow \qquad \vec{P}_1 = \begin{pmatrix} 2\times 0.12\times \sin 47^\circ \times \sin 144^\circ + 0.055 \\ 2\times 0.12\times \sin 47^\circ \times \cos 144^\circ \\ 2\times 0.12\times \sin 47^\circ \times \cos 69^\circ \times \sin 144^\circ \end{pmatrix}$$

$$\Rightarrow \qquad \vec{P}_1 = -0.041\hat{i} - 0.142\,\hat{j} + 0.037\hat{k} \qquad \text{(m)} \qquad \textbf{(E-5)}$$

For the second leg

$$P_2 = \begin{pmatrix} -L_p \sin\gamma_2 \left(\sin\alpha_2 \sin\beta_2 + \sqrt{3}\cos\beta_2\right) - \dfrac{R_B}{2} \\ L_p \sin\gamma_2 \left(\sqrt{3}\sin\alpha_2 \sin\beta_2 - \cos\beta_2\right) + \dfrac{\sqrt{3}R_B}{2} \\ 2L_p \sin\gamma_2 \cos\alpha_2 \sin\beta_2 \end{pmatrix}$$

$$\Rightarrow \qquad \vec{P}_2 = \begin{pmatrix} -0.12\times \sin 49°\times \left(\sin 80°\sin 34° + \sqrt{3}\cos 34°\right) - \dfrac{0.055}{2} \\ 0.12\sin 49°\left(\sqrt{3}\sin 80°\sin 34° - \cos 34°\right) + \dfrac{\sqrt{3}\times 0.055}{2} \\ 2\times 0.12\sin 49°\cos 80°\sin 34° \end{pmatrix}$$

$$\Rightarrow \qquad \vec{P}_2 = -0.108\hat{i} - 0.114\,\hat{j} + 0.0181\hat{k} \qquad \text{(m)} \qquad \textbf{(E-6)}$$

and for the third leg

$$P_3 = \begin{pmatrix} L_p \sin\gamma_3\left(-\sin\alpha_3 \sin\beta_3 + \sqrt{3}\cos\beta_3\right) - \dfrac{R_B}{2} \\ -L_p \sin\gamma_3\left(\sqrt{3}\sin\alpha_3 \sin\beta + \cos\beta_3\right) - \dfrac{\sqrt{3}R_B}{2} \\ 2L_p \sin\gamma_3 \cos\alpha_3 \sin\beta_3 \end{pmatrix}$$

$$\Rightarrow \quad \vec{P}_3 = \begin{pmatrix} 0.12\sin 38°\left(-\sin(-3°) + \sqrt{3}\cos(-3°)\sin 5°\right) - \dfrac{0.055}{2} \\ -0.12\sin 38°\left(\sqrt{3}\sin(-3°) + \cos(-3°)\sin 5°\right) - \dfrac{\sqrt{3}\times 0.055}{2} \\ 2\times 0.12\sin 38°\cos(-3°)\cos 5° \end{pmatrix}$$

$$\Rightarrow \qquad \vec{P}_3 = -0.012\hat{i} - 0.047\,\hat{j} + 0.147\hat{k} \quad \text{(m)} \qquad \textbf{(E-7)}$$

From equation 5-19 the normal vector to the plane is given by

$$\vec{n} = \left(\vec{P}_2 - \vec{P}_1\right) \times \left(\vec{P}_3 - \vec{P}_1\right)$$

Let the vector $\vec{a}$ be given by

$$\vec{a} = \vec{P}_2 - \vec{P}_1 . \qquad \textbf{(E-8)}$$

Substituting E-1 and E-2 into E-4 gives

$$\Rightarrow \qquad \vec{a} = \begin{pmatrix} -0.108 \\ -0.114 \\ 0.018 \end{pmatrix} - \begin{pmatrix} -0.041 \\ -0.142 \\ 0.037 \end{pmatrix}$$

$$\Rightarrow \qquad \vec{a} = -0.066\hat{i} + 0.028\,\hat{j} - 0.019\hat{k} \quad \text{(m)}$$

and the vector $\vec{b}$ is given by

$$\vec{b} = \vec{P}_3 - \vec{P}_1 \qquad \textbf{(E-9)}$$

Substituting E-1 and E-3 into E-5 gives

$$\vec{b} = \begin{pmatrix} -0.097 \\ -0.178 \\ 0.003 \end{pmatrix} - \begin{pmatrix} -0.041 \\ -0.142 \\ 0.037 \end{pmatrix}$$

$$\Rightarrow \qquad b = -0.056\hat{i} - 0.036\,\hat{j} - 0.034\hat{k} \quad \text{(m)} \qquad \textbf{(E-10)}$$

The normal vector is then given by

$$\vec{n} = \vec{a} \times \vec{b}$$

$$\Rightarrow \qquad \vec{n} = \begin{vmatrix} \hat{i} & \hat{j} & \hat{k} \\ -0.066 & 0.028 & -0.019 \\ -0.056 & -0.036 & -0.034 \end{vmatrix}$$

$$\Rightarrow \qquad \vec{n} = -0.001668\hat{i} - 0.001206\,\hat{j} - 0.003958\hat{k} \qquad \textbf{(E-11)}$$

The bisector line for vector $\vec{a}$ is given by

$$\vec{L}_1 = \vec{a} \times \vec{n}$$

$$\Rightarrow \qquad \vec{L}_1 = \begin{vmatrix} \hat{i} & \hat{j} & \hat{k} \\ -0.066 & 0.028 & -0.019 \\ -0.001668 & -0.001206 & 0.003958 \end{vmatrix}$$

$$\Rightarrow \qquad \vec{L}_1 = 0.000088\hat{i} + 0.000295\,\hat{j} + 0.000127\hat{k} \quad \text{(m)} \qquad \textbf{(E-12)}$$

and the bisector line for vector $\vec{b}$ is given by

$$\vec{L}_2 = \vec{b} \times \vec{n}$$

$$\Rightarrow \qquad \vec{L}_2 = \begin{vmatrix} \hat{i} & \hat{j} & \hat{k} \\ -0.056 & -0.036 & -0.034 \\ -0.001668 & -0.001206 & -0.003958 \end{vmatrix}$$

$$\Rightarrow \qquad \vec{L}_2 = -0.000184\hat{i} + 0.000277\hat{j} + 0.000007\hat{k} \text{ (m)} \qquad \textbf{(E-13)}$$

The midpoint of vector $\vec{a}$ is given by

$$\vec{L}_{M1} = \frac{\vec{P}_2 + \vec{P}_1}{2}$$

$$\Rightarrow \qquad \vec{L}_{M1} = -0.074\hat{i} - 0.128\hat{j} + 0.027\hat{k} \text{ (m)} \qquad \textbf{(E-14)}$$

and the midpoint of vector $\vec{b}$ is given by

$$\vec{L}_{M2} = \frac{\vec{P}_3 + \vec{P}_1}{2}$$

$$\Rightarrow \qquad \vec{L}_{M2} = -0.069\hat{i} - 0.16\hat{j} + 0.02\hat{k} \text{ (m)} \qquad \textbf{(E-15)}$$

From equations 5-28 and 5-29 the position of the centre of the contact plate $\vec{r}_c$ can be expressed as

$$\vec{r}_c = \vec{L}_{M1} + \vec{L}_1 t \qquad \textbf{(E-16)}$$

or

$$\vec{r}_c = \vec{L}_{M2} + \vec{L}_2 k \,. \qquad \textbf{(E-17)}$$

Equating E-12 and E-13 for the x- and y-axes and simplifying gives

$$\begin{pmatrix} L_{2x} & -L_{1x} \\ L_{2y} & -L_{1y} \end{pmatrix} \begin{pmatrix} k \\ t \end{pmatrix} = \begin{pmatrix} L_{M1x} - L_{M2x} \\ L_{M1y} - L_{M2y} \end{pmatrix}$$

Substituting values and solving gives

$$\Rightarrow \quad \begin{pmatrix} -0.000184 & -0.000088 \\ 0.000277 & -0.000295 \end{pmatrix} \begin{pmatrix} k \\ t \end{pmatrix} = \begin{pmatrix} -0.075 + 0.069 \\ -0.128 + 0.16 \end{pmatrix}$$

$$\Rightarrow \quad k = 56.2 \qquad \textbf{(E-18)}$$

and

$$t = -56.1 \qquad \textbf{(E-19)}$$

Also, equating E-12 and E-13 for the x- and z-axes and simplifying gives

$$\begin{pmatrix} L_{2x} & -L_{1x} \\ L_{2z} & -L_{1z} \end{pmatrix} \begin{pmatrix} k \\ t \end{pmatrix} = \begin{pmatrix} L_{M1x} - L_{M2x} \\ L_{M1z} - L_{M2z} \end{pmatrix}.$$

Substituting values and solving gives

$$\begin{pmatrix} -0.000184 & -0.000088 \\ 0.000679 & -0.000127 \end{pmatrix} \begin{pmatrix} k \\ t \end{pmatrix} = \begin{pmatrix} -0.075 + 0.069 \\ 0.027 - 0.02 \end{pmatrix}$$

$$\Rightarrow \quad k = 56.2$$

and

$$t = -56.1$$

Substituting the value of ***t*** into E-12 and solving for the components gives

$$r_{cx} = -0.074 + 0.000088 \times -56.1$$

$$\Rightarrow \quad r_{cx} = -0.08 \text{ (m)} \qquad \textbf{(E-20)}$$

$$r_{cy} = -0.128 + 0.000295 \times -56.1$$

$$\Rightarrow \quad r_{cy} = -0.144 \text{ (m)} \qquad \textbf{(E-21)}$$

$$r_{cz} = 0.027 + 0.000679 \times -56.1$$

$$\Rightarrow \qquad r_{cz} = 0.02 \text{ (m)} \qquad \textbf{(E-22)}$$

The orientation of the contact plate is given by

$$\phi = \left(\cos^{-1} \frac{n_{cx}}{\sqrt{{n_{cx}}^2 + {n_{cy}}^2 + {n_{cz}}^2}} \right) - 90° \qquad \textbf{(E-23)}$$

$$\delta = \left(\cos^{-1} \frac{n_{cy}}{\sqrt{{n_{cx}}^2 + {n_{cy}}^2 + {n_{cz}}^2}} \right) - 90° \qquad \textbf{(E-24)}$$

$$\psi = \left(\cos^{-1} \frac{n_{cz}}{\sqrt{{n_{cx}}^2 + {n_{cy}}^2 + {n_{cz}}^2}} \right). \qquad \textbf{(E-25)}$$

Substituting values and solving

$$\Rightarrow \qquad \phi = \left(\cos^{-1} \frac{-0.001668}{\sqrt{0.001668^2 + 0.001206^2 + 0.003958^2}} \right) - 90°$$

$$\phi = 22° \qquad \textbf{(E-26)}$$

$$\delta = \left(\cos^{-1} \frac{-0.003428}{\sqrt{0.001668^2 + 0.001206^2 + 0.003958^2}} \right) - 90°$$

$$\delta = 16° \qquad \textbf{(E-27)}$$

$$\psi = \left(\cos^{-1} \frac{0.003958}{\sqrt{0.001668^2 + 0.001206^2 + 0.003958^2}} \right)$$

$$\psi = -63° \qquad \textbf{(E-28)}$$

APPENDIX F – MATLAB Code

F.1 Calibration Code for the 2-DOF Force Sensor

```
clc
clear all

%------------------- General Parameters ----------------------

lambda = 0.00066;   %wavelength of red light
d = 0.00025;        %Fibre diameter
Msquared = 73;      %Beam qaulity
w0 = 0.21*(d/2);    %Initial beam waist
R = 4700000;        %Resistor value
Sk = 0.6;           %Relative Spectral Sensitivity

v = 0.33;             %poisson's ratio
E = 5500000000;       %Young's Modulus
G = E/(2*(1+v));      %Shear Modulus

%====================== Linear Displacement ==================
%--------- Linear Displacement Physical Parameters -----------

L1 = 0.008;
a1 = 0.004;
b1 = 0.0007;
h1 = 0.0002;

Ixx1 = (b1.*(h1.^3))./12;
Flin = -3:0.1:3;
DeltaX1 = (Flin.*(a1.^3).*(L1 -
a1).^2)./(3.*E.*Ixx1.*(((2.*a1)+L1).^2));
```

```
%-------------- Light Intensity Model Parameters -------------

I0 = 600;
zmax = 0.015;
Kp = 7.4;

z = 0.002 + DeltaX1;
s1 = 1 + power(((z*lambda*Msquared)./((w0.^2)*pi)),0.5);
wz = w0*sqrt(s1);
subplot(2, 2, 1); plot(z, wz);

r1 = d/2;
w2 = I0.*((w0./wz).^2).*exp((-2.*(r1.^2))./(wz.^2));

Pz = (0.5*pi*I0.*(w0.^2))*(1-exp((-2.*(r1.^2))./(wz.^2)));

Vr = R*Sk*Kp*Pz;
subplot(2, 2, 2); plot(z, Vr);
subplot(2, 2, 3); plot(Flin, Vr);
```

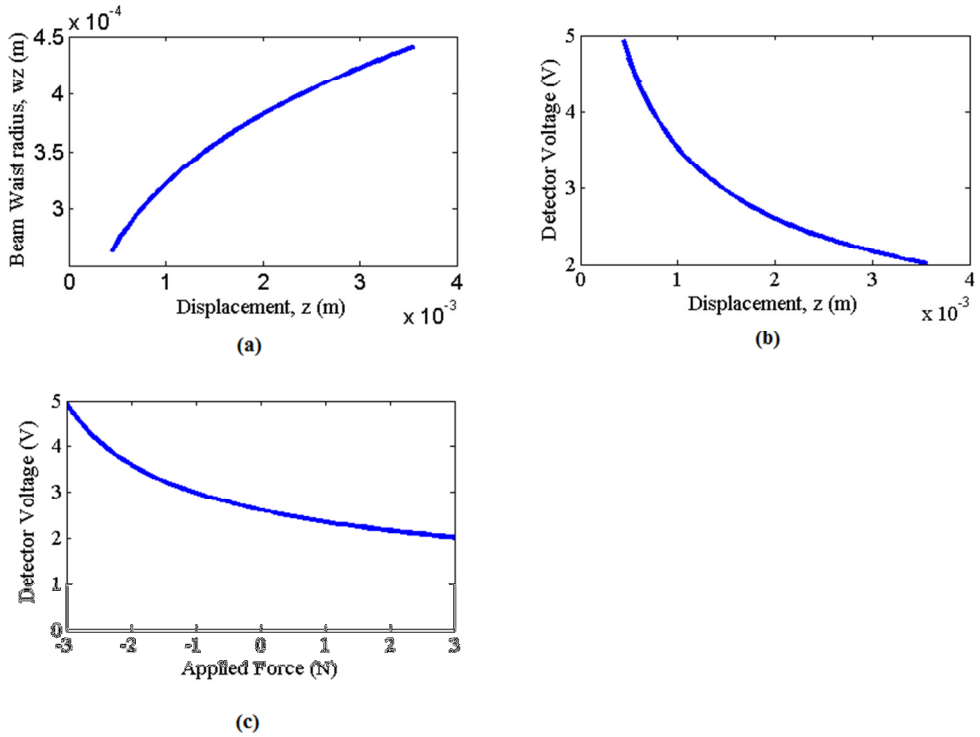

Figure F-1. Calibration model of the force component of the 2-DOF sensor. (a) The graph of the beam waist, w_z as a function of propagation distance, z. (b) The graph of the detector voltage, V_R as a function of propagation distance, z. (c) The graph of the detector voltage as a function of applied force.

F.2 Calibration Code for the 2-DOF Torque Sensor

```
%================= Rotational Displacement ==================

L2 = 0.00065;    %
b2 = 0.0005;     %
h2 = 0.0002;     %strip thickness

v = 0.33;        %poisson's ratio
E = 5500000000;  %Young's Modulus
G = E/(2*(1+v)); %Shear Modulus

thetarad = 0:pi/360:pi/2;
rper = 0.0001:(0.008-0.0001)/180:0.008;

J2 = h2.*(b2.^3).*((1./3)-(((0.21.*b2)./h2).*(1-
((b2.^4))./(12.*(h2.^4)))));

T = (-2.*J2.*G.*thetarad)./L2;
%subplot(2, 2, 1); plot(thetarad, T);

z2 = 0.005;
s2 = 1 + power(((z2*lambda*Msquared)./((w0.^2)*pi)),0.5);
wz2 = w0*sqrt(s2);
Ppol = (0.21.*0.5.*pi.*I0.*(w0.^2).*((cos(thetarad)).^2)*(1-
exp((-2.*(r1.^2))./(wz2.^2))));
%subplot(2, 2, 2); plot(thetarad, Ppol);

Vr2 = R*Sk*Kp*Ppol;
plot(T, Vr2);
```

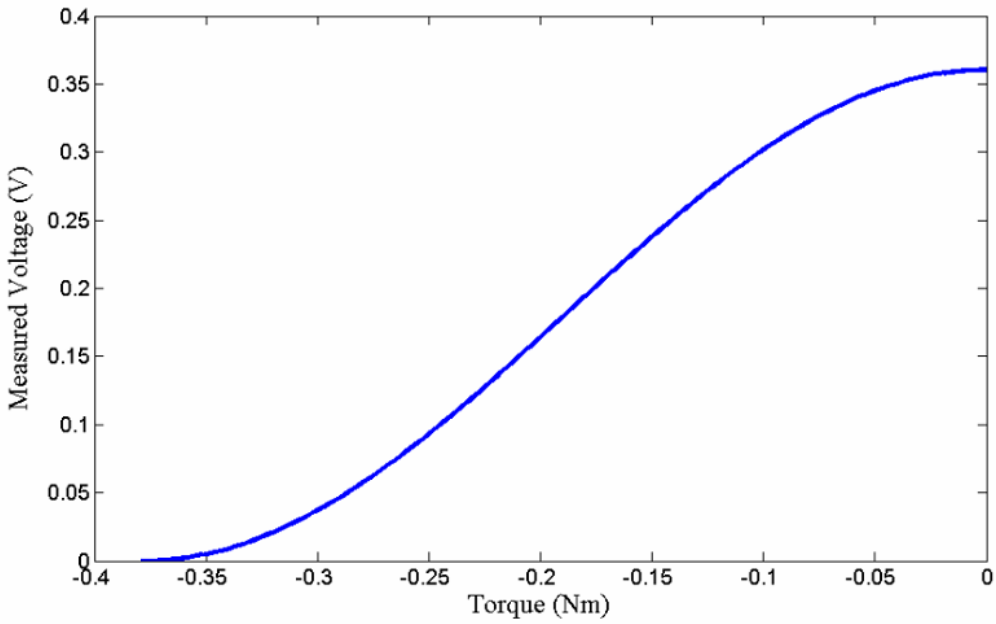

Figure F-2. Graph of the simulated photodetector voltage as a function of input torque during calibration.

REFERENCES

[1] European Robotics Research Network (2002). EURON Research Roadmaps. [Online]. Available: http://www.euron.org/activities/moreroadmap.

[2] Computing Community Consortium (2009). A Roadmap for US Robotics: From Internet to Robotics. [Online]. Available: http://www.us-robotics.us/

[3] National Aeronautics and Space Administration (2010). Draft Robotics, Tele-Robotics and Autonomous Systems Roadmap: Technology Area 04. [Online]. Available: http://www.nasa.gov/pdf/501622main_TA04-Robotics-DRAFT-Nov2010-A.pdf.

[4] H. Iwata and S. Sugano, "Design of Anthropomorphic Dexterous Hand with Passive Joints and Sensitive Soft Skins," in *2009 IEEE/SICE Int. Symp. On Syst. Integration*, Tokyo, Japan, 2009, pp. 129-134.

[5] T. Sugaima, G. Fujii, H. Iwata and S. Sugano, "A Methodology for Setting Grasping Force for Picking up an Object with Unknown Weight, Friction and Stiffness," in *2010 IEEE/RAS Int. Conf. on Humanoid Robots*, Nasville, TN, USA, December 6-8, 2010, pp. 288-293.

[6] T. Sugaiwa, H. Iwata and S. Sugano, "A Motion Control for Dexterous Manipulation with Human Mimetic Hand-Arm System," in *9th IEEE-RAS Int. Conf. on Humanoid Robots*, Paris, France, December 7-10, 2009, pp. 653-659.

[7] T. Sugaiwa, H. Iwata and S. Sugano, "Hand-Arm Coordinated Manipulation Using Active Body-Environment Contact," *SICE J. Control, Measurement and System Integration*, vol. 2, no. 6, pp. 348-356, Nov. 2009.

[8] T. Sugaiwa, M. Nezumiya, H. Iwata and S. Sugano, "Motion-planning Method with Active Body-Environment Contact for a Hand-Arm System including Passive Joints," in *2010 IEEE/RSJ Int. Conf. Intell. Robot. Syst. (IROS)*, Taipei, Taiwan, October 18-22, 2010, pp. 69-74.

[9] B. B. Edin, L. Ascari, L. Beccai, S. Roccella, J. J. Cabibihan and M. C. Carrozza, "Bio-inspired Sensorization of a Biomechatronic Robot Hand for the Grasp-and-lift Task," in *Brain Research Bulletin*, no. 75, pp. 785-795, 2008.

[10] L. Ascari, U. Bertocchi, P. Corradi, C. Laschi and P. Dario, "Bio-inspired Grasp Control in a Robotic Hand with Massive Sensorial Input," *Biol. Cybern*, vol. 100, no. 2, pp. 109-128, Feb. 2009.

[11] N. Thayer and S. Priya, "Design and Implementation of a Dexterous Anthropomorphic Robotic Typing (DART) Hand," *Smart Mater. Struct.*, no. 20, pp. 1-12, Feb. 2011.

[12] R. R. Ma and A. M. Dollar, "On Dexterity and Dexterous Manipulation," in *15th Int. Conf. on Advanced Robotics*, Tallinn, Estonia, June 20-23, 2011, pp. 1-7.

[13] G. Vassura and A. Bicchi, "Whole-Hand Manipulation: Design of an Articulated Hand Exploiting All Its Parts to Increase Dexterity," *NATO ASI Series*, vol. 102, no. 2, pp. 165-177, 1993. [Online]. Available: http://dx.doi.org/10.1007/978-3-642-58069-7_10.

[14] A. M. Okamura, N. Smaby and M. R. Cutkosky, "An Overview of Dexterous Manipulation," in *Proc. IEEE Int. Conf. Robotics and Automation (ICRA)*, San Francisco, CA, Apr. 24-28, 2000, pp. 255-262.

[15] A. Bicchi and V. Kumar, "Robotic Grasping and Contact: A Review," in *Proc. IEEE Int. Conf. Robotics and Automation (ICRA)*, San Francisco, CA, Apr. 24-28, 2000, pp. 348-353.

[16] E. S. H. Hou and N. Sucahyo, "Multi-sensor System for an Articulated Robotic Hand," in *16th Annu. Conf. IEEE Ind. Electron. Soc.*, Pacific Grove, CA, Nov. 27-30, 1990, pp. 627-630.

[17] L. Biagiotti, F. Lotti, C. Melchiorri and G. Vassura, "How Far is the Human Hand?: A Review on Anthropomorphic Robotic End-effectors," [Online]. Available: http://citeseerx.ist.psu.edu/viewdoc/summary?doi=10.1.1.104.7899.

[18] F. F. Khalil and P. Payeur, "Dexterous Robotic Manipulation of Deformable Objects with Multi-Sensory Feedback – A Review," *InTech*. [Online]. Available from: http://www.intechopen.com/books/robot-manipulators-trends-and-development/dexterous-robotic-manipulation-of-deformable-objects-with-multi-sensory-feedback-a-review.

[19] H. Kawasaki, T. Komatsu and K. Uchiyama, "Dexterous Anthropomorphic Robot Hand with Distributed Tactile Sensor: Gifu Hand II," *IEEE/ASME Trans. Mechatron.*, vol. 7, no. 3, pp. 296-303, Sept. 2002.

[20] H. Kawasaki, T. Mouri, J. Takai and S. Ito, "Grasping of Unknown Object Imitating Human Grasping Reflex," in *15th Triennial World Congress of the International Federation of Automatic Control*, Barcelona, Spain, Jul. 21-26, 2002, pp. 1-6.

[21] R. A. Hilhorst and K. Tanie, "Dexterous Manipulation of Objects with Unknown Parameters by Robot Hands," in *Proc. IEEE Int. Conf. Robotics and Automation (ICRA)*, San Diego, CA, May 8-13, 1994, pp. 3098-4003.

[22] R. D. Howe, "Tactile Sensing and Control," *Advanced Robotics*, vol. 8, no. 3, pp. 245-261, 1994.

[23] K. Murakami and T. Hasegawa, "Tactile Measurement of Local Contact Geometry Using Soft Fingertip with Force/Torque Sensor," in *IEEE Int. Conf. Intell. Robots and Syst. (IROS)*, Beijing, China, Oct. 9-15, 2006, pp. 1939-1945.

[24] S. Haidacher, J. Butterfass, M. Fischer, M. Grebenstein, K. Joehl, K. Kunze, M. Nickl, N. Seitz and G. Hirzinger, "DLR Hand II. Hard- and Software Architecture for Information Processing," in *Proc. IEEE Int. Conf. on Robotics and Automation (ICRA)*, Taipei, Taiwan, Sept. 14-19, 2003, pp. 684-689.

[25] Z. Xue, J. M. Zollner and R. Dillmann, "Dexterous Manipulation Planning of Objects with Surface of Revolution," in *IEEE Int. Conf. Intell. Robots and Syst.*, Nice, France, Sept. 22-26, 2008, pp. 2703-2708.

[26] H. P. Saal, J. Tang and S. Vijayakumar, "Active Estimation of Object Dynamics Parameters with Tactile Sensors," in *IEEE/RSJ Int. Conf. Intell. Robots Syst. (IROS)*, Taipei, Taiwan, Oct. 18-22, 2010, pp. 916-921.

[27] C. Melchiorri and G. Vassura, "Implementation of Whole-hand Manipulation Capability in the UB Hand System Design," *Advanced Robotics*, vol. 9, no. 5, pp. 547-560, 1995.

[28] A. Bicchi, "Hands for Dexterous Manipulation and Robust Grasping: A Difficult Road Toward Simplicity," *IEEE Trans. Robot. Autom.*, vol. 16, no. 6, pp.625-662, 2000.

[29] Z. Yu and J. Gu, "A Survey on Real-time Controlled Multi-fingered Robotic Hand," *Canadian Conf. Elect. Comput. Eng.*, Niagara Falls, ON, May 4-7, 2008, pp. 975-980.

[30] T. Matsuoka, T. Hasegawa and K. Honda, "A Dexterous Manipulation System with Error Detection and Recovery by a Multi-fingered Robotic Hand," in *Proc. IEEE/RSJ Int. Conf. Intell. Robots Syst. (IROS)*, Kyongju, South Korea, Oct. 17-21, 1999, pp. 418-423.

[31] C. M. Seguna and M. A Saliba, "The Mechanical and Control System Design of a Dexterous Robotic Gripper," *IEEE Int. Conf. Electron. Circuits Syst.*, Sept. 2-5, 2001, pp. 1195-1201.

[32] M. R. Dogar and S. S. Srinivasa, "Push-Grasping with Dexterous Hands: Mechanics and a Method," in *IEEE/RSJ Int. Conf. Intell. Robots Syst. (IROS)*, Taipei, Taiwan, Oct. 18-22, 2010, pp. 2123-2130.

[33] I. Ebert-Uphoff and P. A. Voglewede, "On the Connections Between Cable-Driven Robots, Parallel Manipulators and Grasping," in *Proc. IEEE Int. Conf. Robotics and Automation (ICRA)*, New Orleans, LA, Apr. 26-May 1, 2004, pp. 4521-4526.

[34] G. F. Liu, J. J. Xu and Z. X. Li, "Automatic Real-time Grasping Force Determination for Multifingered Manipulation: Theory and Experiments," in *Proc. IEEE/RSJ Int. Conf. Intell. Robots Syst. (IROS)*, Lausanne, Switzerland, Oct., 2002, pp. 1675-1680.

[35] J. Saut, A. Sahbani and V. Perdereau, "A Global Approach for Dexterous Manipulation Planning Using Paths in n-fingers Grasp Subspace," in *9th Int. Conf. Control, Automation, Robotics and Vision*, Singapore, Dec. 5-8, 2006, pp. 1- 6.

[36] F. F. Khalil and P. Payeur, "Robotic Interaction with Deformable Objects under Vision and Tactile Guidance – A Review," in *IEEE Int. Workshop*

on Robotic and Sensors Environments, Ottawa, Canada, Oct. 12-13, 2007, pp. 1-6.

[37] T. Inoue, D. Takizawa and S. Hirai, "Modelless and Grasping-forceless Control by Robotic Fingers Capable of Mechanically Coupled Movement," in *IEEE/RSJ Int. Conf. on Intell. Robots Syst. (IROS)*, Taipei, Taiwan, Oct. 18-22, 2010, pp. 5875-5879.

[38] A. M. Okamura and M. R. Cutkosky, "Haptic Exploration of Fine Surface Features," in *Proc. IEEE Int. Conf. on Robotics and Automation (ICRA)*, Detroit, Michigan, May 10-15, 1999, pp. 2930-2936.

[39] K. Murakami and T. Hasegawa, "New Tactile Sensing by Robotic Fingertip with Soft Skin," in *Proc. IEEE Sensors*, vol. 2, pp. 824-827, 2004.

[40] T. Inoue and S. Hirai, "Parallel-distributed Model of Soft Fingertips in Three-dimensional Grasping and Manipulation," in *Proc. IEEE Int. Conf. Robotics and Biomimetics*, Bangkok, Thailand, Feb. 21-26, 2008, pp. 895-902.

[41] Y. Li and I. Kao, "A Review of Modeling of Soft-Contact Fingers and Stiffness Control for Dexterous Manipulation in Robotics," in *Proc. IEEE Int. Conf. on Robotics and Automation (ICRA)*, Seoul, Korea, May 21-26, 2001, pp. 3055-3060.

[42] S. L. Canfield, "Development of the Carpal Wrist: A Symmetric, Parallel-Architecture Robotic Wrist," PhD Dissertation, Dept. Mech. Eng., VirginiaTech, Blacksburg, Virginia, 1997. [Online]. Available: http://scholar.lib.vt.edu/theses/available/etd-24129959711591/

[43] T. Matsuno, K. Kanada, F. Arai, H. Matsuura and T. Fukuda, "Strategy of Picking Up Thin Plate by Robot Hand Using Deformation of Soft

Fingertip," in *Proc. IEEE Int. Conf. Robotics and Automation (ICRA)*, Barcelona, Spain, Apr. 18-22, 2005, pp. 2326-2331.

[44] H. Han and S. Kawamura, "Analysis of Stiffness of Human Fingertip and Comparison with Artificial Fingers," in *IEEE Int. Conf. Systems, Man and Cybernetics*, Tokyo, Japan, Oct. 12-15, 1999, pp. 800-805.

[45] T. Cui, J. Xiao and A. Song, "Simulation of Grasping Deformable Objects with a Virtual Human Hand," in *Proc. IEEE/RSJ Int. Conf. Intell. Robot. Syst. (IROS)*, Nice, France, Sept. 22-26, 2008, pp. 3965-3970.

[46] N. Takahashi, M. Tada, J. Ueda, Y. Matsumoto and T. Ogasawara, "An Optical 6-axis Force Sensor for Brain Function Analysis using fMRI," *IEEE Sensors*, vol. 1, pp. 253-258, 2003.

[47] D. Chapuis, R. Gassert, L. Sache, E. Burdet and H. Bleuler, "Design of a Simple MRI/fMRI Compatible Force/Torque Sensor," in *Proc. IEEE/RSJ Int. Conf. Intell. Robot Syst. (IROS)*, Sendai, Japan, Sept. 28-Oct. 2, 2004, pp. 2593-2599.

[48] T. Tokuno, M. Tada and K. Umeda, "High-Precision MRI-Compatible Force Sensor with Parallel Plate Structure," in *Proc. IEEE/RSJ-EMBS Int. Conf. Biomed. Robot. Biomechatronics*, Scottsdale, AZ, Oct. 19-22, 2008, pp. 33-38.

[49] P. Renaud and M. Mathelin, "Kinematic Analysis for a Novel Design of MRI-compatible Torque Sensor," in *IEEE/RSJ Int. Conf. Intell. Robot Syst.*, St. Louis, USA, Oct. 11-15, 2009, pp. 2640-2646.

===== (Chapter 2) ======

----- Section 2.1 -----

[50] SCHUNK GmbH & Co. KG. (2008). Service Robotics. [Online]. Available: http://www.robotnik.es/ilsupload/robotnik_manos_dextroushand_en.pdf.

[51] SCHUNK GmbH & Co. KG. (2008). http://www.schunk-modular-robotics.com/fileadmin/user_upload/service_robotic/products/actuators/robotic_hands/SDH_GB.pdf.

[52] SCHUNK GmbH & Co. KG. (2012). *Robotics Hands SDH*. [Online]. Available: http://www.schunk-modular-robotics.com/left-navigation/service-robotics/components/actuators/robotic-hands/sdh.html.

----- Section 2.2.1 -----

[53] Leane Net. (2004, October 19). How Strain Gauges Work. [Online]. Available: http://www.leanenet.it/download/howsgw.pdf.

[54] C. Melchiorri, "Slip Detection and Control Using Tactile and Force Sensors," *IEEE Trans. Mechatron.*, vol. 5, no. 3, pp. 235-243, Sept. 2000.

[55] J. G. da Silva, A. A. De Carvalho and D. D. Da Silva, "A Strain Gauge Tactile Sensor for Finger-Mounted Applications," *IEEE Trans. Instrum. Meas.*, vol. 51, no. 1. pp. 18-22, Feb. 2002.

[56] Y. C. Kim, Y. S. Ihn, H. R. Choi, S. M. Lee and J. C. Koo, "Implentation of Force Sensor with Multi Strain Gauges for Enhancing Accuracy and Precision," *IEEE Int. Conf. Mechatronics and Embedded Systems and Applications*, ShanDong, China, Jul. 15-17, 2010, pp. 192-195.

[57] C. Liu, "Piezoresistive Sensors," in *Foundations of MEMS*, New Jersey: Pearson, 2006, pp. 207-243.

----- Section 2.2.2 -----

[58] C. Liu, "Piezoelectric Sensing and Actuation," in *Foundations of MEMS*, New Jersey: Pearson, 2006, pp. 245-276.

[59] PCB Piezotronics Inc. (2012). *Piezoelectricity*. [Online]. Available: http://www.pcb.com/techsupport/tech_gen.php

[60] G. Gautschi. *Piezoelectric Sensorics: Force, Strain, Pressure, Acceleration and Acoustic Emission Sensors, Material and Amplifers*. Berlin, Heidelberg: Springer-Verlag, 2002.

[61] N. Kattavenos, B. Lawrenson, T. G. Frank, M. S. Pridham, R. P. Keatch and A. Cuschieri, "Force-sensitivie Tactile Sensor for Minimal Access Surgery," *Min. Invas Ther & Allied Technol.*, vol. 13, no. 1, pp. 42-46, 2004.

[62] J. Dargahi, M. Parameswaran and S. Payandeh, "A Micromachined Piezoelectric Tactile Sensor for an Endoscopic Grasper – Theory, Fabrication and Experiments," *J. Microelectromechanical Syst.*, vol. 9, no. 3, pp. 329-335, Sept. 2000.

[63] B. Choi, S. Lee, H. R. Choi and S. Kang, "Development of Anthropomorphic Robot Hand with Tactile Sensor: SKKU Hand II," *Int. Conf. Intelli. Robot. Syst (IROS)*, Beijing, China, Oct. 9-15, 2006, pp. 3779-3784.

[64] J. S. Son, E. A. Monteverde and R. D. Howe, "A Tactile Sensor for Localizing Transient Events in Manipulation," in *Proc. IEEE Int. Conf. Robotics and Automation (ICRA)*, San Diego, CA, May 8-13, 1994, pp. 471-476.

[65] E. S. Kolesar, Jr. and C. S. Dyson, "Object Imaging with a Piezoelectric Robotic Tactile Sensor," *J. Microelectromechanical Syst.*, vol. 4, no. 2, pp. 87-96, Jun. 1995.

[66] D. Goeger, N. Ecker and H. Woern, "Tactile Sensor and Algorithm to Detect Slip in Robot Grasping," in *IEEE Int. Conf. Robotics and Biomimetics*, Bangkok, Thailand, Feb. 21-26, 2009, pp. 1480-1485.

[67] L. Paredes-Madrid, P. Torruella, P. Solaeche, I. Galiana and P. Gonzalez de Santos, "Accurate Modeling of Low-cost Piezoresistive Force Sensors for Haptic Interfaces," in *Proc. IEEE Int. Conf. Robotics and Automation (ICRA)*, Anchorage, Alaska, May 3-8, 2010, pp. 1828-1833.

[68] M. F. Barsky, D. K. Lindner and R. O. Claus, "Robot Gripper Control System Using PVDF Piezoelectric Sensors," *IEEE Trans. Ultrasonics, Ferroelectronics and Frequency Control*, vol. 36, no. 1, pp. 129-134, Jan. 1989.

[69] D. P. J. Cotton, P. H. Chappell, A. Cranny, N. M. White and S. P. Beeby, "A Novel Thick-Film Piezoelectric Slip Sensor for a Prosthetic Hand," *IEEE Sensors J.*, vol. 7, no. 5, pp. 752-761, May 2007.

----- Section 2.2.3 -----

[70] L. K. Baxter, "Miscellaneous Sensors" in *Capacitive Sensors: Design and Applications*. New Jersey: IEEE PRESS, 1997, ch. 9, pp. 122-145. ISBN: 0-7803-5351-X.

[71] T. van Roon (2010, Sep. 26). 555 Timer Tutorial. [Online]. Available: http://www.sentex.ca/~mec1995/gadgets/555/555.html.

[72] R. S. Fearing, "Some Experiments with Tactile Sensing During Grasping," in *Proc. IEEE Int. Conf. Robotics and Automation (ICRA)*, Raleigh, North Carolina, Mar., 1987, pp. 1637-1643.

[73] H. Lee, S. Chang and E. Yoon, "A Flexible Polymer tactile Sensor: Fabrication and Modular Expandability for Large Area Deployment," *J. Microelectromechanical Syst.*, vol. 15, no. 6, pp. 1681-1686, Dec. 2006.

[74] K. Chun and K. D. Wise, "A High-Performance Silicon Tactile Imager Based on a Capacitive Cell," *IEEE Transactions on Electron Devices*, vol. 32, no. 7, pp. 1196-1201, Jul. 1985.

[75] F. Castelli, "An Integrated Tactile-Thermal Robot Sensor with Capacitive Tactile Array," *IEEE Trans. Ind. Applicat.*, vol. 38, no. 1, pp. 85-90, Jan. 2002.

[76] H. K. Chu, J. K. Mills and W. L. Cleghorn, "Design of a High Sensitivity Capacitive Force Sensor," in *Proc. IEEE Int. Conf. Nanotechnology*, Hong Kong, China, Aug. 2-5, 2007, pp. 29-33.

[77] A. Schmitz, M. Maggiali, L. Natale, B. Bonino and G. Metta, "A Tactile Sensor for the Fingertips of the Humanoid Robot iCub," in *Proc. IEEE/RSJ Int. Conf. Intell. Robot. Syst. (IROS)*, Taipei, Taiwan, Oct. 18-22, 2010, pp. 2212-2217.

---- Section 2.2.4 -----

[78] D. Jeong, J. Chu and Y. Lee, "Development of KNU Hand with Infrared LED-based Tactile Fingertip Sensor," in *Int. Conf. Control, Automation Syst.*, Seoul, Korea, Oct. 14-17, 2008, pp. 1156-1161.

[79] G. Palli and S. Pirozzi, "Miniaturized Optical-based Force Sensors for Tendon-driven Robots," in *Int. Conf. Robotics and Automation (ICRA)*, Shanghai, China, May 9-13, 2011, pp. 5344-5349.

[80] P. Puangmali, K. Althoefer and L. D. Seneviratne, "Mathematical Modeling of Intensity-Modulated Bent-Tip Optical Displacement

Sensors," *IEEE Trans. Instrum. Meas.*, vol. 58, no. 2, pp. 283-291, Feb. 2010.

[81] P. B. Buchade and A. D. Shaligram, "Influence of Fibre Geometry on the Performance of Two-fibre Displacement Sensor," *Sensors and Actuators A*, no. 136, pp. 199-204, 2007.

[82] A. M. Mazid and R. A. Russell, "A Robotic Opto-tactile Sensor for Assessing Object Surface Texture," in *IEEE Conf. Robotics, Automation and Mechatronics*, Bangkok, Thailand, Jun. 1-3, 2006, pp. 1-5.

[83] P. Polygerinos, A. Ataollahi, T. Schaeffter, R. Razavi, L. D. Seneviratne and K. Althoefer, "MRI-Compatible Intensity-Modulated Force Sensor for Cardiac Catheterization Procedures," *IEEE Trans. Biomed. Eng.*, vol. 58, no. 3, pp.721-726, Mar. 2011.

[84] O. Tohyama, S. Maeda and H. Itoh, "Fibre-Optic Tactile Microsensor for Detecting the Position of the Tip of a Fibrescope," *IEEE J. Selected Topics in Quantum Electronics*, vol. 5, no. 1, pp. 115-118, Jan. 1999.

[85] J. Peirs, J. Clijnen, D. Reynaerts, H. van Brussel, P. Herijgers, B. Corteville and S. Boone, "A Micro Optical Force Sensor for Force Feedback During Minimally Invasive Robotic Surgery," *Sensors and Actuators A*, no. 115, pp. 447-455, 2004.

[86] V. K. Kulkarni, A. S. Lalasangi, I. I. Pattanashetti and U. S. Raikar, "Fibre Optic Micro-displacement Sensor Using Coupler," *J. Optoelectronics and Advanced Materials*, vol. 8, no. 4, pp. 1610-1612, Aug. 2006.

[87] F. Luo, J. Liu, N. Ma and T. F. Morse, "A Fibre Optic Microbend Sensor for Distributed Sensing Application in the Structural Strain Monitoring," *Sensors and Actuators*, no. 75, pp. 41-44, 1999.

[88] J. Heo, C. Han and J. Lee, "System Design and Evaluation of the Robot Tactile Sensor Using the Microbending Fibre Optic Sensors," in *IEEE Int. Conf. Robot and Human Interactive Communication*, Jeju, Korea, Aug. 26-29, 2007, pp. 14-18.

[89] M. Koch, W. Richert and J. Schrage, "Optic-Tactile Robotics and Medical Applications," in *IEEE/ASME Int. Conf. Advanced Intelligent Mechatronics*, Xian, China, Jul. 2-5, 2008, pp. 493-497.

[90] K. Watanabe, K. Tajima and Y. Kubota, "Macrobending Characteristics of a Hetero-Core Splice Fibre Optic Sensor for Displacement and Liquid Detection," *IEICE Trans. Electron.*, vol. E83-C, no. 3, pp. 309-314, Mar. 2000.

[91] M. Nishiyama and K. Watanabe, "Wearable Sensing Glove with Embedded Hetero-Core Fibre-Optic Nerves for Unconstrained Hand Motion Capture," *IEEE Trans. Instrum. Meas.*, vol. 58, no. 12, pp. 3995-4000, Dec. 2009.

[92] F. Arregui, T. G. Brown, J. A. Buck, R. O. Claus, C. DeCusatis, P. J. Delfyett, E. Garmire, J. A. Harrington, K. O. Hill, I. Jacobs, G. Li, P. V. Mamyshev, I. Matias, D. Nolan, U. Österberg, J. C. Palais, A. E. Willner, Y. Xie, *Fibre Optics Handbook: Fibre, Devices and Systems for Optical Communications*. New York: McGraw-Hill, 2002.

[93] G. Rajan, D. Callaghan, Y. Semenova, M. McGrath, E. Coyle and G. Farrell, "A Fibre Bragg Grating-Based All-Fibre Sensing System for Telerobotic Cutting Applications," *IEEE Senors Journal*, vol. 10, no. 12, pp. 1913-1920, Dec. 2010.

[94] P. L. Swart, A. A. Chtcherbakov and A. J. van Wyk, "Dual Bragg Grating Sensor for Concurrent Torsion and Temperature Measurement," *Meas. Sci. Technol.*, no. 17, pp. 1057-1064, 2006.

[95] L. Kruger, P. L. Swart, A. A. Chtcherbakov and A. J. van Wyk, "Non-contact Torsion Sensor Using Fibre Bragg Gratings," *Meas. Sci. Technol.*, no. 15. pp. 1448-1452, 2004.

[96] X. G. Tian and X. M. Tao, "Torsion Measurement Using Fibre Bragg Gratings," *Experimental Mechanics*, vol. 41, no. 3, pp. 248-253, Sep. 2001.

[97] K. Totsu, Y. Haga and M. Esashi, "Ultra-miniature Fibre-optic Pressure Sensor Using White Light Interferometry," *J. Micromech. Microeng.*, no. 15, pp. 71-75, 2005.

[98] C. Chang and J. Sirkis, "Multiplexed Optical Fibre Sensors Using a Single Fabry-Perot Resonator for Phase Modulation," *J. Lightwave Technology*, vol. 14, no. 7, pp. 1653-1663, Jul. 1996.

[99] C. Lee, L. Lee, H. Hwang and J. Hsu, "Highly Sensitive Air-gap Fibre Fabry-Perot Interferometers Based on Polymer-Filled Hollow Core Fibres," *IEEE Photonics Technology Letters*, vol. 24, no. 2, pp. 149-151, Jan. 2012.

[100] S. Kim and J. Lee, "Phase-Shifted Transmission/Reflection-Type Hybrid Extrinsic Fabry-Perot Inteferometric Optical Fibre Sensors," *J. Lightwave Technology*, vol. 21, no. 3, pp. 797-804, Mar. 2003.

[101] T. Someya, T. Sekitani, S. Ibo, Y. Kato, H. Kawaguchi and T. Sakurai, "A large-area, Flexible Pressure Sensor Matrix with Organic Field-effect Transistors for Artificial skin Applications," *Proc. National Academy of Sciences of the United States of America (PNAS)*, vol. 101, no. 27, pp. 9966-9970., Jul. 2004.

[102] R. S. Dahiya, M. Valle, G. Metta, L. Lorenzelli and C. Collini, "Tactile Sensing Arrays for Humanoid Robots," *Proc. Conf. Research in*

Microelectronics and Electronics, Bordeaux, France, Jul. 2-5, 2007, pp. 201-204.

[103] R. M. Voyles, Jr., G. Fedder and P. K. Khosla, "Design of a Modular Tactile Sensor and Actuator Based on an Electrorheological Gel," in *Proc IEEE Int. Conf. Robotics and Automation (ICRA)*, Minneapolis, Minnesota, Apr. 22-28, 1996, pp. 13-17.

[104] N. Wettels, L. M. Smith, V. J. Santos and G. E. Loeb, "Deformable Skin Design to Enhance Response of a Biomimetic Tactile Sensor," in *IEEE RAS& EMBS Int. Conf. Biomedical Robotics and Biomechatronics*, Scottsdale, Arizona, Oct. 19-22, 2008, pp. 132-137.

---- Section 2.3 -----

[105] M. Kaneko, "Twin_head Six-Axis Force Sensor," *IEEE Trans. Robot. Autom.*, vol. 12, no. 1, pp. 146-154, Feb. 1996.

[106] P. J. Berkelman, L. L. Whitcomb, R. H. Taylor and P. Jensen, "A Miniature Instrument Tip Force Sensor for Robot/Human Cooperative Microsurgical Manipulation with Enhanced Force Feedback," in *Proc. Int. Conf. Medical Image Computing and Computer-Assisted Intervention (MICCAI)*, Pittsburg, Pennsylvania, Oct. 11-14, 2000, pp. 897-906.

[107] P. J. Berkelman, L. L. Whitcomb, R. H. Taylor and P. Jensen, "A Miniature Instrument Tip Force Sensor for Robot/Human Cooperative Microsurgical Manipulation with Enhanced Force Feedback," *IEEE Trans. Robot. Auto.*, vol. 19, no. 5, pp. 917-921, Oct. 2003.

[108] I. Fujii, T. Inoue, D. V. Dao, S. Sugiyana and S. Hirai, "Tactile Perception using Micro Force/Moment Sensor Embedded in Soft Fingertip," in *IEEE Sensors*, Daegu, Korea, Oct. 22-25, 2006, pp. 558-562.

[109] V. A. Ho, D. V. Dao, S. Sugiyama and S. Hirai, "Force/Moment Sensing During Sliding Motion Using a Micro Sensor Embedded in a Soft Fingertip," in *Int. Conf. Control, Automation, Robotics and Vision*, Hanoi, Vietnam, Dec. 17-20, 2009, pp. 161-166.

[110] V. A. Ho, D. V. Dao, S. Sugiyama and S. Hirai, "Development and Analysis of a Sliding Tactile Soft Fingertip Embedded with a Microforce/Moment Sensor," *IEEE Trans. Robot.*, vol. 27, no. 3, pp 411-424, Jun. 2011.

[111] Y. Hayashi, N. Tsujiuchi, T. Koizumi, H. Oshima, A. Ito and Y. Tsuchiya, "Optimum Design of the Thin-Type Four-Axis Force/Moment Sensor for a Robot Finger," in *36th Annu. Conf. IEEE Ind. Electron. Soc.*, Glendale, Arizona, Nov. 7-10, 2010, pp. 1287-1292.

[112] Y. Hayashi, N. Tsujiuchi, T. Koizumi, H. Oshima, A. Ito and Y. Tsuchiya, "Performance Evaluation of the Thin-Type Four-Axis Force/Moment Sensor as Two-Times Model for the Robot Hand's Fingertip," in *34th Annu. Conf. IEEE Ind. Electron. (ICON)*, Orlando, Florida, Nov. 10-13, 2008, pp. 1765-1770.

[113] M. S. Bartsch, W. Federle, R. J. Full and T. W. Kenny, "A Multiaxis Force Sensor for the Study of Insect Biomechanics," *J. Mircoelectromechanical Systems*, vol. 16, no. 3, pp. 709-718, Jun. 2007.

[114] A. Ito, N. Tsujiuchi, T. Koizumi, H. Oshima, Y. Nojiri, Y. Tsuchiya, N. Hirama and S. Kurogi, "Development and Structure Evaluation of Small Sensor Element for Distributed-Type Tri-Axial Force Sensor of Robot Finger," in *IEEE Int. Conf. Robotics and Biomimetics*, Sanya, China, Dec. 15-18, 2007, pp. 1309-1314.

[115] W. L. Jin and C. D. Mote, Jr., "Development of a Six-Component Miniature Force Sensor Using Silicon Micromachining and Conventional

Machining Technologies," *IEEE Trans. Instrum. Meas.*, vol. 47, no. 3, pp. 715-719, Jun. 1998.

[116] G. Kim, H. Shin and J. Yoon, "Development of a 6-axis Force/Moment Sensor for a Humanoid Robot's Foot," *Sensors and Actuators A*, no. 141, pp. 276-281, 2008.

[117] M. R. Wolffenbuttel and P. P. L. Regtien, "The Accurate Measurement of a Micromechanical Force Using Force-Sensitive Capacitances," *IEEE Trans. Instrum. Meas.*, vol. 44, no. 2, pp. 188-191. Apr. 1995.

[118] W. A. Lorenz, M. A. Peshkin and J. E. Colgate, "New Sensors for New Applications: Force Sensors for Human/Robot Interaction," in *Proc. IEEE Int. Conf. Robotics and Automation, Detroit, Michigan*, May 10-15, 1999, pp. 2855-2860.

[119] L. Ascari, P. Corradi, L. Beccai and C. Laschi, "A Miniaturized and Flexible Optoelectronic Sensing System for Tactile Skin," *J. Micromech. Microeng.*, no. 17, pp. 2288-2298, 2007.

[120] Z. Cui, Z. Han, H. Pan, Y. Shao and D. Zhu, "Design of a 3-axial Force/Torque Sensor for Arthroscopy Force Sensing," in *Int. Conf. Mechatronics and Automation*, Beijing, China, Aug. 7-10, 2011, pp. 243-248.

[121] J. Butterfab, M. Grebenstein, H. Liu and G. Hirzinger, "DLR-Hand II: Next Generation of a Dextrous Robot Hand," in *Proc. IEEE Int. Conf. Robotics and Automation (ICRA)*, Seoul, Korea, May 21-26, 2001, pp. 109-114.

[122] Y. Yamada and M. R. Cutkosky, "Tactile Sensor with 3-Axis Force and Vibration Sensing Functions and Its Application to Detect Rotational Slip," in *Proc. IEEE Int. Conf. Robotics and Automation (ICRA)*, San Diego, California, May 8-13, 1994, pp. 3550-3557.

[123] J. G. Rocha, C. Santos, J. M. Cabral and S. Lanceros-Mendez, "3 Axis Capacitive Tactile Sensor and Readout Electronics," in *IEEE Int. Symp. Ind. Electron. (ISIE)*, Montreal, Canada, Jul. 9-12, 2006, pp. 2767-2772.

[124] F. Beyeler, S. Muntwyler and B. J. Nelson, "A Six-Axis MEMS Force-Torque Sensor with Micro-Newton and Nano-Newtonmeter Resolution," *J. Microelectromechanical Systems*, vol. 18, no. 2, Apr. 2009, pp. 433-441.

[125] S. Muntwyler, F. Beyeler and B. J. Nelson, "Three-Axis Micro-Force Sensor with Sub-micro-Newton Measurement Uncertainty and Tunable Force Range," *J. Micromech. Microeng.*, no. 20, pp. 1-8, 2010.

[126] F. Beyeler, S. Muntwyler and B. J. Nelson, "Design and Calibration of a Microfabricated 6-Axis Force-Torque Sensor for Microrobotic Applications," in *Proc. Int. Conf. Robotics and Automation (ICRA)*, Kobe, Japan, May 12-17, 2009, pp. 520-525.

[127] Z. Chu, P. M. Sarro and S. Middelhoek, "Silicon Three-Axial Tactile Sensor," *Sensors and Actuators A*, no. 54, pp. 505-510, 1996.

[128] R. A. Brookhuis, R. J. Wiegerink, T. S. J. Lammerink, M. J. de Boer, K. Ma and M. C. Elwenspoek, "Scalable Six-Axis Force-Torque Sensor with a Large Range for Biomechanical Applications," in *IEEE Int. Conf. Micro Electro Mechanical Systems (MEMS)*, Paris, France, Jan. 29 – Feb. 2, 2012, pp. 595-598.

[129] H. Lee, J. Chung, S. Chang and E. Yoon, "Polymer Tactile Sensor Array with a Unit Cell of Multiple Capacitors for Three-Axis Contact Force Image Construction," in *Int. Conf. Micro Electro Mechanical Systems (MEMS)*, Hyogo, Japan, Jan. 21-25, 2007, pp. 623-626.

[130] R. D. Lorenz, K. M. Meyer and D. M. Van De Riet, "A Novel, Compliant, Four Degree-of-Freedom, Robotic Fingertip Sensor," in *IEEE Industry*

Applications Society Annual Meeting, Pittsburgh, Pennsylvania, Oct. 2-7, 1988, pp. 1414-1419.

[131] M. Ohka, N. Morisawa, H. Suzuki, J. Takata, H. Koboyashi and H. B. Yussof, "A Robotic Fingertip Equipped with an Optical Three-Axis Tactile Sensor," in *Proc. Int. Conf. Robotics and Automation*, Pasadena, California, May 19-23, 2008, pp. 3425-3430.

[132] M. Zhu, "A Three-Axis Finger Force Sensor Using Single-layer and Disc-Shaped Sensitive Plate," in *Int. Conf. on Measuring Technology and Mechatronics Automation*, Changsha City, China, Mar. 13-14, 2010, pp. 373-376.

[133] H. Yussof, J. Wada and M. Ohka, "Grasp Synthesis Based on Tactile Sensation in Robot Manipulation of Arbitrary Located Object," in *IEEE/ASME Int. Conf. on Advanced Intelligent Mechatronics*, Singapore, Jul. 14-17, 2009, pp. 560-565.

[134] H. Yussof, J. Wada and M. Ohka, "Sensorization of Robotic Hand Using Optical Three-Axis Tactile Sensor: Evaluation with Grasping and Twisting Motions," *J. Comput. Sci.*, vol. 6, no. 8, pp. 955-962, 2010.

[135] M. Ohka, Y. Mitsuya, Y. Matsunaga and S. Takeuchi, "Sensing Characteristics of an Optical Three-Axis Tactile Sensor Under Combined Loading," *Robotica*, vol. 22, pp. 213-221, Mar. 2004.

[136] R. Gassert, D. Chapuis, H. Bleuler and E. Burdet, "Sensors for Applications in Magnetic Resonance Environments," *IEEE/ASME Trans. Mechatronics*, vol. 13, no. 3, pp. 335-344, Jun. 2008.

[137] A. F. Fernandez, F. Berghmans, B. Brichard, P. Mégret, M. Decréton, M. Blondel and A. Delchambre, "Multi-component Force Sensor Based on Multiplexed Fibre Bragg Grating Strain Sensors," *Meas. Sci. Technol.*, no. 12, pp. 1-4, 2001.

[138] Y. Park, K. Chau, R. J. Black and M. R. Cutkosky, "Force Sensing Robot Fingers using Embedded Fibre Bragg Grating Sensors and Shape Deposition Manufacuring," in *Proc. Int. Conf. Robotics and Automation*, Roma, Italy, Apr. 10-14, 2007, pp. 1510-1516.

[139] M. Luo, X. Luo and C. Pan, "A Stewart Platform-based 3-axis Force Sensor for Robot Fingers," in *Int. Conf. Mechanic Automation and Control Engineering (MACE)*, Hohhot, China, Jul. 15-17, 2011, pp. 37-40.

[140] T. A. Dwarakanath, T. K. Bhaumick and D. Venkatesh, "Implementation of Stewart Platform Based Force-Torque Sensor," in *Proc. IEEE/SICE/RSJ Int. Conf. Multisensor Fusion and Integration for Intelligent Systems*, Taipei, China, Aug. 15-18, 1999, pp. 32-37.

[141] U. Seibold, B. Kübler and G. Hirzinger, "Prototype of Instrument for Minimally Invasive Surgery with 6-Axis Force Sensing Capability," in *Proc. IEEE Int. Conf. Robotics and Automation*, Barcelona, Spain, Apr. 18-22, 2005, pp. 496-501.

====== Chapter 3 ======

[142] Industrial Fibre Optics, Inc., Eska Optical Fibre. [Online]. Available: http://i-fibreoptics.com/eska-optical-fibre.php.

[143] Edmund Optics, Inc., Optical Grade Fibre Optics. [Online]. Available: http://www.edmundoptics.com/optics/fibre-optics/optical-grade-fibre-optics/1352.

[144] Maplin Electronics, SFH300-2 Phototransistor. [Online]. Available: http://www.maplin.co.uk/sfh300-2-phototransistor-17936.

[145] D. Halliday, R. Resnick and J. Walker, "Electromagnetic Waves," in *Fundamentals of Physics, 6th Ed, Extended*, New York: John Wiley & Sons Inc., 2001, ch. 34, pp. 801-832.

[146] W. C. Young and R. G. Budynas, *Roark's Formulas for Stress and Strain 7th Ed*. New York: McGraw-Hill, 2002, pp. 109-406.

[147] CVI Meller Griot. "Gaussian Beam Optics." [Online]. Available: http://www.cvimellesgriot.com/Products/Documents/TechnicalGuide/Gaussian-Beam-Optics.pdf, Jul. 8, 2009, [Dec. 21, 2011].

[148] B. P. PAL, *Fundamentals of Fibre Optics in Telecommunication and Sensor Systems*, New Delhi: New Age International Ltd, 1992, pp.11-332.

[149] B. E. A Saleh and M. C. Teich, *Fundamentals of Photonics*. New Jersey: John Wiley & Sons, 2007, pp.73-363.

[150] C. Awanzino, L. Letellier, J. M. Lavest, M. Dhome and C. Faye, "A Polarization of Light Based System, designed for Real Time Applications in Computer Vision, making Use of Highlights in a Metallic Environment," in *Proc. IEEE Workshop on Applications of Computer Vision (WACV)*, Princeton, New Jersey, Oct. 19-21, 1998, pp. 128-133.

[151] W. Zhang, A. Potts, A. Papakostas and D. M. Bagnall, "Intensity Modulation and Polarization Rotation of Visible Light by Dielectric Planar Chiral Metamaterials," *Applied Physics Letters*, no. 86, pp. 1-3, 2005.

[152] J. Niu and J. Xu, "Coupling Efficiency of Laser Beam to Multimode Fibre," *Optics Communications*, no. 274, pp. 315-319, 2007.

[153] P. V. P. Yupapin and S. Kusamran, "Photoelastic Materials Characteristics Based on the Stress-Induced Effect for Sensor Application," *Smart Mater. Struct.*, no. 2, pp. 157-161, 1993.

[154] Autodesk, Inc., "Autodesk Invemtor Products." [Online]. Available: http://usa.autodesk.com/autodesk-inventor/. Feb. 01, 2013. [Feb. 02, 2013].

====== Chapter 4 ======

[155] Barrett Technology, Inc., "BarrettHand Overview." [Online]. Available: http://www.barrett.com/robot/products-hand.htm. Feb. 01, 2013.

[156] ATI Industrial Automation, Inc., "F/T Sensor: Mini40." [Online]. Available: http://www.ati-ia.com/products/ft/ft_models.aspx?id=Mini40. 2011. [Feb. 03, 2013].

[157] Genlab Ltd, "General Purpose Ovens." [Online]. Available: http://www.genlab.co.uk/laboratory/general-purpose-ovens. [Feb. 03, 2013].

======

[158] H. Su, M. Zervas, C. Furlong and G. S. Fischer, "A Miniature MRI-Compatible Fiber-optic Force Sensor Utilizing Fabry-Perot Interferometer," in *MEMS and Nanotechnology,* vol. 4, *Conference Proceedings of the Society for Experimental Mechanics Series*, New York: Springer, 201, pp. 131-136. ISBN: 978-1-4614-0209-1.

[159] P. Polygerinos, L. D. Seneviratne, R. Razavi, T. Schaeffter and K. Althoefer, "Triaxial Catheter-Tip Force Sensor for MRI-Guided Cardiac Procedures," *IEEE/ASME Trans. Mechatronics*, vol. 18, no. 1, pp. 386-396, Feb. 2013.

========= Chapter 5 =========

[160] R. S. Stoughton and T. Arai, "A Modified Stewart Platform Manipulator with Improved Dexterity," *IEEE Trans. Robotics and Automation*, vol. 9, no. 2, pp. 166-173, Apr. 1993.

[161] J. E. McInroy, G. W. Neat and J. F. O'Brien, "A Robotic Approach to Fault-tolerant, Precision Pointing," *IEEE Robotics & Automation Magazine*, vol. 6, no. 4, pp. 24-31, 37, Dec. 1999.

[162] R. Saltaren, R. Aracil, C. Alvarez, E. Yime and J. M. Sabater, "Field and Service Applications – Exploring Deep Sea by Teleoperated Robot – An Underwater Parallel Robot with High Navigation Capabilities," *IEEE Robotics & Automation Magazine*, vol. 14, no. 3, pp. 65-75, Sep. 2007.

[163] Y. Yu, W. Liang and Y. Ge, "Analysis of Parallel Mechanism for Human Hip Joint Power Assist," in *Proc. 8th World Congress on Intelligent Control and Automation*, Jinan, China, Jul. 6-9, 2010, pp. 1444-1449.

[164] J. S. Navarro, N. Garcia, C. Perez, E. Fernandez, R. Saltaren and M. Almonacid, "Kinematics of a Robotic 3UPS1S Spherical Wrist Designed for Laparoscopic Applications," *Int. J. Med Robotics Comput. Assist. Surg.*, no. 6, pp. 291-300, May, 2010.

[165] H. Tian, D. Wu, Z. Du and L. Sun, "Design and Analysis of a 6-DOF Parallel Robot Used in Artificial Cervical Disc Replacement Surgery," in *Int. Conf. on Information and Automation*, Harbin, China, Jun. 20-23, 2010, pp. 30-35.

[166] L. B. Kratchman, G. S. Blachon, T. J. Withrow, R. Balachandran, R. F. Labadie and R. J. Webster III, "Design of a Bone-Attached Parallel Robot for Percutaneous Cochlear Implantation," *IEEE Trans. Biomed Eng.*, vol. 58, no. 10, pp. 2904-2910, Oct. 2011.

[167] T. Ortmaier, R. Konietschke, B. Kubler, U. Seibold, A. Tobergte, M. Nickl, S. Jorg and G. Hirzinger, "Telemanipulator for Remote Minimally

Invasive Surgery," *IEEE Robotics & Automation Magazine*, vol. 15, no. 4, pp. 28-38, Dec. 2008.

[168] J. Yao, Y. Hou, L. Lu and Y. Zhao, "Analysis of a Pre-stressed Six-component Force/Torque Sensor Based on Stewart Platform," in *Int. Conf. Robotics and Biomimetics*, Kunming, China, Dec. 17-20, 2006, pp. 346-350.

[169] C. Kang, "Closed-form Force Sensing of a 6-Axis Force Transducer based on the Stewart Platform," *Sensors and Actuators A*, no. 90, 2001, pp. 31-37.

[170] T. A. Dwarakanath, T. K. Bhaumick and D. Venkatesh, "Implementation of Stewart Platform Based Force-Torque Sensor," in *Proc. IEEE Int. Conf. Multisensor Fusion and Integration for Intelligent Systems*, Taipei, Taiwan, Aug. 15-18, 1999, pp. 32-37.

[171] J. Zhang, H. Yu, F. Gao and X. Zhao, "Key Issues in Studying Parallel Manipulators," in *Proc Int. Conf. Advanced Mechatronic Systems*, Zhengzhou, China, Aug. 11-13, 2011, pp. 234-244.

[172] Y. Zhao, T. Zhao, R. Wen and H. Wang, "Performance Analysis and Optimization of Sizable 6-Axis Force Sensor Based on Stewart Platform," in *Int. Conf. Mechatronics and Automation*, Harbin, China, Aug. 5-8, 2007, pp. 2189-2193.

[173] C. Jacq, B. Luthi, T. Maeder, O. Lambercy, R. Gassert and P. Ryser, "Thick-film Multi-DOF Force/Torque Sensor for Wrist Rehabilitation," *Sensors and Actuators A*, no. 162, pp. 361-366, 2010.

[174] T. Wu, J. Chen and S. Chang, "A Six-DOF Prismatic-Spherical-Spherical Parallel Compliant Nanopositioner," *IEEE Trans. Ultrasonics, Ferroelectronics and Frequency Control*, vol. 55, no. 12, pp. 2544-2551, Dec. 2008.

[175] K. Zhang, J.S. Dai and Y. Fang, "Geometry and Constraint Based Design of Metamorphic Parallel Mechanisms," in *Proc. ASME 2011 International Design Engineering Technical Conferences & Computers and Information in Engineering Conference (IDETC/CIE)*, Washington, DC, Aug. 28-31, 2011, pp. 1-10.

[176] J. Zhang, H. Yu, F. Gao, D. Zhang, X. Zhao and C. Ma, "A 6-DOF Heavy-Load Parallel Manipulator with RFTA and its Application," in *IEEE Int. Conf. Robotics and Automation (ICRA)*, Shanghai, China, May 9-13, 2011, pp. 470-475.

[177] T. A. Dwarakanath and D. Venkatesh, "Simply Supported, 'Joint less' Parallel Mechanism Based Force-Torque Sensor," *Mechatronics*, no. 16, pp. 565-575, 2006.

[178] R. Frigola, L. Ros, F. Roure and F. Thomas, "A Wrench-Sensitive Touch Pad Based on a Parallel Structure," in *IEEE Int. Conf. Robotics and Automation (ICRA)*, Pasadena, California, May 19-23, 2008, pp. 3449-3454.

[179] S. Lee, W. Kim, B. Yi and I. Suh, "Analysis of Two 3-DOF Parallel Mechanism with Constrained Stewart Platform Structure," in *Proc. IEEE Int. Conf. Robotics and Automation (ICRA)*, Orlando, Florida, May 15-19, 2006, pp. 4227-4233.

==== Noise Reduction ===

[180] J. Peirs, J. Clijnen, D. Reynaerts, H. Van Brussel. P. Herijgers, B. Corteville and S. Boone, "A Micro Optical Force Sensor for Force Feedback During Minimally Invasive Robotic Surgery," *Sensors and Actuators A*, no. 115, pp. 447-455, 2004.

[181] S. Landis and B. Bobrovsky, "1/*f* Baseband Noise Suppression in OFDM Systems," *IEEE Trans. Commun.*, vol. 59, no. 4, pp. 942-947, Apr. 2011.

[182] H. Tian and A. El Gamal, "Analysis of 1/*f* Noise in Switched MOSFET Circuits," *IEEE Trans. Circuits and Systems – II: Analog and Digital Signal Processing*, vol. 48, no. 2, pp. 151-157, Feb. 2001.

[183] F. L. Walls, E. S. Ferre-Pikal and S. R. Jefferts, "Origin of 1/fPM and AM Noise in Bipolar Junction Transistor Amplifiers," *IEEE Trans. Ultrasonics, Ferroelectronics and Frequency Control*, vol. 44, no. 2, pp. 326-334, Mar. 1997.

[184] D. Wenn, "Implementing Digital Lock-In Amplifier Using the dsPIC DSC," [Online]. *AN1115*. Available: http://ww1.microchip.com/downloads/en/AppNotes/01115A.pdf.

[185] Symétrie, "The Right Solution," [Online]. Available: http://www.symetrie.fr/en/hexapod-technology/.

[186] R. Sargeant, L. D. Seneviratne, and K. Althoefer, "An Investigation of the Use of Linear Polarizers to Measure Force and Torque in Optical 6-DOF Force/Torque Sensors for Dexterous Manipulators", *IEEE Int. Conf. Robotics and Automation*, St. Paul, Minnesota, 2012.

[187] Memry Cooperation (2012). Nitinol Strip. [Online]. Available: http://memry.com/products-services/material/strip.